Dissertation

submitted to the

Combined Faculties of the Natural Sciences and Mathematics

of the Ruperto-Carola-University of Heidelberg. Germany

for the degree of

Doctor of Natural Sciences

Put forward by

Sarah Katherine Leslie

born in Perth, Australia

Oral examination: 24 July 2019

The Cosmic Evolution of Star-Forming Galaxies

Referees:

Prof. Dr. Hans-Walter Rix

Prof. Dr. Ralf Klessen

Abstract

Galaxies separate into passive and star-forming galaxies, where star-forming galaxies show a tight correlation between stellar mass and star formation rate (SFR), referred to as the star-forming main sequence. In this thesis, we have measured the average galaxy star formation rate – stellar mass relation out to $z \sim 5$ in the COSMOS (Cosmic Evolution Survey) field. This survey includes deep radio observations taken as part of the VLA-COSMOS 3 GHz large program that provide a dust-unbiased view of star-formation. To measure SFRs over a wide range of galaxy masses, including galaxies too faint to be detected individually, we employed a stacking analysis on the 3 GHz data. We found a flattening of the star-forming main sequence at high masses that can be explained by the increasing fraction of bulge-dominated galaxies which follow a shallower SFR – stellar mass relation than disk-dominated galaxies. As bulges grow more prominent in the low-redshift galaxy population, the flattening of the main sequence becomes more significant. We found that galaxy environment, probed by X-ray-groups and local galaxy number density, has no significant effect on the shape of the star-forming main sequence at $z > 0.3$. We have compared SFRs derived from publicly available mid-infrared (MIR), far-infrared (FIR), radio, and ultraviolet (UV) photometry for massive star-forming galaxies selected consistently at $z \sim 0$ and $z \sim 0.7$. We probed the dust properties of these massive disk galaxies by analysing how their UV luminosity depends on galaxy inclination. By comparing our observed trends with radiative transfer model predictions we constrained the average opacity and clumpiness of the dust. We found that UV attenuation has increased between $z \sim 0$ and $z \sim 0.7$ by a factor of ~ 3.5. A higher fraction of clumpy dust around nascent star-forming regions can explain the substantial UV attenuation at $z \sim 0.7$. If the gas and dust geometry at high-redshift are significantly different than inferred from our current models, this would have significant implications for our SFR calibrations relying on the UV and IR emission from galaxies. Reproducing the spatial distribution of galaxy components like stellar mass, newly formed stars, dust, metals, and gas will be a key objective for future theories of galaxy evolution.

Zusammenfassung

Galaxien werden anhand ihrer Sternentstehungsaktivität unterschieden, wobei aktive Galaxien einen engen Zusammenhang zwischen ihrer Sternmasse und Sternentstehungsrate (SFR) aufzeigen, was als Sternentstehungs-Hauptreihe (engl.:“star-forming main sequence”) bezeichnet wird. In dieser Arbeit haben wir den Zusammenhang zwischen der mittleren Sternentstehungsrate und der Sternmasse von Galaxien im COSMOS (Cosmic Evolution Survey) Feld untersucht. Diese Studie umfasst unter anderem tiefe Radio-Beobachtungen, aufgenommen als Teil des VLA-COSMOS 3 GHz Beobachtungsprogramms, welche von Staub unverfälschte Informationen über die Sternentstehung liefern. Um die SFR über einem großen Intervall von Galaxienmassen zu messen – insbesondere für Galaxien, die aufgrund ihrer niedrigen Leuchtkraft nicht selbst detektiert werden können – haben wir die 3 GHz Daten mit einem Bildstapelalgorithmus analysiert. Wir haben eine Abflachung der Sternentstehungs-Hauptreihe bei größeren Galaxienmassen festgestellt, welche durch den größeren Anteil von Galaxien mit zentraler Bulge-Komponente erklärt werden kann, da diese einem flacheren SFR-Sternmasse Zusammenhang als reine Scheibengalaxien folgen. Dadurch, dass zentrale Bulge-Komponenten zu niedrigen Rotverschiebungen hin häufiger auftreten, wird die Abflachung der Hauptreihe signifikanter. Wir haben herausgefunden, dass die Umgebung von Galaxien, gemessen anhand von Galaxiengruppen mit Röntgenemission und lokaler Galaxiendichte, keinen signifikanten Einfluss auf die Form der Sternentstehungs-Hauptreihe bei $z > 0.3$ hat. Wir haben die SFRs, abgeleitet von öffentlich zugänglicher Mittinfrarot- (MIR), Ferninfrarot- (FIR), Radio- und Ultraviolett- (UV) Photometrie, für massereiche sternbildende Galaxien verglichen, welche auf gleiche Art und Weise bei $z \sim 0$ und $z \sim 0.7$ ausgewählt wurden. Wir haben die Staub-Eigenschaften in diesen massereichen Scheibengalaxien bei $z \sim 0$ und $z \sim 0.7$ untersucht, indem wir die Abhängigkeit ihrer UV-Leuchtkraft von der Galaxien-Inklination analysiert haben. Durch den Vergleich von beobachteten Trends mit Vorhersagen von Strahlungstransportmodellen haben wir die mittlere Opazität und den Anteil des klumpigen Staubs bestimmt. Wir haben herausgefunden, dass die UV-Abschwächung zwischen $z \sim 0$ und $z \sim 0.7$ um einen Faktor ~ 3.5 angesteit. Ein erhöhrter Anteil von Staubwolken um entstehenede Sternbildungsregionen herum kann die erhebliche UV-Abschwächung bei $z \sim 0.7$ erklären. Falls die Verteilung von Gas und Staub bei hohen Rotverschiebungen signifikant von unseren aktuellen Modellen abweicht, würde das auch signifikante Abweichungen für unsere SFR-Kalibration basierend auf der UV- und IR-Emission von Galaxien bedeuten. Die Reproduktion der räumlichen Verteilung der galaktischen Komponenten wie beispielsweise Sternmasse, Sternentstehung, Staub, Metalle und Gas wird das wesentliche Ziel für die zukünftigen Modelle der Galaxienentwicklung sein.

Contents

1 Introduction

1.1. The history of the Universe in one day

Let me tell you the story of the Cosmos; how did our story begin, how did we get to where we are today, and where will the future take us?

The global rate of star formation per unit volume, or the star formation rate density (SFRD), is a fundamental parameter for understanding the formation and evolution of galaxies, and its measurement will be a central topic of this thesis. The overall cosmic SFRD in the Universe as a function of cosmic time, or redshift, is reminiscent of the Sun's motion across the sky (see Figure 1.1). In the astronomical community, extragalactic astronomers have started referring to the epoch where SFRD peaks as "cosmic (high) noon". In this context, we will now compress the 13.8 billion year history of the Universe into a Cosmic Day. Our galaxy, the Milky Way, was formed at least 12 Gyr ago, with the oldest objects in the Milky Way, globular clusters, having ages of ∼12.7 billion years (Krauss & Chaboyer, 2003). The thin disk of the Milky Way formed ∼ 8.8 billion years ago (del Peloso et al., 2005). Our solar system formed ∼4.6 Gyr ago (Bouvier & Wadhwa, 2010) with the oldest rocks known on earth dating back to 4.4 Gyr (Wilde et al., 2001). The first multicellular life appeared 800 Myr ago (Erwin et al., 2011). Mammals appeared 200 Myr ago and non-avian dinosaurs died out 65 Myr ago (Renne et al., 2013). Homo sapiens are thought to have emerged as a species only 200,000 - 500,000 years ago (Trinkaus, 2005).

The infant Universe

Our current understanding is that space and time have not existed forever, they were created in an initial "Big Bang". In the beginning, the Universe was so hot and dense that what occurred before 10^{-32} seconds is outside of our current understanding of Physics. In traditional Big-Bang cosmology the four fundamental interactions or forces emerged in the Plank epoch: gravity, followed by the strong, weak and electromagnetic interactions. Quantum fluctuations caused small perturbations in the homogeneous and isotropically expanding universe. It is believed that the Universe experienced a period of exponential expansion, "inflation", that effectively separated regions initially in causal contact, essentially freezing the quantum fluctuations into large scale perturbations (Guth, 1981; Dodelson, 2003). After the period of cosmic inflation the Universe was filled with hot quark-gluon plasma.

As the Universe expanded and cooled down individual particles decoupled from thermal

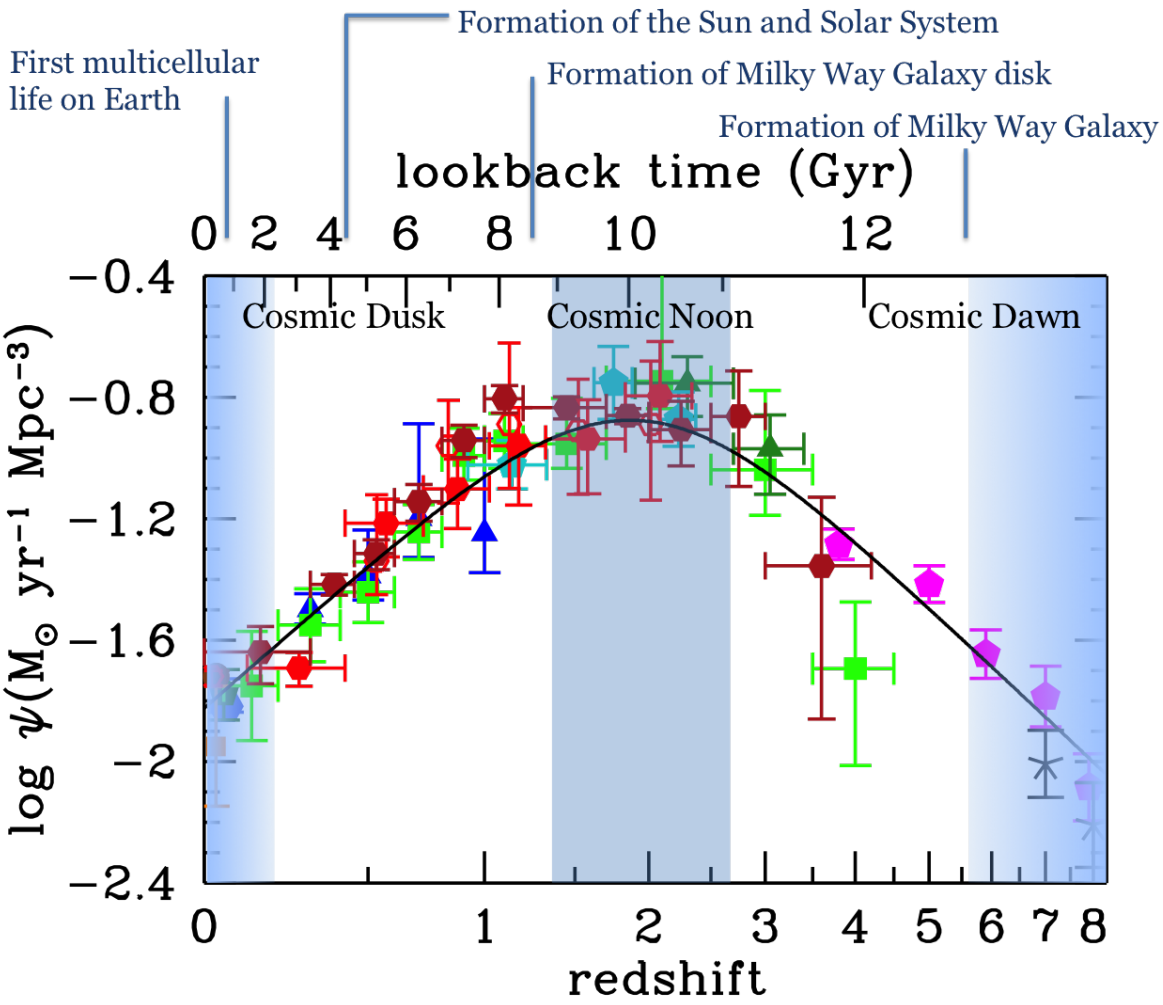

Figure 1.1.: The Cosmic Day: The history of cosmic star formation from a combination of ultraviolet and infrared rest-frame measurements adapted from Madau & Dickinson (2014).

equilibrium. The first species to decouple was the postulated dark matter. Dark matter only weakly interacts with forces other than gravity (Bertone et al., 2004), and thus it started to follow the primordial density fluctuations and helped grow the perturbations.

By one-second after the Big Bang, quarks have been bound into hadrons. A slight matter-antimatter asymmetry resulted in all the anti-hadrons being annihilated. Neutrinos also decoupled from thermal equilibrium. From $t = 3$ - 20 minutes, the conditions were right for nucleosynthesis and around 25% of protons and all neutrons fused into heavier elements including helium-4, and small amounts of deuterium, helium-3, and lithium-7. At this time, the observable Universe was about 300 light-years in radius and most of the energy was in electromagnetic radiation. Unlike the dark matter, the baryon-photon fluid was trapped in standing density waves (baryon acoustic oscillations (BAO)) due to gas pressure. BAO matter clustering provides a standard ruler for length scale in cosmology – the maximum distance the acoustic waves could travel in the primordial plasma while the Universe was too hot to form electrons to bind to nuclei.

At $t = 380{,}000$ years the Universe became cool enough for neutral atoms to form, called

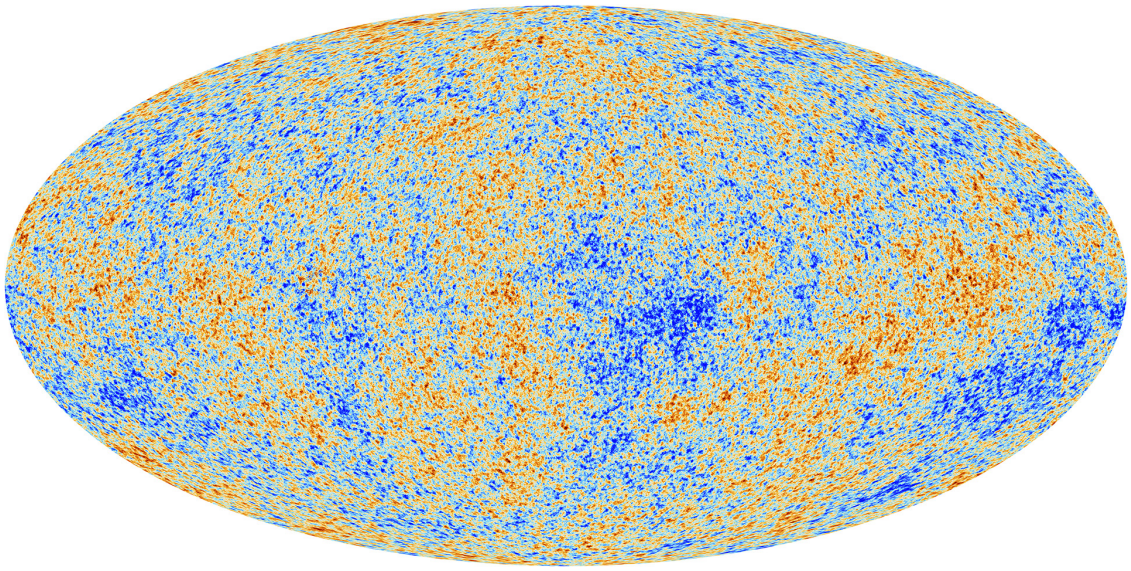

Figure 1.2.: The anisotropies of the cosmic microwave background (CMB) as observed by Planck. The CMB is a snapshot of the oldest light in our Universe, emitted as the first neutral atoms began to form when the Universe was just 380,000 years old. It shows tiny temperature fluctuations that correspond to regions of slightly different densities, representing the seeds of all future structure: the galaxies and clusters of today. Credit: European Space Agency and the Planck Collaboration (2013)

recombination for historical reasons. Photons were no longer in thermal equilibrium with matter, and as a result, the Universe became transparent for the first time. The newly formed atoms (mostly hydrogen and helium and trace amounts of lithium) released photons as they quickly reach their ground state. These photons can be detected today as the cosmic microwave background (CMB), the oldest observation we currently have of the Universe (Figure 1.2). Observations of the CMB power spectrum (the strength of its temperature fluctuations at a given angular scale) have also shown that the Universe must be composed of various forms of energy. Today, the largest fraction of the Universe's energy density is an unknown type of energy called dark energy ($\sim 69\%$) which seems to be driving the accelerated expansion of the Universe. Dark matter contributes $\sim 26\%$ and ordinary baryonic matter (like stars and gas) only contributes $\sim 5\%$ to the energy density of the Universe (Planck Collaboration et al., 2014). Around the same time as recombination, the BAO became embedded in the distribution of matter as it condensed, giving rise to a very slight preference in the distribution of large-scale objects. Therefore, the CMB provides a snapshot of the tiny fluctuations that are the seeds to all future structure in the Universe. After recombination, the energy density of radiation became negligible, and gravity took over as the dominant force, allowing for the accumulation of matter and the growth of structures.

Before we continue our journey, it might be useful to review what redshift means. Redshift, z, quantifies the ratio of the observed wavelength λ_o to the emitted wavelength λ_e of light.

$$1 + z = \frac{\lambda_o}{\lambda_e} = \frac{R(t_{\text{now}})}{R(t_e)} \tag{1.1}$$

where $R(t)$ is the scale factor that describes the time evolution of our approximately isotropic homogeneous Universe. Thus, when we observe a galaxy at $z = 9$, we are observing light that was emitted from a galaxy when the Universe was just 1/10th of its present size. The precise age that this size corresponds to depends on the dynamics of the expansion. From the assumption that the Universe is isotropic and homogeneous on large scales, and Einstein's theory of General Relativity, the Friedmann-Lemaître equations (Friedmann, 1922; Lemaître, 1927) can be derived for the scale factor $a(t) = R(t)/R_0$, describing the expansion of the Universe (Peebles, 1980):

$$\left(\frac{\dot{a}}{a}\right)^2 = \frac{8\pi G}{3}\rho - \frac{Kc^2}{a^2} + \frac{\Lambda}{3}\frac{\ddot{a}}{a} = -\frac{4\pi G}{3}\left(\rho + \frac{3P}{c^2}\right) + \frac{\Lambda}{3} \tag{1.2}$$

where G is the gravitational constant, c is the speed of light, ρ is the energy density of the Universe in matter and radiation and K is the term describing the spatial curvature of the Universe (e.g. open, flat, or closed). The cosmological constant Λ accounts for the effect of Dark Energy and P is the pressure (related to density via the equation of state).

Cosmic pre-dawn: The Dark Ages[1]

In the time between recombination and the formation of the first stars ($0.38 \lesssim t \gtrsim 150$ Myr), the Universe was transparent and there were no new sources of light. The only photons present during this time were those released during recombination (CMB photons) which quickly (within about 3 Myr) redshifted to infrared wavelengths, and the hyperfine 21 cm radio emission occasionally emitted by hydrogen atoms[2]. This period, devoid of visible light, is known as the *dark ages*. During the dark ages, the temperature of the Universe cooled from $\sim$4,000 K to about 60 K.

Due to the gravitational force of both dark matter and baryons, individual over-dense regions grew by accretion in a hierarchical fashion until a network of walls and filaments formed the "cosmic web". At the intersections of dark matter filaments the over-densities are the highest. There, spherical dark matter halos form. The formation of the first stars occurs in systems that have reached sufficiently large masses so that gas cooling becomes important and baryons can go into runaway collapse within the dark matter halo.

The first stars are referred to as *Population III* and have not yet been observed, but they may have been huge and non-metallic with very short lifetimes. There is still little consensus on the physical processes that give rise to the first generation of stars, but numerical simulations indicate that Population III stars should form as members of multiple stellar systems with separations as small as the distance between the Earth and the Sun (Klessen, 2018). The first-star formation likely started 150 Myr after the Big Bang in the rare densest regions, and then rapidly became more possible. The first stars play a key role in enriching their surroundings with metals. As regions of the Universe become more enriched by super-

[1] Despite the motivational saying, it is not actually always darkest before the dawn. In the absence of weather and light pollution, the brightness of the sky is determined mostly by the phase of the Moon. During the two weeks following a new moon, the Moon can be seen after sunset but not before sunrise, and so during this time, it is darkest before the dawn. On the other hand, it is always the coldest before the dawn. But, the Universe was still hot during the Dark Ages, so our analogue breaks down.

[2] Observations are underway to try to detect this, e.g. Low Frequency Array (LOFAR)

novae ejecta, genuine metal-free Population III stars become increasingly rare, and there is a transition to *Population II* star formation.

1.1.1. Cosmic Dawn: The first galaxies

The Dark Ages ended with the formation of the first galaxies that form in the centres of dark matter halos. The first stars and black holes emit ultraviolet radiation above 13.6 eV that ionizes the neutral hydrogen around them, beginning the **Epoch of Reionization**[3]. In the most massive dark matter halos corresponding to 2σ peaks in the Gaussian random field of initial density perturbations, atomic hydrogen cooling is more efficient, allowing sustained star formation.

These first galaxies are predicted to form at roughly 500 Myr after the Big Bang and should be observable with upcoming telescopes such as the *James Webb Space Telescope* (JWST) and 30 m ground-based optical and near-infrared (NIR) telescopes. As reionization progresses with more objects forming that emit ultraviolet (UV) radiation, an evolving patchwork of ionized hydrogen (HII) bubbles grows until the whole Universe is ionized. Much is still unknown about the details of reionization, such as how much ionizing radiation did the first sources produce and how much escapes into the intergalactic medium? Current constraints suggest that this epoch lasts until $z \sim 6$, 1 Gyr after the Big Bang (Fan, 2006). The observational methods for studying reionization include studying the spectra of distant quasars[4]. For example, quasars above $z = 6$ show evidence for a "Gunn-Peterson trough" (Gunn & Peterson, 1965), indicating that neutral hydrogen was present in the intergalactic medium, whereas quasars below $z = 6$ do not, meaning that the hydrogen was ionized. The epoch of reionization represents the last major transition phase of the Universe. At the end of this epoch, the Universe emerged with a neutral hydrogen fraction of 10^{-5}.

In recent years we have witnessed an observational revolution in the study of galaxies in the early Universe ($z > 5$), with thousands of galaxies having been observed at $z > 5$, with the redshift record currently being at $z = 11.09$ (Oesch et al., 2016). Two main techniques are used to locate galaxies at $z > 5$. The dropout technique relies on the fact that the neutral hydrogen in the Universe readily absorbs light bluer than Lyα 121.6 nm, resulting in a distinctive break in the spectrum of an object. For galaxies at high redshift, this break will occur at redder observed wavelengths (e.g. 851 nm at $z = 6$). Taking deep images at both optical and near-infrared wavelengths and identifying objects that disappear in the bluer bands can build samples of Lyman-break or Lyman-dropout galaxies, whose redshifts

[3]Recently, Bowman et al. (2018a) using the Experiment to Detect the Global Epoch of Reionization Signature (EDGES) radio telescope have identified indirect evidence that the earliest stars formed 180 million years after the Big Bang. It is predicted (Pritchard & Loeb, 2012) that the light from the first stars would have altered the excitation state of the 21 cm line from primordial hydrogen. This would allow the gas to absorb photons from the CMB, resulting in a dip in the spectrum of radio emission from the whole sky at frequencies observable today at < 200 MHz. The strength of the dip was at least twice as large as expected which could indicate that the gas was cooled, perhaps by dark matter. Whether this is a true detection of the 21 cm absorption signal from the early Universe is still highly uncertain with concerns regarding the foreground model (Hills et al., 2018; Bowman et al., 2018b).

[4]Quasars are luminous active galactic nucleus (AGN). Most large galaxies today harbour super-massive black hole (SMBH) in their centres (e.g., Kormendy & Richstone 1995; Ferrarese & Ford 2005). An important open question regarding galaxy formation is when and how galaxies first obtained such central black holes.

can be confirmed with follow-up spectroscopy. The other main method involves using a narrow-band filter to target the strong Lyman-α emission line (Stiavelli, 2009).

In the standard Λ-cold dark matter (CDM) picture, the earliest galaxies were small dwarfs which grew by colliding and coalescing with each other. Galaxies also grow by the accretion of gas from the cosmic web. When gas enters the dark matter halo it gets shock heated to the virial temperature (Rees & Ostriker, 1977) and then must cool before it can settle onto the disk of the galaxy. Cold streams might be able to feed gas into the lowest mass halos without getting shock heated (e.g. Silk 1977; Dekel et al. 2009; Mandelker et al. 2019). The dissipational collapse of rotating gas clouds within a virialized dark matter halo is expected to produce a centrifugally supported disk (Fall & Efstathiou, 1980; Mo et al., 1998). Galaxies began to form "proto-clusters" from about $z = 6$.

1.1.2. Cosmic Noon: Period of maximal stellar growth

The cosmic SFRD increases from $z > 5$ to $z \sim 2$. As dark matter (DM) halos grow, more of them host star-forming galaxies (Tacchella et al., 2013). As we will discuss in this thesis, the measurements of the SFRD at $z > 2$ are still uncertain. At $z \sim 2$, the Universe was more active with a peak in black hole accretion (Fan, 2006) as well as a peak in dust extinction, star formation rate (SFR) density, and possibly molecular gas density. This thesis concerns the evolution of galaxies from $z < 5$, and as such, we will discuss the evolution of galaxy properties in more detail in Section 1.2 and throughout this work. On average, galaxies were smaller in the past (e.g van der Wel et al. 2014). This increase in size with time has been described as 'inside-out' growth. The distribution of light or mass within galaxies also changes as galaxies grow in mass, with stellar light being steeper, or more centrally concentrated in massive galaxies (van Dokkum et al., 2010; Patel et al., 2013; Papovich et al., 2015). Because galaxies are building their central surface density, this could indicate 'outside-in' growth. Where in a galaxy are the stars are being formed, and how do they get rearranged over the lifetime of a galaxy? The first question is starting to be answered by spatially resolved observations of recent star formation at cosmic noon. The second question requires a combination of star formation history, dynamics, and simulations in order to be addressed.

Images of galaxies at rest-frame UV wavelengths and Hα represent the distribution of current star formation and have shown that star-forming galaxies at cosmic noon have irregular, clumpy features. However, Wuyts et al. (2012) found that the stellar mass distributions of these galaxies show a smooth stellar mass distribution. The large gas fraction at high redshift could cause the disks to become gravitationally unstable and break up into clumps of gas that rapidly form stars, which show up as the clumpy features at shorter wavelengths. Clumps formed by gravitational instability might be able to rapidly move to the centre of the galaxy and contribute to the formation of a spheroidal bulge (Bournaud et al., 2011). However, strong stellar feedback might disrupt the clumps on short timescales (Genzel et al., 2011). Simulations show that stellar feedback can puff up the stellar disk of galaxies at $z = 2$ (Hopkins, 2011).

Observations of gas in galaxies at cosmic noon show that the galaxies are often disk dominated (rotational velocity to velocity dispersion ratio $V/\sigma > 1$) (Förster Schreiber et al., 2006)), but with high turbulence ($\sigma_0 \sim 55\,\mathrm{km\,s^{-1}}$ at $z = 0$). For a quasi-stable disk, the

gas fraction and V/σ are expected to be inversely related (Genzel et al., 2011; Wisnioski et al., 2015), with larger gas fractions corresponding to higher turbulence, in agreement with observations.

In addition to disk formation, there are other processes occurring within galaxies that can shape the structure of baryons inside the DM halo, including galaxy mergers and SMBH driven outflows, leading to the diversity of galaxy structures we observe (see Section 1.2.2).

1.1.3. Cosmic Dusk: Epoch of disk settling

The current time is $\sim$13.8 billion years after the Big Bang and the average temperature is 2.726 K. Since $t \sim 8$ billion years, the slowing expansion of space has begun to accelerate under the influence of the postulated dark energy (Peebles & Ratra, 2003; Riess et al., 1998). Today, observed baryons comprise 2.1% of the energy density budget (Fukugita et al., 1998) and can be broken into the different forms as shown in Figure 1.3 from Driver et al. (2018). Within galaxy halos, most baryons are in stars (6% of the global budget; Baldry et al. 2012; Wright et al. 2017; Moffett et al. 2016), followed by neutral gas (2%; Zwaan et al. 2005; Marín et al. 2010; Delhaize et al. 2013; Stocke et al. 2013, molecular gas (0.2%; Keres et al. 2003; Walter et al. 2014), dust (0.1%; Vlahakis et al. 2005; Beeston et al. 2018), and SMBHs (0.01%; Shankar et al. 2004; Mutlu-Pakdil et al. 2016). More details on these components will be provided in Section 1.2.1. The intergalactic medium, unbound to any structure, is thought to be made of both hot ionized plasma and the warm-hot intergalactic medium (WHIM) (Shull et al., 2012). The halos of galaxy clusters and groups also retain $4-5$% of the baryons in intra-cluster light. Cosmologists have noticed a baryon deficit (25% of baryons are unaccounted for; Shull et al. 2012) in the low redshift Universe compared to the baryons synthesized in the Big Bang (Fukugita et al., 1998). However, sufficient uncertainty exists in the observed baryon inventories mentioned above (most quantities are uncertain by ~ 50%) and it has also been suggested that the bulk of the missing baryons is most likely in an ionised component, that closely follows the underlying dark matter distribution (Hernández-Monteagudo et al., 2015; Driver et al., 2018).

Since $z \sim 2$, the formation of new stars has slowed and tends to occur in a disk with a smaller scale height (e.g. the formation of thin disks, also known as "disk settling"; Kassin et al. 2012). Galaxies appear structured, with spiral arms, central bars, rings, and central spheroidal bulges often being observed. We will discuss the average properties of galaxies in the local Universe in more detail in the next section. In the local Universe, galaxies forming stars at rates of $> 100\,\mathrm{M_\odot yr^{-1}}$ tend to be the result of rare major galaxy-galaxy mergers where gas is funnelled and compressed into new stars when two galaxies of similar mass collide. Whereas, at cosmic noon these SFRs were commonplace (e.g., Daddi et al. 2007) The most massive galaxies in the local Universe are $M_* > 10^{12}\,M_\odot$, and studies such as Krajnović et al. (2018); Nipoti et al. (2018) argue that they must have been built, in part, by dry (without gas) major mergers.

The cosmological principle is an application of the Copernican principle and postulates that any observer does not reside in a special location. This principle arises because the distribution of matter in the Universe is, as far as we know, homogeneous and isotropic on large scales (meaning that there is no special pace or direction in the Universe). Therefore,

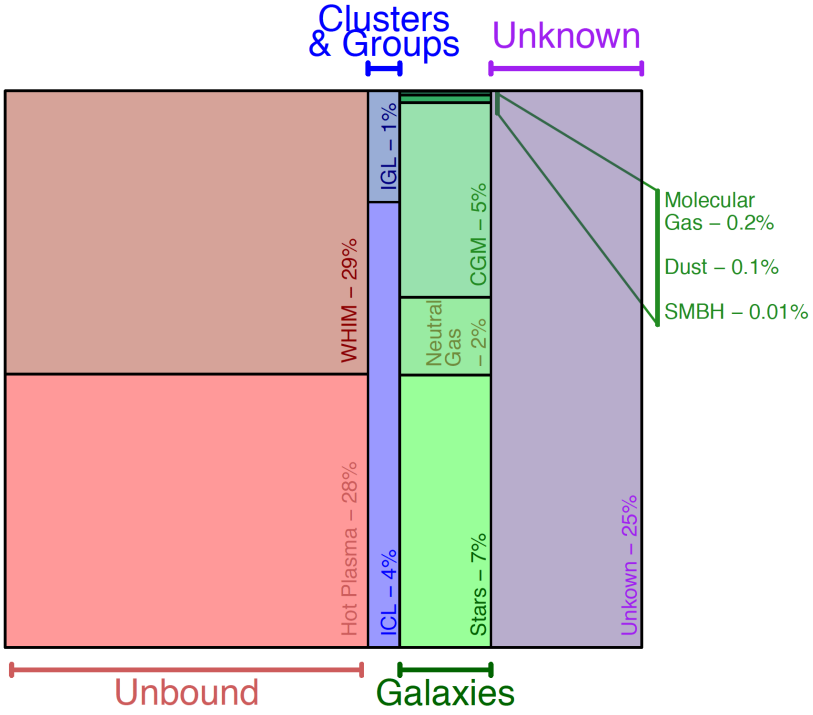

Figure 1.3: The baryon budget divided into bound and unbound material as well as gas, dust, and stellar subcomponents. Outside of galaxies, but within the gravitational bounds of galaxy groups and clusters is the so-called intracluster light (ICL), and intragroup light (IGL) A large fraction of the baryons in the Universe are in the intergalactic medium that consists of hot plasma and a warm-hot intergalactic medium (WHIM). See the text for more detail. Figure from Driver et al. (2018).

viewed on a sufficiently large scale (e.g., >500 Mpc), the Universe that we observe should be a representative sample.

However, on small scales inhomogeneities exist. We are on planet Earth, the third planet from the Sun at a distance of 1.496×10^8 astronomical unit (AU). Our solar system has an estimated radius of about 120 AU (radius of the heliopause; Gloeckler & Fisk 2016). Our star, the Sun, orbits the Galactic Centre at a distance of 8.18 ± 0.031 kpc (Gravity Collaboration; Abuter et al. 2019) and takes about 250 Myr to complete one orbit. The Milky Way (MW) is home to ∼400 billion other stars and is a member of the Local Group. The Local Group is our local cluster comprising of at least 47 galaxies, the largest of which is Andromeda, closely followed by the MW. The Local Group is about 10 Mly across and is a member of the Virgo Supercluster. The Virgo Supercluster is 110 Mly across and contains 2,000 galaxies. The Virgo Supercluster is, in turn, a part of the Pisces-Cetus Supercluster Complex, a galaxy filament.

1.1.4. Cosmic night: Into the darkness

Extending our current understanding of cosmology and the laws of physics into the future, we can predict what will happen. For example, based on measurements of stellar orbits, in 750 million years from now the Sagittarius dwarf spheroidal galaxy will make its next pass of the MW. In 3.9 billion years, the Andromeda Galaxy will make its first pass by the MW, which should correspond to a peak in star formation in both systems (van der Marel et al., 2012). Based on our understanding of stellar evolution, the Sun's core will run out of hydrogen and reach the red giant phase in ~ 5.4 billion years and become a full 2,400 times brighter and 170 times bigger 6.5 billion years from now. When the Sun starts fusing helium it will shrink back down to 10 times bigger and 40 times brighter than today, before entering a second red phase when the Sun runs out of helium (Sackmann et al., 1993). The sun will

eventually throw off all but its inner hot core, becoming a white dwarf (in about 6.9 billion years; Villaver & Livio 2007). Around this time, the cores of the Andromeda and MW will merge to likely form an elliptical galaxy.

Beyond about $t = 100$ billion years, uncertainties in current knowledge mean that we are less sure which path our Universe will take (see e.g., Adams & Laughlin 1999). In 10^{13} years from now, the smallest and longest lived stars today will run out of hydrogen, and after 10^{14} years, all normal star formation will cease. The Universe will then settle down with a population of stars consisting of about 55% white dwarfs, 45% brown dwarfs and a small number of black holes and neutron stars (Laughlin et al., 1997). Galaxies will gradually lose their dead stars to intergalactic space and "evaporate". If the Universe expands exponentially, then it will cool down to a temperature of 10-30 K and all black holes will eventually evaporate (via Hawking radiation; Dalal & Griest 2000) and the Universe will be a very cold, dark, and lonely place.

This thesis is concerned with the history of all galaxies, however, we will focus on analysing the properties of massive star-forming galaxies. In many respects, galaxies are like living beings as they too go through different life stages, from birth to rapid growth, to a decline into old age. Our own Milky Way is a luminous barred spiral galaxy with a central bulge and dominant disk. Based on global properties, the Milky Way looks like it is past its prime; it is not forming stars actively as other galaxies with the same mass (star formation rate 1.65 ± 0.19 $M_\odot yr^{-1}$ (Licquia & Newman, 2015), and stellar mass $M_* = 5 \pm 1 \times 10^{10}$ $M_\odot$ (Bland-Hawthorn & Gerhard, 2016)). However, galaxies are thought to transition through periods of increased and decreased activity (e.g. Tacchella et al. 2016), so this might not be the end for our Milky Way[5]. In the following, we will go into more detail about the different life stages of the average galaxy. First, we will identify the pertinent observable characteristics of galaxies and then, throughout this thesis, we will study how some of those galaxy properties have changed with cosmic time with the aim of inferring important factors that influence galaxy development.

1.2. Galaxies

From our vantage point on Earth, within the disk of the Milky Way, the galaxy appears as a band in the night sky. Ancient Greek philosophers including Anaxagoras (c. $\sim$ 500 - 428 BC) and Democritus (460 - 370 BC) conjectured that the MW consisted of many stars. The proof came in 1610 when Galileo Galilei observed with the first telescope that the MW is composed of a huge number of faint stars. In 1755, Immanuel Kant, inspired by Wright (1750), correctly speculated that the MW is a rotating disk of stars, held together by gravitational forces. Kant also conjectured that some of the "nebulae" visible in the night sky might be separate galaxies, referred to as "island universes" (Murdin, 2000).

However, the idea that there exists stars and galaxies outside our own MW was not accepted until the 20th century. The "Great Debate" was a discussion held in 1920 between Harlow Shapley and Heber Curtis concerning the nature of so-called spiral nebulae and the

[5]Especially given evidence for ongoing gas accretion in the form of the Magellanic gas stream (Putman et al., 1998; Fox et al., 2014)

size of the Universe. Shapely believed that these nebulae were small and lay within the MW, whereas Curtis thought that they were distant large galaxies independent of the MW. In 1924, Edwin Hubble settled the debate by measuring the distance to the spiral nebulae using Cepheid variable stars[6], and found that they were outside the known limits of the MW. Since then, observational capabilities have expanded to give us a more complete inventory of galaxies in the local Universe, and their properties.

1.2.1. Components of galaxies

A summary of some global galaxy properties is shown in Figure 1.4. Galaxies are made of dark matter and baryons, with the majority baryons existing as gas, stars, and dust. The fraction of baryons in these different constituents changes with time as gas is cooled and converted into stars, and dust is created and destroyed. The quantities in Figure 1.4 are summed over all galaxies at each given epoch.

Different physical processes occurring in galaxies each leave their signatures in the spectral energy distribution (SED) of spatially unresolved galaxies. Stars produce the radiation that allows us to observe galaxies over a wide wavelength range, in particular from the UV to infrared (IR). Interstellar gas principally adds line emission or absorption, and interstellar dust affects the SED by absorbing and scattering stellar radiation and reemitting the absorbed radiation in the infrared. Figure 1.5 is an illustration of a model galaxy SED from the UV to radio. Model SEDs can allow many galaxy properties (such as the mass in stars and dust) to be inferred (see Walcher et al. 2011 for a review on fitting the integrated SED of galaxies).

Dark Matter Halo

The first evidence for a non-luminous mass component in the Universe came from Zwicky (1933), whose observations of the Coma cluster showed that the velocity dispersion measured could not be explained by the gravitational force from the baryons measured by stellar light alone (see also, Clowe et al. 2004; Markevitch et al. 2004). Strong evidence that galaxies are surrounded by non-luminous matter comes from measurements of flat rotation curves of spiral galaxies (Babcock, 1939; Freeman, 1970; Roberts & Rots, 1973; Rubin et al., 1978, 1980). It is not clear what DM is, however it is thought to be non-baryonic and collisionless.

Because DM lacks strong and electromagnetic interactions, it is not affected by radiation pressure, unlike baryonic matter, and so is able to collapse into galaxy size halos early on, making it possible to form the high-redshift galaxies observed. DM only N-body simulations can well reproduce the observed large-scale structure evolution. Such simulations have also shown that the radial structure of DM halos is universal and mass-independent (Navarro et al., 1997). The collapse and clustering of DM halos under gravity is dissipationless and

[6]Cepheids are a type of thermally pulsating star that have a well defined relationship between pulsation period and luminosity, as first noticed by Henrietta Leavitt. Thus by monitoring the brightness of these stars one can infer the luminosity or absolute magnitude. Then by comparing the absolute and observed magnitudes, one can calculate distance.

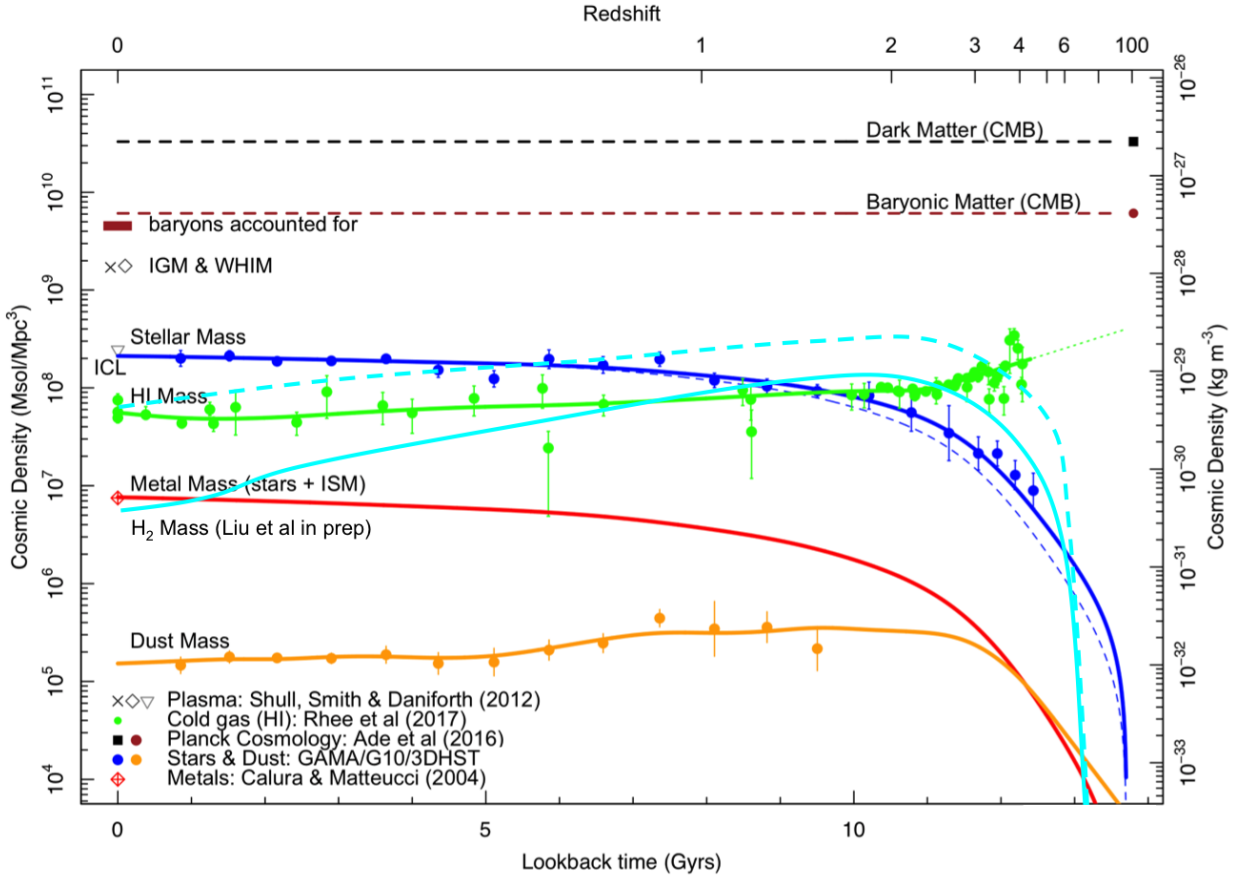

Figure 1.4.: Figure adapted from Driver et al. (2018) showing the evolution of baryons in the Universe. The horizontal lines show the measurements of the dark matter and baryon densities from CMB studies (Planck Collaboration et al., 2016). The local IGM, WHIM and ICL values reported in Shull et al. (2012) are shown as symbols at $z = 0$. Driver et al. (2018) derived the evolution of stellar mass and dust by modelling the panchromatic SED of galaxies. The metal evolution was estimated by adopting a fixed yield and tying metal production to the total mass going into star formation calibrated at $z = 0$ using the value from Calura & Matteucci (2004). Rhee et al. (2018) compiled cosmic HI density values, which are shown as green data. The simple picture from this figure is that gas is turned into stars and not replenished. However, there are very large errors associated with the HI measurements. We have added the cyan lines showing the H_2 density evolution, from the A^{3}COSMOS team (Liu et al. in prep; solid line) and from Scoville et al. (2017; dashed line).

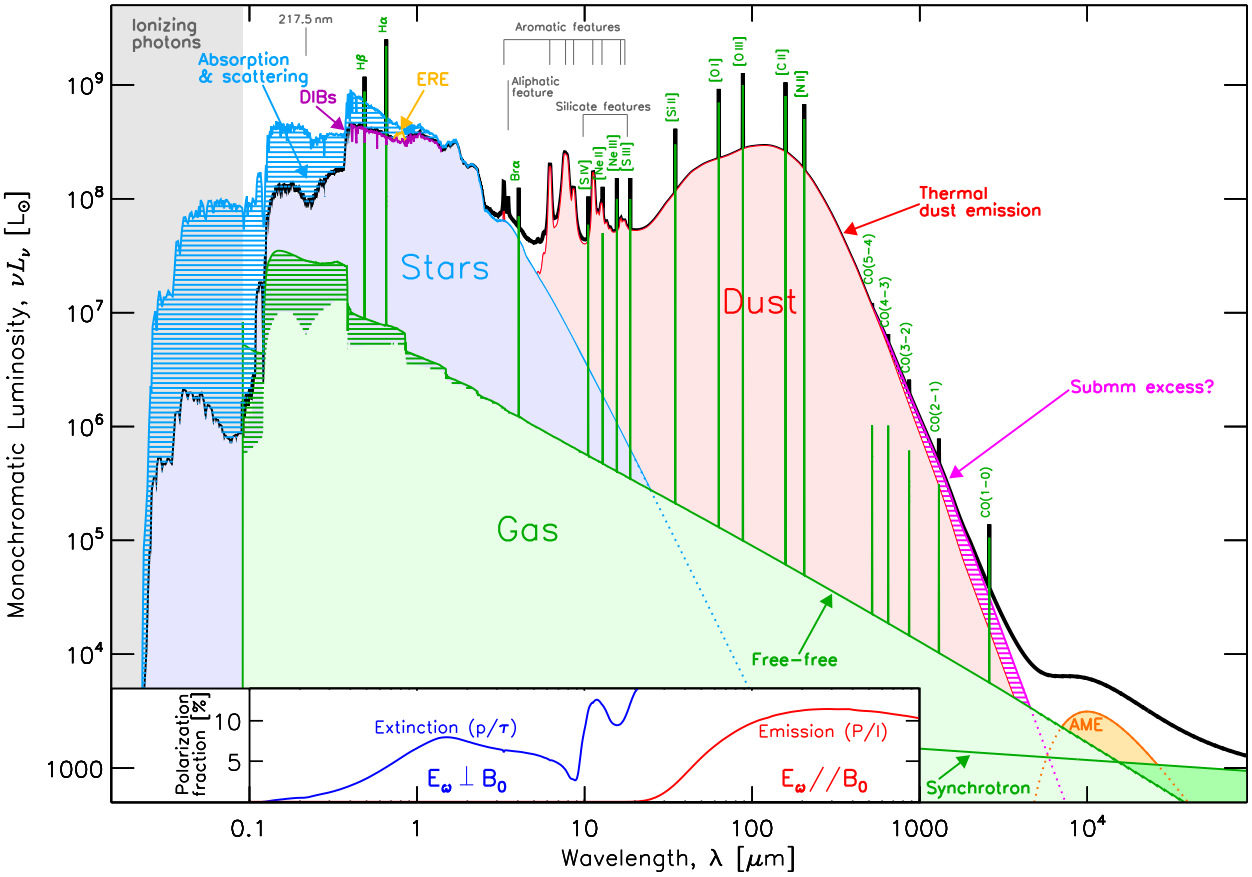

Figure 1.5.: Model spectral energy distribution of a typical late-type galaxy. The blue hatched area shows the stellar emission absorbed by dust. The most relevant gas lines are shown. The inset shows the model D of Guillet et al. (2018). Figure credit Galliano et al. (2018). Synchrotron, free-free, thermal dust, and AME contribute to the observed radio frequency range

the halo settles into virial equilibrium in which

$$\frac{GM_{\rm vir}}{r_{\rm vir}} \sim \sigma^2 \sim \frac{k_B T_{\rm vir}}{m_p}, \tag{1.3}$$

where G is the Gravitational constant, $M_{\rm vir}$ is the mass enclosed in the virial radius $r_{\rm vir}$, σ is the particle velocity dispersion, $T_{\rm vir}$ is the temperature, m_p is the average particle mass, and k_B is the Boltzmann constant. The DM halo density profile can be described by the Navarro Frenk & White (Navarro et al. 1997) (NFW) profile:

$$\rho(r) = \frac{\rho_{\rm crit}\delta_{\rm char} r}{r_s(1+(1/r_s))^2}, \tag{1.4}$$

where $\delta_{\rm char}$ is a (dimensionless) characteristic over-density for collapse, r_s is the scale radius of the halo, and $\rho_{\rm crit} = 3H^2/8\pi G$ is the critical density. Lower mass systems collapsed earlier and are thus more dense.

Dark matter dictates the accretion of gas onto massive galaxies. The feeding of DM and

gas can occur in two modes, hot or cold. Cold streams from thin dense filaments can feed gas and dark matter to galaxies, and spin up the disk (Shlosman, 2013; Mandelker et al., 2019). However, for massive halos, the streams will be shock heated to near the halo virial temperature. If the gas can cool radiatively, then it too can be accreted into the centrifugally supported disk (e.g., Rees & Ostriker 1977; White & Rees 1978; Fall & Efstathiou 1980).

Young Stars

Galaxies contain anywhere from a million to 10^{12} stars, bound together by gravity. The light that stars emit is largely determined by the temperature, surface area, and chemical composition of their outer layers, parameters which are controlled by a star's mass, age, and composition. When a molecular cloud collapses to form stars, the number of stars that have a given mass (at the time they begin hydrogen fusion) is often described by the probability distribution function called the initial mass function (IMF). Therefore the IMF is an important tool for studying galaxies, which are comprised of large numbers of stars. Massive stars ($M > 8\,\mathrm{M}_\odot$; type O and B) are hotter, brighter, and evolve faster than less-massive stars, with the hydrogen burning time $\propto (M/\mathrm{M}_\odot)^{-2.5}$ (Hansen et al., 2004). O-type stars ($T_{\mathrm{eff}} > 30{,}000\,\mathrm{K}$, $M > 16\,\mathrm{M}_\odot$) are very rare, but have a bolometric luminosity $\geq 30{,}000\,\mathrm{L}_\odot$ (Lamers & M. Levesque, 2017). Because of their short lifetimes ($< 10\,\mathrm{Myr}$), O-type stars are often found close to their birthplace (e.g Grasha et al. 2019). Massive stars explode as a Type II supernova, leaving behind a supernova remnant and a dense black hole or neutron star.

Young stellar populations emit the bulk of their energy in the rest frame UV wavelengths ($< 0.3\mu\mathrm{m}$), which is why UV can be used as a SFR tracer (See Chapter 2 and 3). These UV photons can ionise the surrounding gas gives rise to recombination lines. Hydrogen recombination lines are closely related to the photoionisation rates, which (in star-forming regions) is proportional to the formation rate of massive stars, and thus lines such as Hα are often used to measure SFR. These ionised regions are referred to as HII regions (which will be discussed further in Section 1.2.1), and they typically reach temperatures of 10,000 K (Anderson et al., 2009).

Because massive stars formed recently, their emission is a useful probe of the recent SFR. However, there is no easy way to convert the observed integrated emission into a SFR. This conversion depends on multiple factors including IMF (the sampling of and shape), stellar populations (including the particular choice of metallicities, and models for rotation, binarity, atmospheres), dust properties, contamination (from e.g., AGN, evolved stars), and the star formation history. SFR calibrations will be discussed further throughout this work, however, most methods to derive a SFR calibration involve the following steps: 1. A grid of stellar evolution tracks is used to derive the effective temperatures and bolometric luminosities for various stellar masses as a function of time, and these are converted into broadband luminosities (or spectra) using stellar atmosphere models or spectral libraries. 2. The individual stellar templates are then summed together, weighted by an IMF, to synthesize the luminosities, colours, or spectra of single-age populations as functions of age. 3. These isochrones can then be added in linear combination to synthesize the spectrum or colours of a galaxy with an arbitrary (parametrized) star formation history.

Old Stars

Emission from older stars can dominate a galaxy's SED at visible and near-infrared wavelengths. Very low mass stars (e.g., M-type; $M < 0.5\,M_\odot$) make up the largest fraction of all stars by number, and can burn hydrogen for 100s of billions of years; the Universe around is 13.8 Gyr old and so we have not yet observed what happens when these stars cease to produce energy through fusion, but they will likely become white dwarfs. Stars with masses $0.8\,M_\odot$ - $10\,M_\odot$ become red giants, and, depending on their mass, undergo post-main-sequence evolutionary phases like the Asymptotic Giant Branch (AGB) phase during which their outer layers are ejected into the inter-stellar medium (ISM). The total mass of stars in a galaxy can be measured though SED template fitting (Tinsley, 1980) to broadband photometry. However, as for SFR measurements, the best-fitting stellar mass will depend on assumptions (such as the prescription for star formation history, or dust extinction) and model parameter degeneracies.

Stars are on collisionless orbits and can provide a reliable tracer of the gravitational potential in which they sit. An image of a galaxy contains a snapshot of the stars as they travel on different orbits. Stellar populations that are dominated by random motions have spheroidal or triaxial shapes, whereas stellar populations that are rotation-dominated are most often located in a flat and disk-like axisymmetric shape. The varying fractions of stars in these different types of orbits give rise to the diversity of galaxy structure which will be discussed in Section 1.2.2. The outskirts of galaxies observed show a diversity in profiles that seems to depend on recent interactions and accretions (Rodriguez-Gomez et al., 2019; Charlton et al., 2017; Merritt et al., 2016).

Gas

Gas is very important for galaxy evolution. It is the fuel for star formation and plays important roles in galaxy mergers (including fuelling AGN and starbursts, producing dynamical friction; see Ellison et al. 2011; Mayer et al. 2008, respectively). Gas can be divided into different temperature components, hot, warm, and cold, each containing a range of densities. The ISM has been best studied in the MW. In our own galaxy, the six principle sources of energy (thermal energy, hydrodynamic energy, magnetic energy, cosmic ray, starlight and CMB radiation) contribute roughly the same energy density to the ISM to within an order of magnitude ($\sim 1\,\mathrm{eV\ cm^{-3}}$; Ryden & Pogge 2016). By mass, hydrogen and helium contribute 70% and 28% of the gas mass in the ISM, respectively, which in turn is 99% of the total ISM mass (with the remaining 1% in dust).

Atomic gas: The amount of neutral atomic hydrogen in a galaxy is usually measured through the HI line at 21 cm, which can provide a good tracer of both the gas content and kinematics (Ewen & Purcell, 1951). This HI spin-flip transition has a long decay half-life of about $\sim 10^7$ years, however, the large number of hydrogen atoms makes the HI line the strongest thermal line observed in radio astronomy (Dickey, 1991). Under the conditions in most normal disk galaxies, the 21 cm HI line is optically thin, meaning that the brightness along a line of sight can be converted to the HI mass density (Walter et al., 2008).

In local spiral galaxies, the HI gas is detected well beyond the optical disk. For example, in the MW, the neutral gas extends out to $\sim 30\,\mathrm{kpc}$ from the Galactic Center (Diplas &

Savage, 1991). The large extent makes HI doppler shift measurements powerful probes of the galaxy potential (and thus a dynamical probe of the DM halos). Unfortunately, observing HI emission in galaxies at redshifts > 0.2 is extremely challenging (Fernández et al., 2016)[7].

Different mechanisms can dominate atomic gas heating, depending on the temperature, density, and ionization state of the ISM region. Cooling is mainly due to line emission of forbidden lines such as [OI] 63 μm and [CII] 158 μm. The neutral medium can be divided into two categories based on their temperature. About 60% of the HI gas is in the diffuse **Warm Neutral Medium** component, traced by HI emission. This gas has a scale height of ~ 400 pc, typically low densities $n_H \sim 0.3\,\mathrm{cm}^{-3}$ and warm temperatures of 6,000 to 10,000 K (Jenkins, 2013). The **Cold Neutral Medium** has been studied by HI absorption studies (e.g. Mebold et al. 1982), and this medium is primarily associated with molecular gas that exists in compact clumps. In the MW, the cold neutral medium is thought to have a scale height of 100 - 300 pc and temperatures 50 - 100 K (Ferrière, 2001). Under denser conditions, e.g., from $n_H \sim 10 - 100\,\mathrm{cm}^{-3}$, gas transitions to molecular.

Molecular gas: H_2 gas is cold ($\sim$10 - 20 K) and dense ($n \geq 10^3$ to $n \sim 10^6\,\mathrm{cm}^{-3}$), and exists mostly in molecular clouds. Giant molecular clouds are $10^3 - 10^7\,\mathrm{M}_\odot$ and have sizes between 5 to 200 pc (Murray, 2011). In disk galaxies like the MW, molecular gas is confined to a disk that is much thinner than the stellar disk (e.g., scale heights of ~ 80 pc in the MW), and is the dominant mass component in the inner regions of spirals (Young & Scoville, 1991) The densest regions (referred to as dense molecular cores or clumps) will be the sites of new star formation. Dust grains are not only an important catalyst for the formation of H_2, but also shield the molecules from destructive UV radiation.

H_2 molecules are difficult to detect under normal ISM conditions [8]. Therefore, to trace the molecular gas content, the ^{12}CO molecule is used (see Bolatto et al. 2013 for a review). CO is the second most abundant molecule after H_2 and is easily observed through its rotational transitions in the sub-mm wavelengths. CO is optically thick, and so other tracers such as HCN are needed to trace the densest regions inside molecular clouds. The ratio of CO emission to H_2 mass will depend on factors including the metallicity (Bolatto et al., 2013).

Blind CO surveys are now starting to provide constraints on the molecular gas content of galaxies at high-redshift (Pavesi et al., 2018; Decarli et al., 2016, 2019). However, detecting CO emission requires long integration times. A more affordable tracer of the gas mass comes from measuring the dust mass of galaxies and assuming a dust-to-gas conversion factor, generally calibrated on local galaxies (e.g. Scoville et al. 2014; Schinnerer et al. 2016). The molecular gas mass density appears to follow a similar shape as the cosmic SFR density (Figure 1.4).

Ionized gas: In hot, diffuse regions of the ISM matter is primarily ionized, and the density may be as low as 10^{-4} ions per cm^3. O and B stars emit UV photons with energies above the 13.6 eV required to ionize hydrogen from its ground state (creating HII regions). Atoms can also be excited by collisions with electrons, important when the temperature is high.

[7] But in the high-redshift Universe at $z > 2$, Lyman absorption against bright background sources can be used to make precise measurements of the overall HI density, as shown in Figure 1.4 (Rhee et al., 2018).

[8] Only in very hot regions (e.g., 2,000 - 3,000 K) which are affected by shocks is it possible to directly observe emission due to vibrational transitions of H_2 Wolfire & Konigl 1991

Ionized gas makes up the hottest regions of the ISM ($10^4 - 10^7$ K) and can be separated into two components: the warm ionized medium (WIM) and hot ionized medium (HIM).

The WIM (T∼8,000 K) consists of low-density ($n \sim 0.1\,\mathrm{cm}^{-3}$) gas photoionized by hot stars, and takes up a substantial volume of the ISM (∼20-50%; Hill et al. 2015). The WIM of the MW reaches a scale height of ∼1 kpc (Reynolds, 1989, 1984). The denser regions ($n \sim 10^2 - 10^4$) around the young stars, HII regions, constitute < 1% of the ISM volume and are mostly constrained to the mid-plane of the galaxy (scale height ∼70 pc in the MW), as they are formed from within the molecular clouds. The free electrons scattering off ions in these regions emit thermal Bremsstrahlung radiation (often called "free-free" emission) at energies less than their kinetic energy (typically $\lambda > 3\,\mu$m). This component becomes the dominant contribution to the galaxies SED only at radio wavelengths $20 < \nu < 100$ GHz (see Figure 1.5).

The HIM ($T \sim 10^6 - 10^7$ K), or coronal gas, are regions heated by supernovae explosions. The HIM is low density ($n \sim 10^{-3}\,\mathrm{cm}^{-3}$) and fills approximately half the volume of the galactic disk, reaching scale heights of ∼3 kpc in the MW (Draine, 2011). This gas cools by Bremsstrahlung and line transitions in the far-UV and X-ray wavelengths.

Dust

Interstellar dust grains contain carbon and silicon and have a characteristic size of $\sim 0.1\,\mu$m. By mass, dust contributes 1% of mass to the ISM (Boulanger et al., 2000). However, dust absorbs about 30 - 50% of starlight and then re-radiates the energy in the far infrared as dust continuum emission. Dust grains are critical for forming molecules in the ISM. Dust is also important for the temperature balance in the ISM; it provides cooling as well as providing a heating mechanism through the photoelectric effect (Draine, 2003; Tielens, 2005). Dust grains are thought to form in the atmosphere of red giant stars, planetary nebula envelopes of AGB stars, novae and supernovae. However, dust can be destroyed via sputtering (when the grains collide with high-velocity ions produced, for example, in supernova shocks). Modelling the formation and destructions of interstellar grains is an active area of research, and Driver et al. (2018) estimates that 90% of dust ever created has been destroyed.

Physical properties of dust grains can be inferred from the extinction of stellar light, polarization measurements, and analysis of dust emissions. Infrared wavelengths longer than $\sim 20\,\mu$m are dominated by the thermal continuum emission from cold dust grains. At shorter infrared wavelengths ($\sim 3 - 20\,\mu$m), dust emission arises from polycyclic aromatic hydrocarbon (PAH) emission features and continuum emission from small ($< 0.01\,\mu$m) dust grains, (as well as from any thermally emitting hot $T > 150$ K dust). The mid-infrared range ($\sim 20 - 60\,\mu$m) is continuum emission dominated by hot and warm dust ($T > 50$ K) in thermal equilibrium, and single-photon heated small dust grains (Calzetti, 2013). At longer IR wavelengths ($> 60\,\mu$m), the emission is mainly thermal radiation from large grains. The mean temperature of dust contributing to the emission decreases for longer wavelengths, although typical dust temperatures are about ∼30 K in nearby star-forming galaxies (Bendo et al., 2003).

Cosmic Rays and Magnetic Fields

Cosmic rays are high energy charged particles, mostly protons but also electrons and ions, and they provide an important heating and ionizing source in the ISM. Most of their kinetic energy comes from supernovae explosions (about 10% of the energy ejected). High energy (1-10 GeV) cosmic ray protons give rise to gamma rays when they interact with the interstellar gas. Low energy cosmic-rays (100 MeV) are important for ionizing the ISM through collisions.

Magnetic fields are major energy and pressure agents in the ISM. They affect the flow of gas and the onset of star formation. The density, distribution and radiation strength of the cosmic rays is also controlled by the magnetic field. However, the origin of interstellar and intergalactic magnetic fields is not yet well understood. Magnetic fields can be observed by the Zeeman splitting of emission lines from molecular clouds, or polarized thermal emission from aligned dust grains, and synchrotron emission emitted by cosmic rays. Other ways of probing magnetic fields include studying its effect on the intervening medium, such as starlight polarization due to selective extinction by magnetically aligned dust grains, Zeeman splitting of absorption lines from foreground magnetized clouds, and the Faraday rotation of linearly polarized emission in a magnetized medium (Han, 2017). In the MW, the magnetic field is estimated to be about 3-6μG (Ohno & Shibata, 1993; Han & Qiao, 1994), made of both a random (5 - 6 μG, cell size $\sim$50pc) and ordered component (1 - 2 μG). In other galaxies, observations of ordered magnetic fields show coherent orientations parallel to galactic disks and along spiral arms or transitioning from parallel to vertical in the halo of edge-on galaxies. There is also some evidence for magnetic fields in the intergalactic medium (see Han (2017) for a review).

Black Holes

It is believed that the majority of galaxies host a super-massive black hole ($10^6 - 10^{10}$ M$_\odot$) at their centre (Kormendy & Richstone, 1995; Lynden-Bell, 1969). The origin of these super-massive black holes is still unknown (Volonteri, 2012). Two lines of observational evidence have been used to infer that central black holes grow with the bulges of their host galaxy McConnell & Ma (2013)[9] 1) A correlation has been observed between the mass of the black hole and the velocity dispersion, σ, of the stars in the bulge of a galaxy, which traces the gravitational potential (Ferrarese & Merritt, 2000; Gebhardt et al., 2000). 2)The black hole accretion rate of the Universe, as measured through X-ray and infrared observations, has been observed to follow the same shape as the star formation rate density of the Universe shown in Figures 1.1 and 1.4 (Merloni & Heinz, 2007).

Gas accretion onto super-massive black holes can result in the effective conversion of potential and kinetic energy to radiation, making these so-called AGN the brightest beacons in the Universe. AGN emit strongly over the entire electromagnetic spectra. An AGN interacts with gas in its host galaxy through radiation pressure, winds and jets. AGN feedback manifests as AGN-driven outflows or as relativistic jets launched from the accretion disk and will be discussed further in Section 1.2.7.

[9]Some studies have suggested that galaxies typically grow before their black holes, which start to grow when a galaxy is around 10^8 M$_\odot$ and then grow at a faster rate. Supernova feedback can energize gas and suppress black hole accretion in lower mass galaxies (Volonteri, 2012).

Observations of the most luminous quasars at redshift $z > 6$ reveal the existence of numerous super-massive black holes ($> 10^9\,M_\odot$) already in place about 1 Gyr after the big bang (e.g., Bañados et al. 2018). In addition, the ISM of these galaxies are often observed to be chemically mature systems, with moderate metallicities ($Z > Z_\odot$) and dust masses ($> 10^8\,M_\odot$), similar to more local galaxies (Mazzucchelli et al., 2017). Explaining the rapid growth of these SMBH and the fast chemical evolution of the host galaxies is an issue for theoretical models (Simon & Hamann, 2010; Venemans et al., 2017).

1.2.2. Galaxy structure

Galaxies show a wide variety of forms due to both intrinsic structural differences and due to the way the galaxy is oriented with respect to our line of sight. Morphology is the term used by astronomers to refer to the structural properties of galaxies. Classification of objects based on a small number of shared characteristics is the first step towards studying them. Sorting galaxies into morphological categories could lead to important astrophysical insights (Sandage, 1975). In addition, any theory of galaxy formation and evolution will have to account for the diversity of forms observed. In this Section, we will focus on observations in the local Universe, where galaxy morphology is most easily measured. Connecting local morphological features with what is seen at high redshift is a major goal of morphological studies, and will be discussed in more detail in Section 1.3.

Historically, classification is done by visually inspecting images of galaxies. Early classifications of galaxies (then called "nebulae") were rather cumbersome and required a key (e.g. Wolf 1909). To this day, astronomers still use the classification system first developed by Hubble (1926). If every galaxy could be observed along its principal axis of rotation (if there is one), and from the same distance, then a fair comparison could be made. But the random orientation and varying distances can complicate the interpretations of galaxy morphology. Since starting in 2007, volunteers from around the world have helped classify roughly one hundred billion galaxies to date. The success of the first Galaxy zoo, with multiple people classifying whether each galaxy was a "spiral", "elliptical", or "merger", (and asked about the direction of any spiral arms), allowed robust classifications for a million galaxies to be achieved. Since then, more galaxies have been classified, and the second phase of the project asked for more details, including the number of spiral arms and the sizes of bulges. The project is regularly expanding with more data (deeper images, and even simulated images) being added and questions being asked.[10]

Hubble sequence morphological classification

Hubble (1926) and Hubble (1936), recognized four main types of galaxy: ellipticals with a smooth light profile, spirals with a disk-like shape and spiral patterns (often with a central concentration of stars known as the bulge), lenticulars with a bright central bulge surrounded by a disk (and no spirals), and the fourth class "irregulars" for galaxies that would not fit into any of the other categories. More details about these classes will be discussed in this section. Figure 1.6 shows how galaxies were sorted by how much the disk or spheroidal components

[10] See https://www.zooniverse.org/ to get involved with online citizen science projects across many research areas.

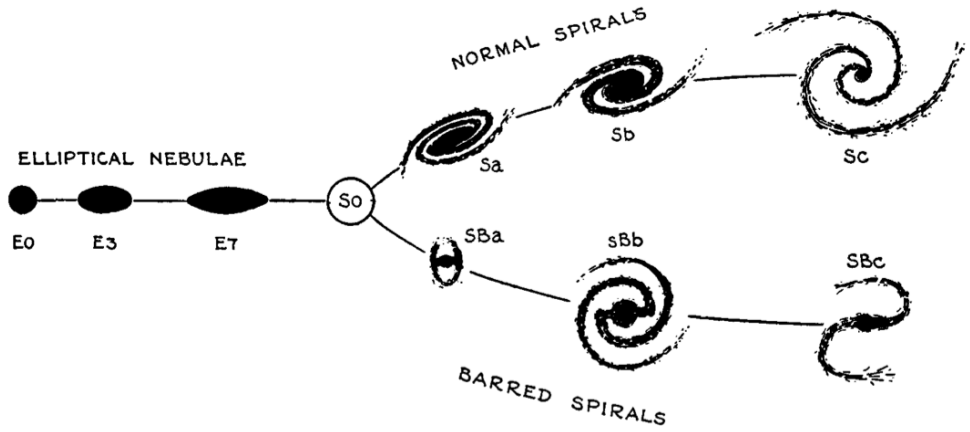

Figure 1.6.: The Sequence of Nebular (Galaxy) Types from Hubble's book "The Realm of the Nebulae"(1936). Elliptical galaxies, on the left of the figure, are referred to as "early-type" and spiral galaxies, on the right of the figure, are referred to as "late-type" galaxies. The spiral galaxy sequence is split between those with a bar and those without a bar (however, mixed types are found between the two sequences of spirals). The transition stage, S0, was hypothetical at the time (1936), but have since been observed frequently in clusters (e.g., Baade 1951; Sandage 1961).

dominate the system. About half of spiral galaxies show a central bar-like feature (bottom of the "fork" in Figure 1.6). The Hubble classification was extended by de Vaucouleurs (1959) to include rings. A more complete classification would include other features observed in galaxies such as extended stellar halos, warps, shells, and tidal tails.

While the Hubble classification was based purely on the inspection of photographic images, it was hoped that the classification scheme could be interpreted as an evolutionary sequence (Jeans, 1919; Hart & Berendzen, 1971). It became common to denote galaxies on the left of the sequence "early-type", and galaxies on the right "late-type". Ironically, it eventually became clear that ellipticals tend to have older stellar populations than spiral galaxies (e.g., Mo et al. 2010).

Spirals: Spiral galaxies are dominated by a thin (radial to vertical scale height ratios of $\sim$0.15 - 0.2; Kautsch 2009; Padilla & Strauss 2008) rotationally supported disk (only $\sim$ 5% of energy in random motions), typically showing a central bulge component, a bar, and spiral patterns when viewed face-on. When spiral galaxies are viewed edge-on, often a thick and thin disk is seen to be embedded in a spherical stellar halo. The thick and thin disks tend to have different kinematics and stellar populations. The thin disk is the sight of on-going star formation, whereas the thick disk contains mostly older stellar populations, suggesting an earlier formation time.

The formation of spiral arms is complex and not well understood. The "density wave model" (Lin & Shu, 1964) stipulates that the spiral arms are regions in the disk that are denser than average. In this picture, the density waves move more slowly around the galaxy than individual stars and other material. As dust and gas are accumulated in these areas, star formation is triggered, resulting in ordered spiral arms. The complimentary "self-

propagating star formation model" (Mueller & Arnett, 1976; Gerola & Seiden, 1978), can explain more flocculant spiral structures. In this second scenario, differential rotation stretches star-forming regions into short-lived spiral patters. In this model shock waves produced by stellar winds and supernovae play an important role in compressing the gas and triggering the next generation of star formation. A combination of both the density wave model and self-propagating star formation model might explain the diversity of spiral structures (Auer, 1999).

Bars are an important perturbation seen in 50 - 70% of disk-shaped galaxies (Eskridge & Frogel, 1999). It is not understood why some galaxies are barred and others are not. Bars develop when stellar orbits in a spiral galaxy become unstable and deviate from a circular path (e.g., via the interaction of stars with a differentially rotating disk; Sparke & Gallagher 2000). Bars rotate with their own pattern speed, but, unlike spiral arms, most of the stars in the bar remain within the bar. Bars are thought to channel gas inwards from the spiral arms through orbital resonance, fuelling central star-cluster formation or AGN (Knapen et al., 2002).

The density of stars in the bulge is greater than in the disk, by $\sim$10,000 times. The formation of bulges is an active topic of research. Bulges built via galaxy mergers should look like an elliptical galaxy, and are referred to as "classical bulges". These bulges are generally round, dominated by random motions, are gas poor, and dominated by older stellar populations. Studies show that major mergers are not the only mechanism to form a bulge (Bell et al., 2017). If gas was able to lose its angular momentum and sink to the centre of the galaxy by secular processes (e.g. driven by a bar) then a "peanut-bulge" or "pseudo-bulge" would be formed (see Kormendy & Kennicutt 2004 for a review of "pseudobulges").

The surface brightness of the disk component(s) can be successfully described by an exponential profile, e.g., $\Sigma(R) = \Sigma_0 \exp(-R/R_D)$. The bulge components have surface brightness profiles similar to elliptical galaxies (e.g. a de Vaucouleurs (1948) profile; see below). At large radii (e.g., $R > 3R_D$), the surface brightness profiles of the stellar disks usually deviate from the pure exponential behaviour, with either a slope much steeper, or much shallower than the exponential (see e.g., Erwin et al. 2005; van der Kruit & Freeman 2011 and references therein for observations, and Herpich et al. 2015, 2017 for formation simulations).

Lenticulars: Galaxies with a bulge and a disk but with no spiral arms are labelled "S0" and are thought of as a transition class between spiral galaxies and elliptical galaxies. Lenticular (S0) galaxies have very little on-going star formation and are considered early-type galaxies. Although devoid of gas, some lenticular galaxies contain dust (Kormendy & Djorgovski, 1989). A number of formation scenarios for lenticular galaxies have been proposed. The disk-like structure of these galaxies could suggest that lenticular galaxies are faded spirals, whose arm features have disappeared once all gas has been exhausted (Blanton & Moustakas, 2009). It has also been suggested that lenticular galaxies might result from a merger (Christlein & Zabludoff, 2004), or they are elliptical galaxies who grew a disk via accretion events (Graham, 2013).

Ellipticals: Elliptical galaxies are spheroidal or ovoid in shape and they cover a large range of luminosity and mass (e.g. 10^5 to $10^{12.5}\,M_\odot$; Fraknoi 2017) and light concentrations[11]. Elliptical galaxies are not supported by rotation; the stars are largely on random orbits, often very elongated. With minimal on-going star formation (Crocker et al., 2011), ellipticals are dominated by older stellar populations. Radio emission powered by central back holes is often detected in elliptical galaxies (Blandford, 1990; Chokshi & Turner, 1992; Kormendy & Richstone, 1995). Elliptical galaxy properties including central velocity dispersion, effective radius, and average surface brightness are correlated.

The surface brightness of an elliptical galaxy can often be modelled by a de Vaucouleurs (1948) profile;

$$I(R) = I_e \exp -7.669 \left(\left(\frac{R}{R_e} \right)^{1/4} - 1 \right) \tag{1.5}$$

where I_e is the surface brightness at R_e, the radius containing half of the total luminosity.

It was originally thought that ellipticals were one component, collisionless stellar systems, containing little to no gas (Gott, 1977; de Zeeuw & Franx, 1991). However, observations have shown that some ellipticals show a range of rotation speeds and shape. Luminous ellipticals (M_B<-20.6) often show X-ray emission, have a triaxial shape, tend to rotate slower (Illingworth, 1977), and often show misaligned kinematic and photometric axes (Franx et al., 1989; Jedrzejewski & Schechter, 1989). On the other hand, less-luminous ellipticals tend to be faster rotators, are flattened oblate objects, and often show a cusp and a steep central power-law SB profile (Lauer et al., 2007).

The dichotomy between bright and faint elliptical galaxies is thought to originate from two independent formation scenarios (Emsellem et al., 2007, 2011). It is widely thought that elliptical galaxies are formed through major mergers, which are thought to be more common at earlier cosmic times. Faint ellipticals are thought to be formed by the merging of gas-rich disk-dominated galaxies, whereas the progenitors of the brightest ellipticals were gas-poor.

Irregulars: The irregular galaxy class (Irr) consists of diverse objects that do not fall into the Hubble sequence. Irregular galaxies have no well-defined shape, or peculiar shape, and may have formed through collisions or close encounters with other galaxies. The best-studied example of an irregular galaxy is the Small Magellanic Cloud. Like Spirals, Irregular galaxies tend to have a mix of old and young stellar populations as well as containing dust and gas (Hunter, 1977). Dwarf (stellar mass $\lesssim 10^9\,M_\odot$) irregular galaxies are interesting to study because they are most common and thought to contain similar ISM conditions to the earliest galaxies (low-metal content and high gas content). Due to their small sizes, they are prone to environmental effects and can be easily disrupted by supernovae feedback.

Other quantitative measurements of galaxy structure

Although the human brain is still the best tool we have for visual pattern recognition and serendipitous discoveries, with large surveys and better computing power, it is common to

[11]However, astronomers are not sure if dwarf ellipticals and giant ellipticals form a continuous physical sequence

use automated techniques for morphological classification. One method is to characterize the light distribution using several parameters (e.g., Sersic 1968; Odewahn et al. 2002), and another is to use a non-parametric approach (e.g., Abraham et al. 1994; Conselice 2003; Lotz et al. 2004). Both types of analysis readily lend themselves for use on large numbers of galaxies and can be easily reproduced (Simard et al., 2011; Scarlata et al., 2007; Griffith et al., 2012; Lackner & Gunn, 2012; Meert et al., 2016). Modern machine learning techniques, with appropriate training, are also being applied to classify morphologies in large datasets (e.g. Huertas-Company et al. 2015; Dieleman et al. 2015).

The intensity of a galaxy with distance R from its center is often described by the one dimensional Sérsic profile (Sersic, 1968):

$$I(R) = I_e \exp\left(-b_n\left(\frac{R}{R_e})^{1/n} - 1\right)\right), \tag{1.6}$$

where I_e is the intensity at the effective radius R_e that encloses half of the total light of the model, n is the so-called Sérsic index, which controls the degree of curvature of the profile, and b_n is defined in terms of n and satisfies $\gamma(2n; b_n) = \frac{1}{2}\Gamma(2n)$, and ensures the integrated profile corresponds to the total luminosity of the galaxy (Graham et al., 2005). At optical and NIR wavelengths where galaxy light reflects the stellar mass content of the galaxies, surface-brightness profiles are able to reflect a galaxy's baryonic content and gravitational potential. NIR images are ideal because the longer wavelengths are less affected by dust extinction, and the variations of stellar mass-to-light ratios inside and among galaxies are small (e.g. Kauffmann et al. 2003). Most galaxies are fit (in optical and NIR) by Sérsic profiles with indices between $0.5 < n < 10$ (Mo et al., 2010). The surface brightness distributions of disk-dominated galaxies are characterised with a Sérsic index of $n = 1$ (exponential profile) with a central excess due to the bulge component (Freeman, 1970). Generally, spiral galaxies can be well modelled by two Sérsic components, an exponential disk and a second inner component with $n > 4$, representing the bulge (de Jong, 1996; Graham, 2001; MacArthur et al., 2003). The ratio of stellar mass in these two components (the bulge-to-disk or bulge-to-total ratios) correlates with qualitative Hubble type classification and is a key quantity used in modern discussions of galaxy morphology[12]. Early-type galaxies have more centrally peaked mass distributions and fit by profiles whose Sérsic index (generally $2 < n < 6$; Sargent et al. 2007; Graham & Dey 1996) correlates with its stellar mass, absolute magnitude, and size (Caon et al., 1993; Binggeli & Cameron, 1991; Bershady et al., 2000; Conselice, 2003). Surface brightness profile fitting with Sérsic profiles assumes that galaxies are well described by smooth, symmetric profiles, an assumption that breaks down for irregular galaxies.

Commonly used non-parametric diagnostics are a combination of the Concentration (C), Asymmetry (A), and Clumpiness (S) parameters (Conselice, 2003), and the second-order moment of the brightest 20% of galaxy pixels (M20) and the Gini coefficient (Lotz et al., 2004). These methods have often been employed as morphological proxies for studying large

[12]However there is often a lot of degeneracy in the best-fitting models, and structures like bars, compact nuclei, and spiral arms can further complicate the interpretation of fits (Balcells et al., 2003). A related approach (and one adopted in this thesis), is to fit a single Sérisc profile to the entire galaxy and interpret profiles with a high Sérsic indices as bulge-dominated, and galaxies with a low Sérsic index as disk-dominated. Naturally, this method will not produce a clean selection (e.g. Carollo 1999) but will be easier to apply to lower signal-to-noise data

survey datasets, particularly when galaxy mergers or irregular galaxies are to be identified (see e.g., Abraham et al. 1996; Conselice 2003; Lotz et al. 2004; Huertas-Company et al. 2008). The concentration quantifies the central density (similar to the Sérsic index), and is $C = 5\log(r_{80}/r_{20})$, where r_{20} and r_{80} are the radii enclosing 20% and 80% of the total light respectively. The "clumpiness" is measured by quantifying the fraction of a galaxy's light in the rest-frame B-band in high spatial frequency structures (Conselice, 2003). The clumpiness of a galaxy's light distribution correlates with the amount and the location of star formation (e.g., Takamiya 1999; Conselice 2003). Asymmetry quantifies the degree of rotational symmetry of the light distribution and is measured by calculating the normalized difference between the galaxy image and the image rotated by 180 deg (Conselice et al., 2000b; Lotz et al., 2004). Merging galaxies often show strong asymmetries in their gas dynamics and stellar light distributions (Conselice et al., 2000a; Sandage, 1961). Spheroids usually have lower values of clumpiness and higher concentration values than spiral galaxies. The Gini-M20 method was introduced to separate mergers from interacting galaxies: The Gini coefficient (G) describes how uniformly the flux is distributed among galaxy pixels. The Gini statistic assumes values from 0 (if the galaxy light is homogeneously distributed among galaxy pixels) up to 1 (if all the light is concentrated in 1 pixel, regardless of its position in the galaxy)[13]. The M20 statistic measures the spatial extent of the brightest regions; it is the second order moment of the brightest 20% of the galaxy flux. M20 correlates with the central concentration C for centrally concentrated sources however, M20 is also sensitive to bright off-centred knots of light.

Galaxies at higher redshifts will have fainter features, making it more difficult to measure morphology. However, studies of massive galaxies at $z \sim 2$, have observed similar morphological trends as in the low-redshift Universe (Bell et al., 2004; Papovich et al., 2005; Huertas-Company et al., 2014). The morphologies of galaxies at $z > 2$ are less well studied in rest-frame optical and early measurements performed on rest-frame UV light found more frequent irregular features at high redshift, and a lack of the traditional Hubble types (e.g., Giavalisco et al. 1996; Steidel et al. 1996; Law et al. 2007. However, studies in the NIR using *Hubble Space Telescope* (HST) Wide Field Camera 3 (WFC3), probing rest-frame optical emission, allowed a variety of galaxy morphologies at $z \sim 2$ to be observed, from massive disks, to compact early-type galaxies, suggesting that the backbone of the Hubble sequence was already in place at $z \sim 2$ (e.g., Szomoru et al. 2011; Cameron et al. 2011; Wuyts et al. 2011a; Lee et al. 2013).

1.2.3. Galaxy colour

Data from large surveys reveal a colour bimodality in the galaxy population at low redshifts (Strateva et al., 2001; Baldry et al., 2004, 2006). In broad terms, late-type (spiral) galaxies are blue and early-type (elliptical) galaxies are red. However, the Galaxy Zoo project found the presence of blue elliptical galaxies and red spirals (e.g. Tojeiro et al. 2013), revealing that galaxy evolution is likely more complex, with multiple pathways for galaxy transformation (see Section 1.3, Schawinski et al. 2014). In rest-frame optical colour– absolute magnitude space, three galaxy populations are identified: the "red sequence", "blue cloud" and the

[13]The Gini coefficient was originally developed as a gauge of economic inequality among a population (Gini, 1912).

relatively underpopulated space between the red and blue distributions called the "green-valley" (Bell, 2003).

In general, galaxies become bluer and fainter along the sequence from S0 to Sd and Sm (the "blue cloud/sequence") as the fraction of young blue stars increases. Some red spiral galaxies have been observed around the outskirts of large clusters (Bamford et al., 2009; Masters et al., 2010b). These unusual galaxies have lower rates of on-going star formation when compared to blue spirals, and could represent disk galaxies whose gas supply for star formation has been gently removed (by strangulation or starvation). The mean colour of the blue cloud becomes redder towards $z = 0$.

Both at visible wavelengths and in the near-infrared K band at 2.2 μm, brighter ellipticals are redder and fainter systems bluer (red sequence). This trend could be explained if small elliptical galaxies were either younger or more metal-poor than large bright ones. More massive galaxies are observed to have older stars and also be more metal-rich. Yet a (small) population of blue early-type galaxies, with high SFRs was also identified by Schawinski et al. (2009) with low velocity dispersions (implying stellar masses $< 10^{11}\,\mathrm{M}_{\odot}$). These galaxies could be explained by major mergers or major cooling events in red early-type galaxies triggering star formation.

1.2.4. Number of galaxies

Galaxy luminosity functions provide important constraints for cosmology and galaxy evolution theories. The Schechter luminosity function provides a parametric description of the space density of galaxies as a function of their luminosity;

$$\phi(L)\mathrm{d}L = \phi^{\star}\left(\frac{L}{L^{\star}}\right)^{\alpha} e^{-L/L^{\star}}\frac{\mathrm{d}L}{L^{\star}}, \tag{1.7}$$

where $\phi(L)\mathrm{d}L$ is the number of galaxies with luminosities between L and $L+\mathrm{d}L$, $L^{\star}$ is a characteristic luminosity where the power-law form of the function cuts off, and the parameter $\phi^{\star}$ provides the normalization and has units of number density. In other words $\phi(L)$ is the number of galaxies per unit luminosity per unit volume. The integration of Equation 1.2.4 gives the total number of galaxies in a given volume whose luminosities are brighter than L; $N(>L) = \int_{L}^{\mathrm{inf}} \phi(L')\,\mathrm{d}L' = \phi^{\star}\gamma(1+\alpha, L/L^{\star})$ and their total luminosity is $L_{\mathrm{tot}}(>L) = \int_{L}^{\mathrm{inf}} L'\phi(L')\,\mathrm{d}L' = \phi^{\star}L^{\star}\gamma(2+\alpha, L/L^{\star})$, where γ is the incomplete gamma function (Jerjen, 2000). For an apparent magnitude limited sample, the volume to which a galaxy with luminosity L can be seen is $\propto L^{3/2}$, thus $n(L) \propto \phi(L)L^{3/2}$ ($\phi(L) = \frac{n(L)}{V(L)}$, where V is volume and n the number of galaxies in the sample). Figure 1.7 shows that there are many more faint galaxies than there are bright galaxies. The luminosity functions are best determined near $L^{\star}$ because galaxies with $L \gg L^{\star}$ are rare, whereas galaxies with $L \ll L^{\star}$ tend to be too faint to observe. Over a wide range of galaxy magnitudes, double Schechter functions provide better fits than a single Schechter function (e.g., Blanton et al. 2005). Fitting single Schechter functions separately to red and blue galaxies shows that the most luminous galaxies in the local Universe are red elliptical galaxies and most of the dim galaxies are blue. Similar distributions can be constructed using stellar mass measurements, i.e. a stellar mass function (e.g., Balogh et al. 2001; Cole et al. 2001). Although spirals and irregulars

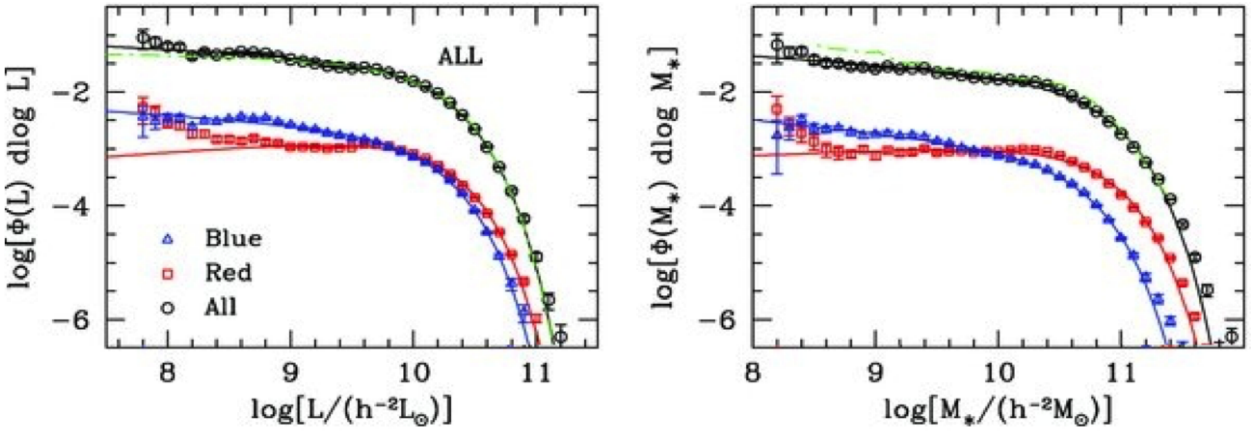

Figure 1.7.: Luminosity (left; r-band) and stellar mass (right) functions of galaxies in SDSS Fourth Data Release from Yang et al. (2009). In each panel, the open circles, squares and triangles with error-bars are the luminosity or stellar mass functions of all, red and blue galaxies, respectively. Blue and red galaxies were separated using the rest-frame g - r colour–magnitude diagram, and their results are scaled down by a factor of 10, for clarity. The black solid lines are the best fitting Schechter functions (Yang et al., 2009). The dot-dashed green line shows a comparison with earlier studies by Blanton et al. (2003) (left), and Bell et al. (2003) (right).

are far more numerous, elliptical galaxies contain about half the total mass in stars in the local Universe (e.g. Kelvin et al. 2014).

1.2.5. Galaxy scaling relations

Most galaxy properties are correlated (e.g., colours, magnitudes, and structural parameters in SDSS; Blanton et al. 2003). A scaling relation is a correlation between two or more properties that is tight given the observational uncertainties for a population of galaxies (Bezanson et al., 2018). The existence of scaling relations is thought to constrain galaxy formation processes and they can be useful for measuring distances to galaxies.

Some classical scaling relations, and relations used in this thesis include:

- The "Faber-Jackson relation": the correlation between stellar mass and luminosities of early-type galaxies (Faber & Jackson, 1976).
- The "Kormendy relation": the correlation between the effective radii of early-type galaxies and their surface brightness at that radius Kormendy (1977).
- The "fundamental plane" showing the correlations between effective radii, luminosities and velocity dispersions of early-type galaxies (in this sense the Faber-Jackson and Kormendy relations are lower-dimensional projections of this plane; Djorgovski & Davis 1987; Dressler 1987).
- The "Tully-Fisher relation": a correlation between mass or luminosity and its asymptotic rotation velocity, or emission line width for late-type galaxies (Tully & Fisher,

1977; Bloom et al., 2017). This is similar to the Faber-Jackson relation for early-type galaxies.[14].

- The "M$-\sigma$ relation" is the correlation between the stellar velocity dispersion of a galaxy bulge and the mass of the supermassive black hole at its centre (Magorrian et al., 1998).

- The size-mass relation, which is different for early-type and late-type galaxies (Shen et al., 2003; van der Wel et al., 2014). At $z = 2$ a star-forming galaxy of 2×10^{10}M$_\odot$ has a half-mass radius of $\sim$1.5 kpc, just like the MW bulge today (Lilly & Carollo, 2016; Mosleh et al., 2017).[15]

- The star-forming main sequence (SFMS) is the correlation between the SFR and stellar mass of late-type galaxies (and will be discussed more below)

- The "mass-metallicity relation" (Tremonti et al., 2004) is the correlation between galaxy stellar mass and stellar or gas phase metallicity. The "fundamental-mass-metallicity relation" adds SFR or gas fraction as a third parameter.[16]

Integral field spectrographs are producing many spatially resolved spectroscopic surveys of relatively nearby galaxies, such as Mapping Nearby Galaxies at Apache Point Observatory (MaNGA; Bundy et al. 2015), Calar Alto Legacy Integral Field Area Survey (CALIFA; Sánchez et al. 2012), and the Sydney-Australian-Astronomical-Observatory Multi-object Integral-Field Spectrograph (SAMI; Croom et al. 2012) surveys, and are finding that many gloabl scaling relations hold at $\sim$kpc scales within galaxies, e.g., see the local mass-metallicity relation (Sánchez et al., 2017) and SFMS (Medling et al., 2018).

The star forming galaxy main sequence: SFMS

The scaling relation between SFR and stellar mass has been dubbed the star-forming main sequence (Brinchmann et al. 2004; Noeske et al. 2007; Elbaz et al. 2011; Whitaker et al. 2012, 2014). At a given epoch, more massive blue galaxies form stars more rapidly than less massive blue galaxies. We will discuss the SFMS at great lengths throughout this thesis. The observed scatter of the SFMS is ~ 0.3 dex, similar to the scatter in the mass accretion rates onto dark matter halos (Rodríguez-Puebla et al., 2016). There is a population of galaxies > 1 dex below the SFMS that are referred to as "passive". We have already seen that structure, mass, and star formation activity are all inter-connected properties of galaxies. Wuyts et al. (2011a) found that on the SFMS, galaxies are star-forming disks with Sérsic indices of $n = 1$. Above and below the SFMS, the light is more compact and more concentrated (i.e., smaller effective radii, larger Sérsic indices). Many ideas about how galaxies grow have stemmed from this, and similar, observations. For example, Whitaker et al. (2015) measured the

[14] Unified dynamical scaling relation: Recent work has used the $S_{0.5}$ parameter that combines the combination of pressure and dynamical support to a galaxy ($S_{0.5} = \sqrt{0.5V_{\rm rot}^2 + \sigma^2}$) and this correlates with the stellar mass for both early and late-type galaxies (Zaritsky et al., 2008; Cortese et al., 2014)

[15] And recently van de Sande et al. (2018) and Barone et al. (2018) found an extremely tight mass–size–age, or "age – shape" relation with older galaxies being rounder.

[16] Barone et al. (2018) showed that the galaxy potential traced by (M$_*$/R) gives the tightest correlation with stellar metallicity.

structure of galaxies on the SFR–M_* plane out to $z = 2.5$ and argue that star formation happens in disks to $z \sim 1$ but that the time before $z \sim 2$ must have been the epoch of bulge building. Building on the Wuyts et al. (2011a) observations with simulations, Tacchella et al. (2015) proposed a scenario in which bulges are built while galaxies are in a specific region of the SFR–M_* space; an event drives gas into the centre (a merger or disk instability), which causes a central starburst, building the central mass concentration. After this burst, the central gas is exhausted and the SFR drops, quenching the galaxy "inside–out".

Understanding feeding and feedback mechanisms responsible for regulating the SFRs of galaxies is key to following how galaxies evolve along the SFMS and for explaining the numbers of both star-forming and quiescent galaxies across cosmic time. Moreover, correctly implementing feedback remains a challenge for simulations (see Somerville & Davé 2015). To use the SFMS as a tool to compare theory and observations consistent ways of measuring both the stellar mass and SFR of galaxies are required (see, for example, Donnari et al. 2018).

1.2.6. The need for feedback

Stellar mass functions, the relative abundance of galaxies as a function of their stellar mass (introduced in Section 1.2.4), can be measured and parametrised by Schechter functions and used to constrain galaxy formation and evolution models. By comparing the stellar mass function with the mass function of dark matter halos from N-body numerical simulations, it was clear that the shapes did not match at the high-mass and low-mass ends. Using abundance matching, Behroozi et al. (2013) matched galaxies with their DM halos and estimated the ratio of the stellar mass to total baryonic mass (green line in Figure 1.8) for redshifts ($0 < z < 4$). The efficiency of star formation (fraction of baryonic mass converted to stars) varies significantly with galaxy mass peaking at halo masses of $M_h \sim 10^{12}\,\mathrm{M}_\odot$; the overall efficiency of star formation must be highly suppressed at high and low stellar masses (e.g., Mo et al. 2010). In addition, models of galaxy evolution also have to explain the overall inefficiency of galaxy star formation, because at most $\sim 20\%$ of the baryons are in a stellar component (Guo et al., 2010).

Early results from hierarchical clustering galaxy formation models (in a ΛCDM universe) predicted a steeply rising mass function towards the faint population end (White & Rees, 1978; Kauffmann et al., 1993; Cole et al., 1994), while significantly flatter luminosity functions were observed (Binggeli et al., 1988; Loveday et al., 1992). To reconcile these results, it was realised that successful models should include supernovae feedback (Lacey & Silk, 1991; Kay et al., 2002) to suppress the star formation efficiency in low-mass halos. At the bright end, White & Frenk (1991) found that the model gas cooling rates in massive halos would result in central galaxies with too much stellar mass without the addition of an extra heating process. Successful models include "AGN-feedback" to suppress the cooling of gas in massive halos (Springel, 2005; Croton et al., 2006; Bower et al., 2006)).

Figure 1.8 shows the ratio of central galaxy stellar mass to halo mass against halo mass for four models: no-feedback (left panel), AGN-only (middle-left panel), supernova (SN)-only (middle-right panel) both SN and AGN feedback (following the Henriques et al. (2015) implementation). This example shows that without feedback almost all baryons are turned into stars in low-mass halos. At high mass, halo shocks delay cooling and reduce star

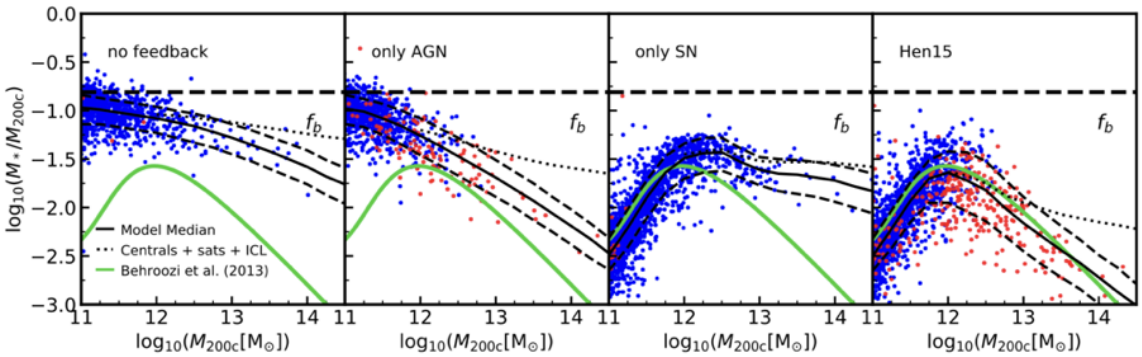

Figure 1.8.: The stellar-to-halo mass ratio versus halo mass for central galaxies in the four models presented in Henriques et al. (2019): no feedback (left panel), AGN feedback only (middle-left panel), SN feedback only (middle-right panel) and including both according to Henriques et al. (2015). The coloured dots show a random sample of galaxies in each model, with blue being star-forming and red being passive objects (divided at $\log(\mathrm{sSFR/yr^{-1}}) = -11.0$). The black lines show the median and scatter for the different models, while the solid green line shows an abundance matching estimate from Behroozi et al. (2013).

formation (Birnboim & Dekel, 2003). In addition, at these high masses, a significant fraction of the baryons are in satellite galaxies or in the intracluster light (as shown by the dotted black line). But, these reductions in efficiency are not enough to explain the stellar mass functions observed. In the Henriques et al. (2015) model, radio-mode feedback (discussed in Section 1.2.7) is proportional to black hole mass and hot halo gas mass, so galaxies quenched by AGN feedback are predominately at high halo mass ($\log(\mathrm{M_{200}/M_\odot}) > 12.5$). Also, supernovae feedback is able to eject hot gas from galaxies. This regulates the supply of cold gas but ceases to be effective at $\log(\mathrm{M_{200}/M_\odot}) \sim 12$, where the potential well becomes too deep for ejection to be possible.The characteristic mass corresponding to peak star formation efficiency appears to be almost independent of redshift (Moster et al., 2012; Behroozi et al., 2013; Henriques et al., 2019).

1.2.7. Quenching star formation

The relative abundance and number densities of blue star-forming galaxies and red passive galaxies at different cosmic epochs have been studied with the aid of large surveys (see Section 1.3.1). Passive galaxies are more abundant at high stellar masses (see Figure 1.7 and e.g, Kauffmann et al. 2003; Brinchmann et al. 2004; Baldry et al. 2004; Brammer et al. 2011; Ilbert et al. 2013; Muzzin et al. 2013; Tomczak et al. 2014). Because colour and star formation are so intimately connected, red galaxies are often referred to as quiescent, passive, or quenched, meaning galaxies with little or no amounts of star formation activity. A galaxy can be thought of as "quenched" when it has no more cold gas from which to form stars. The cosmic gas accretion rate is decreasing towards the present day, so the overall star formation activity of galaxies is slowing down. However, based on the relative numbers of star-forming and quiescent galaxies, it is thought that some of the galaxies must transition from star-forming to quiescent relatively quickly (within 1 billion years), which is much shorter than

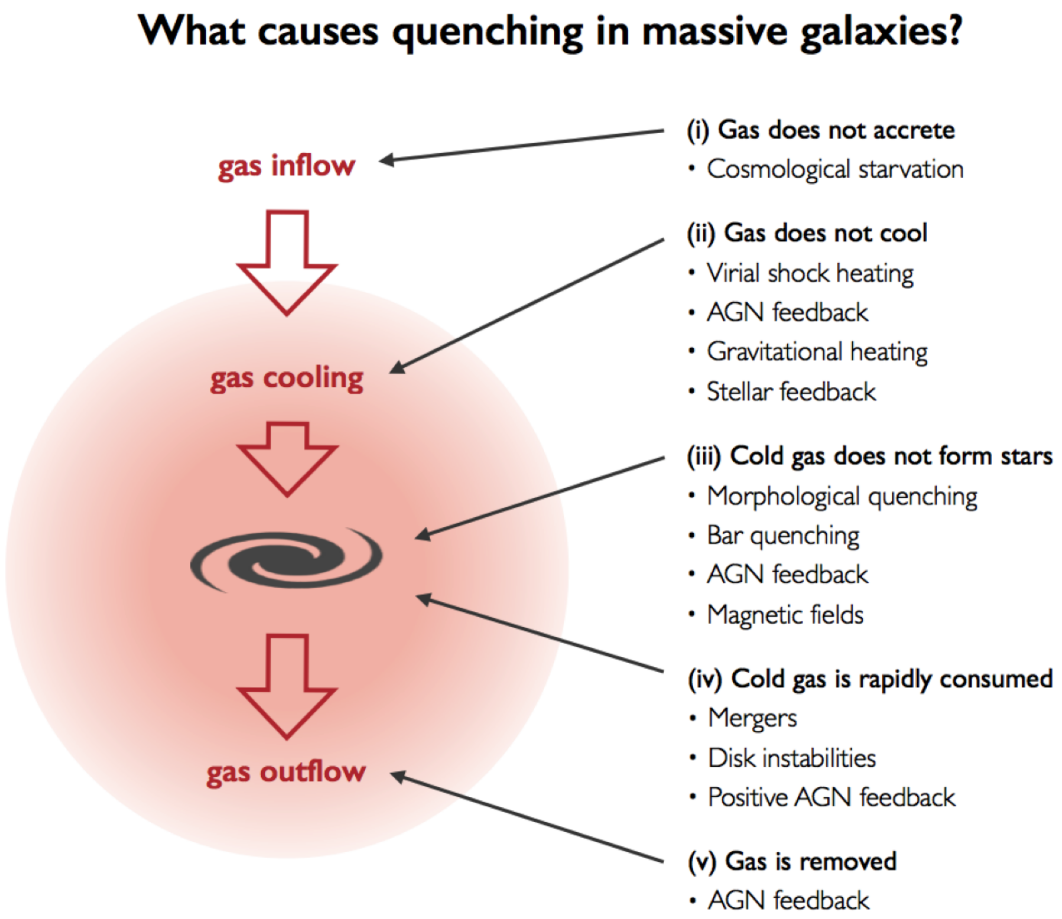

Figure 1.9.: Schematic diagram from Man & Belli (2018) indicating five broad classes of quenching mechanisms for massive galaxies.

the time it would take for a galaxy to simply use up its reservoir of cold gas (Lian et al., 2016; Gabor et al., 2010). Understanding what mechanisms can remove the supply of cold gas in galaxies and shut-down star formation (referred to as "quenching") is a current focus of galaxy evolution studies. These mechanisms can either be preventative; i.e. stop gas from entering the galaxy, or to stop gas from forming stars, or ejective; i.e., removing gas from the galaxy. A summary of proposed mechanisms for massive galaxies is given in Figure 1.9, from Man & Belli (2018).

The likelihood of a galaxy being quenched has been found to correlate with a number of galaxy properties including, stellar mass, halo mass, black hole mass, central density, and environmental properties such as whether a galaxy is a central or a satellite. Peng et al. (2010) found that the probability of a galaxy to be quenched increases strongly with stellar mass, in a redshift-independent way (at least for $z < 1$). In the local Universe, there is a well-known correlation between galaxy morphology and environment, with the fraction of red or spheroidal galaxies being largest in clusters (Dressler, 1980). Peng et al. (2010) analytically separated the effect of "mass-quenching" and "environment-quenching", and suggested that the environmental quenching is likely most important for low-mass satellite galaxies at low redshift ($z < 0.5$). In addition to the mechanisms shown in Figure 1.9, environmental effects

can be relevant for low-mass galaxies. Slow acting (>1 Gyr) environmental effects include merging (Mihos, 2004), harassment (Moore et al., 1996), tidal compression or truncation (Byrd & Valtonen, 1990; Merritt, 1983), starvation (Larson et al., 1980), and thermal evaporation (Cowie & McKee, 1977), and faster acting processes include as ram pressure stripping (Gunn & Gott, 1972), and turbulent viscous stripping (Nulsen et al., 1982).

AGN feedback

As we saw in the previous section, AGN feedback can prevent radiative cooling by heating the surrounding medium and thereby prevent the accretion of gas onto galaxies (e.g., Croton et al. 2006). AGN feedback models come in two flavours, known as the "quasar" mode, and the "maintenance mode" (also referred to as the kinetic or radio mode). In the quasar mode, winds launched by the AGN are thought to quench star formation by expelling gas from the galaxy. This mode occurs when the black hole is accreting close to the Eddington limit (Alexander & Hickox, 2012). Observational evidence for whether this form of feedback is effective at quenching galaxies is still inconclusive, but its effects are likely to vary with redshift and stellar mass (e.g., see Churazov et al. 2005; Leslie et al. 2016; Delvecchio et al. 2018). Jets of charged particles have been observed in some AGN, and with an effective mechanical coupling, these jets could heat the gas in and around galaxies (Ciotti & Ostriker, 1997). The constant heating of hot gas around galaxies is sometimes referred to as a "maintenance mode" of AGN feedback (Fabian, 2012) and now has convincing observational evidence due to observed X-ray cavities associated with radio jets and lobes (McNamara & Nulsen, 2012).

If AGN activity was causally linked to the quenching of a galaxy, one might expect to see a correlation between SFR and AGN luminosity (Lutz et al., 2010; Harrison et al., 2012). However, studies in the literature have found little connection between SFR and AGN luminosity (e.g. Rosario et al. 2012; Mullaney et al. 2012; Stanley et al. 2015; Ramasawmy et al. 2019). The lack of clear correlation between SFR and AGN luminosity could be explained by the cyclical nature of AGN activity and black hole growth, with studies suggesting that AGN flicker on timescales of anywhere from a few years to 10^8 years (with 10^5 years being a common estimate e.g. Schawinski et al. 2015). These timescales are shorter than those we are sensitive to with our SFR tracers (on the order of 10 - 100 Myr depending on the tracer). See Morganti (2017) for a review on how to trace the signatures of past nuclear activity.

Stellar Feedback

In low mass galaxies, stellar-driven winds and supernovae explosions can heat and eject gas (e.g., Hopkins et al. 2012). If the energy is sufficient, out-flowing material may be accelerated to velocities greater than the escape velocity of the galaxy and be ejected into the intergalactic medium (Silk, 2013). But just by imparting energy and momentum into the ISM, supernovae winds and stellar winds from evolved stars[17], are able to suppress star formation, providing a source of turbulence required to regulate the SFR.

[17]Stellar winds are generally important only in young ($< 10^7$ yr) starbursts that form many high mass stars ($> 60\,M_\odot$) in a metal-rich environment. In all other scenarios, supernovae explosions dominate the energetics of the ISM (Veilleux et al., 2005).

Spatially resolved observations of star formation activity in galaxies have shown that galaxy quenching mechanisms must be able to act at all radii, not just in galaxy centres (e.g. Belfiore et al. 2018; Nelson et al. 2016). Interestingly, the observed radial SFR profiles of transitioning galaxies seem to be in tension with simulations (Starkenburg et al., 2019). A variety of mechanisms are likely to be important for different galaxies at different times (see Figure 1.10). But, the overall SFR of a galaxy seems to be modulated by the balance between gas accretion and feedback (Dekel & Mandelker, 2014; Somerville & Davé, 2015).

1.3. Studying galaxy evolution

For our understanding of galaxy formation and evolution, we need to understand many aspects including, cooling, star formation efficiency, galaxy mergers and interactions, stellar evolution, AGN, supernovae feedback, dust formation and distribution, and many more. On one hand, it could be said that galaxies are very simple because they follow tight scaling relations with only a few important parameters controlling their evolution. But from another perspective, galaxies are far more complex because these simple parameters are connected in highly non-linear ways.

Numerical simulations of structure formation using collisionless particle-based N-body methods now yield consistent results (Hockney & Eastwood, 1981; Springel, 2010), but to model the evolution of baryons, hydrodynamic equations have to be solved, including mechanisms such magnetic fields, radiation, and non-thermal particles. It is unrealistic for our computer simulations to cover all the scales relevant for galaxy evolution in one computation. Large-scale structures of the cosmic web have scales on 100s of Mpc and galaxy environment covers scales of 1 - 10 Mpc. Within galaxies, features such as spiral arms have structures on scales of 0.1-1 kpcs. Star formation is a multiscale process: giant molecular clouds are 10s of parsec in size, whereas each star cluster and supernovae can be pc to sub-pc sized. AGN activity is also a multiscale process, with SMBH having event horizons of $< 1{,}000$ AU (Event Horizon Telescope Collaboration et al., 2019), sub-pc sized structures in their accretion disks and jets, with their jet-heating being able to affect the entire halo. In principle, any theory of galaxy formation needs to cover scales from cosmic structure formation down to atomic physics (some 35 orders of magnitude). Thus simulations rely on prescriptions to describe the relevant physical mechanisms that act below the resolution limit of the simulation (sub-grid models).

The latest large cosmological magnetohydrodynamical simulations of galaxy formation include the IllustrisTNG project (Pillepich et al., 2018; Weinberger et al., 2017). By comparing simulated galaxies with observed galaxies, we can further enhance our understanding of the process of galaxy evolution. Nelson et al. (2018) used the simulations to explore the galaxy colour bimodality at low redshift. Tracing individual galaxies through time, they found that the primary driver of galaxy colour transition in their model is AGN feedback at low SMBH accretion rates. However, as Figure 1.10 shows, there are many ways a galaxy can become red at $z = 0$.

Another powerful method to trace galaxies through redshift is to use semi-analytic models (SAMs) (for a review see Benson 2010; Somerville & Davé 2015). SAMs generally combine merger trees from cosmological simulations with simple analytic prescriptions to model the physical processes occurring during galaxy formation and evolution. By finding discrepancies

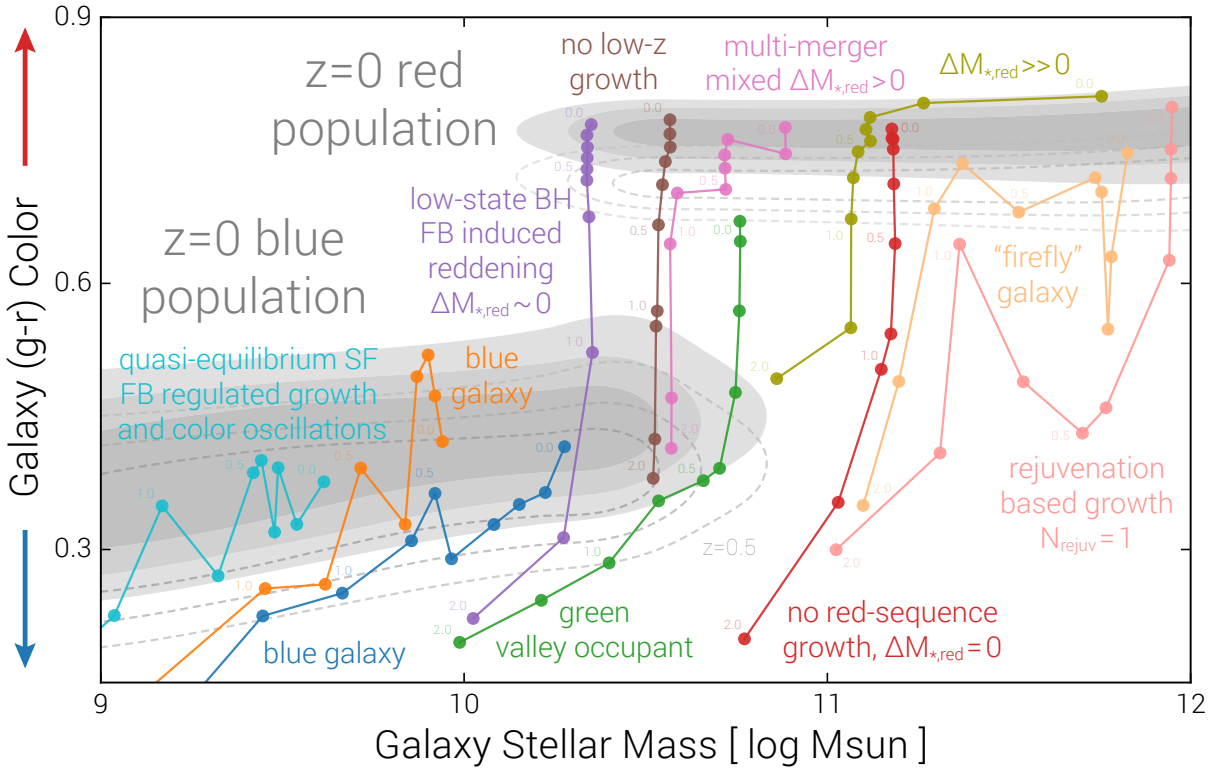

Figure 1.10.: Schematic diagram of galaxy evolution across the colour-mass plane from Nelson et al. (2018), demonstrating the various trajectories of central galaxies towards the red sequence at $z = 0$ (generally from bottom-left to top-right). The distribution of all $z = 0$ galaxies is shown by the gray contours, while the dotted lines indicate the bulk evolution of the red and blue populations to $z \simeq 0.5$, both moving downward in (g-r). Eleven colored lines show the *characteristic evolutionary pathways of individual, central galaxies*, from at most $z = 2$ to the present day drawn from tracks in TNG100. The symbols for each track are placed at $z = \{0, 0.1, 0.2, 0.3, 0.4, 0.5, 0.7, 1.0, 1.5, 2.0\}$, and are thus spaced roughly 1 Gyr apart. Mergers, black-hole (BH), and star formation (SF) feedback (FB), and gas accretion are some of the processes that move galaxies along these tracks.

between the SAMs and observational results, we can find out where key physics is missing or inaccurately treated in our models, and find ways to adapt the models accordingly.

When interpreting results from both observations and simulations, we must remember that different redshifts correspond not only to different times but also to different places in the Universe. Therefore, when we attempt to connect observations of galaxies at different redshifts to infer a picture of galaxy evolution, we are implicitly assuming homogeneity. For this to be true, it is vital that surveys contain enough cosmological volume to be representative of the Universe at the relevant epoch (van Dokkum 2001; see also Figure 1.11).

1.3.1. Wide area pan-chromatic surveys

For conclusions to be drawn from observations made in one area of the sky to be applicable in a general sense, a survey must sample sufficient cosmic volumes to draw representative

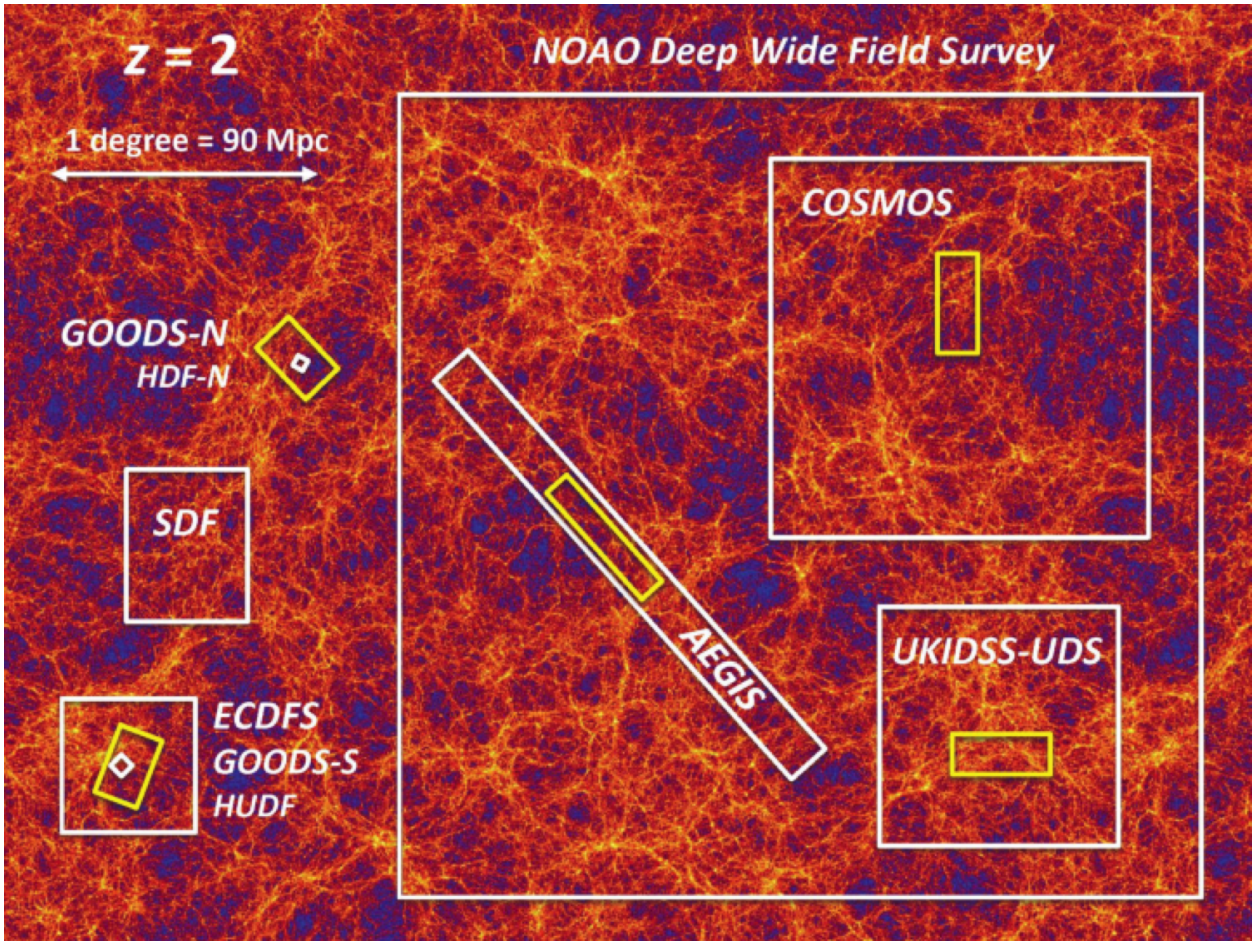

Figure 1.11.: The relative sizes of several important surveys on the sky. The image in the background shows a cosmological N-body simulation from the MultiDark Project, viewed at $z = 2$, more than 10 Gyr ago. The colours represent the matter density in a slice 43 Mpc thick. 1 degree at this redshift represents 90 Mpc co-moving volume. Small surveys are more likely to sample a volume that is over-dense or under-dense. Wider area surveys can average over variations in densities, but for a given amount of observing time, they will not be as sensitive to fainter galaxies. Survey areas shown are the the GOODS fields, the SDF, ECDFS, HDF-N, HUDF, UKIDSS Ultradeep Survey, AEGIS, NOAO Deep wide field survey. The yellow boxes show the five CANDELS fields which are embedded within another famous survey area. Figure from Madau & Dickinson (2014).

samples of galaxies at each redshift, mass, and environment of interest. Due to their complex nature, large samples ($>$ 10,000) of galaxies are required so that the population can be divided into a number of statistically-significant sized bins in each parameter of interest.

Different physical processes dominate in different regions of the electromagnetic spectrum. Only a multiwavelength view of a galaxy reveals the full picture of processes occurring within a galaxy. There has been a long history of observing visible light. However, other parts of the electromagnetic spectrum have grown more accessible with the invention of modern instruments sensitive to a wide variety of photon energies. In general, the wavelength of the radiation is dependent on the temperature of the emitting object. For example, radiation of

longer wavelengths stems from colder objects. Cold dust between stars emits light at long infrared wavelengths, whereas the very hot centres of galaxies emit X-rays.

Local Universe

A particularly important survey for this thesis is the Sloan Digital Sky Survey (SDSS; York et al. 2000; Abazajian et al. 2009), which has obtained deep multi-colour images covering one-third of the sky, and spectra for more than three million astronomical objects. Large amounts of value-added data are available in the public domain, which we will draw on in Chapters 2 and 3.

Higher redshift

Extragalactic astronomy has focused on a small number of well-studied areas on the sky, so-called "deep fields", that are optimized across the electromagnetic spectrum (some of which are represented in Figure 1.11). Surveys generally must be either very deep or very wide (or somewhere in-between), depending on the instruments and observation time available. Studies of high redshift galaxies were enabled by the HST because, being situated above the Earth's atmosphere, it allowed images with sufficient optical resolution to spatially resolve distant galaxies. The very deep, but small (2.4 arcminutes to an edge) Hubble Ultra Deep Field (HUDF; Beckwith et al. 2006) was designed for studies of very high redshift galaxies. The widest-area deep field imaged by HST is the Cosmic Evolution Survey (COSMOS) (Scoville et al., 2007), designed to study the large scale structure in the Universe and its evolution with redshift. The COSMOS field (2 degrees to an edge) was chosen to have low background emission (e.g., from our Galaxy) at all wavelengths, to be free of bright sources at all wavelengths, and to be visible in both hemispheres from the ground; ensuring ultra-deep imaging, large numbers of spectra, and easy follow-up observations.

VLA COSMOS

Since the first interstellar radio emission was detected in the 1930s, radio astronomy has contributed to many groundbreaking discoveries about the Universe. It is now known that radio emission from galaxies ranges from pure star-forming galaxies, whose radio output is dominated by stellar evolution processes, to radio-loud objects whose radio emission is dominated by an AGN. Radio surveys are no longer dominated by exotic objects but are taking their place as a new window from which to view the majority of galaxies. In Chapter 3 we focus on observations of the COSMOS field taken with the Very Large Array (VLA) at 3 GHz. Figure 1.5 demonstrates the mechanisms that contribute to the SED at radio wavelengths. Star formation produces thermal and non-thermal radio continuum emission in galaxies (e.g., Condon 1992). Supernovae remnants accelerate cosmic ray electrons that produce non-thermal synchrotron emission. Both types of emission can be characterized by a power law spectrum $S \propto \nu^{\alpha}$, where S is the flux density at frequency ν, and α is the spectral index. Typical values for α are -0.8 and -0.1 for synchrotron and free-free emission, respectively. The radio SED of star-forming galaxies is, therefore, composed by the superposition of two power laws, where that for synchrotron emission dominates over $1 < \nu < 30$. The lack of terrestrial radio interference at these frequencies and the higher

angular resolution afforded over low-frequency observations, has motivated the development of deep, large scale radio surveys at GHz frequencies in COSMOS, such as the VLA-COSMOS Large Project at 3 GHz that uncovered more than 10,000 galaxies over the redshift range $0 < z < 6$ (Smolčić et al., 2017b,a).

Looking ahead

In the next few years optical surveys such as the Dark Energy Survey (DES), Large Synoptic Survey Telescope (LSST) Survey, and Euclid Wide and Deep Surveys will cover thousands of square degrees. These imaging surveys will contribute to galaxy evolution studies via accurate measurements of photometric redshifts, luminosity functions, and galaxy clustering. Spectroscopy is an invaluable tool for studying galaxy kinematics and obtaining precise redshifts. Upcoming surveys facilitated by new instruments such as 4-metre Multi-Object Spectroscopic Telescope (4MOST) and Multi Object Optical and Near-infrared Spectrograph (MOONS) on the Visible and Infrared Survey Telescope for Astronomy (VISTA), and E-ELT Multi-Object Spectrograph (MOSAIC) on the European Extremely Large Telescope (ELT) telescope will dramatically increase the size of current galaxy samples.

1.4. Outline of this thesis

Galaxies have a wide range of properties, yet it is apparent that many galaxy properties are correlated. Which physical processes are important for controlling the observable properties of galaxies and their diversity is a central question of extragalactic astronomy. The leading Λ Cold Dark Matter cosmology theory for galaxy evolution has great power for predicting large scale matter distribution, and hence the distribution of galaxies. But, it is clear that galaxies are not made of simple collisionless particles and that baryonic physics (e.g., gas hydrodynamics, radiative cooling, star formation, supernova and AGN feedback) play a key role in shaping their observable properties. To progress our understanding of galaxy evolution, we compare theoretical models against measurements of galaxy properties over cosmic time. Disagreements between models and observations can give indications about where our models need improvement. Measuring the SFR of galaxies is therefore fundamental to our understanding of galaxy evolution; we want to find out what controls how stars form, and by extension how many stars form, and where?

When we view galaxies in the distant Universe with photometric surveys, we are averaging the light from millions of stars at various stages in their life. This light is also processed by the presence, properties, and spatial distribution of dust. Our current understanding of dust grains is still very limited and so the degree to which dust attenuation affects our SFR measurements is uncertain. Analyses of the galaxy-integrated IR emission of galaxies out to $z \sim 2-3$ show that the dust attenuation is substantial at these high redshifts (see Figure 1.12), but complete samples at even earlier epochs are not yet available. In this thesis, we will address the role of dust attenuation in our measurements of SFRs, and use dust-independent methods to derive a new stellar mass – SFR (SFMS) relation of star-forming galaxies across cosmic time. Some questions that we will address include:

- How do the amount and spatial distribution of dust affect measurements of SFR? (Chapter 2 and 3)

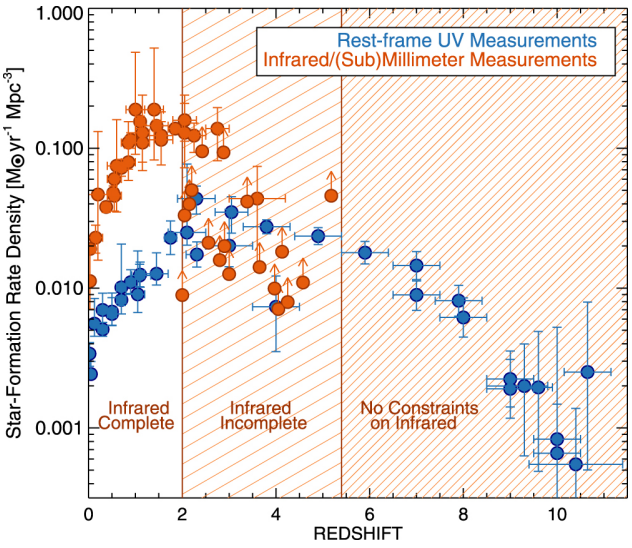

Figure 1.12: The cosmic star formation history of the Universe, as measured at rest-frame UV wavelengths (blue) and infrared through millimeter measurements (orange), taken from Casey et al. (2018). While recent FIR/(sub)mm surveys have mapped obscured star formation with individual galaxy detections out to $z \sim 7$, there are few constraints on their contribution to the overall SFR density at $z > 3$ due to sample incompleteness. Our current understanding of star formation in the early Universe is severely limited by the lack of constraints on dusty star formation particularly beyond $z \sim 4$.

- How do high-z measurements of SFR activity change when we use a dust-free measurement? What does the SFR distribution of the galaxy population look like as a function of cosmic time? (Chapter 3 and 4)
- What role does galaxy morphology and environment play in determining the SFR of galaxies? (Chapter 4)

Specifically, in **Chapter 2** we compare the dust properties of massive galaxies at low and intermediate redshift ($z \sim 0.7$). We compile multiwavelength samples of galaxies at $0.04 < z < 0.1$ and $0.6 < z < 0.8$ and investigate how our measurements of galaxy properties can be biased by the angle at which we view a galaxy. We infer the dust geometry for our two samples and also estimate the overall attenuation of UV light in massive galaxies as a function of redshift. In **Chapter 3** we extend this study to test different UV SFR calibrations that correct for dust attenuation. Our results will be informative for the next generation of SAMs and hydrodynamical simulations that are starting to include prescriptions for the formation, destruction, and redistribution of dust in galaxies.

In **Chapter 4**, we study the redshift evolution of the SFMS out to $z \sim 5$ using new photometric and 3 GHz VLA data from the COSMOS field in a stacking experiment. We separate the relation between SFR and galaxy morphology from stellar mass out to $z < 1.5$, and we investigate the role of galaxy environment on SFRs.

2 Evolution in disk opacity over 7 Gyr

This chapter was published in a similar form in the refereed article **Leslie** *et al. (2018b) "Probing dust and ISM properties using galaxy disk inclination I: Evolution of disk opacity since $z \sim 0.7$"*

Disk galaxies at intermediate redshift ($z \sim 0.7$) have been found in previous work to display more optically thick behaviour than their local counterparts in the rest-frame B-band surface brightness, suggesting an evolution in dust properties over the past ~ 7 Gyr. We compare the measured luminosities of face-on and edge-on star-forming galaxies at different wavelengths (Ultraviolet (UV), mid-infrared (MIR), far-infrared (FIR), and radio) for two well-matched samples of disk-dominated galaxies: a local Sloan Digital Sky Survey (SDSS)-selected sample at $z \sim 0.07$ and a sample of disks at $z \sim 0.7$ drawn from the Cosmic Evolution Survey (COSMOS). We have derived correction factors to account for the inclination dependence of the parameters used for sample selection. We find that typical galaxies are transparent at MIR wavelengths at both redshifts, and that the FIR and radio emission is also transparent as expected. However, reduced sensitivity at these wavelengths limits our analysis; we cannot rule out opacity in the FIR or radio. UV attenuation has increased between $z \sim 0$ and $z \sim 0.7$, with the $z \sim 0.7$ sample being a factor of ~ 3.4 more attenuated. The larger UV attenuation at $z \sim 0.7$ can be explained by more clumpy dust around nascent star-forming regions. There is good agreement between the fitted evolution of the normalisation of the $\mathrm{SFR_{UV}}$ versus $1-\cos(i)$ trend (interpreted as the evolution of the dust clumpiness fraction) and the molecular gas fraction/dust fraction evolution of galaxies found out to $z < 1$.

2.1. Introduction

Dust grains in the interstellar medium (ISM) absorb and scatter light emitted by stars and re-emit radiation in the infrared (IR). Dust often has a large impact on star formation rate (SFR) measurements; for example, global galaxy ultraviolet (UV) fluxes usually suffer from 0-3 magnitudes of extinction (Buat & Xu, 1996). For global galaxy measurements, the term attenuation is used as it refers to the integrated property of an extended distribution, rather than extinction along a line of sight. Dust attenuation depends on the amount and distribution of dust in a galaxy.

Galaxy opacity comes mainly from the presence of dust and is therefore highly dependent on the amount of dust, the dust geometry with respect to the stars, the wavelength of light

under consideration, and the optical properties of the dust grains. Dust exists in spiral galaxies and its distribution can be studied through dust emission in the infrared. Dust has been found out to radial distances 1-2 times the optical radius R_{25} of local galaxies (Smith et al., 2016; Hunt et al., 2015; De Geyter et al., 2014; Ciesla et al., 2012). Despite being present in the outskirts of galaxies, the dust distribution has been found to have a lower scale height than the stars (Xilouris et al., 1999).

Most current models of galaxy dust distributions include at least two dust components: a distribution of diffuse dust and a distribution of optically thick dust clouds at the site of young star-forming regions (Draine & Li, 2007a; Galliano et al., 2011; Jones et al., 2013). The diffuse dust is heated by a combination of young and old stars and plays a major role in the total output of dust emission (Ciesla et al., 2014; Bendo et al., 2012; Boquien et al., 2011; Popescu et al., 2011; Bendo et al., 2010; Draine & Li, 2007a; Mathis, 1990). Observations have indicated that the face-on opacity of the diffuse dust decreases with galaxy radius (e.g. Boissier et al. 2004; Popescu et al. 2005; Holwerda et al. 2005; Pérez-González et al. 2006; Boissier et al. 2007; Muñoz-Mateos et al. 2009). The diffuse component dominates the dust emission at longer wavelengths ($\lambda > 160$ μm) (Dale et al., 2007; Draine & Li, 2007b; De Vis et al., 2017). The second important component comes from dust in the birth clouds of massive stars (Charlot & Fall, 2000; da Cunha et al., 2008). Dust in birth clouds will experience the strong UV radiation from the young stars, with a radiation field 10-100 times more intense than that experienced by the diffuse component (Popescu et al., 2011). Dust emission from these clouds is restricted to the star-forming regions, however it dominates at intermediate wavelengths ($\sim 20 - 60$ μm) (Popescu & Tuffs, 2008; Popescu et al., 2011).

In the local Universe, disk galaxies vary from optically thin to thick depending on wavelength and location in the disk (Huizinga & van Albada, 1992; Peletier & Willner, 1992; Giovanelli et al., 1994, 1995; Jones et al., 1996; Moriondo et al., 1998; González et al., 1998). For example, using the background light technique, studies have found that spiral arms are opaque, but the opacity of the interarm-region decreases with galactic radius (González et al., 1998; White et al., 2000; Keel & White, 2001).

A common method to probe the dust opacity, originally proposed by Holmberg (1958, 1975), is to study the inclination dependence of starlight (e.g. Disney et al. 1989; Valentijn 1990; Jones et al. 1996; Tully et al. 1998; Maller et al. 2009; Masters et al. 2010a). A disk inclined to our line of sight has higher column density and therefore stellar radiation has to pass through more dust before reaching us, meaning more light is scattered or absorbed. Theoretically, for a completely opaque disk, the surface brightness will not change as a function of inclination angle, but for a transparent disk, the surface brightness will increase as the galaxy becomes edge-on. Luminosity trends give complementary information: for an opaque disk, the luminosity will dim with inclination, whereas for a transparent disk the luminosity should be independent of inclination. This method requires a statistical sample of galaxies. Recently this method has been used by Chevallard et al. (2013) and Devour & Bell (2016) on galaxies in the Sloan Digital Sky Survey (at $z < 0.12$) to measure the difference between edge-on and face-on attenuation in the optical SDSS ugriz passbands as a function of parameters drawn from longer-wavelength surveys that are independent of dust attenuation. Devour & Bell (2016) found that the strength of the relative attenuation varies strongly with both specific star formation rate and galaxy luminosity (or stellar mass), peaking at $M_* \approx 3 \times 10^{10}$ $M_\odot$. Our work aims to extend these studies by quantifying the

inclination-attenuation relationship for wavelengths commonly used to measure SFR: UV, mid-IR (MIR), far-IR (FIR) and radio.

Although studied well locally, the opacity of galaxies as a function of redshift has not been investigated at multiple wavelengths. The Cosmic Evolution Survey (COSMOS) covers an area large enough to obtain a significant number of disk galaxies detected at multiple wavelengths. Taking advantage of the high-resolution Hubble Space Telescope (HST) imaging of the COSMOS field, Sargent et al. (2010) were able to study the surface brightness-inclination relation of a morphologically well-defined sample of disk-galaxies at $z \sim 0.7$. A direct comparison of COSMOS spiral galaxies with artificially redshifted local galaxies revealed that the COSMOS galaxies at $0.6 < z < 0.8$ are on average more opaque than local galaxies, having an almost flat rest-frame B band surface brightness-inclination relation. Sargent et al. (2010) suggested that this constant relation could be due to the presence of more attenuating material, or a different spatial distribution of dust at $z \sim 0.7$.

In this Chapter, we extend the analysis of Sargent et al. (2010) to measure the inclination dependence of UV, MIR, FIR, and radio luminosity for a sample of galaxies at $0.6 < z < 0.8$ drawn from the COSMOS survey. We compare these results to what is found using a local sample, matched in galaxy stellar mass and size, drawn from the Sloan Digital Sky Survey (SDSS).

In Section 2.2 we describe the multi-wavelength data sets used and our approach to select a sample of star-forming disk galaxies. In Section 2.2.3 we derive and apply corrections to measurements of stellar mass, g-band half-light radius, and Sérsic index in order to obtain measurements unbiased by dust-related inclination effects. In Section 2.2.4 we show the properties of our sample. We use the inclination-SFR relations to compare the opacity of galaxies in Section 2.3. In Section 2.3.3 we fit our UV results with models of attenuation from Tuffs et al. (2004). In Section 2.3.4 we show that the UV opacity depends on stellar mass surface density. In Section 2.4 we compare the SFRs derived from different wavelengths for galaxies detected in multiple bands. In Section 2.5 we discuss what trends are expected in terms of dust evolution and galaxy opacity at intermediate redshift. Our conclusions are presented in Section 2.6. We find that galaxies show more overall UV attenuation at $z \sim 0.7$, possibly due to a larger fraction of dust that surrounds nascent star-forming regions.

Throughout this work, we use Kroupa (2001) IMF and assume a flat lambda CDM cosmology with (H_0, Ω_M, Ω_Λ) = (70 km s^{-1} Mpc^{-1}, 0.3, 0.7).

2.2. Data and sample selection

To study the inclination dependence of attenuation, we must rely on samples of galaxies that differ only in their viewing angle (Devour & Bell, 2016). To achieve a sample of such galaxies both locally and at intermediate redshift ($z \sim 0.7$), we select galaxies from the SDSS and COSMOS survey regions of the sky, respectively.

High-resolution imaging is required to accurately fit a model galaxy brightness profile. Following Sargent et al. (2010), we choose to compare a sample at $z \sim 0.7$ with a local sample ($z \sim 0$), because the central wavelength of the SDSS g band matches the rest-frame wavelengths of objects observed in the F814W filter at redshift $z \sim 0.7$ (Kampczyk et al., 2007).

At both $z \sim 0$ and $z \sim 0.7$ we selected star-forming galaxies with stellar masses $\log(M_*/\mathrm{M}_\odot) > 10.2$, g-band half-light radii $r_{1/2} > 5$ kpc, and Sérsic index $n < 1.2$. These cuts were made to minimise selection biases whilst maintaining a reasonable number of galaxies in our $z \sim 0.7$ sample and will be discussed in more detail in the following sub-sections.

2.2.1. COSMOS $0.6 < z < 0.8$ disks

The $z \sim 0.7$ COSMOS sample was selected in a similar manner to Sargent et al. (2010), drawn from the complete sample of galaxies with I ≤ 22.5 mag listed in the Zurich Structure and Morphology Catalog (ZSMC; available on IRSA[18]).

We have matched the ZSMC with the COSMOS2015 photometric catalogue of Laigle et al. (2016). The COSMOS2015 catalogue is a near-infrared selected catalogue that uses a combined $\mathbf{z^{++}YJHK_s}$ detection image. The catalogue covers a square field of 2 deg^2 and uses images from UltraVISTA-DR2, Subaru/Hyper-Suprime-Cam, *Spitzer*, *Herschel*-PACs[19], and *Herschel*-SPIRE[20]. Galactic extinction has been computed at the position of each object using the Schlegel et al. (1998) values and the Galactic extinction curve (Bolzonella et al., 2000; Allen, 1976).

We use photometric redshifts (z_{phot}) and stellar masses in the COSMOS2015 catalogue [21]. Photometric redshifts were calculated using LePhare (Arnouts et al., 2002; Ilbert et al., 2006) following the method of Ilbert et al. (2013). Fluxes from 30 bands extracted from a 3″ aperture using SExtractor were used to calculate the redshift probability distribution. The dispersion of the photometric redshifts for star-forming galaxies with $\mathrm{i_{AB}} < 23$ is $\sigma_{\Delta z/(1+z)} < 0.01$.

We limit our sample to $0.6 \leq z_{\mathrm{phot}} \leq 0.8$. At a redshift of $z \sim 0.7$ the observed I-band roughly corresponds to the rest frame g-band and the observed near-ultraviolet (NUV)-band roughly corresponds to the $z \sim 0$ frame far-ultraviolet (FUV), minimising k-corrections and allowing for easy comparison with local samples.

Stellar masses are derived as described in Ilbert et al. (2015), using a grid of synthetic spectra created using the stellar population synthesis models of Bruzual & Charlot (2003).The 90% stellar mass completeness limit for star-forming galaxies in the redshift of our sample ($0.6 < z < 0.8$) is 10^9 M$_\odot$ in the UVISTA Deep field (Laigle et al., 2016). We re-scale the stellar masses from a Chabrier IMF to a Kroupa IMF by dividing by 0.92 (Madau & Dickinson, 2014).

X-ray detected sources from XMM[22]-COSMOS (Cappelluti et al., 2007; Hasinger et al., 2007; Brusa et al., 2010) are not included in our analysis because of potential active galactic nuclei (AGN) contamination. We have also checked for MIR-AGN using the Donley et al. (2012) Infrared Array Camera (IRAC) criteria. Galaxies with associations to multiple radio components at 3 GHz are also excluded because they are radio-AGN (Smolčić et al., 2017a). We select only galaxies classified as star forming in COSMOS2015 which uses the NUV-r/r-J

[18] NASA/IPAC infrared science archive (IRSA): https://irsa.ipac.caltech.edu/data/COSMOS/tables/morphology/

[19] The Photodetector Array Camera and Spectrometer (PACS)

[20] Spectral and Photometric Imaging Receiver (SPIRE)

[21] ftp://ftp.iap.fr/pub/from_users/hjmcc/COSMOS2015/

[22] X-ray Multi-Mirror Mission (XMM)

colour-colour selection adapted from the Williams et al. (2009) classification and described in Ilbert et al. (2013).

Morphology information

Morphological measurements were carried out on HST/Advanced Camera for Surveys (ACS) F814W (I-band) images with a resolution of $\sim 0.1''$(Koekemoer et al., 2007). This corresponds to a physical resolution of ~ 0.67 and 0.75 kpc at redshifts 0.6 and 0.8, respectively. Galaxies are classified as "early type", "late type" or "irregular/peculiar" according to the Zurich Estimator of Structural Types algorithm (ZEST; Scarlata et al. 2007). Late-type galaxies (ZEST Class=2) are separated into four sub-classes, ranging from bulge-dominated (2.0) to disc-dominated (2.3) systems. For simple comparison with the SDSS galaxies, we select disk galaxies based on Sérsic index n <1.2 (described in Section 2.2.1). Increasing the bulge-to-disk ratio at a constant opacity can mimic the effect of increasing the opacity of a pure disk (Tuffs et al., 2004). We have confirmed that our results for the COSMOS sample do not change when selecting pure disks using ZEST Class=2.3 rather than using Sérsic index.

Galaxies in the ZSMC catalogue have been modelled with single-component Sérsic (1968) profiles using the GIM2D IRAF software package (Simard et al., 2002). In the single-component case, GIM2D seeks the best fitting values for the total flux $F_{\rm tot}$, the half-light radius $R_{1/2}$, the position angle ϕ, the central position of the galaxy, the residual background level, and the ellipticity $e = 1 - b/a$, where a and b are the semimajor and semiminor axes of the brightness distribution, respectively. See Sargent et al. (2007) for more details on how the surface-brightness fitting was performed. In order not to miss low-surface galaxies, we cut our sample at $r_{1/2} > 4$ kpc (Sargent et al. 2007, see Fig. 12). This is because at a given size a minimum surface brightness is required for a galaxy to meet the I < 22.5 criterion of the morphological ZSMC catalogue. Including smaller galaxies biases our sample against low brightness galaxies. Our sample is complete for galaxies with $r_{1/2} > 4$ kpc.

Data used for SFR estimation in the COSMOS field

The multi-wavelength photometry used for measuring SFRs at FUV, MIR, FIR, and radio wavelengths is summarised in Table 2.1. For the COSMOS data, all fluxes are found in the COSMOS2015 catalogue, except for the radio 3 GHz fluxes which are from Smolčić et al. (2017a).

At $z = 0.7$, the GALEX NUV filter roughly corresponds to the FUV filter at $z = 0.1$. The COSMOS field was observed as part of the GALEX (Galaxy Evolution Explorer) Deep Imaging Survey (DIS) in the FUV (~ 1500 Å) and NUV (~ 2300 Å).

We also draw 100 μm fluxes from the COSMOS2015 catalogue. These data were taken with PACS (Photoconductor Array Camera and Spectrometer; Poglitsch et al. 2010 on the *Herschel* Space Observatory through the PEP (PACS Evolutionary Probe) guaranteed time program (Lutz et al., 2011). Source extraction was performed by a PSF fitting algorithm using the 24 μm source catalogue to define prior positions.

The VLA-COSMOS 3 GHz Large Project catalogue (Smolčić et al., 2017b) contains 10,830 radio sources down to 5 σ (and imaged at an angular resolution of $0.74''$). These sources

Table 2.1.: Data used for SFR estimation. The area Ω quoted is the overlap between the particular wavelength and the SDSS or ACS surveys from which the morphological parameters are drawn. N_{gals} is the number of galaxies in our sample detected at each wavelength with robust mass, inclination, and SFR measurements (Signal-to-noise ratio (S/N)>3).

Band	Instrument	Survey	Ω (deg^2)	3σ (μJy)	N_{gals}	References
COSMOS						
UV	GALEX (NUV)	DIS	1.7	0.23	296	(1)
MIR	*Spitzer* MIPS (24 μm)	S-COSMOS	1.7	43	373	(2,3)
FIR	*Herschel* PACS (100 μm)	PEP	1.7	5,000	87	(4,5)
Radio	VLA (S-band, 3 GHz)	VLA-COSMOS	1.7	7	58	(6,7)
SDSS						
UV	GALEX (FUV)	MIS	∼1,000	1.8	1,003	(8)
MIR	WISE (W3, 12 μm)	AllWISE	∼8,400	340	8,333	(9,10)
FIR	IRAS (60 μm)	FSC	∼8,400	1.2×10^5	291	(11)
Radio	VLA (L-band, 1.4 GHz)	FIRST, NVSS	∼8,400	450	198	(12,13,14)

(1) Capak et al. (2007); (2)Sanders et al. (2007); (3)Le Floc'h et al. (2009); (4)Poglitsch et al. (2010); (5)Lutz et al. (2011); (6)Smolčić et al. (2017b); (7)Smolčić et al. (2017a); (8)Bianchi et al. (2011); (9)Wright et al. (2010); (10)Chang et al. (2015); (11)Moshir & et al. (1990); (12)Kimball & Ivezić (2014); (13)Becker et al. (1995); (14)Condon et al. (1998).

were matched to COSMOS2015 (as well as other multi-wavelength COSMOS catalogues) by Smolčić et al. (2017a).

2.2.2. Local $0.04 < z < 0.1$ disks in SDSS

The local sample is drawn from the SDSS Data Release 7 (Abazajian et al., 2009). In particular, we select galaxies with publicly available redshifts, stellar masses, and emission line fluxes from the spectroscopic MPA/JHU catalogue[23] described in Brinchmann et al. (2004). We select galaxies in the redshift range $0.04 < z < 0.1$. The lower redshift limit is to ensure that the SDSS fibre covers at least 30% (median coverage 38%) of the typical galaxy to minimise aperture effects (Kewley et al., 2005). The sample is constrained to $z < 0.1$ to avoid incompleteness and significant evolutionary effects (Kewley et al., 2006) and to ensure that the FUV passband lies above the numerous stellar absorption features that occur below 1250 Å.

Total stellar masses were calculated by the MPA/JHU team from ugriz galaxy photometry using the model grids of Kauffmann et al. (2003) assuming a Kroupa IMF. The stellar masses in the MPA/JHU catalogue have been found to be consistent with other estimates (see Taylor et al. 2011; Chang et al. 2015). In the following analysis, we use the median of the probability distribution to represent each parameter, and the 16th and 84th percentiles to represent the dispersion.

We further limit our sample to galaxies classified as 'starforming' ($\log([\mathrm{O\,III}]/\mathrm{H}\beta) < 0.7 -$

[23] http://www.mpa-garching.mpg.de/SDSS/DR7/

$1.2(\log([\mathrm{N\,II}]\,/\mathrm{H}\alpha) + 0.4))$ or 'starburst' (the galaxy is 'starforming' but also has an Hα equivalent width $> 50\,$Å). In this way, we exclude quiescent galaxies and galaxies whose optical emission is dominated by an AGN. We also exclude any galaxies that are classified as AGN based on their WISE colours following Mateos et al. (2012).

Morphology information

Simard et al. (2011) provide morphological information that is consistent with the data provided by Sargent et al. (2007) used for this paper. Simard et al. (2011) performed two-dimensional (2D) point-spread-function-convolved model fits in the g and r band-passes of galaxies in the SDSS Data Release 7. The faint surface brightness limit of the spectroscopic sample was set to $\mu_{50} = 23.0$ mag arcsec^{-2} for completeness. The SDSS images have a typical seeing of $1.4''$ (Simard et al., 2011). This corresponds to a physical resolution of 1.1 kpc and 2.6 kpc at $z = 0.04$ and 0.1, respectively. We use the SDSS g-band GIM2D single Sérsic model fitting results in order to match the rest frame wavelength and model used to derive COSMOS morphological parameters.

To select disk-dominated galaxies, we restrict our sample to galaxies that have a g-band Sérsic index $n < 1.2$. This is motivated by Sargent et al. (2007); in particular, their Figure 9, which shows that pure disk galaxies (ZEST type 2.3) have in general $n < 1.2$.

Data used for SFR estimation in the SDSS field.

The catalogues used for measuring SFRs in our local sample are listed in Table 2.1 as well as some information regarding the instruments used, the sky coverage, and average noise properties. For all wavelengths, we require a S/N of at least three for the fluxes to be used in our analysis.

We make use of FUV data from the GALEX Medium Imaging Survey (MIS) that has been cross-matched with the SDSS DR7 photometric catalogue by Bianchi et al. (2011). We correct the GALEX photometry for galactic reddening following Salim et al. (2016) who use the extinction coefficients from Peek & Schiminovich (2013) for UV bands:

$$A_{\mathrm{FUV}} = 10.47\ \mathrm{E(B\text{-}V)} + 8.59\ \mathrm{E(B\text{-}V)}^2 - 82.2\ \mathrm{E(B\text{-}V)}^3, \tag{2.1}$$

where E(B-V) are the galactic colour-excess values.

We use observations taken by the Wide-field Infrared Survey Explorer (WISE; Wright et al. 2010) telescope to probe the mid-infrared emission of our local galaxy sample. Specifically, we rely on the catalogue compiled by Chang et al. (2015) which contains a match of SDSS galaxies (in the New York University Value-Added Galaxy Catalog; Blanton et al. 2005; Adelman-McCarthy & et al. 2008; Padmanabhan et al. 2008) with sources in the AllWISE catalogue. Fluxes were measured using the profile-fitting method that assumes the sources are unresolved and has the advantage of minimising source blending. Chang et al. (2015) found that most galaxies are typically smaller than the PSF, but results from their simulation showed that there is a difference between the true flux and the PSF flux which is a function of the effective radius (R_e of the Sérsic profile) and this difference is independent of the input flux, axis ratio, or n. Therefore, we use their flux values that have been corrected based on R_e.

Long wavelength infrared data were obtained from the IRAS (Infrared Astronomical Satellite) Faint Source Catalog (FSC) v2.0. (Moshir & et al., 1990). We match the FSC to our parent SDSS sample using the `Sky Ellipses` algorithm in `Topcat` because the IRAS source position uncertainties are significantly elliptical. We match using the 2σ positional uncertainty ellipse of the IRAS sources and assume a circular positional uncertainty on each SDSS source of $1''$.

We make use of the radio continuum flux densities compiled in the Unified Radio Catalogue v2 (Kimball & Ivezić, 2008, 2014). The catalogue was constructed by matching two 20 cm (1.4 GHz) surveys conducted with the Very Large Array (VLA): FIRST (Faint Images of the Radio Sky at Twenty Centimeters; Becker et al. 1995) and NVSS (NRAO-VLA Sky Survey; Condon et al. 1998). The FIRST survey has an angular resolution of $\sim 5''$and a typical rms of 0.15 mJy/beam. The NVSS survey, on the other hand, has an angular resolution of $\sim 45''$ and a typical rms of 0.45 mJy/beam. We use sources with a $\leq 2''$ separation between the FIRST and SDSS positions as recommended by Ivezić et al. (2002) and Kimball & Ivezić (2014). For our analysis, we use the 1.4 GHz fluxes from the NVSS catalogue because it is better suited for measuring the global flux from a galaxy than the FIRST survey due to the more compact observing configuration.

2.2.3. Inclination-independent sample selection

Devour & Bell (2016) describe some of the many potential selection effects which could affect the results of an inclination-dependent study such as ours. If any of the parameters used in our selection, such as stellar mass or radius, is dependent on inclination, then we might get a false signal. We show the relationship between the parameters used for our sample selection and galaxy inclination in Figure 2.1.

The inclination is calculated from axis ratios measured from the rest-frame g-band image using the Hubble (1926) formula

$$\cos^2(i) = \frac{(b/a)^2 - (b/a)^2_{\rm min}}{1 - (b/a)^2_{\rm min}}, \tag{2.2}$$

with $(b/a)_{\rm min} = 0.15$ (following Sargent et al. 2010 and based on Guthrie 1992 and Yuan & Zhu 2004). If galaxies were randomly oriented disks, we would expect to see a flat distribution of $1-\cos(i)$. This is roughly the case for our local parent sample; however, our COSMOS $z \sim 0.7$ parent sample has a distribution of $1-\cos(i)$, slightly skewed towards face-on galaxies. Instances of $b/a \sim 1$ and 0 (and hence $1-\cos(i) = 0$ and 1) are rare due to intrinsic disk ellipticity and the finite thickness of edge-on systems, respectively. The apparent thickness might vary with the apparent size ($R_{1/2}$), with smaller images appearing rounder, even if images are deconvolved with the PSF (Shao et al., 2007). We do not account for this, but it might contribute to the trend we see between inclination and half-light radius in our samples in Figure 2.1.

Driver et al. (2007) performed an empirical correction to remove inclination-dependent attenuation effects on the turn-over magnitude in B-band luminosity function. Inspired by this, we fit a power-law,

$$y = k_1[1-\cos(i)]^{k_2} + y_c, \tag{2.3}$$

to our selection parameters, where y is the stellar mass, half-light radius, or Sérsic index. We first calculate the median 'y' in bins of $1-\cos(i)$ (50 bins for the local sample and 20 bins for the COSMOS $z \sim 0.7$ sample) and then find the best fitting parameters k_1, k_2, and y_c using the Python task scipy.optimize.curve_fit (χ^2 minimisation). For this analysis, we include only galaxies that satisfy our constraints on redshift and star-formation activity (see Sects. 2.1 and 2.2), and $n < 4$ (selecting late-type galaxies), which will be referred to as our "parent samples". The fitted parameters are given in Table 2.2.

In our SDSS sample, there is a trend that more inclined galaxies (those with a low axis ratio) are more likely to have a higher measured stellar mass. On the other hand, in the COSMOS sample, there is no significant ($k_1 = 0$ within the errors) relation between stellar mass and inclination. The stellar masses for our local sample were derived using optical photometry (and spectroscopic redshifts) only, whereas the stellar mass of COSMOS galaxies is derived using 16 photometric bands, including IRAC near-IR data. This might suggest that the mass of the inclined SDSS galaxies is overestimated due to redder optical colours.

We find that the most important inclination effect is that on galaxy size, $r_{1/2}$. Authors such as Yip et al. (2010), Huizinga & van Albada (1992), Möllenhoff et al. (2006), Masters et al. (2010a) and Conroy et al. (2010) have all previously reported that galaxy size measurements (such as half-light or effective radius) are dependent on galaxy axis ratio b/a, with edge-on galaxies appearing larger at a fixed magnitude. Our local results are consistent with results from Möllenhoff et al. (2006) who show that the B-band sizes increase by 10 - 40% from face-on to edge-on due to a reduction of the light concentration by centrally concentrated dust in local galaxies. Our fit for the dependence of radius on inclination for the COSMOS sample results in a size increase of 110% when i is increased from 0 to 88 degrees. However, the large correction only applies at high inclination, ($b/a < 0.3$, $i > 75\,\mathrm{deg}$).

Maller et al. (2009) and Patel et al. (2012) found that inclination corrections have a strong dependence on Sérsic index (in the u band and UVJ bands, respectively). Having even a small bulge will reduce the ellipticity of the isophotes of a galaxy, resulting in a deficiency of galaxies with $b/a \sim 0$. We can see this trend in the spread of inclination values at a given n in Figure 2.2. We also correct for a slight inclination dependency of n with the inclination for the local sample. The distribution of n has a large tail of high n-values which cause even our fit to the median n values to pass above the mode of the distribution.

During our sample selection we account for the inclination dependence using our determined fit values (Table 1) and Equation 2.3. We subtract the inclination-dependent term to correct parameters to their face-on equivalent. To summarise we select galaxies with

- $n_{\mathrm{corr}} < 1.2$
- $r_{1/2,\mathrm{corr}} > 4$ kpc
- $\log(\frac{M_*}{\mathrm{M}_\odot})_{\mathrm{corr}} > 10.2$.

2.2.4. Sample properties

Figure 2.2 shows the distribution of relevant properties for galaxies in the local sample (left) and the COSMOS $z \sim 0.7$ sample (right) after the selection cuts detailed in the previous

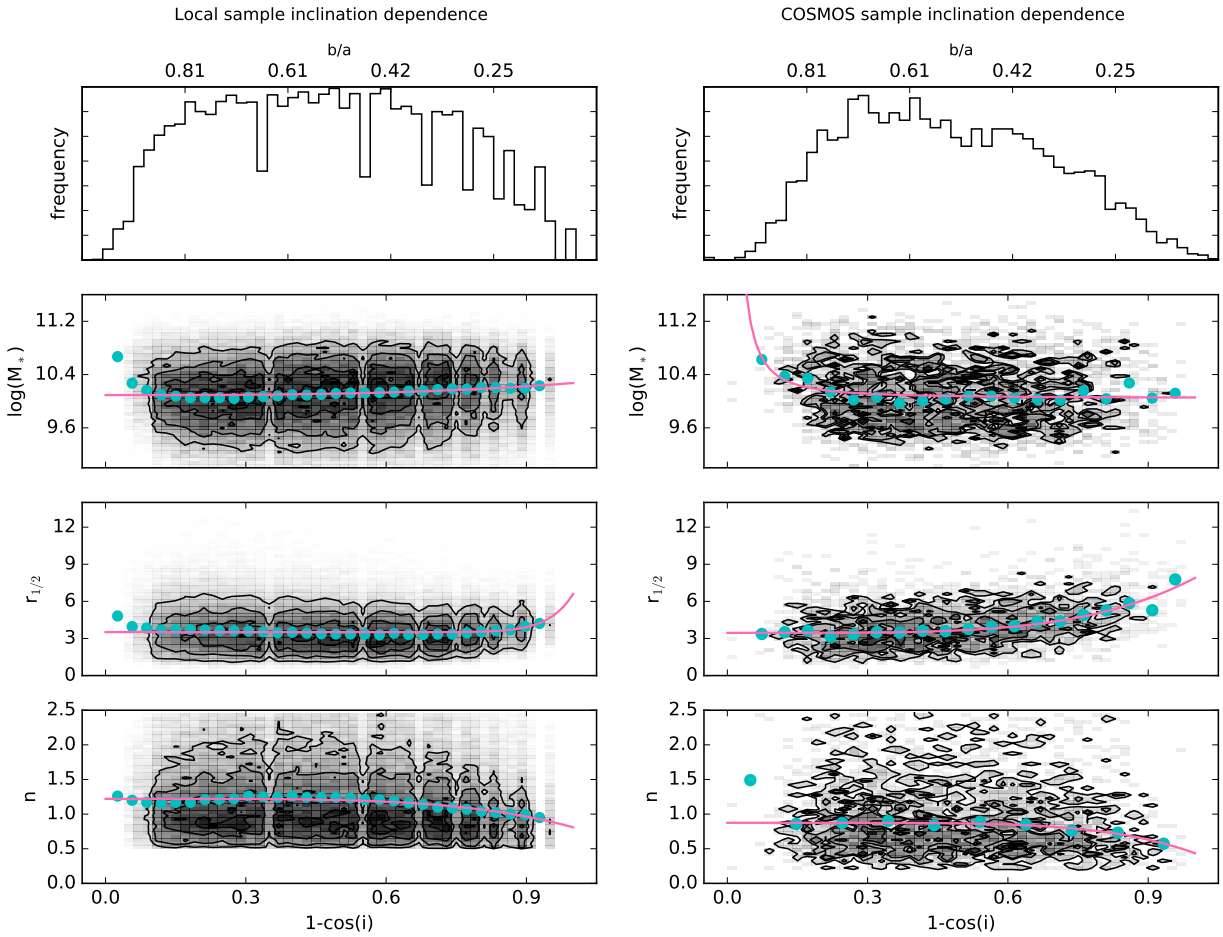

Figure 2.1.: Relationship between parameters used for sample selection (stellar mass M_* [$M_\odot$], half-light radius in rest-frame g-band $r_{1/2}$ [kpc], and Sérsic index n) with inclination (in the form of $1-\cos(i)$). The distributions are shown for galaxies in our parent samples (See Sects. 2.1, 2.2, and 2.3). A histogram of the inclination distribution (or equivalently axis ratio distribution) is shown in the top panels. Galaxies randomly oriented would produce a flat distribution. Dips in the local b/a distribution are caused by numerical issues in the Simard et al. (2011) fitting. Teal dots trace the median values in bins of inclination and the pink curves show the resulting power-law fit (Eq. 2.3) to the medians. We subtract the inclination dependent term from our parameters before performing our final sample selection to avoid artificially introducing inclination trends in our results.

Table 2.2.: Fitted parameters that describe the inclination dependence of galaxy properties that we use for sample selection. We fit the relation $y = k_1[1-\cos(i)]^{k_2} + y_c$ to our parent samples of star-forming galaxies based on the SDSS and COSMOS surveys.

y	k_1	k_2	y_c
SDSS $\log(M_*/\mathbf{M}_\odot)$	0.18±0.04	3.0±1.4	10.09±0.02
COSMOS $\log(M_*/\mathbf{M}_\odot)$	0.01±0.01	-1.6±0.5	10.05±0.04
SDSS $r_{1/2}$ (kpc)	3.1±2.5	19±9	3.52±0.04
COSMOS $r_{1/2}$ (kpc)	4.4±0.4	4.4±0.7	3.5±0.1
SDSS n	-0.41±0.05	4.5±0.7	1.22±0.01
COSMOS n	-0.44±0.05	5.6±1.2	0.87± 0.01

Section were applied. Each histogram shows the distribution of galaxies detected at a particular wavelength. The total number of galaxies in each subsample is indicated in Table 2.1.

The distribution of $1-\cos(i)$, where i is the inclination, is shown in the top panels of Figure 2.2. As mentioned above, a sample of randomly oriented thin disks should produce a constant $(1-\cos(i))$ distribution. In the local sample, galaxies detected in FIR, MIR, and UV catalogues have very similar (flat) distributions of galaxy inclination $(1-\cos(i))$. In both the local and COSMOS sample, the inclination distribution of radio-detected galaxies is skewed towards more inclined galaxies. In the COSMOS sample, the FIR-detected subsample is also skewed towards more inclined galaxies. It is possible that this skewness is caused by a surface-brightness effect – for a fixed global flux limit, an edge-on galaxy will have a higher surface brightness than a face-on galaxy because the area on the sky is smaller ($\propto \sin(i)$). This effect is true especially in the radio, which is unobscured by dust[24].

The distributions of redshifts in the COSMOS field are similar for the different wavelengths. Locally, the FIR sample peaks at lower redshifts because of the limited sensitivity of the IRAS catalogue. The number of galaxies of the UV and MIR subsamples increases with redshift in our local sample as an increasing volume of space is sampled.

The third panels show the half-light radius distributions of the sample after inclination correction. The local galaxy sample has a median $r_{1/2,\mathrm{corr}} = 5.04$ kpc, whereas the COSMOS sample has a median of $r_{1/2,\mathrm{corr}} = 5.25$ kpc. The size distributions of the different subsamples are consistent.

The distribution of Sérsic index, n, is shown in the fourth row of Figure 2.2. For our sample, we selected galaxies with $n < 1.2$. The distribution of n for local galaxies does not go below 0.5 because this was the lowest n value allowed by Simard et al. (2011) in their pure Sérsic profile model fits. The distribution of n for local galaxies peaks at higher values than the distribution at $z \sim 0.7$. This could be due to star-forming galaxies becoming more mature over time (Scoville et al., 2013).

The stellar mass distributions (Fig. 2.2, bottom row) show some important biases between the subsamples. For the COSMOS sample, the radio and FIR subsamples are peaked at larger stellar masses than the UV and MIR subsamples. In the local sample the FIR $\log(M_*)$ distribution starts to fall off at lower stellar masses due to the shallow detection limit of

[24]We found more galaxies with larger b/a when considering NVSS detected sources compared to FIRST detected sources, but this difference was not statistically significant.

IRAS survey and the correlation between stellar mass and galaxy luminosity. Adopting the relationship between SFR and stellar mass (Eq. 2.4), the local FIR observations can only detect a main sequence galaxy with $\log(M_*/\mathbf{M}_\odot) > 10.2$ at $z \sim 0.04$. For this calculation, a galaxy with SFR 0.3 dex (1σ) below the SFMS given in Section 3 was considered. Similarly, the COSMOS FIR observations are complete down to $\log(M_*/\mathbf{M}_\odot) > 10.4$ at $z \sim 0.6$.

2.2.5. SFR estimates

To calculate SFR, we use the UV and TIR calibrations compiled in Kennicutt & Evans (2012). These calibrations assume a Kroupa IMF and a constant star formation rate. Star formation rates are given in units of $\mathrm{M}_\odot\ \mathrm{yr}^{-1}$.

Young stars emit the bulk of their energy in the rest-frame UV. The FUV emission from star-forming galaxies is dominated by radiation from massive O and B stars. We use the SFR calibration derived for the GALEX FUV bandpass to calculate $\mathrm{SFR_{UV}}$ for our local sample (see Table 1 of Kennicutt & Evans 2012). At $z = 0.7$ the GALEX NUV filter samples approximately the same rest-frame wavelength as the GALEX FUV filter at $z = 0.1$ (Zamojski et al., 2007). The GALEX NUV flux is used with the local FUV calibration. No correction for dust attenuation is applied. FUV attenuation corrections and their inclination dependence will be discussed in Chapter 3.

For both the mid- and far-IR monochromatic tracers, we convert the monochromatic flux density to the total infrared luminosity (8 - 1,000 μm) using the Wuyts et al. (2008) spectral energy distribution (SED) template and then calculate the SFR using the $\mathrm{L_{IR}}$ calibration of Murphy et al. (2011). The Wuyts et al. (2008) template was constructed by averaging the logarithm of the Dale & Helou (2002) templates resulting in a SED shape reminiscent of M82 (Wuyts et al., 2011c). Wuyts et al. (2008) and Wuyts et al. (2011b) use their template to derive $\mathrm{L_{IR}}$ from monochromatic IR bands and show that the 24 μm-derived SFR is consistent with a multiband FIR SFR over $0 < z < 3$. The SED is valid for SFMS galaxies; however, the use of a single template for all the galaxies may introduce some scatter in the estimate of the FIR luminosity[25]. We do not use templates that rely on a priori knowledge of the SFR and distance from the SFMS (such as e.g. Magdis et al. 2012) because the SFRs could be biased due to inclination effects (see e.g. Morselli et al. 2016 on how galaxy inclination impacts the measured scatter of the SFMS).

We calculate the luminosity density L_ν, in a given filter following da Cunha et al. (2008). For the IRAS and *Spitzer*/IRAC photometric systems, the convention is to use the calibration spectrum $\nu C_\nu = \lambda C_\lambda = \text{constant}$ (see C. & et al. 1988 and the IRAC data Handbook [26]). The *Spitzer* Multiband Imaging Photometer (MIPS) system was calibrated using a black body spectrum of s temperature 10,000K, such that $C_\lambda = B_\lambda(10,000\mathrm{K})$ (MIPS Data Handbook[27]). For the WISE system we assume $C = 1$ [28]. For each galaxy, we redshift the SED and convolve it with the appropriate filter response to determine the expected measured luminosity. We then scale the SED to match the measured single-band luminosity and integrate the scaled SED between 8 and 1,000 μm (rest-frame) to obtain the total infrared luminosity.

[25] We have also confirmed that using the MIR SFR calibrations of Battisti et al. (2015) does not qualitatively change our analysis.

[26] http://irsa.ipac.caltech.edu/data/SPITZER/docs/irac/iracinstrumenthandbook/

[27] http://irsa.ipac.caltech.edu/data/SPITZER/docs/mips/mipsinstrumenthandbook/

[28] http://wise2.ipac.caltech.edu/docs/release/allsky/expsup/sec4_4h.html#conv2ab

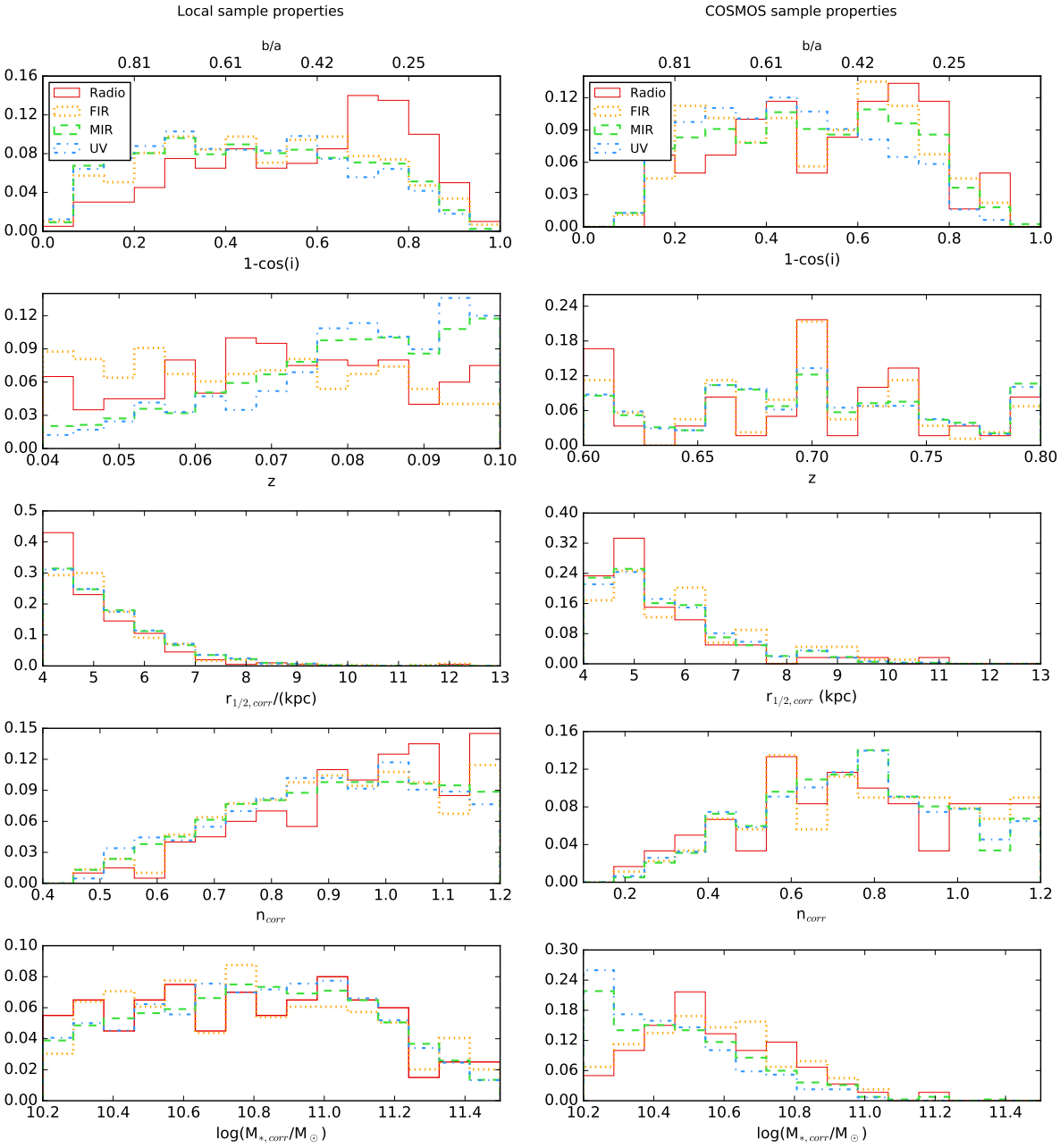

Figure 2.2.: Normalised histograms of the galaxy properties of our multi-wavelength subsamples after selection cuts. Histograms show the inclination-corrected values for $r_{1/2}$, n (derived from single Sérsic profile fits to rest-frame g-band light profiles), and $\log(M_*)$. The y-axis shows the fraction of galaxies (in that subsample) in each bin. Radio-detected galaxies have a distribution of optical axis-ratios skewed towards edge-on galaxies.

Locally we use the corrected WISE 12μm fluxes from Chang et al. (2015) to calculate $\mathrm{SFR_{MIR}}$. At $z = 0.7$, we use MIPS 24 μm fluxes, which correspond to a rest-frame 14 μm flux. We use IRAS 60 μm luminosity to probe $\mathrm{SFR_{FIR}}$ of local galaxies, as it probes near the peak of the dust SED. For galaxies in our COSMOS sample, we use the observed 100 μm PACS data, which correspond to rest frame $\sim 60\,\mu$m. Filter responses were obtained from the SVO Filter Profile Service[29]. WISE 12 μm luminosities have been observed to correlate well with Hα SFR (Lee et al., 2013; Cluver et al., 2014) above solar metallicity.

To calculate radio-SFRs in our local SDSS sample, we use empirical 1.4 GHz SFR calibration derived recently by Davies et al. (2017) for star-forming galaxies in the Galaxy and Mass Assembly (GAMA;Driver et al. 2011) and FIRST surveys. We use the calibration anchored to the UV+TIR SFR (after converting from a Chabrier to Kroupa IMF by adding 0.025 dex; Zahid et al. 2012). Recently, Molnar et al. (2017) used IR data from *Herschel* and 3 GHz VLA observations for a sample of star-forming galaxies in the COSMOS field to measure the infrared-radio correlation out to $z < 1.5$. Molnar et al. (2017) separated disk-dominated from spheroid-dominated galaxies using the ZEST catalogue. We use their finding that for disk-dominated galaxies, the IR-radio ratio scales as $q_{\mathrm{TIR}} \propto (1+z)^{-0.04\pm0.01}$, and by relating the radio luminosity to the TIR luminosity, we are able to use the TIR SFR calibration in Kennicutt & Evans (2012).

For a comparison of the SFR tracers used in this work, we refer the reader to Appendix B.

2.3. Inclination-dependent SFR

In this Section, we consider the inclination dependence of galaxy SFRs derived from multiple wavelengths. There are different galaxies included in the different wavelength subsamples. For the local UV sample, this is largely due to the different survey areas. But different emission mechanisms occurring in different galaxies can result in different SED shapes of galaxies, meaning some galaxies are brighter (and detectable) or dimmer (and non-detectable) at particular wavelengths. We have made a size, mass, and Sérsic index cut to select star-forming galaxies to ensure that galaxies do not have drastically different SED shapes for both our local and COSMOS samples. Nonetheless, the different depths of the different observations can bias the subsample towards particular galaxies. For example, the radio and FIR subsamples might select more starburst galaxies with high SFRs due to their shallow depth.

Star-forming galaxies fall on a particular locus in the SFR-stellar mass plane with the logarithmic properties being linearly correlated. We refer to this relation as the star-forming galaxy main sequence (SFMS; Noeske et al. 2007). The normalisation and (less strongly) slope of the SFMS have been reported to evolve with redshift, with galaxies at high redshift having higher SFRs at a given mass than local galaxies. The normalisation evolution is thought to reflect the increased amount of cold gas available to galaxies at high redshift (e.g. Tacconi et al. 2013). The average galaxy at a given mass forms more stars at $z \sim 0.7$ than the average galaxy at $z \sim 0$. To place the SFRs of the two samples on a comparable scale, we normalise our multi-wavelength SFRs by the average SFMS SFR expected for a galaxy with a given stellar mass and redshift. The locus of the SFMS is known to depend on

[29] http://svo2.cab.inta-csic.es/svo/theory/fps3/index.php?mode=browse

sample selection (e.g. Karim et al. 2011) and, in particular, on how actively 'star forming' the sample under consideration is. We adopt the best-fit SFMS relation for an updated version (M. Sargent, private communication) of the data compilation presented in Sargent et al. (2014).

$$\log\left(\frac{\mathrm{SFR_{SFMS}}}{\mathrm{M_\odot yr^{-1}}}\right) = 0.816\log\left(\frac{M_*}{\mathrm{M_\odot}}\right) - 8.248 + 3\log(1+z). \tag{2.4}$$

By combining different measurements from the literature that employ different selection criteria, different SF tracers (UV, IR, or radio), and different measurement techniques, Sargent et al. (2014) were able to derive a relation that is representative of the average evolution of the sSFR of main sequence galaxies. The new relation presented in Equation 2.4 has been recalculated using recent works such as Chang et al. (2015). However, the IMF (Chabrier, 2003) and cosmology (WMAP-7; Larson et al. 2011) assumed by Sargent et al. (2014), differs from ours. To convert the relation from a Chabrier to a Kroupa IMF, we add 0.03 dex to the stellar mass (Madau & Dickinson, 2014; Speagle et al., 2014). The different cosmologies will affect the SFR through the square of the luminosity distance for a given redshift. The correction is redshift dependent: For $0.04 < z < 0.1$, we adjust the SFR by -0.004 dex and for $0.6 < z < 0.8$ we adjust the SFR by +0.006 dex.

Between $z = 0.07$ and $z = 0.7$, (median redshifts of our two samples) the normalisation changes such that an average $\log(M_*/\mathrm{M_\odot}) = 10.5$ main sequence galaxy located exactly at the core of the SFR-$\mathrm{M_*}$ relation has a SFR of 2.6 $\mathrm{M_\odot\ yr^{-1}}$ at $z = 0.07$ and 11 $\mathrm{M_\odot\ yr^{-1}}$ at $z = 0.7$. We investigate the affects of using different SFMS relations in Appendix A.

Figure 2.3 shows the relation $\log(\mathrm{SFR}_\lambda)$ - $\log(\mathrm{SFR_{SFMS}})$ with inclination where $\mathrm{SFR_{SFMS}}$ is the main sequence SFR for a galaxy of a given mass. To quantify trends present in Figure 2.3, we fit a robust linear model to the data:

$$y = \log(\mathrm{SFR}/\mathrm{SFR_{SFMS}}) = \mathrm{slope}\cdot(1-\cos(i)) + \mathrm{intercept}, \tag{2.5}$$

using the statsmodels.api package in Python that calculates an iteratively re-weighted least-squares regression given the robust criterion estimator of Huber (1981).

To estimate the uncertainties in our results, we resampled the data by drawing (with replacement) a new sample of galaxies 1,000 times. We then drew the new galaxy inclination and $\mathrm{SFR/SFR_{SFMS}}$ values from the measurement uncertainty distribution. The COSMOS sample has asymmetric errors in inclination and stellar mass, and the local sample has asymmetric errors in stellar mass. To sample these asymmetric distributions, we combined two Gaussian distributions with widths given by the upper and lower limits of the error, normalised so that a new sample data-point is equally likely to lie above or below the measurement. Linear regression was performed on each sample drawn, and the best-fitting slopes and intercepts with their uncertainties are shown in Figure 2.4.

Projecting the best-fitting parameter pairs in Figure 2.4 onto the horizontal and vertical axes, we obtain a distribution of the best fitting slopes and intercepts, respectively. The 50th (median), 5th and 95th percentiles are given in Table 2.3. The dashed lines in Figure 2.3 indicate the median of the fitted parameters.

The flux limits of the surveys correspond to a minimum observable luminosity, and hence

SFR, that increases with redshift. We show the SFR that corresponds to this minimum for our redshift ranges coloured in orange in Figure 2.3. The limits show that we are limited in our analysis of the FIR and radio-opacity of galaxies both for the local and $z \sim 0.7$ samples, however, they were not taken into account in our fits.

2.3.1. Slopes: Opacity

If disk galaxies are transparent or optically thin then the luminosities and hence SFRs should not depend on inclination angle. In this case, we would see no gradient in Figure 2.3. If galaxies are optically thick, or opaque, then the luminosity observed can only originate from the stars at the outer surface visible to our line of sight. The projected area varies with $\cos(i)$ for a circular disk. Therefore, for an opaque galaxy, we expect the measured SFR to decrease with the inclination angle (and $1-\cos(i)$), producing a negative slope in Figure 2.3.

A negative slope is clear in both the local and COSMOS $\mathrm{SFR_{FUV}}$ inclination relations. We find that highly inclined galaxies suffer from more FUV attenuation than face-on galaxies, indicating that disk galaxies are optically thick at FUV wavelengths at both redshifts. The fitted values for the slopes are -0.79 ± 0.09 and -0.5 ± 0.2, for the $z \sim 0$ and $z \sim 0.7$ samples.

Davies et al. (1993) explained that when measuring surface-brightness-inclination relations to study disk opacity, a survey limited by surface brightness might not be able to probe a large enough range of surface brightnesses required to detect a slope, even if some opacity is present. Similarly, if the survey is not deep enough to probe a range of luminosities, then we might incorrectly conclude that a lack of slope indicates that the disks are transparent. We find that the radio and FIR data are not deep enough for us to reliably analyse a SFR-inclination gradient at these wavelengths, due to the potential for selection bias. However, the samples do not show any inclination trend in the upper envelope SFR (not affected by limits) probed by the surveys. Secondly, the fraction of limits to detections is approximately constant in bins of inclination. Therefore, our data are consistent with galaxies being transparent at FIR and radio wavelengths.

The FUV samples give slightly shallower slopes at $z \sim 0.7$ than at $z \sim 0$. This could be partially influenced by the flux limits of the COSMOS surveys meaning that only galaxies with relatively large $\mathrm{SFR/SFR_{SFMS}}$ are detected. These limitations were not taken into account in our linear model.

The $z \sim 0$ and $z \sim 0.7$ slopes for the UV are consistent at the 1.65 σ level. In Appendix A we show that using the $\mathrm{SFR_{12\mu m}}$ for normalisation rather than the $\mathrm{SFR_{SFMS}}$ gives fully consistent slopes of -0.6 at both redshifts. This suggests that no significant evolution has occurred in the dust properties or dust-star geometry between $z = 0$ and $z = 0.7$.

2.3.2. Intercept: SFR calibration and selection effects

The y-intercept represents how the SFR measured for a face-on galaxy compares to the main sequence SFR at our given redshifts and stellar mass. In absence of other effects such as foreground dust at high scale height, the y-intercept approximately represents the ratio between $\mathrm{SFR_\lambda}$ of a face-on galaxy and the average total SFR (i.e. $\mathrm{SFR_{IR}}$+$\mathrm{SFR_{UV}}$) of a SFMS galaxy.

The UV SFR observed is lower than the SFMS SFR at all given inclinations, resulting in

Table 2.3.: Best-fit parameters of SFR vs. inclination where SFR is normalised by the SFMS SFR given the galaxy mass: Median, 5th and 95th percentile of the distribution.

λ	Slope	Intercept
SFR_{UV} $z \sim 0$	-0.79 $^{+0.08}_{-0.09}$	-0.20 $^{+0.04}_{-0.03}$
SFR_{MIR} $z \sim 0$	-0.12 $^{+0.03}_{-0.02}$	0.05 $^{+0.01}_{-0.01}$
SFR_{FIR} $z \sim 0$	-0.06 $^{+0.22}_{-0.20}$	0.67 $^{+0.09}_{-0.09}$
SFR_{radio} $z \sim 0$	-0.10 $^{+0.20}_{-0.22}$	0.52 $^{+0.11}_{-0.09}$
SFR_{UV} $z \sim 0.7$	-0.54 $^{+0.18}_{-0.17}$	-0.74 $^{+0.08}_{-0.08}$
SFR_{MIR} $z \sim 0.7$	-0.03 $^{+0.10}_{-0.09}$	0.28 $^{+0.05}_{-0.05}$
SFR_{FIR} $z \sim 0.7$	-0.02 $^{+0.23}_{-0.25}$	0.54 $^{+0.15}_{-0.13}$
SFR_{radio} $z \sim 0.7$	-0.17 $^{+0.31}_{-0.33}$	0.68 $^{+0.19}_{-0.18}$

a negative y-intercept. We find that the UV SFR under-predicts the SFMS SFR by ~ 0.74 dex at $z \sim 0.7$, compared to ~ 0.2 at $z \sim 0$. This implies that a larger fraction of the stellar light is attenuated and re-emitted in the infrared in the higher-redshift galaxies. We discuss this further in Sections 2.3.3 and 2.5.

The distributions of y-intercepts for the FIR and radio wavelength subsamples, all of them positive, are dominated by sample-selection effects, in particular, the flux limit of the surveys. The radio and infrared samples lie above the SFMS due to their shallow observations not being able to detect emission from SFMS galaxies.

If the SFR calibrations or main-sequence relations were incorrect, we would expect this to alter the absolute offset value. However, using a 'concordance' SFMS evolution fitted to a compilation of data (as done here) is expected to average out differences in normalisation arising due to different methods or SFR tracers. Normalising the $\mathrm{SFR_{UV}}$ to the $\mathrm{SFR_{MIR}}$ for galaxies detected in both UV and MIR wavelengths gave intercept values of -0.27 ± 0.03 and -1.0 ± 0.1 for the $z \sim 0$ and $z \sim 0.7$ samples (see Appendix A.1). However, this result is still dependent on the accuracy of the SFR calibrations at each redshift.

The SFMS has a scatter of ~ 0.3 dex (Schreiber et al., 2015), meaning that some of the scatter seen in Figure 2.3 is due to the fact that galaxies might have true SFRs higher or lower than the average SFMS SFR used for normalisation.

2.3.3. Opacity at UV wavelengths: Tuffs et al. (2004) models

At UV wavelengths our observations show a clear trend of increasing attenuation with galaxy inclination and a clear evolution of the overall attenuation with redshift. Tuffs et al. (2004) calculate the attenuation of stellar light for a grid of disk opacity and inclination, providing a direct comparison to our observations.

Tuffs et al. (2004) calculated the attenuation of stellar light from local spiral galaxies using geometries that are able to reproduce observed galaxy SEDs from the UV to the submillimetre. The model predictions of Tuffs et al. (2004), which are based on the dust

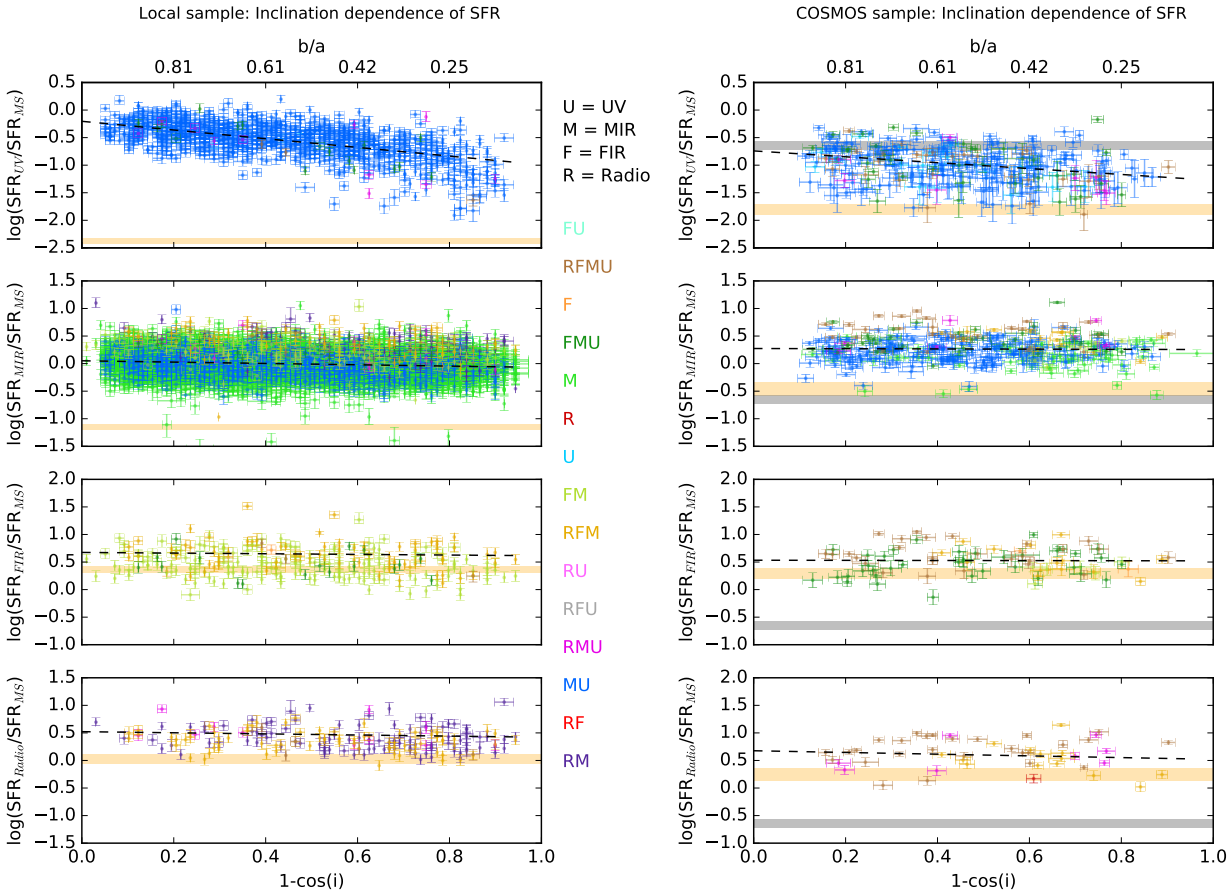

Figure 2.3.: Inclination dependence of multiwavelength SFRs. y-axis: $\log(\mathrm{SFR}_\lambda)$ - $\log(\mathrm{SFR}_{\mathrm{SFMS}})$. Top to bottom shows UV, MIR, FIR, and radio-determined SFR. x-axis: $1-\cos(i)$, where i is the galaxy inclination. Face-on galaxies are on the left of the plot (at 0) and edge-on galaxies are on the right-hand side (at 1). The left panels show SDSS galaxies ($0.04 < z < 0.1$) and the right panels show COSMOS galaxies ($0.6 < z < 0.8$). The colour index at the centre indicates which bands were detected; R=radio, F=FIR, M=MIR, and U=UV). The orange shaded region shows the minimum SFR that could be detected across the redshift ranges given the flux limits of the respective surveys. The dashed lines show the median best-fit obtained from 1,000 realisations of the data. The grey regions on the right panels show where the local ($0.04 < z < 0.1$) main-sequence SFR lies with respect to the main sequence at $z = 0.7$. This shows how the normalisation of the main sequence evolves over our redshift range.

model of Popescu et al. (2000), are shown in Figure 2.5. The model includes an exponential diffuse dust disk that follows a disk of old stars, a second diffuse dust disk that is designed to emulate the dust in spiral arms by having the same spatial distribution of the young stellar population (the thin disk), a distribution of clumpy, strongly heated grains, correlated with star-forming regions, and a dustless de Vaucouleurs bulge. The so-called clumpy dust component was required to reproduce the FIR colours and is associated with the opaque parent molecular clouds of the massive stars (Tuffs et al., 2004). The diffuse dust disk associated with the spiral arms was needed to account for the sub-millimetre emission.

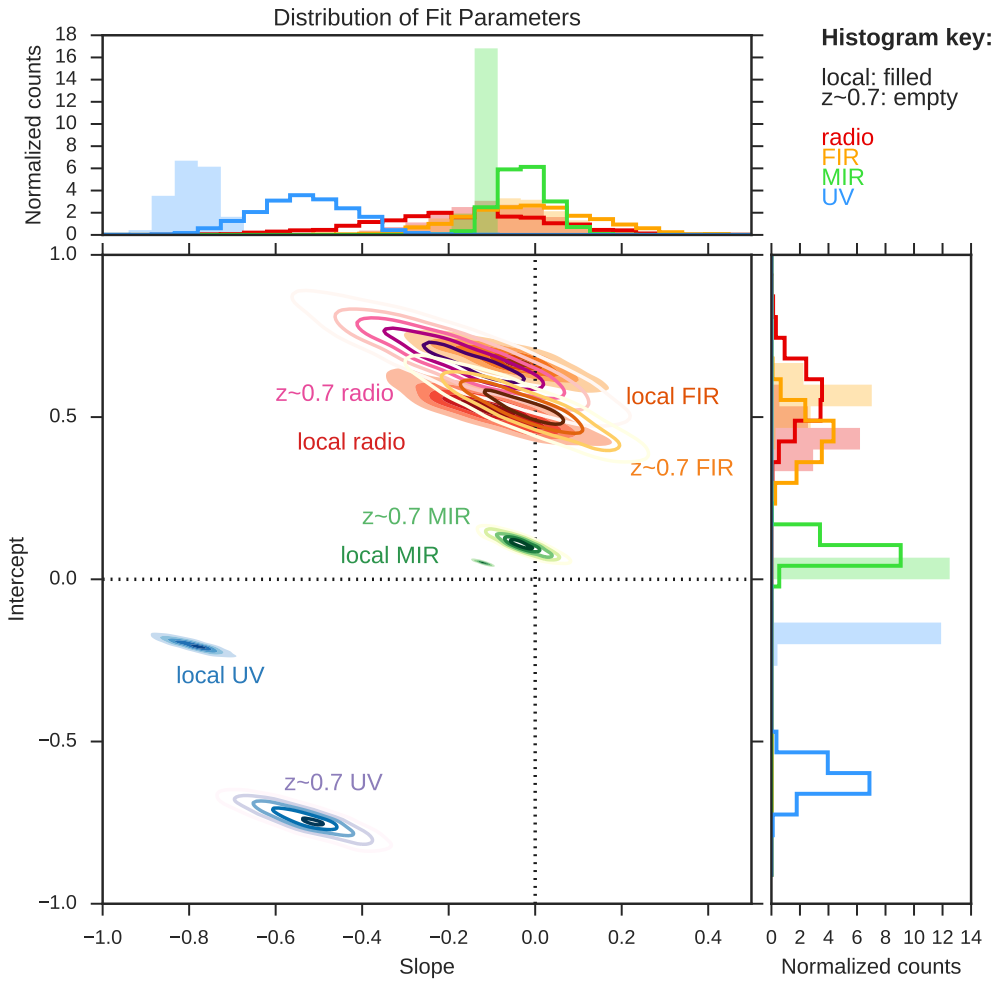

Figure 2.4.: Joint and marginalised distributions of the linear model parameters fit to the data shown in Figure 3. Filled histograms correspond to SDSS-based samples and the open histograms correspond to COSMOS-based samples. Distributions for the slope and the intercept are shown with histograms normalised so that they encompass an area of 1. The median of each parameter distribution is given in Table 3.

Tuffs et al. (2004) have calculated attenuation curves (the change of magnitude Δm due to dust attenuation) of the thin disk, thick disk, and bulge component (Δm vs. $1-\cos(i)$) and they have been represented with a fifth-order polynomial at various τ_B^f and wavelengths, where τ_B^f is the opacity through the centre of a face-on galaxy in the B-band. Since τ_B^f is the opacity through the centre of the galaxy where most of the dust is concentrated, $\tau_B^f \leq 1.0$ corresponds to an optically thin galaxy over most of its area. The attenuation calculations in the UV range were only performed on the thin disk because the thick disk is assumed not to emit in the UV.

We linearly interpolated the relation for UV attenuation at 1350 and 1650 Å, tabulated in Tuffs et al. (2004) for B-band opacities of $\tau_B^f = 0.5$, 1.0, 2.0, 4.0, and 8.0 to obtain the expected UV attenuation at 1542Å, the effective wavelength of the GALEX FUV filter. We show how the expected UV attenuation affects the $\mathrm{SFR_{UV}}$ using the tabulated relation at B-band opacities of $\tau_B^f = 0.5$, 1.0, 2.0, 4.0, and 8.0 in Figure 2.5.

The attenuation by the clumpy dust component is independent of the inclination of the galaxy, unlike the diffuse dust component. The clumpy dust component is associated with opaque parent clouds of massive stars; no UV light will escape the cloud independent of the viewing angle. The wavelength dependence of the attenuation is also not determined by the optical properties of the grains because the clouds are opaque at each wavelength. Instead, wavelength dependence arises because stars migrate away from their birth cloud over time, and therefore lower-mass, redder stars are more likely to have left their birth clouds and thus their starlight will be less attenuated (Tuffs et al., 2004). The Tuffs et al. (2004) models analytically treat the attenuation due to the clumpy component separately, parametrized by the fraction of attenuation by clumpy component, F.

Assuming that only the thin disk emits in the UV range and the disk and bulge only in the optical/NIR range as suggested by Tuffs et al. (2004), we can vary the fraction of the emitted FUV flux density, F_{FUV} , that is locally absorbed in the star-forming regions by the clumpy dust component. The total attenuation would then be

$$\Delta m_{\mathrm{UV}} = \Delta m_{\mathrm{UV}}^{\mathrm{tdisk}} - 2.5 \log\left(1 - F_{\mathrm{FUV}}\right), \tag{2.6}$$

where $\Delta m_{\mathrm{UV}}^{\mathrm{tdisk}}$ is the thin disk attenuation given in Tuffs et al. (2004) and $F_{\mathrm{FUV}} = f_{\mathrm{FUV}} \times F$, where F is the clumpiness fraction and $f_{\mathrm{FUV}} = 1.36$ at 1542 Å (the wavelength dependence of the probability that a UV photon will be completely absorbed locally). In this way F will change the overall normalisation of the $\mathrm{SFR_{UV}}$ inclination relation.

We use the Goodman-Weare Monte Carlo Markov Chain (MCMC) sampling method implemented in *python* package *emcee.py* (Foreman-Mackey et al., 2013) to find posterior distributions of τ_B^f and F for our local UV galaxy sample. We use an uninformative flat prior between τ_B^f = [0,10] and F = [0,0.61]. The maximum F = 0.61 constraint corresponds to the case where there is a complete lack of cloud fragmentation due to feedback and the probability that photons will escape into the diffuse ISM is determined only by the migration of stars away from their birth-clouds (Popescu et al., 2011). We keep 800 steps (after a 200 step burn-in) from 50 MCMC walkers. The posterior median values of parameters with 68% credible intervals for the Tuffs et al. (2004) models at $z \sim 0$ are $\tau_B^f = 3.95^{+0.16}_{-0.15}$ and $F = 0.09^{+0.02}_{-0.02}$. In Figure 2.5, we show in green 100 samples drawn randomly from the chain.

The attenuation curves for models with τ_B^f ranging from 0.5 (light grey) to 8 (dark grey) and $F = 0.22$ are also shown with our data in Figure 2.5. Tuffs et al. (2004) suggested using $F = 0.22$ because it was the median value obtained from fitting five nearby edge-on spirals, and that value was also obtained for the prototype galaxy NGC 891. On the other hand, Popescu et al. (2011) find a clumpiness fraction of $F = 0.41$ for typical spiral galaxies in the local universe. Using the FUV, which is most sensitive to the clumpiness factor, we find lower values for F in local galaxies than Tuffs et al. (2004) and Popescu et al. (2011). However, we are insensitive to dust clouds that are completely obscured in the FUV but still radiate in the infrared. This is likely the reason why the clumpiness factors we measure for the FUV are lower than the SED results that include infrared emission (by a factor of ~ 2).

Driver et al. (2007) found $\tau_B^f \sim 3.8 \pm 0.7$, derived from integrated galaxy properties of $\sim$ 10,000 galaxies with bulge-disk decompositions, consistent with our result at $z \sim 0$. At this face-on central optical depth, less than half the bolometric luminosity is actually absorbed by dust (Tuffs et al., 2004).

For the $z \sim 0.7$ sample, we noticed that the fits were dominated by the high-S/N data points with high SFRs, giving preferentially shallower slopes. The S/N effects are more important at $z \sim 0.7$ because the detection threshold is close to the data (as opposed to $z \sim 0$, where the detection threshold is well below our data). Ignoring the errors on the SFR by setting them all to a constant 0.3 dex, and considering only galaxies with $1 - \cos(i) < 0.75$, where we are more complete in sSFR, we obtain $\tau_B^f = 3.5^{+1.1}_{-1.8}$ and $F = 0.55^{+0.06}_{-0.04}$. Including all data points gives a smaller $\tau_B^f = 2.0^{+0.5}_{-0.3}$ and a correspondingly larger $F = 0.60^{+0.01}_{-0.02}$.

The spread in attenuations in the COSMOS sample could also be partially explained by the fact that galaxies have different clumpy dust fractions. Misiriotis et al. (2001) found that F varies by 30% between galaxies.

In this analysis, τ_B^f decreases with redshift while F increases, meaning the overall opacity increases as it is dominated by F at UV wavelengths. The decrease in τ_B^f is in apparent contradiction with the Sargent et al. (2010) result that reported more opaque galaxies at $z = 0.7$ in the B band. However, we note that the errors on τ_B^f are so large that the decrease reported in this analysis is not statistically significant. Furthermore, we find that normalising the $\mathrm{SFR_{UV}}$ by a different SFMS produces an increase in τ_B^f with redshift, while changing the normalisation did not change the fact that F increases between $z \sim 0$ and $z \sim 0.7$, a key result which we discuss in Section 2.4.

2.3.4. UV opacity and stellar mass surface density

Grootes et al. (2013) found that the opacity of spiral galaxies in the local Universe ($z \leq 0.13$) depends on the stellar mass surface density μ_*. De Vis et al. (2017) also report a mass surface density dependence of the B-band opacity and suggest that the increased stellar mass potential associated with higher stellar mass surface density creates instabilities in the cold ISM, which lead to the formation of a thin dust disk that increases the attenuation (Dalcanton et al., 2004). Williams et al. (2010) show that the stellar mass surface density increases with redshift out to $z \sim 2$. We re-compute our $\mathrm{SFR_{FUV}}$-inclination relations in bins of μ_* to investigate this dependence. We compute μ_* for each galaxy using the stellar

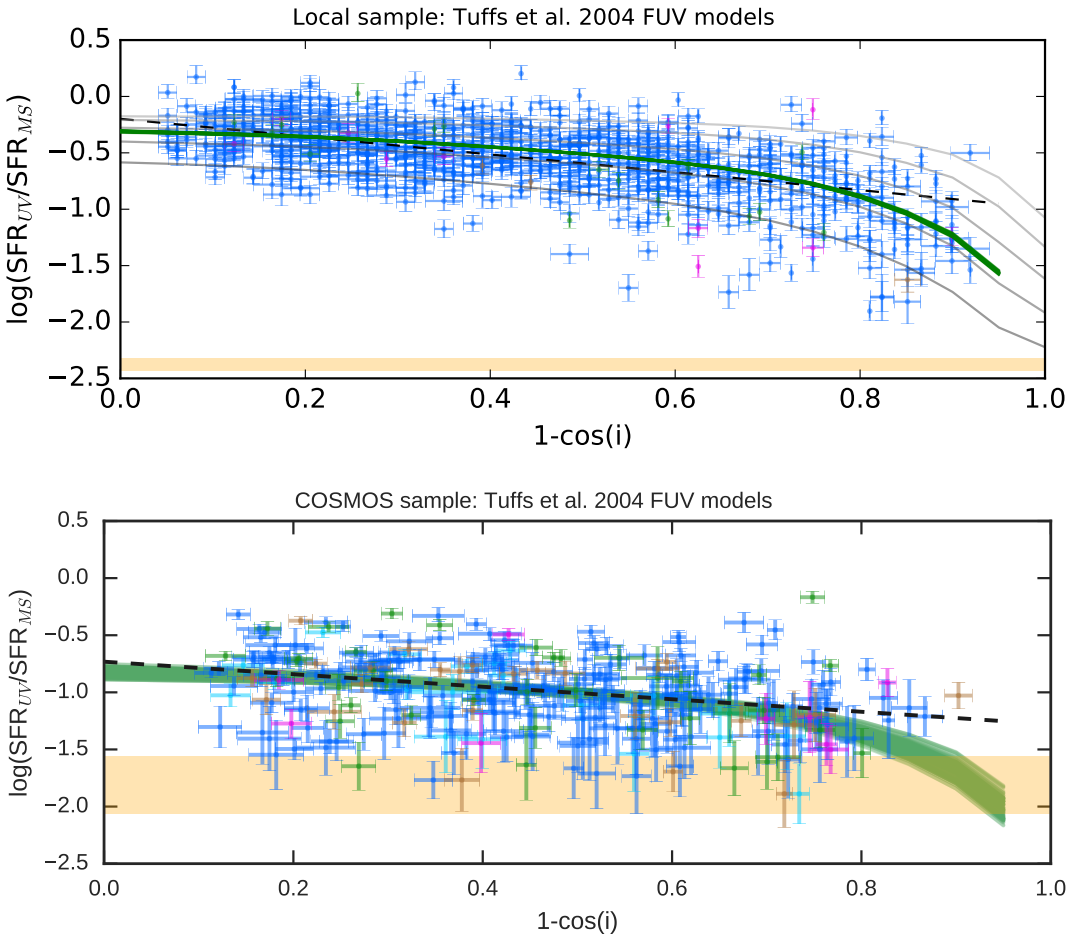

Figure 2.5.: $\mathrm{SFR_{UV}}$ - inclination relation shown in the top panels of Figure 3, but with the attenuation curves of Tuffs et al. 2004 showing the expected change in flux, and hence $\mathrm{SFR_{UV}}$, with inclination. Green trends show the relations that best fit our data, with $\tau_B^f = 3.95^{+0.16}_{-0.15}$ and $F = 0.09^{+0.02}_{-0.02}$ for the local sample (top) and $\tau_B^f = 3.5^{+1.1}_{-1.8}$, $F = 0.55^{+0.06}_{-0.04}$ for the COSMOS sample (bottom). In the left panel, models shown have face-on B-band opacities of τ_B^f= 0.5, 1.0, 2.0, 4.0, and 8.0 (from light to dark grey) and $F = 0.22$.

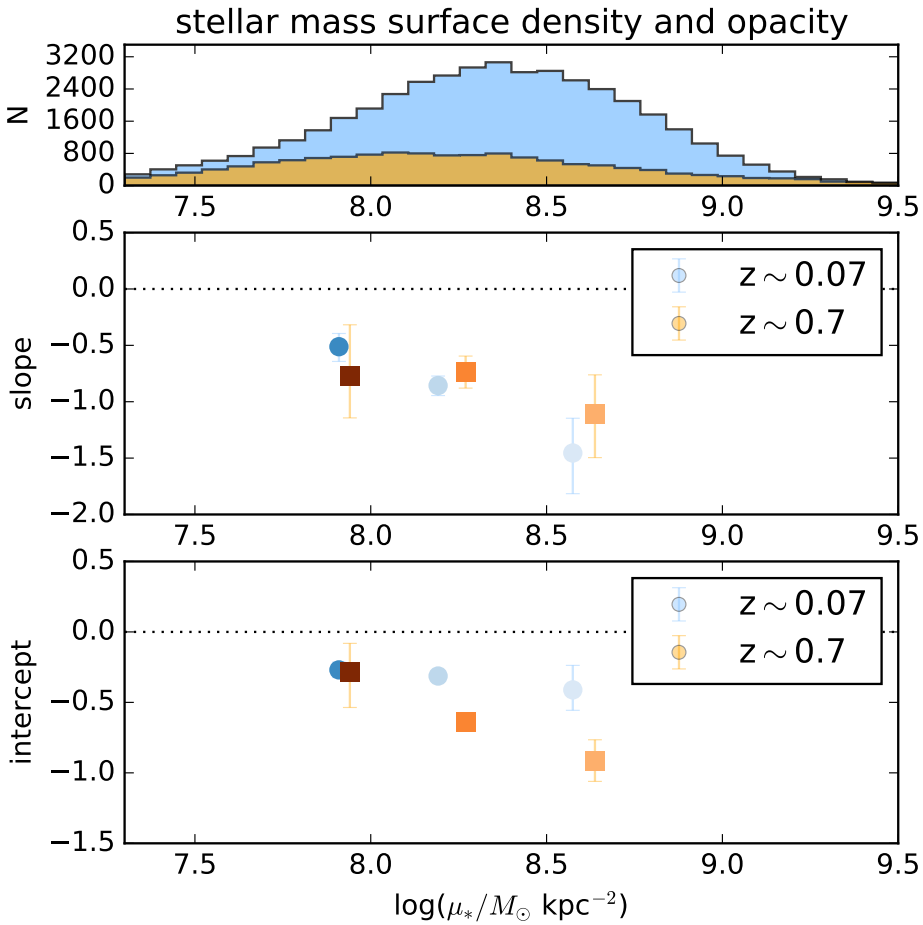

Figure 2.6.: Top panel: Distribution of stellar mass surface densities, μ_*, for our two redshift ranges. Middle panel: The relation between opacity, represented by the slope of the SFR_{FUV} -inclination relation, and stellar mass surface density. Bottom panel: The relation between overall UV attenuation, represented by the intercept of the SFR_{FUV}-inclination relation, and μ_*. Data are colour-coded by the median size, $r_{1/2}$, of each bin in the bottom panel, with colours ranging from 4 kpc (light) to 7 kpc (dark).

mass and the physical half-light radius from the rest-frame g band GIM2D fits,

$$\mu_* = \frac{M_*}{2r_{1/2}^2}. \tag{2.7}$$

Figure 2.6 shows the distribution of $\log(\mu_*)$ for our samples at $z \sim 0$ and $z \sim 0.7$. We note that μ_* was calculated with the original stellar mass and half-light radius values, without any inclination corrections. Before slicing the samples into bins of μ_*, we corrected $\log(\mu_*)$ for inclination dependence as done in Section 2.2.3.

Figure 2.6 shows that in the local Universe, the slope of the SFR_{FUV}- the inclination is steeper for galaxies with higher μ_* when considering our sample of large and massive galaxies. This supports the trend reported in Grootes et al. (2013) that opacity is proportional to μ_*.

At $z \sim 0.7$, no trend between slope and μ_* is discernible within the scatter (some bins have scatters smaller than the symbol size). On the other hand, the intercept of the $\mathrm{SFR_{FUV}}$-inclination relation (the attenuation of face-on disks), clearly decreases (increases) with μ_* for both samples.

Grootes et al. (2013) constrained τ_B^f using the FIR SED to measure the dust mass while keeping the clumpiness factor fixed at $F = 0.41$. We might expect that the IR-derived τ_B^f of Grootes et al. (2013) should be more closely related to our values for the intercept of the $\mathrm{SFR_{FUV}}$-inclination relation. For the total attenuation corrections, both the slope and the intercept are important.

We also find that the slope of the $\mathrm{SFR_{UV}}$ – inclination relation becomes steeper at higher stellar masses at both $z \sim 0$ and $z \sim 0.7$ (not shown). This indicates that the most massive galaxies are more opaque, and their SFRs are most affected by galaxy inclination.

2.4. Comparison of SFR tracers

Figure 2.7 shows how the multiwavelength SFRs of galaxies used for our analysis compare in the cases where galaxies are detected in the relevant bands. It is important to recognise that these different SFR tracers come from emission produced in different regions (from the HII regions, dust, supernovae remnants) and trace processes on different timescales. FUV, TIR, 24 μm and 1.4 GHz emission come from stellar populations 0-100 Myr old (Kennicutt & Evans, 2012), but the values are sensitive to the star formation history.

We fit a linear function to relate the logarithmic SFRs using the same fitting and resampling techniques used in Section 3. However, in this case, we re-sample the data N times, where N is the number of galaxies in our sample detected at both wavelengths. The best fit lines from each re-sampled data-set are shown as magenta lines in Figure 2.7. We report the median and error bars (given by the 5th and 95th percentile) in the equations below. The numbers in the brackets show the number of galaxies available for the fit.

$$\log(\mathrm{SFR_{UV}}) = 0.31^{+0.04}_{-0.06}\log(\mathrm{SFR_{MIR}}) + 0.44^{+0.01}_{-0.01} \quad (1019)$$

$$\log(\mathrm{SFR_{UV}}) = 0.1^{+0.1}_{-0.5}\log(\mathrm{SFR_{FIR}}) + 1.0^{+0.1}_{-0.2} \quad (20)$$

$$\log(\mathrm{SFR_{UV}}) = 0.2^{+0.4}_{-0.1}\log(\mathrm{SFR_{1.4GHz}}) + 1.09^{+0.05}_{-0.07} \quad (14)$$

$$\log(\mathrm{SFR_{MIR}}) = 0.79^{+0.08}_{-0.08}\log(\mathrm{SFR_{FIR}}) + 0.38^{+0.07}_{-0.07} \quad (290)$$

$$\log(\mathrm{SFR_{MIR}}) = 0.56^{+0.15}_{-0.07}\log(\mathrm{SFR_{1.4GHz}}) + 0.4^{+0.1}_{-0.1} \quad (83)$$

$$\log(\mathrm{SFR_{FIR}}) = 0.53^{+0.07}_{-0.10}\log(\mathrm{SFR_{1.4GHz}}) + 0.3^{+0.1}_{-0.1} \quad (83)$$

COSMOS $z \sim 0.7$ results:

$$\log(\mathrm{SFR_{UV}}) = 0.15^{+0.09}_{-0.08}\log(\mathrm{SFR_{MIR}}) + 1.30^{+0.03}_{-0.03} \quad (277)$$

$$\log(\mathrm{SFR_{UV}}) = 0.04^{+0.1}_{-0.1}\log(\mathrm{SFR_{FIR}}) + 1.62^{+0.05}_{-0.05} \quad (65)$$

$$\log(\mathrm{SFR_{UV}}) = 0.2^{+0.1}_{-0.2}\log(\mathrm{SFR_{3GHz}}) + 1.74^{+0.04}_{-0.05} \quad (35)$$

$$\log(\mathrm{SFR_{MIR}}) = 0.7^{+0.2}_{-0.2}\log(\mathrm{SFR_{FIR}}) + 0.5^{+0.4}_{-0.4} \quad (85)$$

$$\log(\mathrm{SFR_{MIR}}) = 0.8^{+0.2}_{-0.1}\log(\mathrm{SFR_{3GHz}}) + 0.5^{-0.4}_{+0.3} \quad (41)$$

$$\log(\mathrm{SFR_{FIR}}) = 0.6^{+0.2}_{-0.2}\log(\mathrm{SFR_{3GHz}}) + 0.7^{+0.3}_{-0.3} \quad (41)$$

A large scatter exists between the $\mathrm{SFR_{UV}}$ and longer wavelength SFR tracers. The UV suffers from dust attenuation that is dependent on viewing angle amongst other factors. The data in Figure 2.7 are coloured by their inclination angle, and it is clear that the $\mathrm{SFR_{UV}}$ strongly depends on inclination. Face-on galaxies ($1 - \cos(i) = 0$) having $\mathrm{SFR_{UV}}$ that lie closer to $\mathrm{SFR_{12\mu m}}$ values in the local sample. However, in almost all galaxies, in both the local and COSMOS samples, $\mathrm{SFR_{UV}} < \mathrm{SFR_{MIR}}$ as there will be some level of FUV attenuation even for face-on galaxies (as discussed in Sects. 3.2 and 4).

In the COSMOS sample at $z \sim 0.7$, we find a good agreement between the 24 μm, 100 μm, and 3 GHz SFRs. This is encouraging as all three are tied to TIR calibration (through SED fitting or via the IR-radio correlation). Locally the $\mathrm{SFR_{FIR}}$ is greater than the SFRs derived from 12 μm and 1.4 GHz. The 1.4 GHz SFR calibration of Davies et al. (2017) used for the local sample depends sub-linearly on SFR. Therefore it follows that 60 μm SFR is higher than the 1.4 GHz SFR because there is a linear relation between 1.4 GHz and FIR (FIRRC). However, this would imply that the FIR emission traced by 60 μm does not correlate linearly with SFR. On the other hand, our best fits show that $\mathrm{SFR_{12\mu m}}$ is also larger than $\mathrm{SFR_{1.4GHz}}$ at high SFRs. This could imply that the $\mathrm{SFR_{1.4GHz}}$ relation used by Davies et al. (2017) underestimates the SFR.

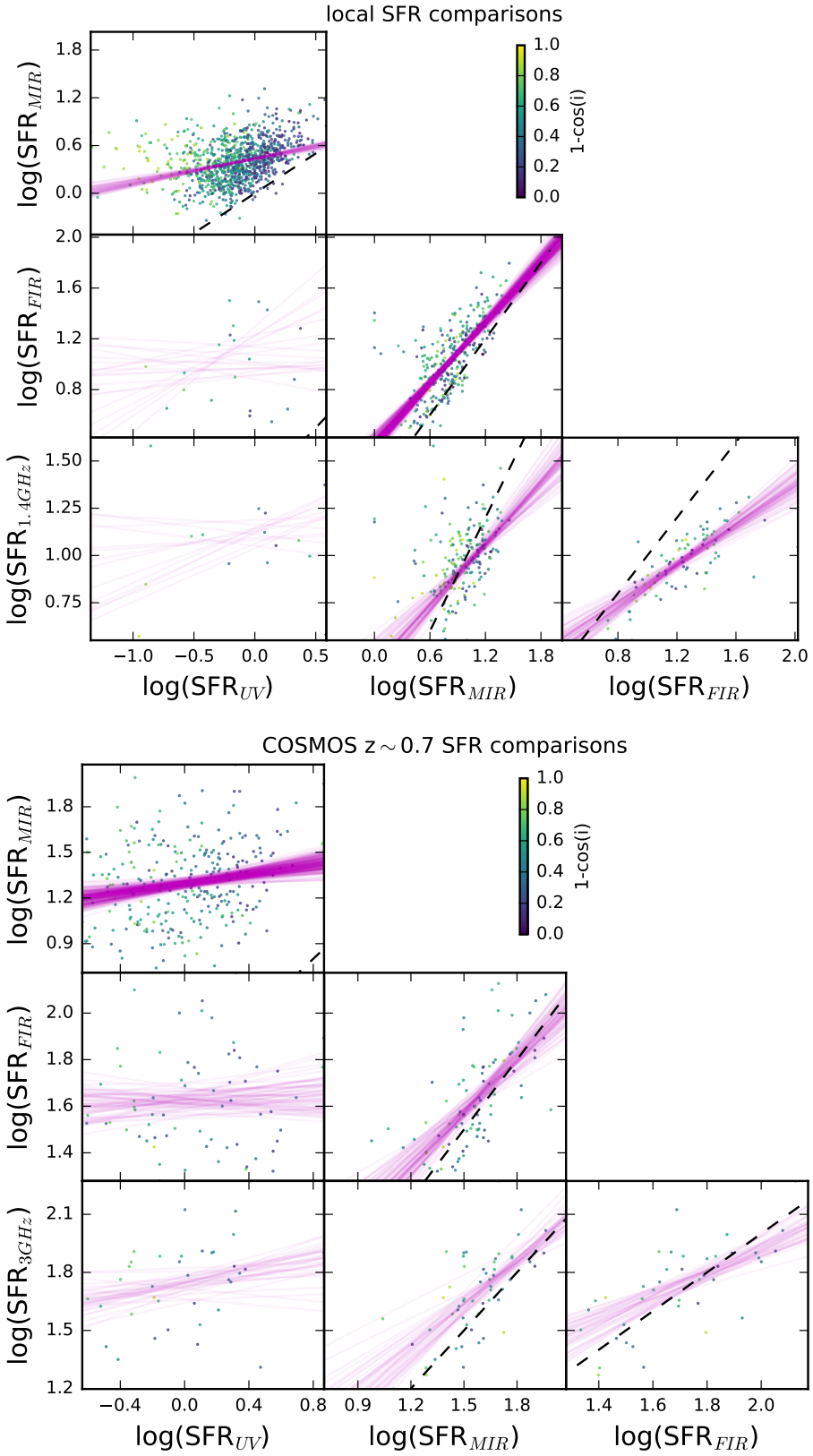

Figure 2.7.: Comparison of the SFRs derived using the different monochromatic calibrations used in this Chapter. The dashed line represents the one-to-one line. Magenta lines show best fit linear relations to resampled data, with the number of fits shown equal to the number of galaxies in each panel. The SFR_{UV} is not corrected for dust attenuation and so is expected to be smaller than the other indicators. Data are colour-coded by galaxy inclination angle.

2.5. Evolution of disk opacity

Ultra-violet observations are sensitive to dust attenuation, showing trends that other wavelengths do not, allowing us to probe disk opacity. We study the UV-derived SFR of disk-dominated galaxies at $z \sim 0$ and $z \sim 0.7$ and find a strong inclination dependence that appears to be redshift independent. We infer that the overall FUV attenuation has increased between $z \sim 0$ and $z \sim 0.7$ from the collective decreased fraction of $\mathrm{SFR_{UV}/SFR_{SFMS}}$ ratios. To try to understand how the combination of (a) a largely unchanging slope of the UV attenuation-inclination relation, and (b) an evolving overall attenuation might arise we employ the Tuffs et al. (2004) models. We find that an increased dust clumpiness can explain most of the increase in attenuation while keeping the slope consistent.

In the models of Tuffs et al. (2004), the FUV emission and the clumpy dust component surrounding the HII regions are assumed to only be associated with the thin disk. The

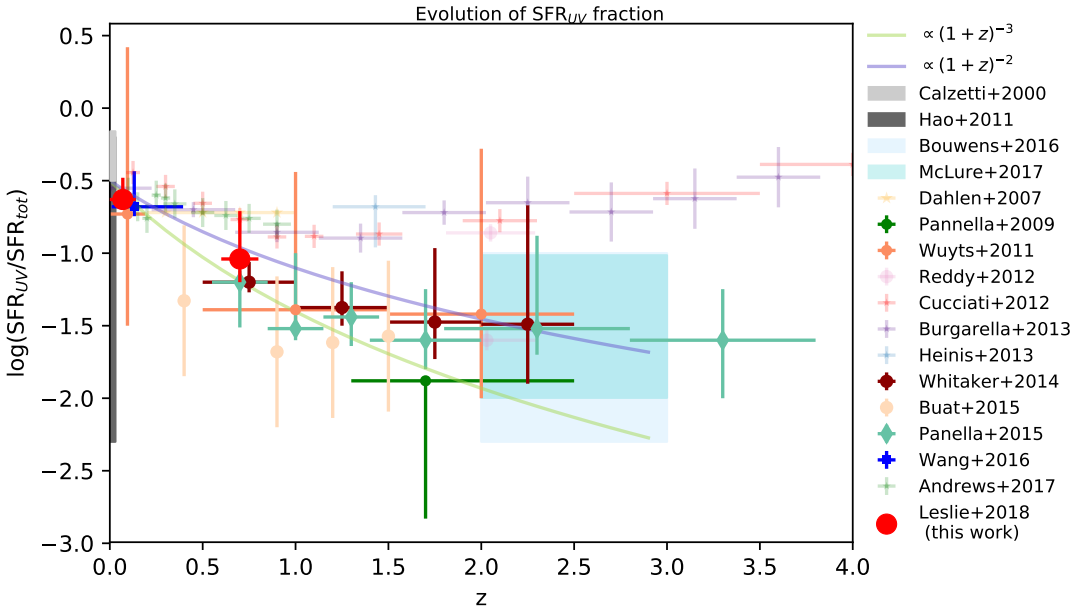

Figure 2.8.: Evolution of $\mathrm{SFR_{UV}/SFR_{tot}}$ for statistical samples of galaxies at $z < 4$. $\mathrm{SFR_{tot}}$ is the sum of the attenuated ($\mathrm{SFR_{IR}}$) and non-attenuated ($\mathrm{SFR_{UV}}$) emission. Studies that included mass-dependent measurements are Wuyts et al. (2011b), Pannella et al. (2009a), Pannella et al. (2015), Whitaker et al. (2014), McLure et al. (2017), and Bouwens et al. (2016). For these studies, the error-bars show the range of $\mathrm{SFR_{UV}/SFR_{tot}}$ for galaxies with stellar masses $10.2 < \log(M_*/\mathrm{M_\odot}) < 11.4$, to match the sample of massive galaxies used in this work. Bouwens et al. (2016) and McLure et al. (2017) combined literature results and are shown as shaded areas. Studies that include less-massive galaxies (shown with transparent symbols) have, on average, less attenuated UV emission, so the $\mathrm{SFR_{UV}/SFR_{tot}}$ ratio is higher. The red dots show the value of $\mathrm{SFR_{UV}/SFR_{SFMS}}$ we obtained for a disk galaxy inclined at $1-\cos(i) = 0.5$ ($i = 60\,\mathrm{deg}$). More information about the studies included in this Figure is provided in Appendix A.2. To convert the y-axis to A_{FUV} we multiply by -2.5. Two solid lines show evolution of $\mathrm{SFR_{UV}/SFR_{tot}}$ between $(1+z)^{-2}$ (purple) and $(1+z)^{-3}$ (lime green) normalised to -0.5 at $z = 0$. The evolution of FUV attenuation for massive galaxies evolves as $(1+z)^{2-3}$ up to $z \sim 2$.

fraction of dust mass in the clumpy component is parametrized by F and we find best fitting values $F = 0.09^{+0.02}_{-0.02}$ and $F = 0.55^{+0.06}_{-0.04}$ for the $z \sim 0$ and $z \sim 0.7$ samples, respectively. We find that the fraction of SFR that is attenuated increases by a factor of ~ 3.4 for face-on galaxies, which corresponds to the increase in the viewing-angle-independent clumpy dust fraction F by a factor of ~ 6 from $z = 0.07$ to $z = 0.7$. We also find that the average face-on B-band opacity, τ_f^B, does not evolve strongly with redshift when traced by the FUV emission ($\Delta\tau_B^f = -0.45^{+1.1}_{-1.8}$; consistent with zero). At $z \sim 0.7$, galaxies at fixed stellar mass had more mass in gas, and therefore higher SFRs, by factors of $\sim 3-4$. Stars are born from the dusty molecular clouds and the young stars then heat the dust that is encompassing them; the warm clumpy component thus somewhat traces the recent star formation. An increased clumpy-dust fraction should change the shape of the infrared SED with redshift. Indeed, many studies find that the peaks of the IR SEDs move to shorter rest frame wavelengths with redshift (implying a warmer component in the FIR emission, e.g. Magnelli et al. 2014; Béthermin et al. 2015).

The star and dust geometry are crucial to understanding how galaxy properties such as observed size $r_{1/2}$ or UV emission are affected by dust attenuation. We note that the geometry of the Tuffs et al. (2004) model may not be valid at $z > 0$. We caution that measuring the slope or normalisation of the $\mathrm{SFR_{FUV}}$ – inclination equation alone does not give a full picture of the dust. For example, a lack of slope could be because a large amount of dust at large scale heights heavily absorbs light even when the galaxy is face-on. Therefore, the slope and the intercept should be considered together for a better understanding of the dust content. Gas disks are observed to become puffier at higher redshift, having larger scale heights perhaps due to a larger gas fraction and turbulence (e.g. Kassin et al. 2012; Förster Schreiber et al. 2009; Wisnioski et al. 2015). If the stellar disk height also increases with redshift, then the minimum axis ratio used in calculating inclination (Eq. 2.2) must be adjusted accordingly. To date, no studies have conclusively measured the scale height of stellar disks as a function of redshift. However, we find no significant difference in the minimum observed axis ratio of our two samples (see Fig. 1), suggesting that the stellar disk height has not increased significantly by $z = 0.7$. The Tuffs et al. (2004) model assumption of the thick disk not emitting at UV wavelengths might still be a valid assumption at $z \sim 0.7$. A comparison to simulations that include different dust components, such as those presented recently by Nelson et al. (2018), or other hydrodynamical and radiative transfer simulations such as Jonsson et al. (2010) or Trayford et al. (2017), should allow us to test our assumptions about the relative stellar and dust geometries at $z \sim 0.7$ and verify whether an increase of the clumpy dust-component is responsible for the increase of the FUV attenuation of massive galaxies with redshift.

In Figure 2.8, we compare the FUV attenuation as represented by $\mathrm{SFR_{UV}/SFR_{tot}}$ for our two redshift bins with other studies from the literature. We find a large variation in $\mathrm{SFR_{UV}/SFR_{tot}}$ when considering galaxies drawn from different studies that have different sample selections. Our findings cannot be extrapolated to the general galaxy population. Studies that include less massive galaxies (represented by symbols with higher transparency) tend to show larger $\mathrm{SFR_{UV}/SFR_{tot}}$ ratios, that is, less UV attenuation than samples restricted to more massive galaxies ($\log(M_*/\mathbf{M}_\odot) > 10.2$). Studies at redshifts $z > 1.5$, such as Pannella et al. (2015) and McLure et al. (2017), find that stellar mass provides a better prediction of UV attenuation than β, the UV slope itself. Wuyts et al. (2011b) compared

their observed SFR_{UV}/SFR_{IR} with what would be expected from the SFR surface density, assuming a simple model with a homogeneously mixed star-gas geometry. They found that more NUV (2800 Å) emission escaped than expected from the simple model at $z > 1$, which they suggest could be due to a more patchy geometry in high-redshift galaxies. For more information about the data included in Figure 2.8, please refer to Appendix A.2.

We find that the overall FUV attenuation increases with redshift for large, massive star-forming galaxies. Interstellar dust is produced in stars which in turn form from the gas; the fact that the dust- and gas-mass fractions vary similarly with redshift is a good consistency check, displayed in Figure 2.9. However, the amount of total dust depends on the balance between dust creation and destruction. Keeping track of the interstellar dust that is produced in the ejecta of asymptotic giant branch (AGB) stars and supernovae, the growth of dust grains in dense regions of the ISM, and the destruction of dust in supernovae shocks and collisions is, nevertheless, a difficult task (e.g. Aoyama et al. 2017; Popping et al. 2017). If we assume, simply, that the increased dust mass with redshift all goes into the clumpy dust component, and that the clumpy component is related to the molecular gas (in terms of amount and distribution) then the amount of overall attenuation could follow the evolution in molecular gas mass. Figure 2.9 shows that the FUV attenuation does not evolve as strongly as the gas mass fraction (as found recently by Whitaker et al. (2017) out to $z \sim 2.5$); however, the fraction of dust in the clumpy component (F) does evolve strongly with redshift, similar to the gas-mass fraction.

da Cunha et al. (2010), Smith et al. (2012), Sandstrom et al. (2013), and Rowlands et al. (2014) found that, in the local Universe, M_d/M_* is proportional to sSFR. Studies such as Sargent et al. (2012) and Tasca et al. (2015), that look at how sSFR changes with redshift, find that the sSFR varies as sSFR $\propto (1+z)^{2.8}$ out to redshifts $z < 2$. This would give a sSFR increase by a factor of ~ 3.6 between $z = 0.07$ and $z = 0.7$. We note, however, that this trend also is stellar mass dependent (e.g. Schreiber et al. 2015), and that lower-mass galaxies have a shallower evolution in sSFR than the most massive galaxies.

Recent studies of molecular gas at high redshifts indicate that the cosmic density of molecular gas, similar to the cosmic density of star formation, peaks between redshifts 2 and 3 (Decarli et al., 2016). Genzel et al. (2015), Sargent et al. (2014), and Tacconi et al. (2017) used compilations of studies that measure gas mass via CO line luminosities and found that M_g/M_* varies like $(1+z)^{2.7}$, which corresponds to an increase by a factor of ~ 3.5 between $z = 0.07$ and $z = 0.7$. On the other hand, Bauermeister et al. (2013) expect M_g/M_* $\propto (1+z)^{3.2}$ which would imply an increase in the gas mass fraction by a factor of ~ 4.4. In any case, the gas mass is expected to increase by a factor of ~ 4 between our two redshift slices. In Figure 2.8, we show with two solid lines the relations $SFR_{UV}/SFR_{tot} \propto (1+z)^{-2}$ and $\propto (1+z)^{-3}$.

The parameter that most strongly controls the dust-to-gas mass is the metallicity (e.g. Leroy et al. 2011b; Accurso et al. 2017). According to the parametrization of Zahid et al. (2014), a galaxy with $\log(M_*/M_\odot) = 10.2$ would have a metallicity of 0.069 dex less at $z = 0.7$ than at $z = 0.07$. A galaxy at $M_* \sim 10^{10.5} M_\odot$, on the other hand, will have a change in metallicity of 0.035 dex between the same two redshifts. For our sample, the dust to gas ratio should not change significantly between $z \sim 0$ and $z \sim 0.7$, however, we take this change into account in Figure 2.9 when calculating the expected M_d/M_* evolution based on the dust-to-gas ratio.

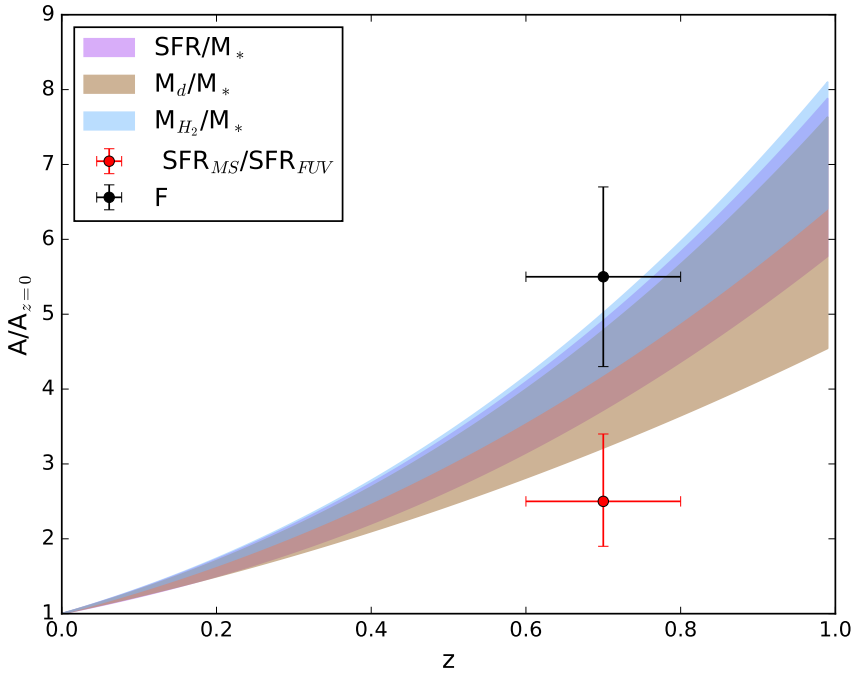

Figure 2.9.: Evolution of massive galaxy properties from their local values out to $z \sim 1$. The evolution of the dust-mass fraction (M_d/M_*) was determined from a power-law fit to data from Santini et al. (2014), Béthermin et al. (2015) (for $z \leq 1$), and Rémy-Ruyer et al. (2014) for $z = 0$. The upper bound to the M_d/M_* evolution is given by assuming $M_d \sim 0.5 \times Z \times M_g$, and the evolution of gas and metallicity over this redshift and stellar mass range. The evolution of specific SFR is shaded purple between the relationship in Sargent et al. (2014) and $(1+z)^3$. The evolution of the molecular gas fraction (blue) is from Tacconi et al. (2017). We find that the fraction (F) of dust in clumps surrounding nascent star-forming regions has increased by a factor of ~ 5.5, and that the overall attenuation of UV (SFR_{SFMS}/SFR_{UV}) has increased by a factor of ~ 2.5 (ranging from 3.4 to 1.9 for face-on to edge-on galaxies, respectively).

To summarise, out to $z < 2$, sSFRs increase as $(1+z)^{2.8}$ and M_g/M_* and M_d/M_* increase at a similar rate for galaxies more massive than 10^{10} $M_\odot$ (Santini et al., 2014). Since $z = 0.7$, SFRs and gas and dust masses have decreased by factors of ~ 3.5. We see a larger systematic FUV attenuation in the $z \sim 0.7$ sample compared to the $z \sim 0$ sample. The SFR_{FUV} of a face-on galaxy lies ~ 0.21 dex below the SFMS at $z = 0.07$, and ~ 0.74 dex below the SFMS at $z = 0.7$. Assuming the main-sequence SFR to be the unobscured SFR, or SFR_{UV}+SFR_{IR}, the FUV attenuation of face-on galaxies has thus increased by a factor of ~ 3.4.

Galaxies are thought to grow in size over time ('inside-out growth'). For example, Wuyts et al. (2011b) shows that galaxies on the main sequence at a fixed stellar mass have a larger size on average at $z \sim 0.1$ than at $z \sim 1$. Due to this evolution, and the fact that opacity also varies with radius in galaxies out to at least $z < 2$ (Tacchella et al., 2017; Wang et al., 2017), we cannot interpret the slopes of the attenuation-inclination relation reported in this paper in the context of an evolutionary picture for particular galaxies. Instead, we emphasise that the inclination dependence of the UV attenuation in the largest and most massive star-

forming disk galaxies at $z \sim 0.7$ (which are not necessarily the same galaxies that will end up in our sample at $z = 0.07$), behaves similarly to that in galaxies selected to have the same stellar mass and radius at $z \sim 0$. However, the overall FUV attenuation has increased, presumably due to the larger amount of dust at higher redshifts.

The importance of inclination-dependent FUV SFRs, even when common attenuation corrections have been applied, will be the subject of Chapter 3.

2.6. Conclusions

We parametrize the attenuation of starlight as a function of galaxy disk inclination to investigate the global dust properties by fitting a simple linear function to the SFR – inclination relation for a sample of galaxies at $z \sim 0$ (in SDSS) and $z \sim 0.7$ (in COSMOS). We compiled two samples of galaxies at four different wavelengths: FUV, MIR (12 μm), FIR (60 μm) and radio (20 cm) with well measured optical morphology for which we calculated monochromatic SFRs. Our findings can be summarised as follows. Massive disks ($\log(M_*/\mathbf{M}_\odot) > 10.2$) larger than 4 kpc, show strong FUV SFR – inclination trends at both $z \sim 0$ and $z \sim 0.7$. Our fit to this relation is sensitive to selection effects, in particular, to flux limits and size cuts. The FUV SFR of face-on galaxies at $z \sim 0.7$ is less than that expected from the main-sequence relation by a factor of 0.74 ± 0.09 dex, compared to 0.20 ± 0.03 dex at $z \sim 0$. This corresponds to an increase of the FUV attenuation of face-on galaxies by a factor ~ 3.4 over the last 7 Gyr. An increased fraction of dust in warm clumpy components surrounding the HII regions (by a factor of about 6) could explain this increased overall attenuation while simultaneously allowing the opacities (the slope) to remain constant. This increase in the warm clump component and UV attenuation between $z \sim 0$ and $z \sim 0.7$ is consistent with the increased molecular gas content in galaxies at redshift 0.7. Overall FUV attenuation increases with stellar mass surface density at both $z \sim 0$ and $z \sim 0.7$. It is likely that no opacity is present in the FIR and radio, however, we were unable to confirm this for our FIR and radio subsamples as our data did not span a sufficient range in luminosity due to survey flux limits. MIR and radio SFRs are inclination independent and therefore MIR and radio data can provide a useful tracer of SFRs also for galaxies with a high inclination angle.

The increase in FUV attenuation for massive galaxies follows the amount of evolution in sSFR, gas, and dust mass fractions over the past 7.5 billion years. These phases (gas, dust and star formation) are therefore closely related, probably even spatially related; an assumption which is used for deriving gas masses from dust continuum emission and for energy balancing SED codes that assume the dust emission and star formation come from similar regions.

3 Testing typical FUV attenuation corrections out to $z \sim 0.7$

This chapter was published in a similar form in the refereed article **Leslie** *et al. (2018a) "Probing dust and ISM properties using galaxy disk inclination II: testing typical FUV attenuation corrections out to $z \sim 0.7$"*

We evaluate dust-corrected far-ultraviolet (FUV) star formation rates (SFRs) for samples of star-forming galaxies at $z \sim 0$ and $z \sim 0.7$ and find significant differences between values obtained through corrections based on UV colour, from a hybrid mid-infrared (MIR) plus FUV relation, and from a radiative transfer based attenuation correction method. The performances of the attenuation correction methods are assessed by their ability to remove the dependency of the corrected SFR on inclination, as well as returning, on average, the expected population mean SFR. We find that combining MIR (rest-frame $\sim 13\,\mu$m) and FUV luminosities gives the most inclination-independent SFRs and reduces the intrinsic SFR scatter of the methods we tested. However, applying the radiative transfer based method gives corrections to the FUV SFR that are inclination independent and in agreement with the expected SFRs at both $z \sim 0$ and $z \sim 0.7$. SFR corrections based on the UV-slope perform worse than the other two methods we tested. For our local sample, the UV-slope method works on average, but does not remove inclination biases. At $z \sim 0.7$, we find that the UV-slope correction we used locally flattens the inclination dependence compared to the raw FUV measurements, but was not sufficient to correct for the large attenuation observed at $z \sim 0.7$.

3.1. Introduction

Robust measurements of SFR are a key ingredient in the context of galaxy evolution studies. The far-ultraviolet (FUV; ~ 1550 Å) is dominated by radiation from O and B stars and thus traces recent star formation, provided the timescale for significant fluctuations is longer than a few 10^7 years (Madau & Dickinson, 2014)). Extragalactic UV SFR calibrations have been revolutionised by the launch of the Galaxy Evolution Explorer mission (GALEX; Martin et al. 2005), which imaged approximately two-thirds of the sky at FUV and near-UV (NUV) wavelengths. Murphy et al. (2011) and Hao et al. (2011) used the Starburst99 stellar population synthesis code (Leitherer et al., 1999) to derive conversions between GALEX FUV

luminosity and SFR at an age of 100 Myr, assuming a constant SFR and solar metallicity:

$$\log\left(\frac{\mathrm{SFR}}{\mathrm{M}_\odot\ \mathrm{yr}^{-1}}\right) = \log\left(\frac{L_{\mathrm{FUV}}}{\mathrm{erg\ s}^{-1}}\right) - 43.35. \tag{3.1}$$

The great disadvantage for UV-based SFR measurements is that the light is heavily attenuated by dust. When stars are not individually resolved, the effective reddening of the emerging radiation is influenced by the dust-stars-gas geometry of the observed region (Natta & Panagia, 1984; Calzetti, 1997). Furthermore, the reddening laws are not the same for all galaxies, nor for regions within galaxies, due to a combination of different dust grain size distributions and compositions, and differing geometries. The amount of unattenuated starlight is negligible in dusty starbursts, but is almost 100% in dust-poor dwarf galaxies.

Dust is present in stellar birth clouds and in the diffuse interstellar medium, and both components absorb starlight and re-emit it in the infrared (IR). However, the dust–star geometry appears to evolve with redshift, with results from Chapter 2 (**Leslie** et al. 2018b, L18) indicating that the fraction of dust in stellar birth clouds was higher at earlier times ($z \sim 0.7$).

To infer dust-unbiased, total SFRs, corrections accounting for UV attenuation are necessary. A promising way to obtain the total SFR of a galaxy is to combine the UV emission with infrared emission, thereby capturing both the attenuated and unattenuated emission. Combined UV + IR SFRs have been used with success out to at least $z < 3$ (Wuyts et al., 2011c; Santini et al., 2014; Magnelli et al., 2014). However, older stellar populations can contribute to dust heating and infrared emission (Bendo et al., 2010; Groves et al., 2012). Therefore, the exact relation between infrared emission and recent SFR will depend on the relative contribution of the young and old stellar populations to the general stellar radiation field, which varies from galaxy to galaxy, see for example Boquien et al. (2016).

Corrections at high redshift ($z > 2$) often rely on empirical calibrations based on the UV spectral slope or UV colours. However, these calibrations are uncertain due to potential intrinsic variations in the UV slope and dust attenuation (Battisti et al., 2016; Salmon et al., 2016) Further testing of the UV slope and hybrid UV + IR attenuation correction methods are still required, particularly to ascertain that they are applicable at $z > 0$.

We can evaluate UV-attenuation corrections by testing whether the corrected SFR is independent of galaxy inclination. Inclined galaxies suffer from more line-of-sight attenuation than face-on galaxies because light has a larger column to pass through before escaping the galaxy. An ideal correction would account for this extra attenuation and result in a total SFR that is independent of viewing angle. In Chapter 2, we used the inclination - SFR (uncorrected for attenuation) relation of star-forming galaxies at different wavelengths (UV, mid-IR, far-IR, and radio) to probe the disk opacity of two matching samples of massive ($\mathrm{M}_* > 1.6 \times 10^{10}\ \mathrm{M}_\odot$), large ($r_{1/2} > 4$ kpc), disk-dominated ($n < 1.2$) galaxies: a local Sloan Digital Sky Survey (SDSS) sample at $z \sim 0.07$ and a sample of discs at $z \sim 0.7$ drawn from the Cosmic Evolution Survey (COSMOS). We found that correcting the FUV flux for dust attenuation is critical even for face-on galaxies because the observed UV fluxes can underestimate the true SFR by a factor of ~ 1.6 for face-on massive star-forming galaxies at $z \sim 0$ and ~ 5.5 at $z \sim 0.7$.

In this Chapter we test the inclination dependence of UV-derived SFRs that have been

corrected for attenuation using common empirical approaches: UV-slope corrections (Section 3.3.1), hybrid UV + MIR SFRs (Section 3.3.2), and SFRs corrected for the attenuation expected from the radiative transfer model of Tuffs et al. (2004) and Popescu et al. (2011) (Section 3.3.3). We apply these attenuation corrections to two samples of massive star-forming galaxies, $\sim$3,500 galaxies at $z \sim 0$ and $\sim$1,000 galaxies at ~ 0.7, and test for inclination dependence following the methodology of L18.

Throughout this work, we use the Kroupa (2001) initial mass function (IMF) and assume a flat Λ CDM (cold dark matter) cosmology with (H_0, Ω_M, Ω_Λ) = (70 km s^{-1} Mpc^{-1}, 0.3,0.7).

3.2. Data and sample selection

L18 described the data and sample selection, which we only briefly review here. We selected a local sample ($0.04 < z < 0.1$) from the spectroscopic SDSS matched with the GALEX Medium Imaging Survey (MIS) by Bianchi et al. (2011). Our intermediate-redshift sample ($0.6 < z < 0.8$) from the COSMOS field is centred at $z \sim 0.7$, where we have high-resolution rest-frame morphological measurements in the I band (Sargent et al., 2007) that match our SDSS g-band morphological measurements (Simard et al., 2011) in terms of rest-frame wavelength. Additionally, the GALEX NUV filter at $z \sim 0.7$ matches the FUV filter at $z \sim 0.1$, ensuring that our FUV fluxes obtained from the GALEX Deep Imaging Survey (DIS) do not require k corrections.

L18 found that inclination affects the derived galaxy properties that are used for sample selection. After fitting and subtracting a power law from the relations of inclination versus galaxy property for M_*, g-band half-light radius $r_{1/2}$, and Sérsic index n, we obtained "face-on" equivalent values for each galaxy. The inclination-corrected parameters, denoted with the subscript "corr", were only used for sample selection. Our selections from L18 are as follows and are referred to as the "restricted" sample:

- $\log(\mathrm{M}_{*,\mathrm{corr}}/\mathrm{M}_\odot) > 10.2$,
- $n_{\mathrm{corr}} < 1.2$,
- $r_{1/2,\mathrm{corr}} > 4$ kpc
- $L_{\mathrm{FUV}}/\sigma_{L_{\mathrm{FUV}}} > 3$.

Star-forming galaxies were selected using their emission line ratios or colours for the local and COSMOS samples, respectively. The restricted sample contains 1,021 galaxies in the local sample and 295 galaxies in the $z \sim 0.7$ sample. The size cut ensures completeness in surface brightness, and the Sérsic index cut reduces contamination by bulge-dominated galaxies. However, to make our results applicable to a wider population of galaxies, we also present results for a sample that is not subject to size restrictions and has a less restrictive constraint on the Sérsic index:

- $\log(\mathrm{M}_{*,corr}/\mathrm{M}_\odot) > 10.2$,
- $n_{corr} < 2$

- $L_{\rm FUV}/\sigma_{L_{\rm FUV}} > 3$.

We refer to this sample as the "full" sample, and it contains 3,489 galaxies at $z \sim$0 and 1,021 galaxies at $z \sim 0.7$. Before requiring an FUV detection at a signal-to-noise ratio > 3, the full local sample contains 8,576 galaxies and the full COSMOS sample contains 1,135 galaxies. Although the signal-to-noise ratio cut biases the sample towards galaxies with higher SFRs, it is necessary for reliable results. In our COSMOS sample we are likely missing the most highly inclined ($1-\cos(i) > 0.75$; $i = 75.5^o$) galaxies with lower $SFR_{\rm FUV}$ because of the sensitivity limit of GALEX DIS data.

In addition to the previous UV and MIR samples of L18, we also include here a UV-slope-corrected sample (Section 3.3), which requires the addition of rest-frame NUV data. This results in a smaller subsample, especially at $z \sim 0.7$ (Table 1).

3.3. Corrected FUV star formation rates, $\mathrm{SFR_{FUV,corr}}$

In this section, we apply three common $\mathrm{SFR_{FUV}}$ attenuation corrections to test whether any residual trends of SFR with inclination persist.

We chose to normalize the $\mathrm{SFR_{UV,corr}}$ by the SFR expected for a galaxy lying exactly on the galaxy SFR-stellar mass relation (galaxy main-sequence, SFMS). As in L18, we adopted the best-fit SFMS relation for an updated version of the $z \lesssim 1$ data compiled in Sargent et al. (2014) (private communication),

$$\log\left(\frac{\mathrm{SFR_{SFMS}}}{\mathrm{M_\odot yr^{-1}}}\right) = 0.816\log\left(\frac{M_*}{\mathrm{M_\odot}}\right) - 8.248 + 3\log(1+z). \tag{3.2}$$

We took into account the different IMF (Chabrier, 2003) and cosmology (WMAP-7; Larson et al. 2011) assumed by Sargent et al. (2014) (see L18 for more details). Figure 3.1 shows the relation between $\log(\mathrm{SFR_{FUV,corr}}/\mathrm{SFR_{SFMS}})$ and galaxy inclination (1-cos(i)), where $\mathrm{SFR_{SFMS}}$ is the main-sequence SFR expected given the mass and redshift of each galaxy.

The fits shown in Figure 3.1 are of the form

$$\log\left(\mathrm{SFR_{FUV,corr}}/\mathrm{SFR_{SFMS}}\right) = k_1(1-\cos(i)) + k_2. \tag{3.3}$$

Best fits were obtained using the Monte Carlo Markov chain implementation *emcee* (a Python package) (Foreman-Mackey et al., 2013), incorporating errors on the SFRs and inclination and fitting for an intrinsic variance term, σ^2, following Foreman-Mackey (2017). For simplicity, the intrinsic scatter was assumed to be in the y-direction only (SFR). We used 64 walkers that created a chain of 6,000 samples each for a total of 340,000 samples. The first 150 samples were discarded as an initialisation period (burn-in). The fitted parameters for the original uncorrected and corrected SFR relations are shown in Table 3.1, where we give the median, and the 5th and 95th percentile of the MCMC distribution.

The top panels of Figure 3.1 show the observed $\mathrm{SFR_{FUV}}$. The restricted samples span the same range of inclinations as the larger full samples. However, the restricted samples tend to be skewed towards higher $\mathrm{SFR_{FUV}}$ values, showing a lack of $\mathrm{SFR_{FUV,obs}}$ at all inclinations. The restricted samples' galaxies are larger and more disk dominated than the full samples.

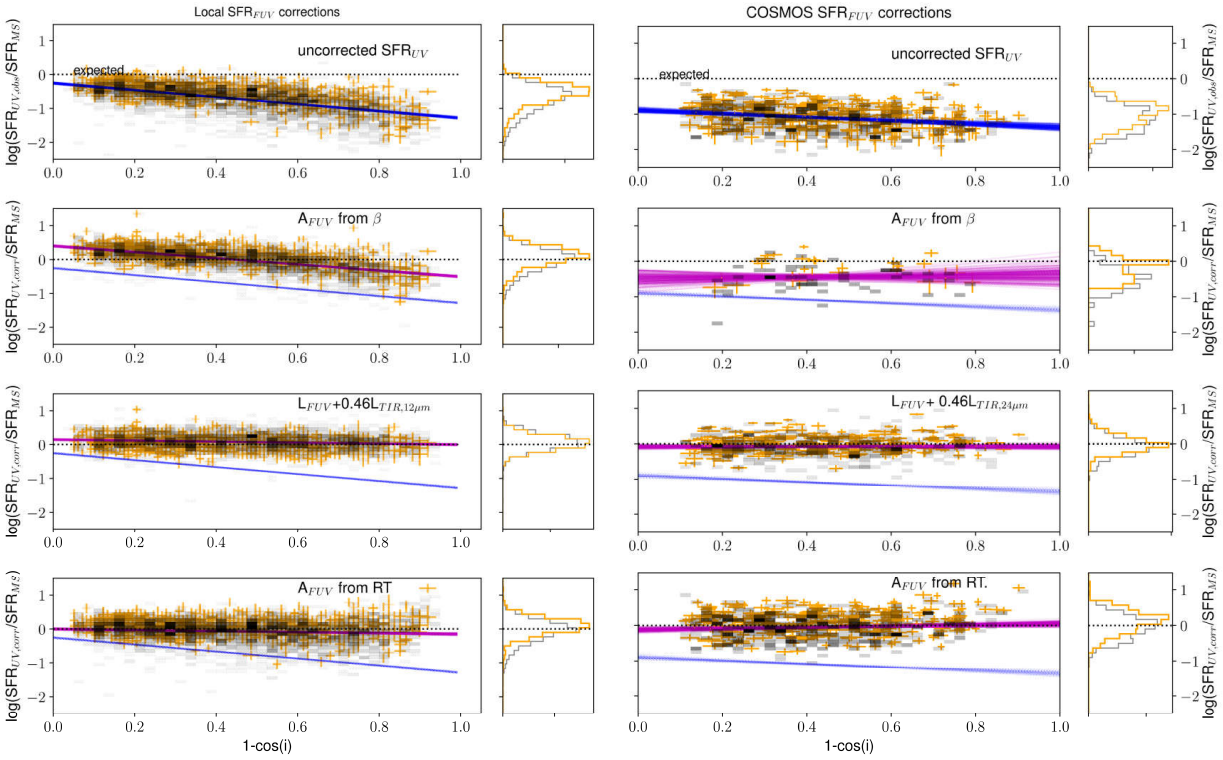

Figure 3.1.: Evaluating the inclination dependence of dust-corrected $\mathrm{SFR_{FUV}}$ values. From top to bottom, the panels show the observed UV SFR, the SFR corrected based on the UV-slope, the hybrid MIR + UV determined SFR, and the SFR corrected based on the Tuffs et al. (2004) radiative transfer models as a function of inclination angle. Face-on galaxies are lie to the left, 1-cos(i) ~ 0, and edge-on galaxies lie to the right, 1-cos(i) ~ 1. The blue lines show the inclination relation for $\mathrm{SFR_{FUV}}$ as observed with no dust corrections (top panel). The dust correction factors work to increase the $\mathrm{SFR_{FUV}}$ and lessen the inclination dependence of the SFR. Fitted parameters are given in Table 3.1. Orange data points show the "restricted sample", and the full sample is shown as a 2D density histogram. Magenta lines show 150 random realisations of linear parameters from our MCMC chain. Distributions of the y-axes, $\log(\mathrm{SFR_{FUV}}/\mathrm{SFR_{SFMS}})$ are also displayed as histograms. The dotted line shows where the $\mathrm{SFR_{FUV}} = \mathrm{SFR_{SFMS}}$.

These values indicate a mean attenuation factor of $A_{\mathrm{FUV}} \sim 1.9$ mag (~ 1.5 mag) at $z \sim 0$ and $A_{\mathrm{FUV}} \sim 2.9$ mag (~ 2.4 mag) at $z \sim 0.7$ for the full (restricted) samples.

The fitted slope of the $\mathrm{SFR_{FUV}}$-inclination for the COSMOS (-0.44 ± 0.15) and local (-0.9 ± 0.06) restricted samples differ from the slopes found in L18 (-0.54 ± 0.09 and -0.79 ± 0.04 for the COSMOS and SDSS samples, respectively) because different fitting methods were adopted. The fitting algorithm in this work is more lenient towards outliers, but was selected in order to evaluate the scatter of our SFR values before and after corrections. We chose to test the correction methods described below, which are representative of those commonly applied in the literature.

3.3.1. UV slope correction

The observed relationship between the rest-frame UV continuum slope β, where $F_\lambda \propto \lambda^\beta$, and the ratio of UV to IR light of a galaxy (IRX, log(LIR/LUV)) has been used to calibrate β as an attenuation correction tool since the correlation was first observed for starburst galaxies by Meurer et al. (1999) and Calzetti (1997). Longer-lived ($\sim$200 Myr), lower-mass stars contribute substantially to the NUV emission at later times. For a constant SFR, the UV spectral slope therefore reddens moderately with time, complicating the conversion from luminosity into SFR. For this analysis we estimated β by fitting $\log(F_\lambda) = \beta \log(\lambda(1+z)) + c$ using the PYTHON package POLYFIT, with data weighted by their flux errors. For our $\mathrm{SFR_{FUV,corr}}$ error values, we used and propagated the errors on the fitted slope given by POLYFIT. When only two data points were available, we calculated the gradient and the corresponding error. We then used the Boquien et al. (2012) relation (see their Section 4.2),

$$A_{\mathrm{FUV}} = 0.87(\beta + 2.586), \tag{3.4}$$

to determine the amount of attenuation and correct $\mathrm{SFR_{FUV}}$. We were unable to avoid photometric bands with emission or absorption lines, as suggested for example by Calzetti et al. (1994), which increases the uncertainty β. However, Leitherer et al. (2011) found a good agreement between UV spectral slopes determined from International Ultraviolet Explorer spectra and from the GALEX FUV and NUV magnitudes of nearby galaxies. The A_{FUV} – β relation in Eq. 3.4 was derived for normal face-on star-forming spiral galaxies. This relation varies from that of starburst galaxies (e.g. Overzier et al. 2011; Meurer et al. 1999), largely due to intrinsic UV colour differences between galaxies and yields systematically lower attenuation for a given β. Observations of a wide range of galaxies have shown a large scatter in the UV colour-extinction relation (Boquien et al., 2012) and about two orders of magnitudes of scatter in actual FUV attenuations for a fixed FUV-NUV colour. Studies such as Catalán-Torrecilla et al. (2015) have shown that even with a UV colour correction, the FUV alone is not a reliable tracer of SFR in individual galaxies. This is because of the large extinction correction needed at FUV wavelengths, and the variation of different attenuation laws in the UV.

Local sample: For our SDSS sample, we have access to photometry from only two UV bands: GALEX NUV ($\lambda_{\mathrm{eff}} = 2,274$ Å) and FUV ($\lambda_{\mathrm{eff}} = 1,542$ Å). Using $\mathrm{A_{FUV}}$, we corrected the observed $\mathrm{L_{FUV}}$ used to calculate SFR in Equation 3.1 and show the trend of $\mathrm{SFR_{FUV,corr}}$ with the inclination in Figure 3.1. Figure 3.2 shows the distribution of β, peaking close to $\beta \sim -1$ for both the full and restricted samples.

The colour-corrected $\mathrm{SFR_{FUV}}$ show a slightly shallower inclination dependency (slope of -0.8 ± 0.02 instead of -1.0 ± 0.03 for the full sample, and -0.79 ± 0.03 instead of -0.9 ± 0.04 for the restricted sample) and overall SFRs that are closer to the SFMS, but further improvements are required because the slopes are significantly different from zero and one will tend to over-estimate the SFR for face-on galaxies and under-estimate the SFR for edge-on galaxies.

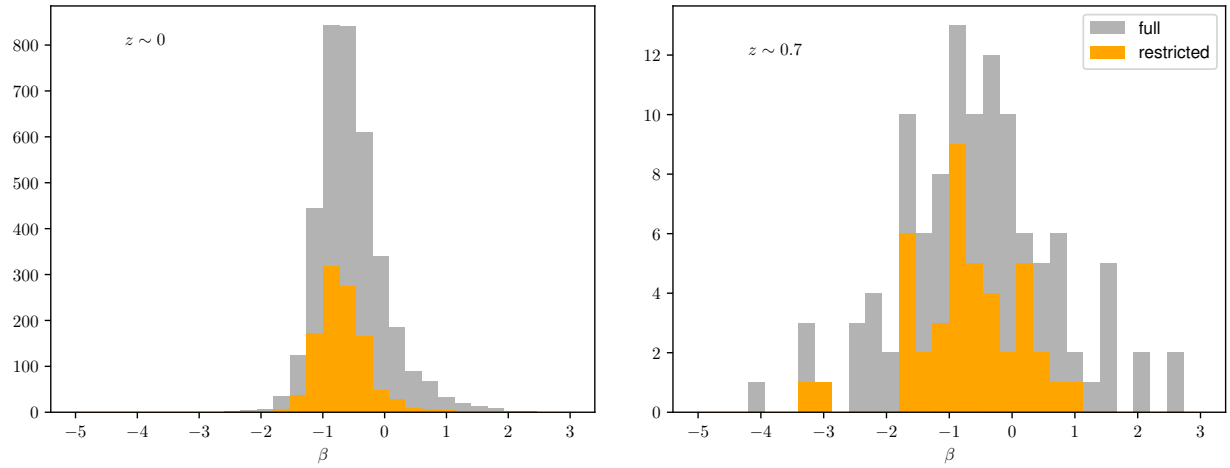

Figure 3.2.: UV-slope, β, distribution for restricted (orange) and full samples (grey) in our local sample (top) and $z \sim 0.7$ sample (bottom).

COSMOS sample: For the COSMOS sample, we fit the UV spectral slope β using flux densities observed between rest-frame 1,250 - 2,500 Å. For our redshift range, this corresponds to the COSMOS2015 B, IB427, u, or GALEX NUV bands. To fit the spectral slope, we did not use flux values with a flag > 0 (Laigle et al., 2016). Our data show β values ranging between 2 and -3, with most galaxies having $\beta \sim -0.8$ for both the full and restricted samples.

The limiting factor is the small number of photometric data points in the rest-frame wavelength range 1,250 - 2,500Å over our redshift range. For $z < 0.705$, only the NUV and u band lie in the rest-frame 1,250-2,500Å range. Between $0.70 < z < 0.78$, the IB427 band can also be used to constrain β, and for $0.78 < z < 0.8$, we can use the u, IB247, and the B band along with GALEX NUV to constrain β. No redshift dependency on our fitted β slopes arises because different bands were used for the full and restricted samples.

The $\mathrm{SFR_{FUV}}$ corrected for attenuation using the spectral slope appears to remove most of the inclination dependence at $z \sim 0.7$. The slopes are 0.05 ± 0.45 for the full sample and -0.05 ± 0.51 for the restricted sample; however, these slopes are poorly constrained because of the small number of galaxies (56 in the full and 28 in the restricted samples, respectively) with robust β measurements at $z \sim 0.7$. The average SFR has also increased, but the corrected values are still below the SFMS by -0.46 ± 0.20 dex for the full sample and -0.12 ± 0.25 dex for the restricted sample for face-on galaxies. Figure 3.2 shows the distribution of β is very similar for the $z \sim 0.7$ and $z \sim 0$ samples, peaking around $\beta \sim -1$.

In Section 3.4 we explore the effects of assuming a constant attenuation factor of $A_V = 1$ for all galaxies in the COSMOS sample. Assuming a constant factor is, in some cases, the only way to build a statistically significant sample of galaxies with SFR measurements. While this assumption ignores any inclination effects, it can correct the systematic offset observed in the top right panel of Figure 1. We also show the results for an alternative $\mathrm{A_{FUV}}-\beta$ relation from Wang et al. (2016) in Section 3.4.

3.3.2. MIR hybrid correction

The most widely used composite tracers combine the UV observations with IR measurements using an energy-balancing approach that in the simple case assumes that the IR and UV light comes from a similar optical depth. This is generally a valid assumption and means that a linear combination of observed L_{FUV} and L_{IR} luminosity can correct the UV fluxes for dust attenuation (Kennicutt et al., 2009; Hao et al., 2011; Catalán-Torrecilla et al., 2015),

$$L_{\mathrm{UV,corr}} = L_{\mathrm{UV,observed}} + \eta L_{\mathrm{IR}}. \tag{3.5}$$

The coefficient η can be calibrated theoretically with evolutionary synthesis models or empirically using independent measurements of dust-corrected SFRs (Treyer et al., 2010; Hao et al., 2011). In most cases, $\eta < 1$ because dust is significantly heated by old stars and by emission arising from the IR cirrus. Different sample selections result in different determinations of η because of different contributions of the old and young stellar populations in the dust-heating, inter-stellar radiation field. For example, early studies were restricted to luminous starburst galaxies and star-forming regions (e.g. Buat et al. 1999; Meurer et al. 1999), and yielded values of ~ 0.6 (Kennicutt & Evans, 2012). With the advent of GALEX, *Spitzer,* and *Herschel*, subsequent analyses of normal star-forming galaxies typically find lower η values, for instance Hao et al. (2011), and Wang et al. (2016) (although see Boquien et al. 2016). In this analysis, we have access to MIR fluxes through WISE (local sample) and *Spitzer*-MIPS (COSMOS sample). The MIPS 24 μm data samples rest-frame 14 μm fluxes at $z \sim 0.7$. The short-wavelength MIR range ($\sim$3 - 20 μm) dust emission arises from strong polycyclic aromatic hydrocarbon (PAH) emission features and continuum (Leger & Puget, 1984; Allamandola et al., 1985; Dopita et al., 2003; Smith et al., 2007). The continuum emission comes from both single-photon, stochastically heated small dust grains (typically $< 0.01\mu$m) and from thermally emitting hot (T>150 K) dust (Calzetti, 2013).

We correct the UV luminosity following Hao et al. (2011)

$$L_{\mathrm{FUV,corr}} = L_{\mathrm{FUV,obs}} + 0.46 L_{\mathrm{IR}}. \tag{3.6}$$

For our analysis we adopted $\mathrm{SFR_{FUV,corr}}$ errors given by the uncertainties on the UV and MIR fluxes alone. However, we note that η has been found to vary with stellar mass and morphological type by up to factors of 4 for local late-type galaxies (Boquien et al., 2016; Catalán-Torrecilla et al., 2015).

Local sample: The WISE W3 band is broad, covering 7.5-16.5 μm at half-power (Jarrett et al., 2011). This wavelength range encompasses multiple PAH features as well as H_2 and forbidden neon emission lines. PAH fractions tend to be high in regions of active star formation, and the WISE 12 μm emission has been shown to correlate well with SFR (Cluver et al., 2014, 2017). We followed the method in L18 to convert the W3 flux into total infrared luminosity using the spectral energy distribution (SED) template of Wuyts et al. 2008. Additionally, we discuss the use of other monochromatic-to-total infrared (TIR) calibrations making use of WISE 12 μm and 22 μm data in Section 3.5.

We then corrected our L_{FUV} according to Equation 3.6 and calculated $\mathrm{SFR_{FUV,corr}}$. The resulting $\mathrm{SFR_{FUV,corr}}$ values show very little inclination dependence on slopes $k_1 = -0.15 \pm$

0.03 and -0.21 ± 0.05 for the full and restricted samples, respectively. The fitted intrinsic scatter of the hybrid SFR-inclination relation is smaller than the other local SFR-inclination relations. The corrected SFRs of face-on galaxies lie above the expected $\mathrm{SFR_{SFMS}}$ by 0.15 ± 0.02 and 0.14 ± 0.02 dex for the edge-on and face-on samples, while the corrected SFRs of edge-on galaxies are entirely consistent with the SFMS.

COSMOS sample: For the COSMOS sample, we have 24 μm flux measurements, or rest-frame $\sim 14\,\mu$m. We followed the method in L18 to convert this flux into total infrared luminosity (using the SED template of Wuyts et al. 2008). The resulting hybrid $\mathrm{SFR_{FUV,corr}}$ – inclination relation has a slope consistent with zero for both the full and restricted subsamples. The y-intercept values are also low: -0.16 ± 0.09 and -0.03 ± 0.06 for the full and restricted samples, respectively. For the COSMOS hybrid corrections, the restricted sample has, on average, slightly higher $\mathrm{SFR_{FUV,corr}}$ than the full sample. The scatter is not reduced as significantly as it was in the local sample for the hybrid SFRs, but is still the smallest out of the four $\mathrm{SFR_{FUV}}$–inclination relations shown. Other authors such as Izotova & Izotov (2018) also found a smaller scatter in the MIR + UV hybrid SFRs than for SFRs derived from either of the original UV or MIR bands.

3.3.3. Radiative transfer correction

Integrated SED models fitted to observations can constrain physical properties of a galaxy, including the SFR. The radiative transfer (RT) method self-consistently calculates the dust emission SED based on the radiation field of the attenuated stellar population. When creating model SEDs using the RT method, the geometry and distribution of the stars, dust, and gas in the galaxy can be determined either from a hydrodynamical model or a toy model of the galaxy. In L18, $\mathrm{SFR_{FUV,obs}}$-inclination relations were fit with the model predictions of the Tuffs et al. (2004) RT calculations based on a simple geometric model for a spiral galaxy. For the UV attenuation calculations, it was assumed that UV emission comes only from the thin disk of a galaxy, simplifying the calculation by removing the bulge or thick-disk stellar and dust model components. Under this assumption, the parameters required for the model are inclination angle, B-band opacity through the centre of the galaxy as seen face-on (τ_B^f), and the mass fraction of dust in a clumpy dust component associated with star-forming regions in the thin disk (as opposed to the diffuse dust component), F.

The model of Tuffs et al. (2004) derives the attenuated stellar population, and the resulting dust emission expected was calculated in Popescu et al. (2011). Recently, Grootes et al. (2013), Davies et al. (2016), and Grootes et al. (2017), have used RT dust corrections based on the Tuffs et al. (2004) and Popescu et al. (2011) models to correct NUV luminosities for dust attenuation.

Tuffs et al. (2004) fit the attenuation curves (the change of magnitude Δm due to dust attenuation; Δm vs 1-cos(i)) of the thin-disk component with a fifth-order polynomial at various τ_B^f values and wavelengths. We interpolated the Tuffs et al. (2004) models to derive the Δm at 1542Å, which is the effective wavelength of the GALEX FUV filter. Then L_{FUV} was corrected with Δm to give $\mathrm{SFR_{FUV,corr}}$.

For the errors on the SFRs corrected by this method, we adopted a constant $\sigma = 0.09$ dex as suggested by Davies et al. (2016) in their Appendix A. Davies et al. (2016) found that the

RT method produces the most consistent slopes and normalisations of the SFR-M_* relation out of the 12 different SFR metrics compared for local spiral galaxies [30].

Local sample: We repeated the analysis introduced in Chapter 2, and fit the Tuffs et al. (2004) models to our full sample. We find best-fitting parameters of $\tau_B^f = 4.42^{+0.11}_{-0.11}$, $F = 0.209^{+0.009}_{-0.01}$. We then used these fixed parameters to correct the SFR for each galaxy, given its inclination angle. Our best-fit slope values become significantly flatter than for the uncorrected sample, being -0.01 ± 0.02 and -0.06 ± 0.06 for the full and restricted samples, respectively. However, this correction does not reduce the observed dispersion σ^2 for the full sample. By using the best-fitting parameters for the full galaxy sample to correct $SFR_{\rm FUV}$, we would expect the normalisation and intercept to be close to zero for the full sample.

Grootes et al. (2017) used an empirical relation between stellar mass surface density and B-band optical depth (Grootes et al., 2013) to set τ_B^f, fixing $F = 0.41$ (Popescu et al., 2011). Adopting this method gives $(k_1 k_2, \sigma^2) = (0.14 \pm 0.03,\ 0.18 \pm 0.02,\ 0.25 \pm 0.01)$ for the full and $(0.20 \pm 0.05, 0.22 \pm 0.02, 0.16 \pm 0.01)$ for the restricted samples, respectively. This correction over-estimates the FUV SFRs on average, and leaves a positive residual inclination dependency. On the other hand, adopting the Grootes et al. (2013) τ_B^f, and keeping our fitted value of $F = 0.209$, we find $(k_1, k_2, \sigma^2) = (0.14 \pm 0.03, -0.03 \pm 0.02, 0.26 \pm 0.01)$ for the full sample and $(0.19 \pm 0.05, 0.22 \pm 0.02, 0.16 \pm 0.01)$ for the restricted sample. Naturally, using different τ values for each galaxy reduces the scatter in the $\rm SFR_{FUV,corr}$ values. However, the parameters of τ_B^f and F are correlated, and therefore must be set consistently with each other, as done for our adopted method in Table 3.1 ($\tau_B^f = 4.42$, $F = 0.209$ for all galaxies).

COSMOS sample: We find best-fitting parameters for the full $z \sim 0.7$ sample to be $\tau_B^f = 2.85^{+0.24}_{-0.17}$ and $F = 0.607^{+0.003}_{-0.006}$. Using these values to determine the required UV attenuation correction, we obtain best-fit values that show a positive slope of 0.16 ± 0.13 and 0.16 ± 0.16 for the full and restricted samples, respectively. These slopes are different from zero at the 2 and 1.6 σ levels for the full and restricted samples, respectively; moreover, it appears that they are driven by galaxies with the highest inclination angles, where the correction is most uncertain. The intrinsic scatter has increased from the scatter of the uncorrected SFRs by this correction.

[30] Davies et al. (2016) calculated τ_B^f for each galaxy by assuming an empirical relation between τ_B^f and stellar mass surface density (Grootes et al., 2013). We chose not to follow this assumption for our analysis as it requires a fixed $F = 0.41$ and was not derived for galaxies at $z \sim 0.7$

Table 3.1.: Best-fit parameters of the relation $\log(SFR_{FUV,corr}/SFR_{\rm SFMS}(M_*,z)) = k_1(1-cos(i))+k_2$, where $\rm SFR_{FUV,corr}$ is measured using three different methods. An intrinsic scatter of variance σ^2, assumed to be in the SFR direction, is also fitted following Foreman-Mackey (2017). N is the number of galaxies used for the fits. Errors represent the 5th and 95th percentiles of the parameters given by the MCMC.

	Local $z\sim0$				COSMOS $z\sim0.7$			
Method	N	k_1	k_2	σ^2	N	k_1	k_2	σ^2
No corr	3489	$-1.03^{+0.04}_{-0.04}$	$-0.25^{+0.02}_{-0.02}$	$0.31^{+0.01}_{-0.01}$	575	$-0.48^{+0.12}_{-0.12}$	$-0.90^{+0.06}_{-0.05}$	$0.28^{+0.02}_{-0.02}$
UV slope	3489	$-0.91^{+0.03}_{-0.03}$	$0.40^{+0.02}_{-0.02}$	$0.25^{+0.01}_{-0.01}$	56	$0.05^{+0.45}_{-0.44}$	$-0.46^{+0.21}_{-0.20}$	$0.29^{+0.06}_{-0.07}$
FUV + MIR	3454	$-0.15^{+0.03}_{-0.03}$	$0.15^{+0.02}_{-0.02}$	$0.20^{+0.01}_{-0.01}$	527	$0.02^{+0.15}_{-0.15}$	$-0.16^{+0.09}_{-0.09}$	$0.27^{+0.02}_{-0.02}$
FUV+RT	3489	$-0.15^{+0.04}_{-0.04}$	$-0.01^{+0.02}_{-0.02}$	$0.31^{+0.02}_{-0.02}$	565	$0.16^{+0.13}_{-0.13}$	$-0.12^{+0.06}_{-0.06}$	$0.32^{+0.02}_{-0.02}$
	Restricted $z\sim0$ sample				Restricted $z\sim0.7$ sample			
No corr	1021	$-0.90^{+0.06}_{-0.06}$	$-0.16^{+0.03}_{-0.03}$	$0.23^{+0.01}_{-0.01}$	295	$-0.44^{+0.15}_{-0.15}$	$-0.75^{+0.07}_{-0.07}$	$0.26^{+0.02}_{-0.02}$
UV slope	1021	$-0.79^{+0.05}_{-0.05}$	$0.45^{+0.03}_{-0.03}$	$0.20^{+0.01}_{-0.01}$	28	$-0.05^{+0.51}_{-0.50}$	$-0.12^{+0.25}_{-0.24}$	$0.25^{+0.07}_{-0.09}$
FUV + MIR	1015	$-0.21^{+0.05}_{-0.05}$	$0.14^{+0.02}_{-0.02}$	$0.17^{+0.01}_{-0.01}$	284	$0.10^{+0.12}_{-0.12}$	$-0.03^{+0.06}_{-0.06}$	$0.22^{+0.02}_{-0.02}$
FUV+RT	1021	$-0.06^{+0.06}_{-0.06}$	$0.11^{+0.03}_{-0.03}$	$0.21^{+0.01}_{-0.01}$	295	$0.16^{+0.16}_{-0.16}$	$0.04^{+0.08}_{-0.08}$	$0.31^{+0.02}_{-0.02}$

3.4. Different UV-slope-related corrections at $z\sim0.7$

In Section 3.3.1, our ability to test the performance of using the galaxy rest-frame UV slope β to correct attenuated FUV SFRs was limited for the COSMOS ~0.7 sample by the small number of galaxies (56 in the full and 28 in the restricted samples). In this section, we test the performance of the assumption that $\rm A_{FUV}=2.035$ (which can be applied to all galaxies) and the use of a different $\beta-\rm A_{FUV}$ relation. The results of these tests are summarised in Table 3.2 and Figure 3.3. We find no obvious difference in the performance of $\rm SFR_{FUV}$ attenuation corrections assuming the Wang et al. (2016) or Boquien et al. (2012) $\beta-\rm A_{FUV}$ relation or a constant $A_V=1$ for our limited sample of galaxies.

To build a statistically significant sample of galaxies in COSMOS at $z\sim0.7$, we followed a standard assumption and assumed $A_V=1$. First, to judge whether assuming $A_V=1$ performs better than β at correcting the systematic $\rm SFR_{FUV}/SFR_{SFMS}$ offset, we have calculated $\rm SFR_{FUV,corr}$ assuming $A_V=1$ for the 56 (28) galaxies with determined UV-slopes in the full (restricted) samples. We assumed the average Milky Way attenuation curve of Cardelli et al. (1989) and an $R_V=3.1$, resulting in an attenuation of 1 magnitude in the V band, corresponding to a FUV attenuation of $\rm A_{FUV}=2.035$ (or a y-intercept offset of ~1.2 dex). After correcting the galaxies with fitted β values by $\rm A_{FUV}=2.035$, the best fits for the $\log(\rm SFR_{FUV,corr}/SFR_{SFMS})$–inclination relation are $(k_1,k_2,\sigma^2)=(-0.03^{+0.40}_{-0.39},\ 0.27^{+0.18}_{-0.18},$ and $0.24^{+0.02}_{-0.03})$ for the full sample and $(k_1,k_2,\sigma^2)=(-0.05^{+0.50}_{-0.51},\ -0.12^{+0.25}_{-0.24},$ and $0.25^{+0.07}_{-0.09})$ for the restricted sample. Interestingly, the slope has improved (SFRs have become more inclination independent) compared to no correction, and the y-intercept is also closer to zero. Compared to the β corrections from Boquien et al. (2012) used in Section 3.3.1, the slopes are consistent given the large uncertainties, and the y-intercept has not improved at all for the restricted sample, with SFRs remaining 0.12 ± 0.25dex below the SFMS. However, the

small sample size of galaxies with β still inhibits a robust comparison.

Applying the correction $A_V = 1$ to all the galaxies in the COSMOS sample results in best-fit values of $(k_1, k_2, \sigma^2) = (-0.48^{+0.12}_{-0.12}, -0.08^{+0.06}_{-0.05}$, and $0.28^{+0.02}_{-0.03})$ for the full sample and $(k_1, k_2, \sigma^2) = (-0.44^{+0.15}_{-0.15}, 0.06^{+0.07}_{-0.07}$, and $0.26^{+0.02}_{-0.02})$ for the restricted sample. As expected, the slope and scatter remain the same as for the uncorrected case, and the y-intercept becomes more consistent with zero. This indicates that using $A_{\rm FUV} = 2.035$ is an appropriate method for correcting the average dust attenuation for our sample of massive galaxies at $z \sim 0.7$, but a larger $A_{\rm FUV}$ is required to bring the average SFR in line with the expected SFMS SFR for the full sample; a galaxy in the full sample or restricted sample with 1-cos(i)=0.5 lies 0.32 or 0.16 dex below the SFMS, respectively.

Combining the two approaches, we also fitted our samples adopting the UV-slope-derived attenuation where available and adopting $\rm A_{FUV} = 2.035$ where β was unavailable. Applying attenuation corrections based on the UV-slope or $A_V = 1$ at $z \sim 0.7$ does not remove the inclination dependency of the $\rm SFR_{FUV}$: $k_1 = -0.48 \pm 0.12$ and -0.47 ± 0.16 for the full and restricted samples, respectively. These results would suggest that applying $A_V = 1$ performs similarly to the $\beta - \rm A_{FUV}$ relation from Boquien et al. (2012) at $z \sim 0.7$, but larger samples of galaxies with well-determined UV-slopes would be required to confirm this. In addition, further corrections would still be required to remove the inclination dependence of the SFRs when applying a constant $\rm A_{FUV}$ correction.

We found that Equation 3.4 from Boquien et al. (2016) may not be appropriate for our sample of massive disk galaxies at $z \sim 0.7$ because the resulting SFRs lie below the expected SFMS, therefore we also tested the relation from Wang et al. (2016):

$$A_{\rm FUV} = 1.58 \quad \beta + 2.62. \tag{3.7}$$

Comparing rows 2 and 3 of Figure 3.3, it appears that the Wang et al. (2016) and Boquien et al. (2012) corrections perform similarly. The key difference is the increased scatter in the Wang et al. (2016) SFRs due to the stronger dependence on β. Further progress in determining the attenuation law for these galaxies at intermediate redshift could be made by 1) improving our measurements of β by using rest-frame UV spectra or more photometric observations, and 2) by increasing our sample size.

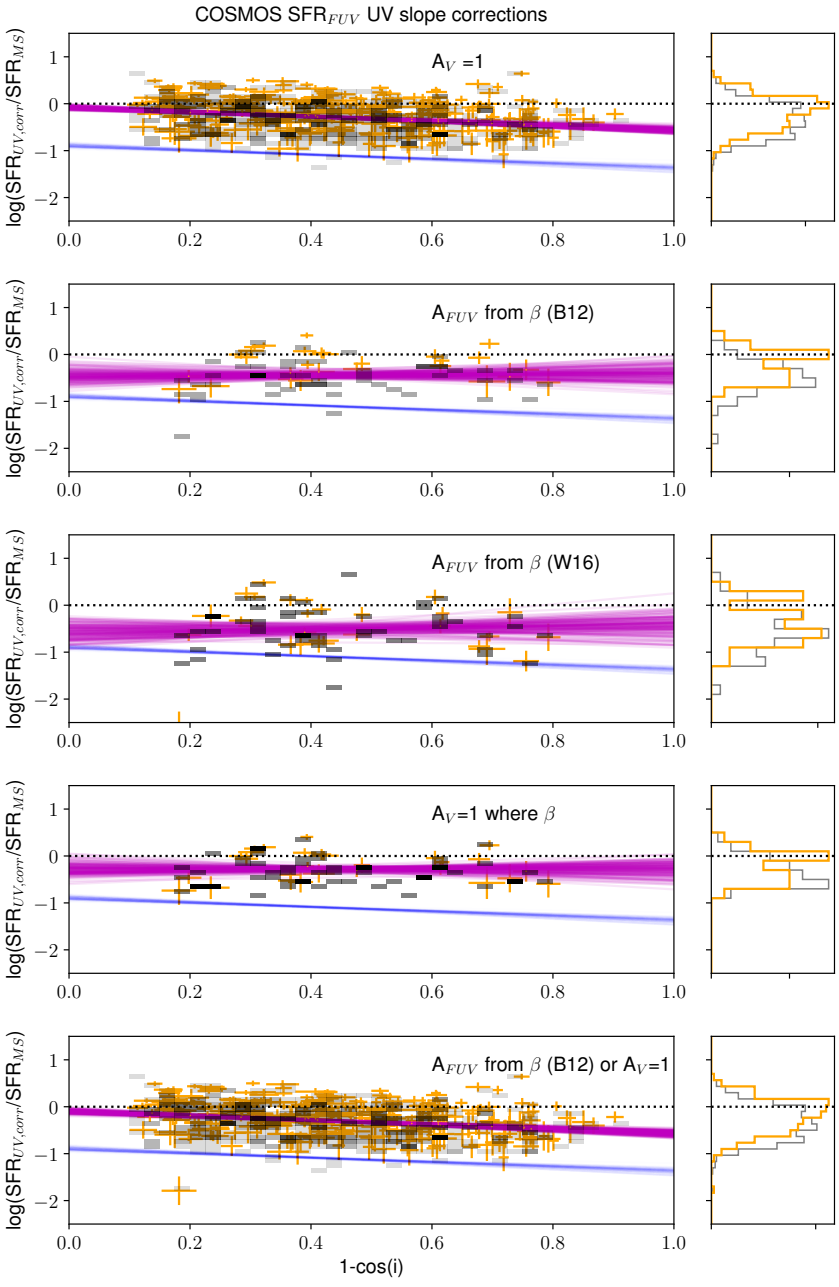

Figure 3.3.: SFR$_{FUV,corr}$ vs. inclination for different UV-slope-related correction methods, as described in Section 3.4.

Table 3.2.: COSMOS $z \sim 0.7$ UV slope corrections or $A_V = 1$. Fits for relations indicated in Figure 3.3. The top half shows the full sample and the bottom half the restricted sample. The "No corr" and and β (B12) methods are repeats of rows 1 and 2 in Table 1 to facilitate comparison.

Method	N	k_1	k_2	σ^2
No corr	575	-0.47 $^{+0.12}_{-0.12}$	-0.89 $^{+0.06}_{-0.05}$	0.28 $^{+0.02}_{-0.02}$
$A_V = 1$	575	-0.48 $^{+0.12}_{-0.12}$	-0.08 $^{+0.06}_{-0.05}$	0.28 $^{+0.02}_{-0.02}$
β (B12)	56	0.05 $^{+0.45}_{-0.45}$	-0.46 $^{+0.21}_{-0.20}$	0.29 $^{+0.06}_{-0.07}$
β (W16)	56	0.12$^{+0.62}_{-0.60}$	-0.56 $^{+0.29}_{-0.28}$	0.48 $^{+0.08}_{-0.10}$
A_V=1 where β	56	-0.03 $^{+0.40}_{-0.39}$	-0.27 $^{+0.18}_{-0.18}$	0.24 $^{+0.05}_{-0.06}$
β (B12) or A_V=1	575	-0.48 $^{+0.12}_{-0.12}$	-0.10 $^{+0.06}_{-0.06}$	0.29 $^{+0.02}_{-0.02}$
No corr	295	-0.44 $^{+0.15}_{-0.15}$	-0.75 $^{+0.07}_{-0.07}$	0.26 $^{+0.02}_{-0.02}$
A_V=1	295	-0.44 $^{+0.15}_{-0.15}$	0.06 $^{+0.07}_{-0.07}$	0.26 $^{+0.02}_{-0.02}$
β (B12)	28	-0.05 $^{+0.51}_{-0.50}$	-0.12 $^{+0.25}_{-0.24}$	0.25 $^{+0.07}_{-0.09}$
β (W16)	28	-0.16 $^{+0.77}_{-0.81}$	-0.36 $^{+0.40}_{-0.41}$	0.53 $^{+0.12}_{-0.17}$
A_V=1 where β	28	-0.05 $^{+0.50}_{-0.51}$	-0.12 $^{+0.25}_{-0.24}$	0.25 $^{+0.07}_{-0.09}$
β (B12) or A_V=1	295	-0.47 $^{+0.16}_{-0.16}$	0.06 $^{+0.07}_{-0.07}$	0.27 $^{+0.02}_{-0.03}$

3.5. Different hybrid UV + MIR dust corrections at $z \sim 0$

Using different values for η in Equation 4 or different monochromatic L_{TIR} conversions will naturally result in different hybrid $SFR_{FUV,corr}$ values. In this section, we test MIR + UV hybrid methods that use the WISE 12 μm and WISE 22 μm fluxes to correct for FUV attenuation in our local samples.

We used the relation of Cluver et al. (2017, C17,) to convert the W3 spectral luminosity into total-infrared luminosity (5 – 1,100 μm):

$$\log(L_{\rm IR}) = 0.889 \log(L_{12}) + 2.21, \tag{3.8}$$

where L_{12} is in units of solar luminosities. This relation was calibrated on the SINGS/KINGFISH sample (Dale et al., 2017) supplemented with several more luminous galaxies from the literature. Cluver et al. (2017) found a 1σ scatter of 0.15 dex in Equation 3.8. Correcting the FUV luminosity using the Cluver et al. (2017) relation and Equation 6 results in $SFR_{FUV,corr}$ that are systematically ~ 0.3 dex above the expected SFMS (see Table 3.3) for both the restricted and full samples. This may indicate that 1) a lower value of η is required for our sample, 2) the Cluver et al. (2017) relation might give higher L_{TIR} luminosities for our sample of galaxies because different WISE flux measurement methods were used in their study and ours, as well as a different definition of L_{IR} , or 3) the adopted SFMS relation is ~ 0.1 dex too high at $z \sim 0.07$. If we had used the 22 μm (W4) data rather than the 12 μm (W3) fluxes to calculate L_{TIR}, and the W4 calibration from Cluver et al. (2017), then our UV + MIR SFRs would be only slightly different, with a larger intrinsic scatter, as shown in Figure 3.4 and Table 3.3. Cluver et al. (2017) also found a larger scatter in the W4 – TIR relation (σ =0.18 dex) than the W3 – TIR relation ($\sigma = 0.15$). The uncertainty in the SFMS from using different SFR calibrations is about $0.1 - 0.2$ dex, which is not sufficient to

Table 3.3.: Local $SFR_{FUV,corr}$ from the hybrid relations indicated in Figure 3.4

Method	N	k_1	k_2	σ^2
12 μm, C17	3453	$-0.15^{+0.05}_{-0.05}$	$0.315^{+0.03}_{-0.03}$	$0.174^{+0.005}_{-0.005}$
22 μm, C17	2111	$-0.15^{+0.02}_{-0.02}$	$0.32^{+0.03}_{-0.03}$	$0.20^{+0.01}_{-0.01}$
12 μm, W08	3453	$-0.15^{+0.02}_{-0.02}$	$0.15^{+0.02}_{-0.02}$	$0.190^{+0.005}_{-0.005}$
22 μm, W08	1562	$-0.14^{+0.03}_{-0.03}$	$0.10^{+0.05}_{-0.05}$	$0.18^{+0.01}_{-0.01}$
22 μm, CT15	2111	$-0.15^{+0.03}_{-0.03}$	$0.10^{+0.03}_{-0.03}$	$0.22^{+0.01}_{-0.01}$
12 μm, C17.	1015	$-0.21^{+0.05}_{-0.05}$	$0.31^{+0.02}_{-0.02}$	$0.15^{+0.01}_{-0.01}$
22 μm, C17.	518	$-0.21^{+0.08}_{-0.06}$	$0.29^{+0.03}_{-0.03}$	$0.14^{+0.01}_{-0.01}$
12 μm, W08.	1015	$-0.21^{+0.05}_{-0.05}$	$0.14^{+0.02}_{-0.02}$	$0.16^{+0.01}_{-0.01}$
22 μm, W08.	333	$0.18^{+0.10}_{-0.10}$	$0.05^{+0.05}_{-0.05}$	$0.12^{+0.01}_{-0.01}$
22 μm, CT15	518	$-0.21^{+0.08}_{-0.08}$	$0.06^{+0.03}_{-0.03}$	$0.165^{+0.014}_{-0.014}$

explain the 0.3 dex offset seen by the hybrid SFRs using the Cluver et al. (2017) relation for TIR luminosity. However, it is clear that the different assumptions that go in to calculating the monochromatic infrared luminosity and combining this with the FUV luminosity can alter the SFRs by ~ 0.3 dex.

We also tested hybrid SFRs using the Wuyts et al. (2008) SED (W08), following the methods used in L18 for both W3 (used in Section 3.6) and W4 fluxes. These methods give SFRs closer to the expected SFMS values, $k_2 = 0.15$ and 0.14 for the 12 μm (W3) full and restricted samples, respectively, and $k_2 = 0.1$ and 0.05 for the 22 μm (W4) full and restricted samples, respectively. However, the slope of the relation is still ~ -0.15 dex for the full sample. The Wuyts et al. (2008) W4 correction on the restricted sample is the only hybrid example that shows a positive correlation between W4-corrected SFRs and inclination ($k_1 = 0.18 \pm 0.1$), but this is also the sub-sample with the fewest detected galaxies.

Rather than using a flux density to LIR conversion, Catalán-Torrecilla et al. (2015, CT15), gives the following prediction based on the energy balance approach:

$$L_{\mathrm{FUV,corr}} = L_{\mathrm{FUV}} + 4.08 L_{22\mu m}. \tag{3.9}$$

This correction results in SFRs similar to the W08 W4 hybrid SFRs. A galaxy in the full sample with inclination $1 - \cos(i) = 0.5$ lies 0.025 dex above the SFMS. On the other hand, a galaxy in the restricted sample at $1 - \cos(i) = 0.5$ lies -0.05 dex below the SFMS. Catalán-Torrecilla et al. (2015) found a coefficient of ~ 4.5 (rather than 4.08 from the energy balance argument) when fitting to star-forming CALIFA galaxies, which would again increase the SFRs.

Figure 3.3 shows that the different hybrid SFR methods are able to bring the FUV-SFRs of local galaxies into rough agreement with our best-fit SFMS and remove most of the inclination dependence. However, different calibrations can change the overall $SFR_{FUV,corr}$ by up to 0.2 dex. Table 3.3 gives the best-fit values for the different hybrid correction methods discussed above. WISE band 4 is less sensitive than W3, so we have about half the number of galaxies in our samples when we use 22 μm corrections. Moreover, signal-to-noise ratio cuts were applied on SFRs and therefore depend on L_{TIR}, explaining the different number of galaxies for our analysis using W08.

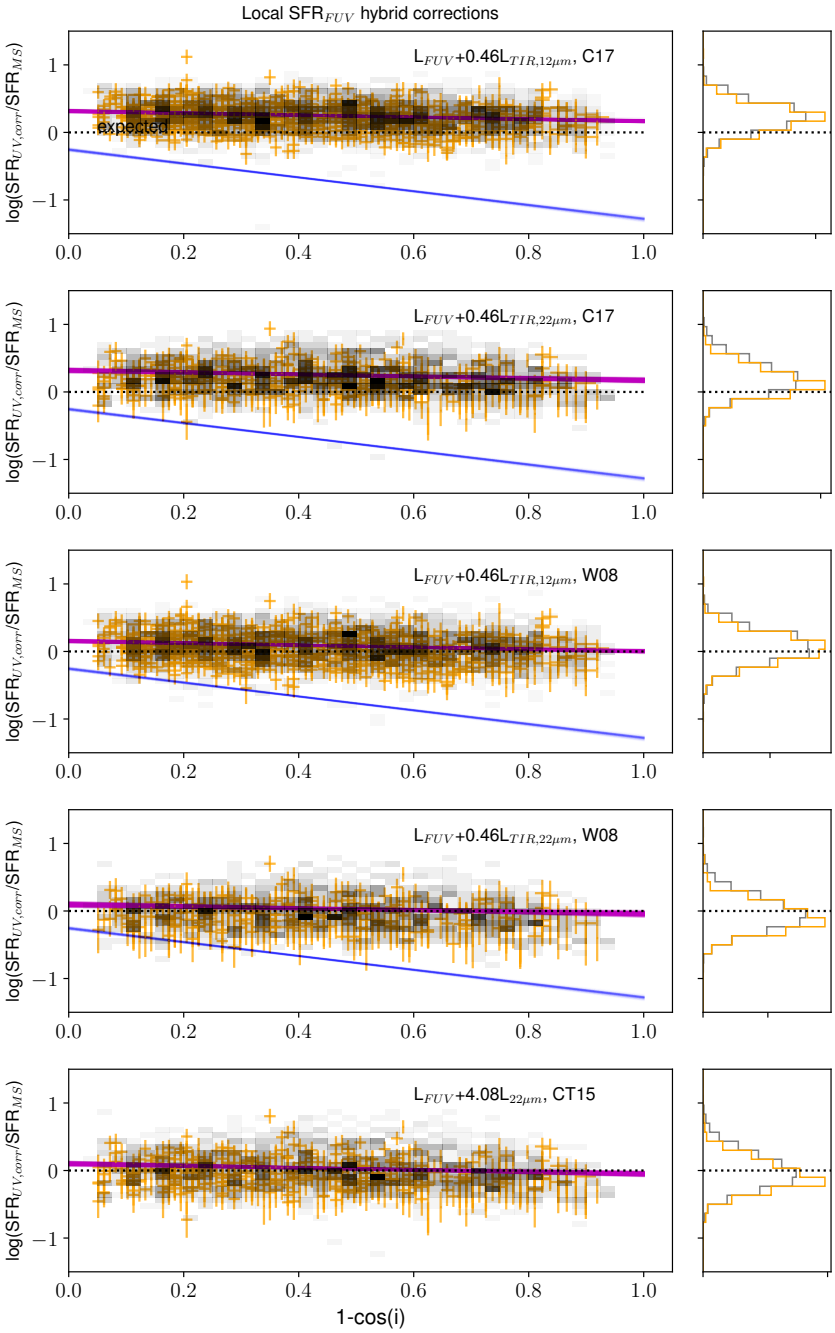

Figure 3.4.: $SFR_{FUV,corr}$ vs. inclination for different MIR hybrid correction methods, as indicated in the panels. C17 refers to Cluver et al. (2017), W08 to Wuyts et al. (2008), and CT15 to Catalán-Torrecilla et al. (2015).

3.6. Discussion and conclusion

We have tested a number of global galaxy FUV attenuation correction methods for samples of massive ($M_* > 1.6 \times 10^{10}\,M_\odot$) galaxies at $z \sim 0$ and $z \sim 0.7$ selected to be representative of corrections applied in the literature. FUV SFRs are very difficult to properly correct for dust attenuation. Conversely, SFR calibrations at different wavelengths are sensitive to stellar populations over different timescales. SFR estimators at longer wavelengths are not able to capture variations on short timescales, leading to important discrepancies on the estimates of the instantaneous SFR. Despite these many uncertainties, we find that hybrid MIR and RT attenuation correction methods can remove the overall offset from the SFMS and decrease the inclination dependency of UV SFRs.

Hybrid MIR + UV SFR calibrations remove a significant fraction of the inclination dependency displayed by uncorrected SFR_{FUV} at $z \sim 0.7$ and at $z \sim 0$. However, there is some remaining uncertainty regarding the normalisation of the calibration due to differences in IR templates and intrinsic SFRs. The scatter of SFR from galaxy to galaxy is decreased when this technique is used. We also found that the RT method of Tuffs et al. (2004) works reasonably well for correcting the normalisation and inclination dependency of SFR_{FUV} at both $z \sim 0$ and $z \sim 0.7$ and is not highly dependent on the choice of input parameters τ_B^f and F.

We find that the SFR correction methods tested give similar results, in that they perform similarly well, for both the full sample of star-forming galaxies and our restricted samples (with a cut for larger sizes and lower Sérsic indexes) of large disk-dominated galaxies. One difference between the samples is that the dispersion is smaller for the restricted sample at $z \sim 0$. This might be because the restricted sample spans a smaller range of galaxy morphologies, only including large exponential discs.

Despite the small number of galaxies detected in COSMOS at multiple UV wavelengths, we are able to learn something from the UV slope measurements at $z \sim 0.7$. The attenuation at higher redshift is so substantial that inclination dependency is probably not the dominant concern for the SFR_{FUV} measurements because accurately correcting the average attenuation of the population gives the most improvement in terms of SFRs. At both $z \sim 0$ and $z \sim 0.7$, applying an attenuation correction based on the UV slope is better than no correction, but at $z \sim 0.7$, the SFRs on average still lie below the SFMS by ~ 0.44 dex and ~ 0.15 dex for the full and restricted samples, respectively (for a galaxy at $1 - \cos(i) = 0.5$).

In Chapter 2 we found that found that dust at $z \sim 0.7$ is most closely associated with star-forming clumps rather than the disc. Therefore, we expect the UV attenuation curve to be relatively constant with disk inclination angle. In the local sample, we found that adopting a single UV-slope attenuation relation was unable to remove the inclination bias. The attenuation for face-on galaxies is dominated by the clumpy dust component, whereas the attenuation for edge-on galaxies is more affected by the diffuse dust disc, and these two components have different UV-attenuation laws (e.g. Wild et al. (2011); da Cunha et al. (2008); Charlot & Fall (2000)). Therefore, a different A_{FUV}–β relation would be required at different galaxy inclinations. Perhaps at the highest inclination angles, where birth-clouds might overlap along the line of sight and photons would have to escape through more optically thick material, we might see a drop-off in FUV light. A cross-over of star-forming clouds would depend on the cloud number density. Galaxies around cosmic noon ($z \sim 2$)

were forming stars at a faster rate, having more birth clouds. On one hand, the higher SFR would increase the probability that the birth clouds overlap along the line of sight for inclined galaxies. On the other hand, the scale-height of the gas disk is also expected to be larger at this redshift (Förster Schreiber et al., 2009; Kassin et al., 2012; Stott et al., 2016; Turner et al., 2017). A larger scale-height would dampen any expected inclination dependency. Therefore it would be interesting to repeat this exercise at $z = 1.5$ in the era of the *James Webb Space Telescope*, where high-resolution rest-frame optical imaging can provide morphology and inclination measurements of massive galaxies.

4 The VLA-COSMOS 3 GHz Large Project: Evolution of specific star formation rate out to $z \sim 5$

This chapter is being prepared to be submitted to the Astrophysical Journal as S. K. Leslie, E. Schinnerer, I. Davidzon, G. Gozaliasl, B. Groves, E. F. Jiménez-Andrade, A. Karim, P. Lang, D. Liu, B. Magnelli, M. Novak, M. T. Sargent, Vernesa Smolčić, E. Vardoulaki, G. Zamorani, and the COSMOS collaboration, "The VLA-COSMOS 3 GHz Large Project: Evolution of specific star formation rate out to $z \sim 5$"

In this Chapter, we provide a coherent, uniform measurement of the evolution of the star formation rate (SFR) – M_* relation for star-forming and all galaxies, respectively. We measure the galaxy SFR – M_* relation out to $z \sim 5$ using median stacks of the 3 GHz radio continuum to derive average SFRs for $\sim$500,000 galaxies in the COSMOS field. We describe the logarithmic SFR – M_* relation adopting a model that incorporates a steep linear relation at low stellar mass ($\log(M_*/\mathrm{M}_\odot)$<10) and a flattening at high stellar mass that becomes more prominent at low redshift ($z < 1.5$):

$$\log(\mathrm{SFR}) = S_o + a_1 r - \log\left(1 + \left(\frac{10^M}{10^{M_0 + a_2 r}}\right)^{-(1+e^{-a_3 r})}\right),$$

with $r = \log(1+z)$, and $(S_0, M_0, a_1, a_2, a_3)$ $=(0.38 \pm 0.13, 9.28 \pm 0.18, 4.49 \pm 0.53, 3.70 \pm 0.70, 7.71 \pm 2.66)$ for star forming galaxies and $(0.19 \pm 0.11, 9.09 \pm 0.19, 4.10 \pm 0.51, 3.10 \pm 0.46, 4.62 \pm 2.84)$ when including star-forming and passive galaxies. We explore variations in the star-forming SFR – M_* relation as a function of galaxy environment and morphology. We find no significant evidence for variations in the SFR–M_* relation for galaxies in different environments traced by the galaxy number density at $0.3 < z < 3$, nor for galaxies in X-ray groups at $z \sim 0.75$. We confirm that massive bulge-dominated galaxies have SFRs lower than disk-dominated galaxies at fixed stellar mass at $z < 1.5$. Disk-dominated galaxies follow a steeper SFR – M_* relation than bulge-dominated galaxies. The increase in bulge-dominated galaxies in the local star-forming population leads to a flattening of the overall SFMS. Our results imply that bulges are important for quenching, but that the presence of a bulge with no star-formation is roughly sufficient to explain the decrease in specific star formation rate (sSFR) observed between disk-dominated and bulge-dominated galaxies. However, the difference in SFRs becomes more prominent when using radio infrared ratio q-values more appropriate for disk/bulge galaxies; using these SFR calibrations, we find that the star formation is suppressed by $\sim$0.2 dex in the disks of massive galaxies with a prominent bulge.

4.1. Introduction

Observations show that the global star formation rate (SFR) density of the Universe is a rapidly evolving quantity. Madau & Dickinson (2014; and references therein) concluded that the SFR in a co-moving volume, (SFR density; SFRD), has undergone a rapid decline over the last ~ 8 billion years after having peaked at redshift ~ 2. The SFRD at early cosmic times ($z > 4$), as inferred from ultraviolet luminosity functions, declines steeply to higher redshifts (out to $z \sim 10$; Oesch et al. 2013; Bouwens et al. 2014, 2015). In the presence of interstellar dust, UV light is heavily obscured, and attenuation corrections have to be applied. The amount of dust-obscured star formation at these redshifts is highly uncertain and could be between 0 to ~ 10 times that currently observed (Casey et al., 2018).

Bouwens et al. (2010) traced the rest-frame UV continuum of galaxies at redshifts ~ 7 and inferred that the galaxies are essentially dust-free. Alternatively, Novak et al. (2017) concluded that UV-based SFRs are underestimated by factors of 15-20% at $z > 4$. The contrast between inferred dust correction factors required for early times and late times highlights the critical need for dust-unbiased measurements at these high redshifts. Measuring the star formation rates (SFRs) of galaxies using the long-wavelength radio continuum can provide a dust-unbiased view of the cosmic SFR history of the Universe.

Radio continuum SFRs have been successfully applied at low redshifts (Tabatabaei et al., 2017), and at high-redshifts (Karim et al., 2011; Zwart et al., 2014; Pannella et al., 2009a, 2015). Radio continuum observations are not affected by source confusion that limits current infrared data from e.g. *Spitzer* and *Herschel*, primarily due to the higher angular resolution observations that can be achieved with radio interferometers. Thanks to the tight correlation between galaxy IR and radio emission in the local Universe, the radio continuum has been used as SFR tracer. At frequencies < 20GHz, the radio continuum emission of star-forming galaxies is typically composed of a dominant synchrotron component ($\sim 90\%$ at $\nu = 1.4$ GHz, e.g., Condon 1992; Tabatabaei et al. 2017) from supernovae and their remnants and a thermal flat-spectrum element from warm HII regions; these two physical processes render radio continuum emission a robust SFR tracer on timescales of 0-100 Myr (Murphy et al., 2011; Kennicutt & Evans, 2012). The radio-infrared correlation has recently been reported to evolve mildly with redshift and thus it can be used to constrain an empirical radio-SFR calibration (e.g. Delhaize et al. 2017; Magnelli et al. 2015). A widespread concern about using the radio as a SFR tracer is the fact that an AGN can be hidden at all other wavelengths but contribute to, or dominate (in the case of radio-AGN), the radio continuum emission (e.g. Wong et al. 2016)[31]. However, studies such as Novak et al. (2018) report that faint radio sources are overwhelmingly star-forming sources (e.g. 90-95% at fluxes between 0.1 and 10μJy). Novak et al. (2017) made use of the deep Karl G. Jansky Very Large Array (VLA) COSMOS radio observations at 3 GHz (Smolčić et al., 2017b) to constrain the evolution of radio luminosity function of star-forming galaxies out to $z \sim 5$ based on 6,040 direct detections with robust optical counterparts. Even with the deep 2.3 μJy beam^{-1} RMS observations, the faint end of the luminosity function could not be constrained.

Despite our growing knowledge about the cosmic SFRD, key details about the factors driving the evolution remain unclear. In the SFR-stellar mass plane, observations indicate

[31] We would like to caution that measuring the SFR of AGN-host galaxies remains a fundamental challenge for all tracers including SED models.

that galaxies reside in two main populations. One population consists of star-forming galaxies whose SFR is positively correlated with stellar mass out to redshifts of at least 4. (e.g. Elbaz et al. 2007; Brinchmann et al. 2004; Whitaker et al. 2014; Karim et al. 2011; Lee et al. 2015; Magdis et al. 2010). Since first reported, this tight relationship, referred to as the star-forming main sequence (SFMS; Noeske et al. 2007), has been used widely by the astronomical community as a tool for understanding galaxy evolution, from sample selections to constraints or validation tests for simulations. The second population consists of quiescent galaxies which are no longer actively forming stars. Quiescent galaxies fall ~ 1 dex below the SFMS and typically reside at the high-mass end (i.e. they have lower specific star formation rates; sSFR = SFR/M_*). However, in the sSFR – stellar mass space there appears to be a more-or-less continuous distribution of galaxies in the local Universe. Feldmann (2017), and Eales et al. (2018a) suggest the observational bi-modality could be due to uncertainties and observational bias, challenging the paradigm in which star-forming and quiescent galaxies are distinct populations.

There is no established consensus in the literature on the proper form of the SFMS: whether it is linear across all redshifts (e.g. Wuyts et al. 2011a; Speagle et al. 2014; Pearson et al. 2018), or has a turn-over at high stellar mass ($\log(M_*/\mathrm{M}_\odot) \approx 10.5$) (e.g. Whitaker et al. 2014; Lee et al. 2015; Tomczak et al. 2016; Schreiber et al. 2015) remains a matter of debate. This discrepancy seems to be driven by selection effects; for instance, studies requiring more active or bluer star-forming galaxies generally report a linear SFMS relation (e.g. Johnston et al. 2015), similar to studies that include only the SFR and stellar mass residing in a disk component (Abramson et al., 2014). Furthermore, the normalization of the SFMS relation depends on the SFR tracer and calibrations used (Speagle et al., 2014; Bisigello et al., 2018).

The position of galaxies on the SFMS is intimately related to both galaxy colour and structural morphology, with galaxies lying on the local SFMS being predominantly blue and disk-like and most galaxies below the SFMS are red and spheroidal (McPartland et al., 2019; Wuyts et al., 2011a). Various evolutionary channels from the blue cloud to the red sequence have been proposed and more dramatic pathways that involve the shutdown of star formation are referred to as quenching (Faber et al., 2007). Authors such as Bremer et al. (2018) have used optical and near-infrared morphological measurements to address questions of whether secular processes like bulge growth or disk fading can explain the evolution of galaxy colour and morphology. On the other hand, studies including Arnouts et al. (2007), Ilbert et al. (2010), and Brammer et al. (2011) have found that the growth of the stellar mass density in the quiescent population (since $z \sim 2$) must be due to the shut-off of star formation in active galaxies. Peng et al. (2010) introduced the idea of a mass-dependent quenching process, "mass-quenching", which is dominant above stellar masses of $\sim 10^{10.2}\,\mathrm{M}_\odot$. In contrast, at low stellar masses $M_* < 10^{10}\,\mathrm{M}_\odot$, environmental quenching effects like satellite quenching and merging are believed to dominate quenching (Peng et al., 2010).

In previous work, in order to push to lower radio luminosities, Karim et al. (2011) performed stacking on the 1.4 GHz data in the COSMOS field (VLA-COSMOS Large, Deep and Joint projects; Schinnerer et al. 2004, 2007, 2010), drawing on a deep 3.6 μm-selected parent sample of $> 10^5$ galaxies. Karim et al. (2011) found that the sSFRs of star-forming and quiescent galaxies demonstrate a linear relationship with stellar mass and that there is a mass-independent power-law-like increase of sSFR with redshift out to $z < 3$.

The COSMOS field with a coverage of 2 deg^2 is the largest cosmological deep field to-date with HST coverage (Scoville et al., 2007) and contains a rich set of panchromatic data and ancillary data products, making it an ideal choice for a consistent study of galaxy properties over a sufficient range of stellar masses and redshifts. Now with updated multiwavelength photometry (Laigle et al., 2016) and stellar mass functions (Davidzon et al., 2017) available in the COSMOS field, it is timely to revisit the analysis of Karim et al. (2011) and better constrain the SFMS, the evolution of sSFR, and the SFRD of the Universe out to $z \sim 5$. With the latest COSMOS2015 catalog (Laigle et al., 2016) containing new K_s-band photometry 0.7 mag deeper than previously available (e.g. Ilbert et al. 2013), we are able to select a 90% mass-complete sample down to 10^{10} $M_\odot$ at $z = 4$. Recent radio data at 3 GHz (Smolčić et al., 2017b) is also deeper (assuming a standard spectral index of $S_\nu \propto \nu - 0.7$) than the previous 1.4 GHz imaging maps available (Schinnerer et al., 2010), allowing for better constraints on the average radio flux. The higher angular resolution of the radio images also allows for better matching to multi-wavelength counterparts.

We introduce the relevant datasets in Section 4.2 and determine the average SFRs of galaxies employing a stacking analysis outlined in Section 4.3. We present our results for the SFMS relation for star-forming and all galaxies and discuss the functional form of the inferred SFMS in Section 4.4.1. In Section 4.4.5 we combine our SFR measurements with the stellar mass functions of Davidzon et al. (2017) to explore the total SFR activity in the universe as a function of mass and redshift. We report SFR – M_* measurements for galaxies with different morphological classifications in Section 4.4.7 and for galaxies in different bins of local density, including a comparison between X-ray group members and field galaxies in Section 4.4.8. We discuss the implications of our most important results in Section 4.5 and provide a summary and outlook in Section 4.6. We use a Chabrier (2003) initial mass function (IMF), AB magnitudes, and the cosmological parameters $(\Omega_M, \Omega_\Lambda, h)$=(0.30,0.70,0.70).

4.2. Datasets and sample selection

4.2.1. Radio data

The VLA-COSMOS 3 GHz Large Project (hereafter VLA-3 GHz LP), described in Smolčić et al. (2017b) observed the COSMOS field for 384 hours using the VLA S-band centered at 3 GHz with a 2048 MHz bandwidth. Imaging was performed with a multiscale, multi-frequency synthesis algorithm for each pointing separately, tapering each with a Gaussian to achieve a circular beam before creating a final mosaic in the image plane. Across the entire 2.6 square degrees surveyed, 10,830 sources were detected above 5σ using the Blobcat software of Hales et al. (2012). By eye, 67 multicomponent objects were identified, i.e. objects composed of two or more detached radio components (Smolčić et al., 2017b; Vardoulaki et al., 2019). 20% of 3 GHz sources lie outside the UltraVISTA regions (see Figure 4.1). The astrometry is estimated to be accurate to $0.01''$ based on a comparison to the Very Long Baseline Array - COSMOS survey (Herrera Ruiz et al., 2018).

The observing layout was designed to achieve a uniform rms (median 2.3 μJy at $0.75''$ resolution) over the inner 2 square degrees with 192 pointings. Because the outermost regions of the map do not contain overlapping pointings, the noise increases rapidly towards the edge. We define a region where the rms of the 3 GHz map is < 3 μJy/beam to use for the

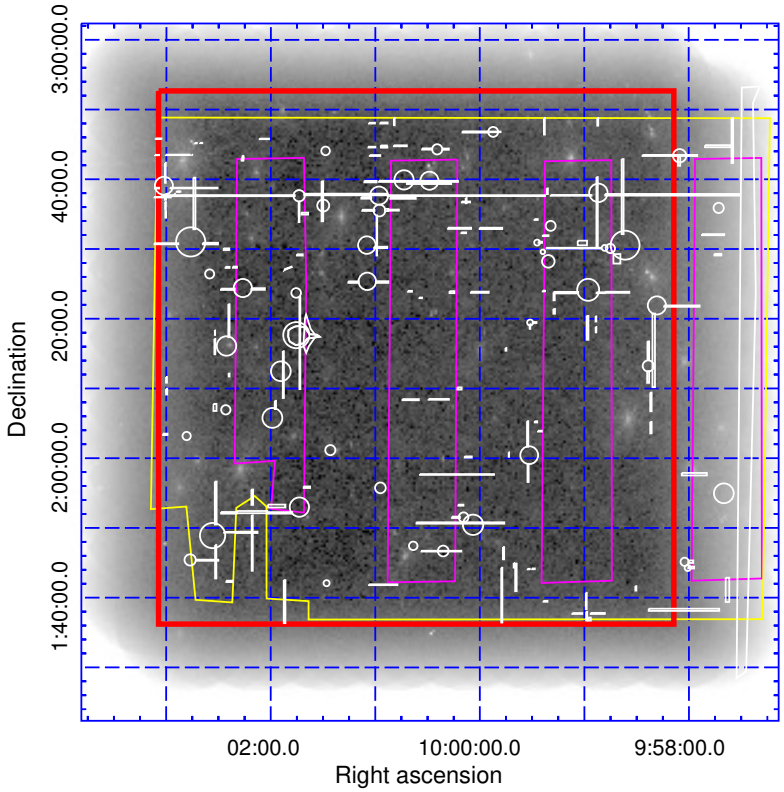

Figure 4.1.: Schematic of the COSMOS field showing the regions of data used. The background image is the VLA-3 GHz LP RMS image, with units of Jy/beam. The region used for stacking (where the RMS noise is $< 3\,\mu$Jy/beam is drawn in red.The yellow area is the region covered by the UltraVISTA-DR2 observations. The ultra-deep stripes in the UltraVISTA-DR2 observations are indicated in magenta. White regions indicate masked areas in the optical images.

stacking experiment (Figure 4.1). This area can be defined by $149.53 < \mathbf{RA}(\mathrm{J2000}) < 150.76$ deg and $1.615 < \mathbf{DEC}(\mathrm{J2000}) < 2.88$ deg.

4.2.2. COSMOS2015 photometry for a stellar mass selected sample

The COSMOS2015 catalogue published in Laigle et al. (2016) provides optical and NIR photometry (in over 30 bands) for over 1 million sources detected in z^{++} (SuprimeCam) $YJHK_s$ (UltraVISTA[32]-DR2) stacked detection images. The new catalogue is improved compared to previous releases through the inclusion of new, deeper NIR data from the UltraVISTA (McCracken et al., 2012) and SPLASH (*Spitzer* Large Area Survey with Hyper-Suprime-Cam) projects (see Capak 2016) and new extraction pipeline. The catalogue covers a square of 2 deg^2 and uses the UltraVISTA DR2 "deep" and "ultra-deep" stripes, resulting in a depth and completeness that is not uniform across the field. The increased exposure time

[32]VISTA

in the "ultra-deep", covering an area of 0.62 deg^2, doubles the number of sources compared to the previous version of the catalogue (Ilbert et al., 2013). Regions saturated by stars or bright sources are masked out in the optical to NIR bands, resulting in a total coverage of 1.77 square degrees. Catalogue fluxes were extracted using SExtractor using $2''$ and $3''$ apertures on point spread function homogenized optical/NIR maps. IRAC photometry was similarly extracted, while also using IRCLEAN (Hsieh et al., 2012) to de-blend sources. Corrections to total magnitudes are described in detail in Laigle et al. (2016), as well as corrections for galactic dust extinction. The catalogue also includes a match with X-ray, near ultraviolet (NUV), IR and Far-IR data coming from Chandra (Civano et al., 2016; Marchesi et al., 2016; Cappelluti et al., 2007), GALEX (Zamojski et al., 2007), *Spitzer* -MIPS (Le Floc'h et al., 2009), *Herschel* -PACS (Lutz et al., 2011) and *Herschel* -SPIRE (Oliver et al., 2012), respectively.

Photometric redshifts (z_p) were computed using LePhare (see also Arnouts et al. 1999; Ilbert et al. 2009, 2013) and have been calibrated using spectroscopic data. The spectral energy distribution (SED) fitting library used includes early and late-type galaxy templates from Polletta et al. (2007), 14 SEDs of star-forming galaxies from Bruzual & Charlot (2003). Extinction is added as a free parameter, constrained to E(B-V)<0.5, and a number of extinction/attenuation curves were considered. The photometric redshift assigned to each galaxy is the median of the probability distribution function (PDF) obtained after scanning the whole template library. The z_p error corresponds to the redshift interval around the median that delimits 68% of the integrated PDF area. The same definition of 1σ error is adopted for stellar mass estimates and rest-frame colours. By comparing to spectroscopic redshifts (z_s), Laigle et al. (2016) report a photometric redshift (z_p) accuracy, defined as $\sigma = 1.48 \times \mathrm{median}(|z_p - z_s|/(1+z_s))$, of 0.007 for the brightest sources ($16 < i^+ < 21$ mag) and 0.057 for the faintest ones ($21 < i^+ < 26$ mag).

Stellar masses are derived as described in Ilbert et al. (2015), using a grid of synthetic spectra created using the stellar population synthesis models of Bruzual & Charlot (2003) with a Chabrier (2003) IMF for two metallicities, τ (i.e. declining and delayed) star formation histories, two different dust attenuation curves, and emission line prescriptions.

We not only require accurate photometric redshifts and stellar masses for selecting our parent samples and sub-samples for stacking and SFR calculations, but accurate source positions are also required in order to stack the radio images at the locations of the galaxies of interest. A positional matching of the VLA-3 GHz LP sources with the COSMOS2015 catalog performed using a search radius of $0.8''$ by Smolčić et al. (2017a) found small systematic positional offsets that also depend on sky locations[33]. Therefore, before using the optical positions reported in COSMOS2015 as inputs in our stacking routine, we correct for the systematic offset using the best fitting linear relations as reported in Smolčić et al. (2017a):

$$\mathrm{RA} = \mathrm{RA}_{L16} + (-0.041\mathrm{RA}_{L16} + 6.1)/3600 \quad (4.1)$$

$$\mathrm{Dec} = \mathrm{Dec}_{L16} + (0.058\mathrm{Dec}_{L16} - 0.147)/3600 \quad (4.2)$$

[33]These offsets arise due to the astrometry of the COSMOS2015 being tied to Megacam $i-band$ data (McCracken et al., 2010, 2012) and will not be an issue in future releases of Ultra-VISTA data which are to be tied to Gaia astrometry

High-z optimised parameters from Davidzon et al. (2017)

Laigle et al. (2016) explored the entire parameter space between $z = 0$ and 6 to create redshift probability distribution functions, PDF(z), for all galaxies detected in COSMOS2015. Due to computational limits, only a subset of SED templates could be used for fitting the full COSMOS2015 sample. In order to optimise the SED fitting for high redshift galaxies ($z >$ 2.5) Davidzon et al. (2017) expanded the grid of allowed redshifts out to $z = 8$. Using the same COSMOS2015 photometry as Laigle et al. (2016), Davidzon et al. (2017) re-fit SEDs with LePhare using additional high-z templates of extremely active galaxies with a rising star formation history (SFH) as well as allowing highly attenuated galaxies; the new constraint is E(B-V)< 0.8.

As in Laigle et al. (2016), Davidzon et al. (2017) select the median of the PDF(z) to be the best-fit redshift for each galaxy. However, for 2442 galaxies identified as having more than one peak with similar likelihoods, or a very broad PDF(z) using the criteria ($|z_{\rm median} - z_{\rm best}| > 0.3(1 + z_{\rm best})$, the redshift with the highest probability (rather than the median redshift) was adopted.

The Davidzon et al. (2017) catalogue (private communication, February 2017) provides improved removal of stellar contaminants; in addition to 10,013 photometric objects already classified as stars in Laigle et al. (2016), a further 1,231 stars were found using a combination of classification techniques There were also 2,116 galaxies incorrectly labelled as stars in COSMOS2015 (Davidzon et al., 2017). Overall, there is good agreement between the Laigle et al. (2016) and Davidzon et al. (2017) redshifts, however, there is a subsample of objects that moved from $z_{L16} < 1$ to $z_{D17} \sim 3$ because they are now classified as dusty galaxies at high redshift. Other groups of galaxies that changed significantly their redshift had no statistical impact on the analysis of Davidzon et al. (2017). In Sections 4.4.5 and 4.4.6, we use the stellar mass functions calculated from Davidzon et al. (2017).

Due to the range of templates used, the Davidzon et al. (2017) catalogue is not as robust for low-z galaxy properties as the Laigle et al. (2016). Therefore, to combine the low- and high-z optimised catalogs of Laigle et al. (2016) and Davidzon et al. (2017) we adopt the Davidzon et al. (2017) values (such as stellar mass, photometric redshift, and rest-frame colors) for all galaxies with $z_{D17} > 2.5$, and the Laigle et al. (2016) values for all galaxies with $z_{D17} < 2.5$. In this way, we do not double count any galaxies in our sample, however, we note that 18,902 galaxies with $z_{D17} < 2.5$ still have $z_{L16} > 2.5$. Therefore, we are biasing our results towards higher redshifts by adopting the z_{L16} in these cases. 464,672 galaxies have good $z_{phot} > 0$ in both Laigle et al. (2016) and Davidzon et al. (2017) catalogues and 2,078 objects are excluded consistently in both catalogues because they were stars or due to poor photometry.

4.2.3. Sample selection: a stellar-mass complete sample.

For our analysis, we base our redshift bins on those used by Laigle et al. (2016) and Davidzon et al. (2017) to calculate the stellar mass functions in the COSMOS field. Stellar mass bins are chosen in order to have statistically significant numbers of galaxies within each bin (see Figure 4.2).

The K_s band traces stellar mass of galaxies out to $z \sim 4$. At $z > 4$, the K_s band lies blueward of the Balmer break and no longer traces stellar mass and therefore cannot be

used to select a stellar-mass complete sample (Laigle et al., 2016; Davidzon et al., 2017). Between $2.5 < z < 4$, where our SED parameters come from Davidzon et al. (2017), either the K_s or 3.6 μm bands can be used, however, 3.6 μm is preferred due to its tighter relationship to the total stellar mass. For our highest redshift-bin, we only select galaxies detected in the UltraDeep UltraVISTA regions, and use a limiting magnitude cut of 24.0 at 3.6 μm, which represents the 70% completeness level. In order to maximise the number of galaxies in each stack, we use the Deep UltraVISTA limits across the entire UltraVISTA COSMOS region out to $z < 4$. The COSMOS2015 UltraVISTA Deep field has a 3σ depth of $K_s = 24$.

To select a stellar mass-based sample, we apply the following selection criteria:

- $K_s < 24.0$ for $0.2 < z_{phot} < 2.5$,
- $3.6\mu\text{m} < 24.0$ for $2.5 < z_{phot} < 4$, and
- $3.6\mu\text{m} < 25.0$ and FLAG_DEEP $= 1$ for $z_{phot} > 4$.

where the FLAG_DEEP=1 requirement in the COSMOS2015 catalog means that the galaxies are in the UltraDeep UltraVISTA regions.

Stellar mass completeness is calculated empirically across our subsamples, following Laigle et al. (2016). For each galaxy we calculate an estimate of the stellar mass it would need in order to be observed at the magnitude limit (in K_s band for galaxies $z < 2.5$ and at ch1 3.6 μm for galaxies $z > 2.5$: $\log(M_{*\text{lim}}) = \log(M) - 0.4(\mathcal{M}_{*\text{Ks,lim}} - \mathcal{M}_{\text{Ks}})$. We then adopt the stellar mass completeness limit as the the stellar mass limit $M_{*\text{lim}}$ above which 90% of the galaxies lie. Using the 99.7% (70%) limiting magnitudes, $\mathcal{M}_{\text{Ks lim}} = 24$ ($\mathcal{M}_{3.6\mu\text{m,lim}} = 24$) we find limiting masses consistent with Laigle et al. (2016), as shown in Table 4.1. For Sections 4.4.7 and 4.4.8, where different binning schemes are used, mass completeness limits are calculated as stated above.[34]

4.2.4. Spectral and AGN Classifications

The galaxy population is often quoted as being bi-modal, with star-forming galaxies and quiescent galaxies having different sSFR distributions (although see Eales et al. 2018a). The SFMS is observed to be a tight linear relation for star-forming galaxies. However, without a measure for SFR to begin with (obtaining SFRs is the aim of our radio-stacking), then we cannot a-priori separate star-forming and quiescent galaxies using their sSFR distributions. Instead, we rely on galaxy colors to select SFGs. Another concern to be addressed in this section is the uncertain contribution of AGN emission to the radio fluxes used to measure star-formation activity.

Speagle et al. (2014) showed that studies selecting bluer galaxies, such as those using a Lyman Break or $sBzK$ selection, find steeper (linear) SFMS slopes of 0.75-1 than "mixed" studies, such as those using color-color cuts (which tend to find slopes of ~ 0.6), and that studies making no pre-selection for star-forming galaxies find slopes ≤ 0.4. The important dependence of the SFMS on galaxy color selection has also been shown by Karim et al. (2011). In this work, we adopt the color-color selection of Ilbert et al. (2013); quiescent galaxies

[34] Future work will be to use SED modelling to calculate mass completeness limits for different galaxy types using representative SED templates for each type.

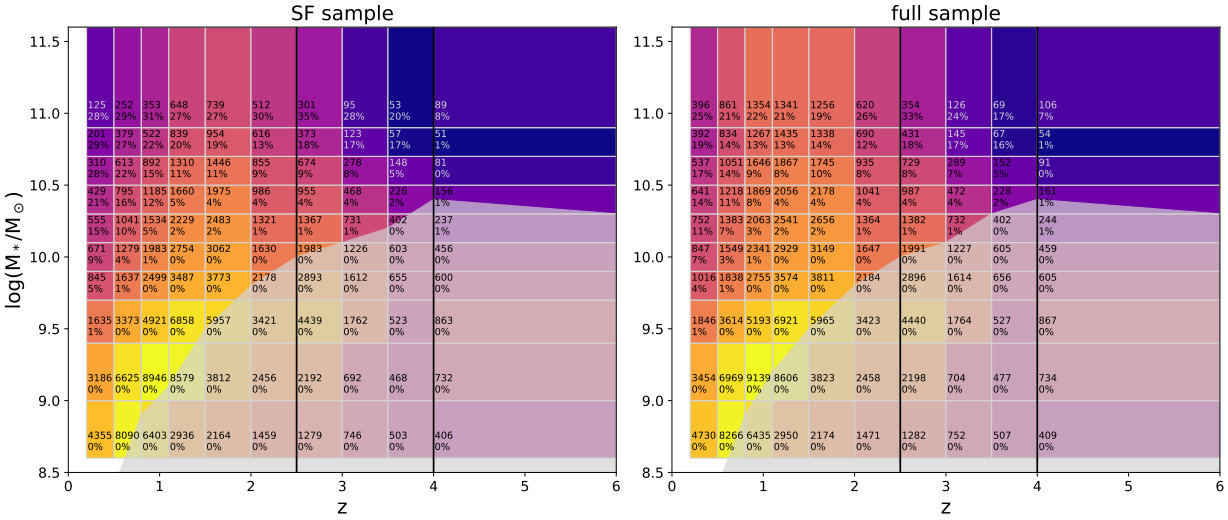

Figure 4.2.: Binning scheme in stellar mass and redshift used for our primary stacking analysis. The colour represents the number of galaxies in the bin (also indicated by the top number in the box) that meet our selection criteria (ranging from 51 to 9,100 galaxies). The left panel shows galaxies classified as star-forming according to their NUVrJ colours and the right panel shows our scheme for all galaxies (both star-forming and quiescent galaxies that meet our magnitude and area cuts). The vertical black lines at z=2.5 and z=4 show where we transition from using the Laigle et al. (2016) catalogue to the Davidzon et al. (2017) catalogue and from selecting galaxies across the full COSMOS field to selecting galaxies from the UltraVISTA Ultra-Deep regions, respectively. The lower number in each bin shows the percentage of galaxies detected in the 5σ VLA-3 GHz catalogue; ranging from ∼30% in the most massive bins to 0% at stellar masses $< 10^{9.6}$ $M_{\odot}$. Regions below the stellar mass-completeness limits from Table 4.1, are shaded grey.

are those with rest-frame $M_{\rm NUV} - M_r > M_r - M_J$ and $M_{NUV} - M_r > 3.1$. The redshift dependent evolution of the distribution of galaxies in this color-color space is presented in Laigle et al. (2016). This method has the advantage of separating dusty star-forming galaxies and quiescent galaxies and done in Laigle et al. (2016), Ilbert et al. (2017) and Davidzon et al. (2017). We want to emphasise that measuring the SFMS depends critically on the sample selection, so we discuss it in further detail in Section 4.4.4, and show our results for the commonly used UVJ selection as well as our NUVrJ selection.

One might expect AGN contamination to be a problem for radio emission due to the fact that there are radio-loud AGN which cannot be easily identified as AGN at other wavelengths. However, these galaxies tend to live in systems with redder colors (Smolčić, 2009; Morić et al., 2010) and should have thus been removed from our star-forming galaxy sample. For our main analysis we only remove galaxies classified as multi-component radio sources in Vardoulaki et al. (2019), which are sources whose radio emission breaks into multiple components (e.g. a radio jet comprised of a core and two radio lobes)[35] In Appendix B.2, we find that our results are not sensitive to AGN removal techniques (including MIR, radio-excess, and X-ray criteria).

[35]Including the 9/57 multi-component galaxies in Vardoulaki et al. (2019) classified as star-forming in our stacks does not change our measurements of median SFRs.

4.2.5. Morphological parameters

Morphological measurements were carried out on HST/Advanced Camera for Surveys (ACS) F814W (I-band) images with a resolution of $\sim 0.15''$ (Koekemoer et al., 2007) to create the Zurich Structure and Morphology Catalog (ZSMC[36]). We have matched the ZSMC, complete down to I $\leq$24 mag, with the COSMOS2015 photometric catalogue of Laigle et al. (2016). Galaxies were classified as "early type", "late type" or "irregular/peculiar" according to the Zurich Estimator of Structural Types algorithm (ZEST; Scarlata et al. 2007). The ZEST algorithm performs a principal component analysis on five non-parametric structural estimators: asymmetry, concentration, Gini coefficient, M_{20}, and ellipticity. Late-type galaxies (ZEST Class=2) were separated into four sub-classes, ranging from bulge-dominated (2.0) to disk-dominated (2.3) systems. The bulginess classification of late-type galaxies was additionally based on Sérsic indices derived from single-component GIM2D fits (Sargent et al., 2007), available for the brightest galaxies I ≤ 22.5.

To study the sSFR of galaxies in different morphology classes, we separate galaxies into four classes, ZEST type =0 (early type), ZEST type = 2.0 or 2.1 (bulge-dominated late type), ZEST-type = 2.2 or 2.3 (disk-dominated late type), and ZEST type = 3 (irregular). Because we only have HST imaging in one band, we are unable to account for morphological k-corrections (colours gradients in galaxies), however, this should not have a significant impact on the classification of galaxy type for $z < 1.5$, where the I-band traces the stellar light. The binning scheme and mass completeness limits are tabulated in Table 4.1.

4.2.6. Environmental parameters

Scoville et al. (2013) probed the large scale structure of the COSMOS field by measuring galaxy surface density in 127 redshift slices between $0.15 < z < 3.0$ using 155,954 K_s band-selected galaxies from the photometric redshift catalogue of Ilbert et al. (2013). These environmental density estimates in the COSMOS field were obtained from the IPAC/IRSA COSMOS archive[37]. We use the Voronoi tessellation results which provide a density estimate for all galaxies because it yields a 2D surface density in each redshift slice. As a proxy for the local environment, we use δ, the density per comoving Mpc^2 at the location of each source with the mean density of the redshift slice subtracted. In Section 4.4.8 we look for variations in sSFR within four local density bins: $-1.5 < \delta < -0.15$, $-0.15 < \delta < 0.15$, $0.15 < \delta < 4$, $4 < \delta < 80$, (where -1.5 Mpc^{-2} and 80 Mpc^{-2} are the minimum and maximum values in the catalog). These bins represent regions of low to high density respectively.

We also investigate the average radio-based SFR properties of galaxies lying inside X-ray groups in the COSMOS field. The primary X-ray galaxy groups catalogues in this field were presented by Finoguenov et al. (2007); George et al. (2011). These catalogues used available X-ray data of Chandra and XMM-Newton with photometric datasets and identified groups with secure redshift out $z = 1.0$.

The sample of X-ray galaxy groups used in this study is selected from two recent catalogues of 247 and 73 groups presented by Gozaliasl et al. (2019) and Gozaliasl et al. in preparation. Gozaliasl et al. (2019) have also revised the X-ray centre and redshift of initial groups

[36]available on IRSA https://irsa.ipac.caltech.edu/data/COSMOS/ tables/morphology/
[37]http://irsa.ipac.caltech.edu/data/COSMOS/

catalogues by combining all X-ray observations of Chandra and XMM-Newton observatories and multi-band photometry of COSMOS2015 (Laigle et al., 2016) and the master catalogue of spectroscopic redshifts of COSMOS (Salvato et al. in preparation). The X-Ray emission peak/centre of groups are determined with an accuracy of $\sim 5''$, using the smaller scale emission, detected by high-resolution Chandra imaging. The new X-ray groups consist of a mass range of $M_{200c} = 8{\times}10^{12}$ to 3×10^{14} $M_\odot$ with a secure redshift range of $0.08 < z < 1.53$. M_{200c} is the total mass of groups which is determined using the scaling relation $L_X - M_{200c}$ with a weak lensing mass calibration as presented by Leauthaud et al. (2010). For the full details of groups identification and their properties, we refer readers to Gozaliasl et al. (2019).

For the purpose of our study, we focus on one particular redshift bin (highlighted with magenta area), $0.64 < z < 0.88$, including 73 groups with $M_{200c} = 10^{12}$ to 2.5×10^{14} $M_\odot$ where a full range of environments are present within the COSMOS field (see Fig. B.9 in the Appendix). Altogether, 57 out of 73 groups have been assigned a secure spectroscopic redshift.

X-ray group members within R_{200c} from the group X-ray centroid are identified using the COSMOS2015 photometric redshift catalogue, with a redshift that agrees with that of the hosting group with a redshift precision of $\pm 0.01(1 + z_{spec})$. We note that $\sim 31\%$ of the group galaxies consist of spectroscopic redshifts. For our analysis, we stacked separately X-ray group members of halos with $M_{200} > 10^{12}\,M_\odot$ and members of haloes $M_{200} > 10^{14}\,M_\odot$ (members of the most massive halos will be in both stacks). Galaxies not in X-ray groups were stacked separately to provide a field comparison sample.

Table 4.1.: Summary of binning schemes (in redshift) and stellar mass above which our parent samples (star forming galaxies only and all galaxies) are 90% complete.

Redshift	SFGs: $\log\left(\frac{M_{\rm lim}}{\rm M_\odot}\right)$	All: $\log\left(\frac{M_{\rm lim}}{\rm M_\odot}\right)$
Main sample		
0.2-0.5	8.4	8.4
0.5-0.8	8.9	8.9
0.8-1.1	9.1	9.2
1.1-1.5	9.5	9.5
1.5-2.0	9.8	9.8
2.0-2.5	10.0	10.0
2.5-3.0[a]	10.1	10.1
3.0-3.5	10.2	10.3
3.5-4.0	10.4	10.4
4.0-6.0[b]	10.3	10.3
Morphology subsample		
0.3-0.6	8.6	8.7
0.6-0.9	9.0	9.2
0.9-1.2	9.2	9.3
1.2-1.5	9.5	9.6
Local density subsample		
0.2-0.6	8.5	8.6
0.6-0.9	9.0	9.1
0.9-1.2	9.2	9.3
1.2-1.5	9.5	9.5
1.5-2.0	9.8	9.8
2.0-3.0	10.1	10.1
X-ray catalog subsample[c]		
0.64-0.88	9.1	9.2

[a] Above $z > 2.5$ we use the 3.6 μm flux to calculate mass completeness. [b] Ultra Deep UltraVISTA fields only. [c] Calculated for all galaxies in X-ray groups.

4.3. Methods: radio stacking, flux measurement, and SFR calculation

We summarize our stacking workflow here and will justify the choices made in Appendix B.1. In principle, stacking is a straightforward process, but in practice, there are many subtleties which we discuss here and in Appendix B.1.

1. First, an input list of coordinates is created for the $N_{\rm objs}$ galaxies to be stacked, taking into consideration the selection criteria and positional offsets described in the previous section.

2. Using the stacking routine developed by Karim et al. (2011)[38], we create $40'' \times 40''$ (8000×8000 pixels) cutouts of the 3 GHz image, centered on the input position of each

[38] We have verified the performance of the routine by inserting artificial Gaussian sources into the 3 GHz map and recovering the stacked images.

galaxy. The cutouts are saved together as a data-cube of size $N_{\rm objs} \times 8000 \times 8000$. The stacking routine also calculates the median image of the cutouts and saves the central pixel value (which should be the peak flux) and the RMS, that we use for initial conditions in the subsequent step.

3. To calculate the total flux, we fit a 2D Gaussian function to the median image[39]. We input initial conditions for the fit using the peak flux from the stacking routine and the beam size.

4. To estimate the uncertainty on the total flux, we perform a bootstrap analysis. This involves randomly drawing, with replacement, $N_{\rm objs}$ galaxy cutouts (from our initial list of galaxies) and creating a new median stack. We then record the total flux on each resulting stack and repeat the process 1,000 times. We record the 5th, 16th, 50th, 84th, and 95th percentiles of the total fluxes (Tables 4 and 5 show the 5th and 95th percentile as the lower and upper errors.).

5. We follow Schreiber et al. (2015)'s scatter-stacking technique and measure the flux dispersion for our stacks by calculating the median absolute deviation (MAD) for each pixel location using the ASTROPY function MAD. We measure the MAD values using an aperture with radius $0.75''$ for our bootstrapped samples and report the median and confidence limits as done for the total fluxes.

A note on total fluxes: Point sources can be described entirely by their peak cleaned flux, which, if the optical and radio centres are aligned, should correspond to the central pixel in each cutout. Galaxies in the 3 GHz image are not just point sources, and so we have to take into account the source extent. Indeed, Bondi et al. (2018) found 77% of star-forming galaxies are resolved in the VLA-3 GHz LP. Jiménez-Andrade et al. (2019) show that the physical size of the 3 GHz component is 1-2 kpc in star-forming galaxies and is relatively constant with stellar mass and evolves shallowly with redshift. Astrometric uncertainty plays a role in the determination of total flux and is a second key reason why the peak flux from the stack cannot be used to represent the total flux. Jittering of sources due to astrometric offsets between the optical catalogue and the true 3 GHz source position causes an effective blurring of the stacked image. For sources in the 5σ VLA catalogue, the difference between the 3 GHz and COSMOS2015 positions have a spread of $\sigma = 0.1''$ (after correcting for the systematic offset; Smolčić et al. 2017a), which is half the size of a pixel. We discuss more details about stacking radio interferometric images and compare different methods to calculate total flux in Appendix B.1.

4.3.1. Radio SFR calibration

The most commonly used radio SFR calibrations are bootstrapped from the empirical IR-radio correlation. For our results we have adopted a SFR calibration based on the IR-radio correlation determined by Magnelli et al. (2015), and a radio spectral index[40] of $\alpha = -0.8$

[39] We discuss the advantages and disadvantages of a median and mean stacking in Appendix B.1.2

[40] $S_\nu \propto \nu^\alpha$

unless stated otherwise. The following explains how we convert observed flux at 3 GHz to a SFR.

Observed 3 GHz fluxes ($S_{3\mathrm{GHz}}$; W Hz^{-1} m^{-2}) are converted to rest-frame 1.4 GHz luminosities ($L_{1.4\mathrm{GHz}}$; W Hz^{-1}) because the infrared-radio correlation is traditionally calibrated at 1.4 GHz, via:

$$L_{1.4\mathrm{GHz}} = \frac{4\pi D_L^2}{(1+z)^{\alpha+1}} \left(\frac{1.4\mathbf{GHz}}{3\mathbf{GHz}}\right)^{\alpha} S_{3\mathrm{GHz}}, \tag{4.3}$$

where D_L is the luminosity distance to the galaxy in meters and α is the spectral index. It is standard in the literature to assume a single spectral index for the radio spectral energy distribution (SED; usually taken to be $\alpha = -0.7$ or $\alpha = -0.8$). The spread in spectral indices is usually observed to be $\sigma = 0.35$ (e.g., Smolčić et al. 2017b) and the uncertainty of the spectral index can induce significant errors in the derived radio luminosity for a single object. However, on a statistical basis, the symmetry of the spread is expected to cancel out the variations, typically yielding a valid average luminosity for the given population (see Novak et al. 2017; Delhaize et al. 2017; Smolčić et al. 2017a for more specific discussions on this).

The linear relation between the radio and total infrared (TIR) luminosities of star-forming galaxies is assumed to arise because both emissions depend on the recent massive star formation (e.g., Condon 1992; Yun et al. 2001; Bell 2003; Lacki et al. 2010). Helou et al. (1985) first introduced the commonly used parameter q, the ratio of infrared-to-radio flux:

$$q_{\mathrm{TIR}} = \log\left(\frac{L_{\mathrm{TIR}}}{3.75\times10^{12}\mathrm{Hz}}\right) - \log\left(\frac{L_{1.4\mathrm{GHz}}}{\mathrm{W\ Hz^{-1}}}\right). \tag{4.4}$$

The infrared-to-radio ratio q has been observed to decrease with redshift, (Magnelli et al. 2015, Delhaize et al. 2017, Seymour et al. 2009, Ivison et al. 2010a, Ivison et al. 2010b, Basu et al. 2015, and Calistro Rivera et al. 2017; but we note some studies have found no significant evolution e.g. Garrett 2002; Appleton et al. 2004; Sargent et al. 2010). The reason for this observed evolution is currently unclear, however, evolution in the SFR surface density, selection effects, and the presence of radio AGN in bulge-dominated galaxies have been suggested as possible explanations (Magnelli et al., 2015; Molnár et al., 2018).

Finally, we derive SFRs using the total infrared calibration in Kennicutt & Evans (2012). In Figure 4.3 we compare the IR and radio SFRs from IR and radio stacks to test the consistencies of different IR-radio correlations, namely, Bell (2003), Delhaize et al. (2017) (using the fit that excludes any radio-excess sources), Molnár et al. (2018) (using the fit for disk-dominated galaxies). The IR luminosities were derived from fitting Draine & Li (2007b) templates to stacked *Herschel* data, following Magnelli et al. (2015), the 1.4 GHz radio fluxes are from Karim et al. (2011), and the 3 GHz fluxes are calculated following the method described in Section B.1.1. We use the same 3.6 μm-selected star-forming parent samples from Karim et al. (2011) for the comparison.

Based on the trends and scatter seen in Figure 4.3, we choose to adopt the evolution of Magnelli et al. (2015):

$$q_{\mathrm{TIR}}(z) = (\log(1.91) + (2.35 \pm 0.08)) \times (1+z)^{-0.12\pm0.04}, \tag{4.5}$$

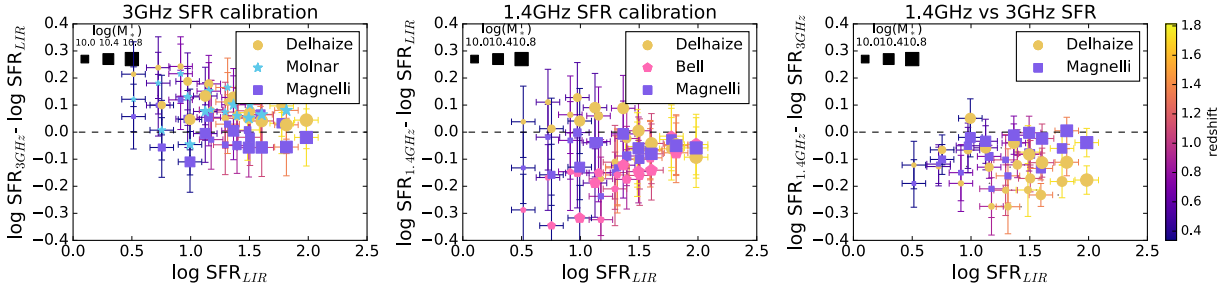

Figure 4.3.: Comparison of infrared and radio SFRs using different SFR (or $q_{\rm TIR}$) calibrations (described in Section 4.3.1). Star-forming galaxies from Karim et al. (2011) were median stacked in bins of stellar mass and redshift at the five *Herschel* wavelengths to estimate the total IR luminosity. The size of symbols represents the average stellar mass of the stack. The colour of the error bars represents the redshift as indicated in the colour bar on the right-hand side. Purple squares correspond to radio-SFRs calculated following the $q_{\rm TIR}$ evolution from the stacking analysis of Magnelli et al. (2015) and $\alpha = -0.8$. Amber circles show SFRs calculated assuming the Delhaize et al. (2017) $q_{\rm TIR}$ evolution with $\alpha = -0.7$. *Left:* Comparison of 3 GHz and IR SFRs. Blue stars correspond to the 3 GHz-SFR that relies on the $q_{\rm TIR}$ evolution for pure disk galaxies in Molnár et al. (2018). *Center:* Comparison of 1.4 GHz and IR SFRs. Pink hexagons show the 1.4 GHz SFR calibration of Bell (2003) used in Karim et al. (2011). There is increased scatter between the calibrations for galaxies of lower stellar mass. *Right:* Comparison of the 1.4 GHz and 3 GHz SFRs as a function of IR-SFR. We find that the Magnelli et al. (2015) calibration provides 1.4 GHz and 3 GHz SFRs that do not have a luminosity (or redshift) dependent $\rm SFR_{1.4GHz}/SFR_{IR}$ ratio.

where we have converted FIR to TIR using the average multiplicative value $1.91^{+0.10}_{-0.05}$ found by Magnelli et al. (2015). This calibration was derived from stacking analysis and confirmed that q does not depend significantly on the position from the SFMS, and nor does the radio-spectral index. Magnelli et al. (2015) found a spectral index from stacked 1.4 GHz and 610 MHz flux densities to be consistent with $\alpha = -0.8$ in all bins. Their sample was complete to $M_* > 10^{10} M_\odot$ and $z < 2.3$. We found, in comparison, that Delhaize et al. (2017) SFR calibration gives a $\rm SFR_{3\,GHz}/SFR_{IR}$ that is dependent on luminosity (or redshift). For these calculations, we have assumed $\alpha = -0.7$ to be consistent with their median α. Similarly, the Bell (2003) calibration, for which we have assumed $\alpha = -0.8$, produces a luminosity-dependent result. Discussing the details behind the various radio-infrared calibrations will be the subject of future work (e.g., Molnar et al. in prep.). We also note the above SFR calibrations have not been tested on quiescent galaxies, therefore our SFR measurements for "all" galaxies must be taken with caution.

4.4. Results

4.4.1. SFR – M_* relation for star-forming galaxies

In this section, we present our measurement of the SFMS relation and discuss its functional form. Measurements for median redshift, peak 3 GHz flux, total flux, and SFR are given in Tables at the end of this Chapter for stacks of star-forming and all galaxies. The SFMS

derived from these data is shown in Figure 4.4.

Star-forming galaxies show a positive correlation between SFR and stellar mass at all redshifts. As expected, the SFRs of "all" galaxies agree well with "SFGs" (star-forming galaxies) at lower masses where most galaxies are classified as star-forming galaxys (SFGs), but disagree at higher masses. Including quiescent galaxies in the sample of all galaxies results in a flatter SFR – M_* relation at $z < 1.5$ for $\log(M_*/\mathbf{M}_\odot) > 9.2$. A less-extreme flattening is also present in the star-forming galaxy sample at low-z for high masses.

4.4.2. The functional form of the SFMS across redshift

How should we define the SFMS? Is there a definition that gives a natural insight into the physical processes involved, or one that makes it the most straight-forward to conduct inter-sample studies? Renzini & Peng (2015) suggested the SFMS should be defined as the ridge-line of the star-forming peak in a 3D SFR – M_*–number plane, and similar definitions have been adopted by, e.g., Hahn et al. (2019) and Magnelli et al. (2014). Naturally, this method requires robust SFR, M_* measurements for large numbers of galaxies, and the SFRs of passive galaxies are highly uncertain. At the high-mass end in the local Universe, $M_* > 10^{11}\,\mathrm{M}_\odot$ there are very few star-forming galaxies and their SFRs are highly uncertain, and depend sensitively on the SFR calibration used (Popesso et al., 2019); these galaxies are critical for determining the flattening of the SFMS. As previously mentioned, many studies find star-forming galaxies follow a log-normal SFR distribution at a fixed stellar mass (Popesso et al., 2019). In this case, the mode and the median of the SFR should follow each other, but the mean SFR will be higher than the median. For a log-normal SFR distribution, our median SFMS should be more consistent with the definition proposed by Renzini & Peng (2015) than if we had performed mean stacking.

The appropriate form of the SFMS depends on the stellar mass range under consideration. Using the deep GOODSs fields in addition to the COSMOS field allowed Whitaker et al. (2014) to constrain the steeper lower-mass end ($\log(M_*/\mathrm{M}_\odot) < 10.0$) of the SFMS. To combine the steep low and shallow high mass relations, a turn-over is required (see also Bisigello et al. 2018). In this section, we are concerned with how to best represent the SFR – M_* relation given by our data. First, we fit the SFMS relation at each redshift bin comparing a power-law and the Lee et al. (2015) "turn-over" model. Then, we discuss different functional forms that take both stellar mass and redshift as independent variables. For readability, we will omit units in the equations of this section, but all SFRs have units of $\mathrm{M}_\odot\mathrm{yr}^{-1}$, and stellar mass is denoted M_* with units of $\mathrm{M}_\odot$.

We fit models to the data using SCIPY's OPTIMIZE.CURVE_FIT that uses the Levenberg-Marquardt least squares algorithm, and only consider mass-complete data (opaque points in Figure 4.4). To estimate the parameter uncertainties we resample the data, varying the stellar mass, SFR and redshift values of each stack by a random amount that follows an asymmetric Gaussian distribution with σs given by our upper and lower errors. The SFR error comes from the flux error (of our bootstrapping analysis) and for this, we have assumed that the errors follow a normal distribution in flux. The σ for stellar mass and redshift values come from the standard deviations of stellar masses and redshifts of galaxies within the bin. We have resampled the data with replacement 50,000 times (or 10,000 times per redshift slice for our first experiment) and recorded the best-fit (from least squares) for each new

sample. The median, 16th and 84th percentile from all our runs are reported for the model parameters.

For the best fits, we report reduced χ^2, which is the weighted sum of the squared deviations in log(SFR) per degree of freedom (number of observations minus the number of fitted parameters). A $\chi^2_r > 1$ indicates that the fit has not fully captured the data or that the error variance has been underestimated and a $\chi^2_r < 1$ indicates the model is over-fitting the data or the error variance has been overestimated.

Table 4.2 gives the results of fitting the log(SFR)-log(M_*) relation for individual redshift slices (out to $z = 2$, where we have enough data in each bin to constrain a 3 parameter model) using a linear form:

$$\log(SFR) = a_1 \log(M_*/10^9) + a_2 \tag{4.6}$$

and the Lee et al. (2015) form:

$$\log(\mathrm{SFR}) = S_0 - \log\left(1 + \left(\frac{10^M}{10^{M_0}}\right)^{-\gamma}\right), \tag{4.7}$$

where M is $\log(M_*/\mathrm{M}_\odot)$, γ is the power-law slope at lower stellar masses, and S_o is the maximum value of log(SFR) approached at higher stellar masses.

To compare the relative quality of different models we have computed the Akike Information Criterion (AIC):

$$\mathrm{AIC} = 2k - 2\ln\left(\sum_n \frac{(\log(\mathrm{SFR}) - \widehat{\log(\mathrm{SFR})})^2}{n}\right), \tag{4.8}$$

where $\widehat{\log(SFR)}$ is the predicted value, n is the number of observations, and k is the number of parameters estimated by the model plus the constant variance of the errors. The preferred model is the one with the minimum AIC. We also report a second definition of the AIC, with a correction for small sample sizes that addresses the tendency for overfitting (selecting a model with too many parameters) that often occurs for small sample sizes (e.g. Cavanaugh & Shumway 1997; Hurvich & Tsai 1989),

$$\mathrm{AICc} = 2k - 2\ln\left(\sum_n \frac{(\log(\mathrm{SFR}) - \widehat{\log(\mathrm{SFR})})^2}{n}\right) + \frac{2k^2 + 2k}{n - k - 1}, \tag{4.9}$$

The AIC does not give information on the absolute quality of the model, but rather only the quality of a model relative to other models. Only differences in AIC are meaningful; we interpret ΔAIC>2 to be evidence against the model with the higher AIC, > 6 to be strong evidence and > 10 to be very strong evidence against the model with the higher AIC (or strong evidence for preferring the model with the lower AIC).

In general, the bent SFMS produces more favourable reduced χ^2 (closest to 1), there is very strong evidence from the AIC that a bent SFMS relation is preferred to a linear relation at $z < 1.1$, and strong evidence at $1.1 < z < 1.5$ as well. Using the AIC criteria based on Eq 4.8 (rather than Eq. 4.9) implies that the linear form is preferred at $z > 1.1$. This is likely

due to our smaller number of mass-complete measurements that do not probe the low-mass regime at higher redshift. These results are consistent with Lee et al. (2018), who found that the SFMS can be described by a simple linear relation in $\log(M_*)$ and $\log(\mathrm{SFR})$ at $z > 2$, whereas, below $z \sim 1.5$, there is a statistically significant flattening at high stellar masses.

It is most convenient to provide a functional form that takes stellar mass and redshift as independent parameters and returns a SFR. Next, we will fit our data with functional forms adopted in the literature that allow this. Looking at the fitted parameters of the Lee et al. (2015) form in Table 4.2, it is clear that S_0 and M_0 increase with redshift (M_0 evolution is illustrated in Figure 4.9). The low-mass slope also monotonically decreases over the redshift range probed. We took this into consideration when developing a new parameterisation (Eq 4.13).

The simplest functional form adopted in the literature is that of a linear relationship between $\log(\mathrm{SFR})$ and $\log(M_*)$. Speagle et al. (2014) compiled 25 studies from the literature and fitted the following linear form to the SFMS that allows for evolution of both the slope and normalisation[41]:

$$\log(\mathbf{SFR}) = (a_1 - a_2 t)\log(M_*) - (a_3 - a_4 t), \tag{4.10}$$

where t is the age of the Universe in Gyr. We have fit this functional form to our data and report the best fitting parameters $\Theta = (a_1, a_2, a_3, a_4)$ in Table 4.3. This form performs poorly for our low redshift ($z < 1$) data, but matches our high-z data well.

Figure 4.4 shows that below $z < 1$, a flattening in the SFMS is observed in our sample, therefore we would like to fit a functional form that allows this. The following functional forms allow for a flattening at high-masses in the SFMS. We have investigated fitting the functional form used by Schreiber et al. (2015), namely:

$$\log(\mathbf{SFR}) = m - m_0 + a_0 r - a_1[\max(0, m - m_1 - a_2 r)]^2 \tag{4.11}$$

where $r = \log(1+z)$ and $m = \log(M/10^9)$. This relation constrains the low-mass slope by assuming a constant sSFR (i.e. a low-mass slope of 1). The posterior distribution of these parameters is not smoothly distributed. To produce reasonable constraints on our parameters, we added the following bounds: $a_0 > 0$, $a_1 > 0$, and $a_2 > 0$ and $-3 < m_1 < 12$ [42].

Tomczak et al. (2016) fit the Lee et al. (2015) function with a quadratic evolution of parameters with redshift:

$$\begin{aligned} \log(\mathbf{SFR}) &= S_0' - \log\left(1 + \left(\frac{M_*}{10^{M_0'}}\right)^{-\gamma}\right), \\ S_0' &= s_0 + a_1 z - a_2 z^2 \\ M_0' &= m_0 + a_3 z - a_4 z^2 \\ \gamma &= 1.091 \end{aligned} \tag{4.12}$$

[41] Although most studies agree that the slope remains relatively constant over time e.g. Wuyts et al. (2011a).

[42] For this case, the "Trust Region Reflective" algorithm, was used for optimization in SCIPY.OPTIMIZE.

Tomczak et al. (2016) (and Lee et al. (2018)) also found that the turnover mass increases with redshift.

We cannot constrain the low-mass slope at high redshifts due to the mass completeness limitations imposed by the current COSMOS data (Table 4.1). Recent simulations observe a constant log(sSFR) at low stellar masses ($< 10^{9.5}\,\mathrm{M}_\odot$, out to $z \sim 5$ (e.g. Torrey et al. (2018); Matthee & Schaye (2019), see also Iyer et al. (2018) for low-mass slope constraints based on star-formation histories reconstructed from observations), supporting observational works that fix the low-mass power-law slope to one (e.g. Schreiber et al. 2015). Our stacking results show values of $\gamma > 1$ at low redshift, with γ becoming less steep at higher redshift.

Here, we introduce a new form inspired by Lee et al. (2015):

$$\begin{aligned} \log(\mathrm{SFR}) &= S_o + a_1 r - \log\left(1 + \left(\frac{10^M}{10^{M_t'}}\right)^{-\gamma'}\right), \\ M_t' &= M_0 + a_2 r, \\ \gamma' &= (1 + e^{-a_3 r}), \end{aligned} \tag{4.13}$$

where M is $\log(M_*/\mathrm{M}_\odot)$. Our new parametrisation takes into account the evolution of the normalization ($S_0 + a_1 r$), turn-over mass (M_t'), and a low-mass slope (γ') that starts steeper than and approaches 1 at high redshift. The choice of redshift or time evolution, e.g. z, $\log(1+z)$ or t, plays an important role in the number of parameters required for a good fit. After some experimentation, we adopt $r = \log(1+z)$.

The best fit (medians) are shown in Figure 4.4. $(s_0, m_0, a_1, a_2, a_3) = (0.38^{+0.14}_{-0.12}, 9.28^{+0.19}_{-0.16}, 4.49^{+0.49}_{-0.56}, 3.70^{+0.64}_{-0.76}, 7.71^{+3.32}_{-1.99})$. The best fit parameter distributions are also shown in Figure 4.5. The reduced χ^2 is highest for the linear model, and lowest (closest to one) for the model proposed in this work (Eq. 4.13). When considering all galaxies the models with a high-mass flattening (or turn-over) are more strongly preferred than when only considering the star-forming sample. For the remainder of this work, we adopt our results using Equation 4.13 unless stated otherwise.

Missing in our description of the SFMS for star-forming galaxies is the fact that there is a population of galaxies that lie above the SFMS, starburst galaxies. Bisigello et al. (2018) finds that the multi-Gaussian decomposition reveals the presence of a starburst population which increases towards low stellar masses and high redshifts and has a steeper slope than the SFMS (almost 1). But other studies such as Schreiber et al. (2015) and Sargent et al. (2012) find that the fraction of starburst galaxies is constant with redshift (to within a factor of 2). However, the number of starburst galaxies that lie above the SFMS is small, and should not drastically affect our median SFR results.

At all epochs, the most massive galaxies have the lowest sSFR. For galaxies following the functional form proposed in this work, the sSFRs are highly consistent across stellar mass at high redshift (where the slope of the SFMS approaches 1), and become more divergent towards the present time, with massive galaxies evolving faster, decreasing their sSFR. Figure 4.6 shows how our form compares with the canonical Speagle et al. (2014) SFMS at four different mass bins. The Speagle et al. (2014) SFMS follows our data better for high mass galaxies at $z > 3$.

Davidzon et al. (2018) used the differential evolution of the galaxy stellar mass function

Table 4.2.: Linear (Eq 4.6) and non-linear (Eq 4.7 from Lee et al. (2015)) SFMS models fit to mass-complete data at $z < 2$. ΔAIC is $\mathrm{AIC_{linear}}$-$\mathrm{AIC_{Lee}}$ calculated using Equation 4.8. ΔAICc was calculated without the second term for penalising models with more parameters when there is a low number of data points. The larger the positive difference, the more the Lee et al. form is preferred. The more negative ΔAIC, the more the linear form is preferred.

Redshift	Linear form (a_1, a_2)	χ^2_r	Lee form (S_0, M_0, γ)	χ^2_r	ΔAIC	ΔAICc
$0.2 < z < 0.5$	$(0.57^{+0.11}_{-0.14}, -0.02^{+0.20}_{-0.14})$	8.54	$(0.94^{+0.09}_{-0.07}, 9.88^{+0.26}_{-0.20}, -1.15^{+0.34}_{-0.32})$	1.15	13.7	17.7
$0.5 < z < 0.8$	$(0.59^{+0.10}_{-0.11}, 0.33^{+0.16}_{-0.12})$	10.1	$(1.43^{+0.07}_{-0.06}, 10.18^{+0.19}_{-0.13}, -1.11^{+0.22}_{-0.20})$	0.41	15.5	21.5
$0.8 < z < 1.1$	$(0.73^{+0.09}_{-0.13}, 0.33^{+0.19}_{-0.11})$	15.8	$(1.71^{+0.13}_{-0.16}, 10.35^{+0.31}_{-0.25}, -1.14^{+0.33}_{-0.17})$	3.04	5.9	11.9
$1.1 < z < 1.5$	$(0.71^{+0.06}_{-0.06}, 0.53^{+0.10}_{-0.07})$	10.2	$(1.97^{+0.10}_{-0.05}, 10.53^{+0.21}_{-15.5}, -1.06^{+0.31}_{-0.16})$	3.06	-0.4	6.6
$1.5 < z < 2.0$	$(0.63^{+0.06}_{-0.11}, 0.82^{+0.19}_{-0.11})$	6.1	$(2.18^{+0.90}_{-0.27}, 10.63^{+11.3}_{-0.41}, -1.02^{+0.47}_{-0.59})$	5.28	-27.5	0.5

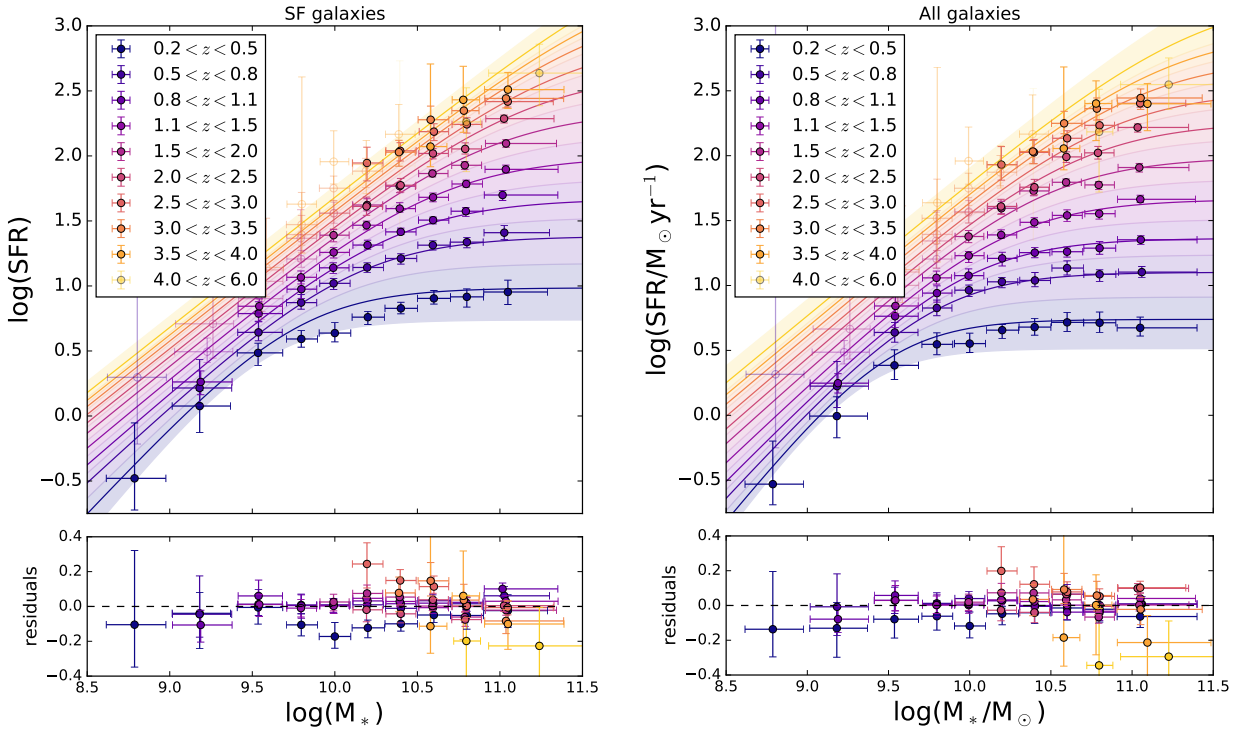

Figure 4.4.: Galaxy radio SFR – stellar mass relation. Left: SF-galaxies, Right: All galaxies. We show errors (2σ) on the median SFR from our bootstrapping analysis of the stacked fluxes. The error bars in the x-direction show the 2σ variation of stellar masses within each redshift bin. Only stellar mass complete bins (shown as opaque circles) are used for the fitting. Bins suffering from mass incompleteness are shown as transparent symbols. We parametrize the relation according to Eq. 4.13, allowing for a turn-over at high stellar masses. The solid line shows the relation at the median galaxy redshift across each redshift bin, and the shaded areas show the evolution of the SFMS over the redshift bin. Bottom panels show residuals measured as log(SFR) - model log(SFR).

Table 4.3.: SFMS model fits to all mass-complete data simultaneously.

SFMS form ($\mathscr{M}$)	parameters (Θ)	best fit values	χ^2_r
SF, Speagle et al. (2014), Eq 4.10	(a_1, a_2, a_3, a_4)	$(0.787^{+0.115}_{-0.114}, 0.021^{+0.020}_{-0.019}, 5.91^{+1.21}_{-1.22}, 0.060^{+0.211}_{-0.198})$	7.7
SF, Schreiber et al. (2015), Eq 4.11	$(m_0, a_0, a_1, m_1, a_2)$	$(0.149^{+0.167}_{-0.443}, 1.116^{+0.506}_{-0.748}, 0.258^{+0.098}_{-0.159}, -0.361^{+0.623}_{-2.24}, 3.22^{+2.67}_{-1.78})$	4.1
SF, Tomczak et al. (2016), Eq 4.12	$(s_0, m_0, a_1, a_2, a_3, a_4)$	$(0.655^{+0.158}_{-0.131}, 9.819^{+0.262}_{-0.229}, 1.295^{+0.211}_{-0.209}, 0.177^{+0.055}_{-0.044}, 0.840^{+0.320}_{-0.330}, 0.117^{+0.081}_{-0.067})$	4.9
SF, This work, Eq 4.13	$(s_0, m_0, a_1, a_2, a_3)$	$(0.383^{+0.135}_{-0.119}, 9.280^{+0.193}_{-0.163}, 4.490^{+0.494}_{-0.559}, 3.699^{+0.636}_{-0.762}, 7.714^{+3.316}_{-1.989})$	3.8
All, Speagle et al. (2014) Eq 4.10	(a_1, a_2, a_3, a_4)	$(0.699^{+0.135}_{-0.128}, 0.027^{+0.025}_{-0.021}, 4.95^{+1.43}_{-1.37}, 0.103^{+0.264}_{-0.222})$	14.4
All, Schreiber et al. (2015), Eq 4.11	$(m_0, a_0, a_1, m_1, a_2)$	$(0.257^{+0.162}_{-0.206}, 1.354^{+0.522}_{-0.485}, 0.365^{+0.080}_{-0.089}, -0.132^{+0.362}_{-0.536}, 2.410^{+1.08}_{-1.12})$	4.0
All, Tomczak et al. (2016), Eq 4.12	$(s_0, m_0, a_1, a_2, a_3, a_4)$	$(0.425^{+0.112}_{-0.103}.9.656^{+0.227}_{-0.237}, 1.198^{+0.150}_{-0.145}, 0.147^{+0.043}_{-0.037}, 0.619^{+0.299}_{-0.281}, 0.0601^{+0.080}_{-0.065})$	3.8
All, This work, Eq 4.13	$(s_0, m_0, a_1, a_2, a_3)$	$(0.189^{+0.117}_{-0.109}, 9.086^{+0.184}_{-0.186}, 4.100^{+0.507}_{-0.518}, 3.103^{+0.841}_{-0.0811}, 4.618^{+2.847}_{-2.842}$	3.1

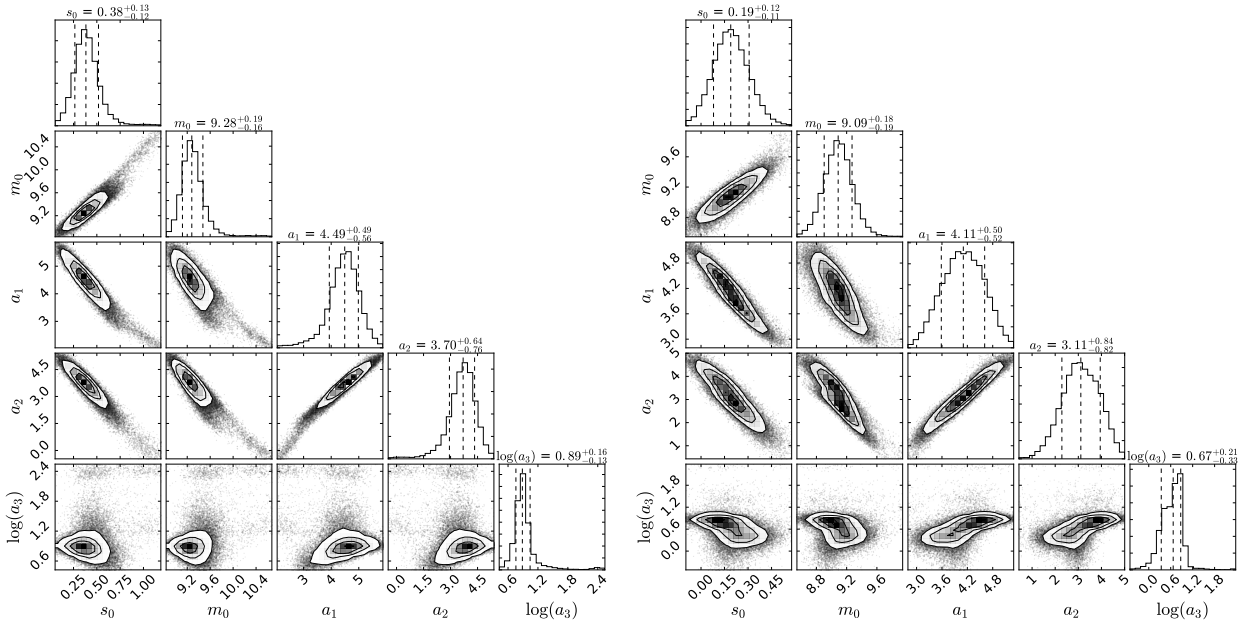

Figure 4.5.: The one and two dimensional projections of the margianalized posterior probability distributions of parameters in our model (Eq. 4.13) from our resampling. Left: Results fitting the model to star-forming galaxies. Right: Results for all galaxies. Medians and widths of the marginalised distribution for each parameter are given above the histograms of each parameter and are also reported in Table 4.3.

to infer the sSFR evolution of galaxies. Using the stellar mass functions from Davidzon et al. (2017) and Grazian et al. (2015) (for $z > 4$), they report a shallow evolution of the sSFR $\sim (1+z)^{1.1}$ at $z > 2$ consistent with e.g., Tasca et al. (2015). We also show the results from Davidzon et al. (2018) in Figure 4.6 for their lowest and highest stellar mass bins, $\log(M_*/\mathrm{M}_\odot)$=10.3, and 11 respectively. The evolution with redshift matches well the evolution seen in our data, however, our sSFRs are systematically higher by a factor of ~ 0.4 dex (although our results are consistent within the large error bars). The origin of this offset requires further investigation, although we will discuss the effect of different SFR calibrations in Section 4.4.6.

4.4.3. Scatter

The scatter of the SFMS can reveal the stochasticity in galaxy star formation efficiency and gas accretion history (Leitner, 2012; Behroozi et al., 2013; Tacchella et al., 2016; Mitra et al., 2017). For example, individual galaxies are expected to move above and below the average SFMS relation if gas is funnelled to the centre triggering star formation and then depleted (Tacchella et al., 2016). Observationally, the measured scatter should depend on the SFR indicator chosen. Instantaneous SFR tracers such as nebular emission lines return higher σ than tracers that are sensitive to longer timescales because they are sensitive to rapid variations in the star-formation histories (Davies et al., 2016; Caplar & Tacchella, 2019).

We follow the method of Schreiber et al. (2015) to measure the flux dispersion for our stacks. As well as calculating the median image for each set of galaxy positions, we also

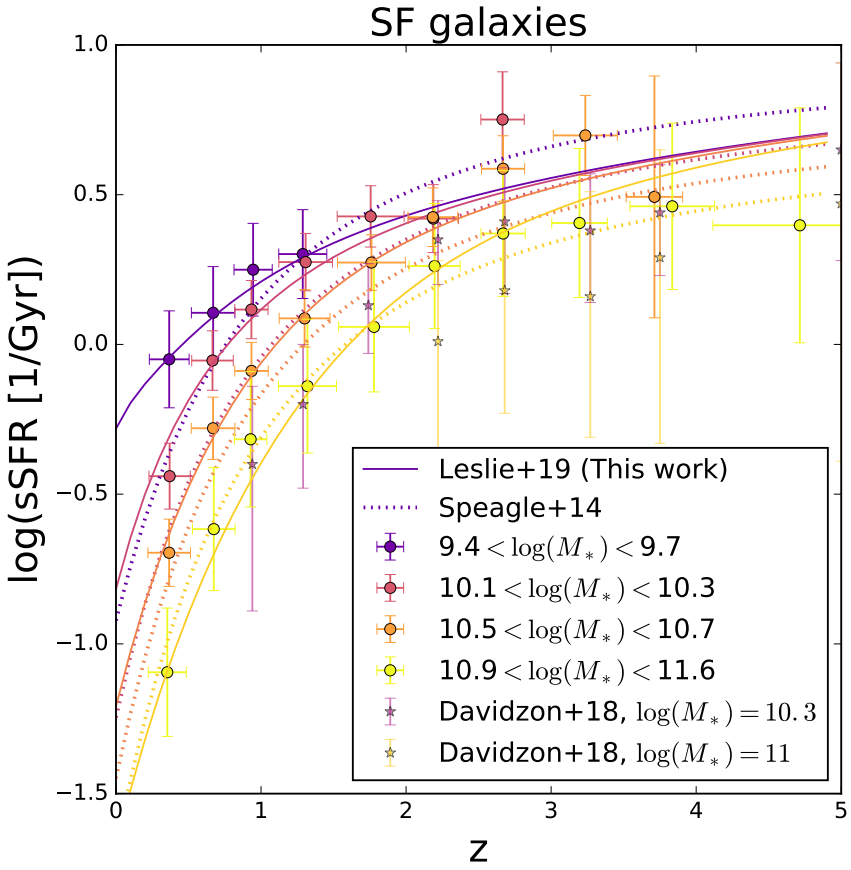

Figure 4.6.: Evolution of sSFR for galaxies at four stellar masses. Solid lines show the best fit of Equation 4.13. The Speagle et al. (2014) SFMS, converted to our Chabrier (2003) IMF, is shown in dotted lines for comparison. Only four stellar mass bins are shown for clarity, and data-points indicate redshifts where the COSMOS sample is complete. Our data and fitted SFMS is particularly different from the Speagle et al. (2014) SFMS at the low and high-mass ends, where our functional form results in a shallower and steeper evolution in sSFR than the Speagle et al. (2014) MS, respectively.

compute the dispersion image by computing the median absolute deviation (MAD) of the flux densities. The scatter around the median value at the source location will be caused by flux variations of the stacked population. We determine $\sigma_{\rm SFR}$ by creating SFR stacks; i.e. calculating 3 GHz SFR cubes using the photometric redshift of each individual galaxy. To take into account smearing due to evolution within the redshift bin width, we normalize the SFR image for each galaxy in the stack by our SFMS relationship (given in Equation 4.13) evaluated at the stellar mass and photometric redshift of the galaxy.

Assuming the source-population follows a log-normal distribution[43] in $\rm SFR_{3GHz}$, then we can use Eq. 8 of Schreiber et al. (2015):

$$\sigma_{\rm SFR} \simeq \frac{1.171 \times \rm SFR}{\rm MAD} \left(1 - \sqrt{1 - \left(\frac{\rm MAD}{0.953 \times \rm SFR}\right)^2}\right) \tag{4.14}$$

to calculate $\sigma_{\rm SFR}$. Errors on the MAD are calculated from bootstrapping. Following previous studies, we do not account for the impact of errors on SED photo-z and stellar mass estimates.[44]

Figure 4.7 shows the dispersion of the SFRs around the median as a function of stellar mass and redshift for star-forming galaxies. We limit the analysis to stellar mass and redshifts at which at least 10 % of the stacked galaxies are detected. Values at the lower-masses (not shown) rise quickly to values well above what is expected from the literature, likely indicating that the method is not valid here where there are only non-detections.

At the high-mass end, our results show that the scatter is relatively constant with stellar mass (we note there is a slight dependency on stellar mass but do not believe that it is a robust result). Pearson et al. (2018) also found that the scatter is nearly constant with stellar mass (as did, e.g. Whitaker et al. 2012, Speagle et al. 2014, and Tomczak et al. 2016). On the other hand, observational studies such as Guo et al. (2013), Ilbert et al. (2015), and Popesso et al. (2019), as well as simulations (Donnari et al., 2018) have found the dispersion in sSFR increases with stellar mass. Their dispersion values are indicated as horizontal dashed lines on Figure 4.7. In the IllustrisTNG simulations, Donnari et al. (2018) found a constant scatter in the mass range $10^9 - 10^{10.5}$ $\rm M_\odot$. A recent analysis of the EAGLE simulations suggests the scatter is minimal at a characteristic mass $M_* \sim 10^{9.5}\,\rm M_\odot$ and increases both at lower and higher masses (Katsianis et al., 2019). It is evidently important to consider the mass range probed when comparing trends reported by different studies.

Observational studies including Pearson et al. (2018) and Erfanianfar et al. (2016) find the dispersion of the SFMS to decrease with redshift. On the other hand, studies like Schreiber et al. (2015) report a scatter that is constant with both mass and redshift. We measure the scatter of the SFMS to be between 0.3 and 0.2 dex (at $z > 0.8$), but slightly higher, ~ 0.4 dex, at $z \sim 0.5$. We find that the scatter of the SFMS, for galaxies $M_* > 10^{10.2}$ $\rm M_\odot$, decreases smoothly with redshift (shown in the right hand panel of Figure 4.7), approaching values

[43] This assumption is not strictly true because we expect a $\sim 10\,\%$ contribution to our stack from starburst galaxies; Rodighiero et al. 2011; Sargent et al. 2012; Gladders et al. 2013; Guo et al. 2013.

[44] Reddy et al. (2012) and Schreiber et al. (2015) describe how if the SED fitting is too simplistic and erases the diversity of the population, the measured dispersion could be decreased. However, a good solution has yet to be developed, although non-parametric SFHs are a good step forward (see e.g. Chauke et al. 2018; Iyer et al. 2019).

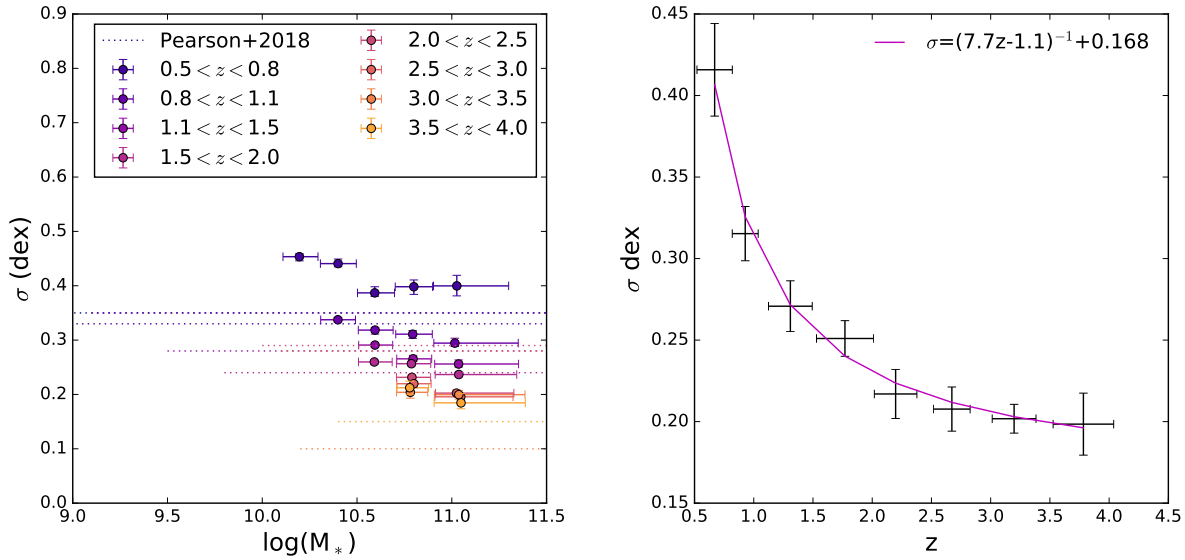

Figure 4.7.: Left: SFMS scatter measured for star-forming galaxies in stellar mass and redshift bins where $> 10\%$ of galaxies are detected individually at 5σ. The mass-independent fitted scatter from Pearson et al. (2018) is shown as dashed line spanning the mass completeness limits reported by their study at each redshift. We find some trend for decreasing scatter with increasing stellar mass, but this trend is not robust with our current data. Right: Average scatter as a function of redshift (averaging the data for different stellar masses shown in the top panel). Error-bars represent both the scatter between σ values for the stellar mass bins included in the average, plus the average error from the bootstrapping analysis added in quadrature.

of ~ 0.2 dex at $z \sim 4$ (compared to Pearson et al. (2018) values of ~ 0.1 dex). This trend is also seen qualitatively in EAGLE (Matthee & Schaye, 2019; Katsianis et al., 2019) and IllustrisTNG (Donnari et al., 2018), however, the degree to which the scatter evolves depends on stellar mass. Donnari et al. (2018) reported a slight decrease for increasing redshift, from $\sigma = 0.35$ dex at $z = 0$, to 0.2 dex at $z = 2$. This IllustrisTNG result matches the values we observe at $M* = 10^{10.5}$ $M_\odot$.

Care should be taken when comparing results because selection functions might include or exclude starbursts and passive galaxies on different levels and some of the differences seen might be attributable to this (Katsianis et al., 2019). Our results are roughly consistent with other studies and simulation results, but more a careful comparison is required for a quantitative comparison.

4.4.4. Selection effects: selecting star-forming galaxies

The selections used in constructing the parent sample affect the resulting SFMS. Studies without a cut to separate star-forming and quiescent galaxies (e.g. Sobral et al. 2014) show reduced SFMS slopes because the quiescent galaxies "contaminate" the highest mass bins across a wide range of redshift. Using stricter SFG selections results in a straighter or steeper SFMS (Johnston et al., 2015; Karim et al., 2011). In Figure 4.8, we compare the difference between two commonly used colour-colour cuts from the literature, the UVJ and NUVrJ

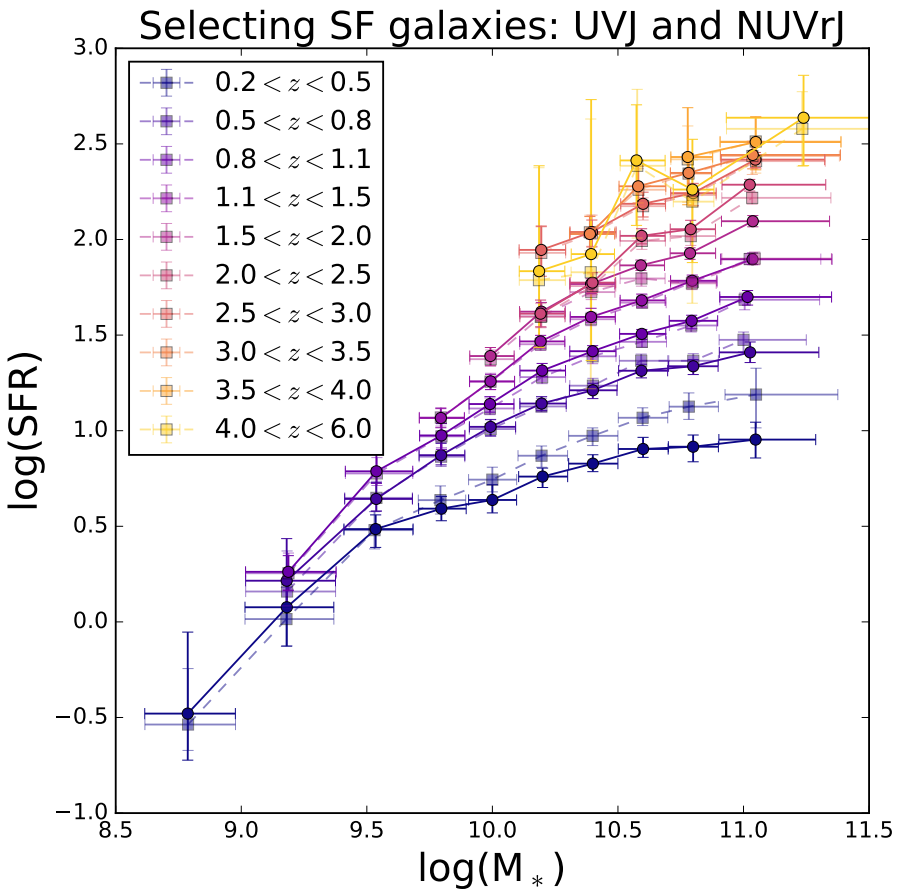

Figure 4.8.: Different methods for selecting star-forming galaxies result in different SFR-stellar mass relations. We show results using the Laigle et al. (2016) catalogue photo-z and stellar mass determinations and from rest-frame UVJ or NUVrJ colours for selecting star-forming galaxies. The NUVrJ selection used for this work is shown as solid circles a solid line. We show UVJ selected data as transparent squares with dashed lines between data points. The SFRs from the two samples are most discrepant in our lowest redshift bin $0.2 < z < 0.5$ at stellar masses $\log(M_*/\mathrm{M}_\odot) > 10$.

selections. Color-color cuts are empirical criteria based on the number density of galaxies in these 2D planes. The UVJ selection uses the redshift-dependent rest-frame U-V, V-J colour-colour cuts described in Whitaker et al. (2011). The number density of galaxies in the COSMOS field on the NUVrJ diagrams can be seen in Laigle et al. (2016). The resulting SFR – M_* relations are consistent between the two selections within the uncertainties except for our lowest redshift bin ($0.2 < z < 0.5$) where the UVJ colour cut selects galaxies with a higher median SFR as compared to the NUVrJ colour cut. Our NUV-r colour requirement misses the most star-forming sources at $0.2 < z < 0.3$ that are included the U-V criteria because to the different sensitivities of the NUV and U band observations at this low redshift and the small volume probed.

4.4.5. Characteristic Stellar Mass

Karim et al. (2011) found that the majority of new stars formed since $z \sim 3$ were formed in galaxies with a mass of $M_* = 10^{10.6\pm0.4}$ $M_\odot$. Stellar mass functions reported in Davidzon et al. (2017) provide information on the number of galaxies that exist per co-moving cubic Mpc as a function of stellar mass and at each redshift. In this section we combine our 3 GHz SFMS results with the stellar mass functions reported for star-forming galaxies ("active galaxies") in Davidzon et al. (2017) (see their Table 1) to determine the cosmic star-formation rate density. At $0.2 < z < 3.0$ a double Schechter (1976) stellar mass function function was fit to the data:

$$\Phi(M)\mathrm{d}M = e^{-\frac{M}{M\star}} \left[\Phi_1^\star \left(\frac{M}{M_\star}\right)^{\alpha_1} + \Phi_2 \left(\frac{M}{M_\star}\right)^{\alpha_2} \right] \frac{\mathrm{d}M}{M_\star}, \tag{4.15}$$

whereas at higher redshift, a single Schechter function was used (Davidzon et al., 2017).

Firstly, the SFR density as a function of stellar mass is estimated by multiplying the stellar mass function and our SFMS for star-forming galaxies and the results are shown in Figure 4.9[45]. Vertical lines in the figure show the stellar mass above which the COSMOS sample is 90% complete. The top left panel, showing all redshifts together, reveals that the SFR density peaks at $1.5 < z < 2$. The SFR density per stellar mass bin is peaked, showing a characteristic stellar mass that contributes most to the SFR density at a given redshift out to $z = 2.5$. We find that the SFR density becomes more and more tightly peaked out to $z = 2.5$ and that most new stars are formed in galaxies with a characteristic stellar mass that increases with redshift (see upper right panel of Fig. 4.9). Contrary to the finding of Karim et al. (2011) (whose SFMS was well fit with a power-law relation), with our deeper parent catalogues, we find an evolving characteristic mass that shows signs of cosmic downsizing, in which the most massive galaxies formed first (Siudek et al., 2017; Davé et al., 2016; Rodighiero et al., 2010; Thomas et al., 2010).

The evolving characteristic mass is closely connected to the turn-over mass of the SFMS. In Fig. 4.9 (top right panel), we show the evolution in the characteristic mass corresponding to the peak SFR density and the evolution of the turn-over mass of the MS from both this work and from Tomczak et al. (2016), Lee et al. (2018), and Gavazzi et al. (2015). Our SFMS turnover mass (shown in blue) only matches well with Tomczak et al. (2016) at $z < 2$ and matches with Lee et al. (2018) for $z > 2$. However, our characteristic mass (red squares) match well the trend in the SFMS turnover seen in Tomczak et al. (2016) at all redshifts. At $z > 3$ our COSMOS data is no-longer complete past the characteristic mass, so it is unconstrained in the highest z-bin shown ($3.5 < z < 4$).

[45] Actually, since we are using a median SFR at each mass, rather than the mean SFR which should be used for this calculation, this is not completely correct, except in the low-SNR case where the median stacking can approximate the mean of the distribution (White et al., 2007). For most SFR distributions the mean would be higher than the median. However, this would systematically shift the SFRDs upwards by an amount that depends on the dispersion of the correlation, making our SFRD even more discrepant with the literature (see Section 4.4.6).

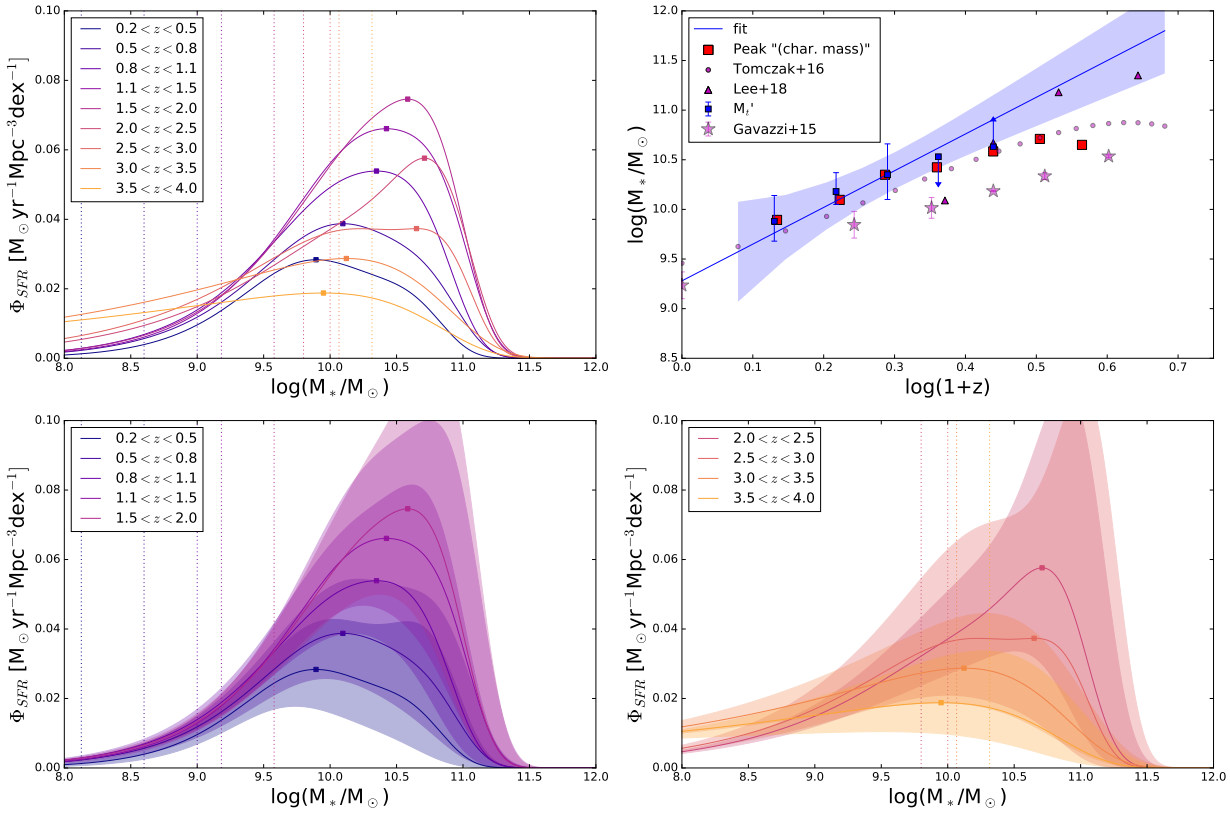

Figure 4.9.: The distribution of the SFR density as a function of stellar mass at different epochs out to $z \sim 4$. We plot the function that results from multiplying the best-fit radio derived SFR-sequence at a given epoch with the corresponding mass function for star-forming galaxies from Davidzon et al. (2017). The top left panel shows a summary of all redshift bins together. The bottom left panel shows data at $z < 2$ where the SFR density is rising, and the bottom-right panel shows $z > 2.0$. The uncertainty range was obtained by combining the uncertainties on the stellar mass function's Schechter parameters with the SFMS at the minimum and maximum redshift of our bins. At each epoch, our COSMOS data is not mass-complete below the stellar mass limits indicated by vertical dotted lines. The stellar mass corresponding to the peak SFR density is indicated as a square. The top right panel shows how this "characteristic" mass evolves with redshift (out to $z = 3$; red squares). The evolution in characteristic mass is driven by the evolving turn-over mass in our SFMS. We fit the Lee et al. (2015) SFMS form for each z bin individually in Section 4.4.2, which gives M_0 (blue squares; see Table 4.2). Our best-fit functional form $M_t = M_0 + a_2 \log(1+z)$ in Eq. 4.13 is shown as a blue line (with 1σ confidence level shaded).

4.4.6. Cosmic SFR density of the Universe

By integrating the curves shown in Figure 4.9 over the stellar mass range $M = 10^7 - 10^{12.5}\,M_\odot$, we report the contribution of star-forming galaxies to the SFR density of the Universe as a function of redshift in Figure 4.10. In addition to our results, we show the Madau & Dickinson (2014) and Davies et al. (2016) literature compilation curves and recent radio (purple symbols) or IR (red symbols) studies. Our SFRs (blue squares) lie above the classic Madau & Dickinson (2014) results but are in agreement with the Davies et al. (2016) relation which was derived including additional results from the Hopkins & Beacom (2006) compilation. A more straightforward way of calculating the cosmic SFRD, free from assumptions about the SFMS form and stellar mass function, is to multiply the average radio flux in each stack by the number of galaxies in the stack and normalize by the co-moving volume probed by the redshift range considered. The area used for our stacking experiment is 1.55 deg^2 (section 4.2), and the cosmological volume was calculated for each redshift slice using the CELESTIAL package by A. Robotham. The resulting SFRD are shown as orange symbols in Figure 4.11. We only sum over mass-complete bins and do not apply a completeness correction because that would assume a stellar mass function (e.g., Liu et al. 2018). This is why our SFRD estimates drop to low values at high redshift where we are no longer probing past the knee of the stellar mass function.

In Figure 4.11 we show the systematic effects that different choices of stellar mass function, SFR calibration, and SFMS form can make on the CSFD measurements. Novak et al. (2017) derived the cosmic SFRD using radio luminosity functions of the 6,000 VLA-COSMOS 3 GHz detections with reliable optical counterparts. The faint and bright end shape of the radio luminosity function was fixed to the local values. One key difference between their study and ours is the use of the Delhaize et al. (2017) radio-SFR calibration. However, we have re-run our SFMS analysis using the Delhaize et al. (2017) SFR calibration and found worse agreement at low redshifts (teal circles in Figure 4.11) between the Madau & Dickinson (2014) curve and our results. We report the best-fitting SFMS parameters found for this calibration, and the others mentioned below, in Table 4.4. In Chapter 2, we used the power-law 1.4 GHz SFR calibration from Davies et al. (2017). Although this non-linear SFR calibration works well with our 3 GHz data (blue stars in figure 4.11) for reproducing the local literature cosmic SFRD values from Davies et al. (2016) at $z < 0.7$, the SFRD implied at $z > 2$ are lower than canonical values. Karim et al. (2011) adopted the Bell (2003) 1.4 GHz radio SFR calibration (purple circles in Figure 4.10). This SFR calibration applied to our 3 GHz stacks, assuming a spectral index of $\alpha = -0.8$, gives lower SFRs than our Magnelli et al. (2015) prescription at $z < 2$, more consistent with the Madau & Dickinson (2014) relation, but higher SFRs at $z > 3$.

To investigate the effect of the stellar mass functions used, we have repeated our main analysis using the Ilbert et al. (2013) stellar mass function, which results in slightly lower SFR densities (shown as light blue pentagons). Liu et al. (2018) constrain the contribution from optically undetected dusty star-forming galaxies at $z < 6$ in the GOODS-North field. They reported the SFRD obtained using either the Davidzon et al. (2017), Ilbert et al. (2013), or Muzzin et al. (2013) SMF (dark red circles to transparent red circles, respectively) stellar mass function to correct for incompleteness. The choice of stellar mass function has a large effect on the measured SFRD at $z > 2$ where current IR and radio data are incomplete.

Table 4.4.: Fitted parameters of our SFMS model (Eq 4.13) to all mass-complete data for SFGs under different assumptions. See 4.3.1 for more information about the different SFR calibrations.

SFR calibration	best fit values $(s_0, m_0, a_1, a_2, a_3)$	χ^2_r
Magnelli et al. (2015)[a]	$(0.383^{+0.135}_{-0.119}, 9.280^{+0.193}_{-0.163}, 4.490^{+0.494}_{-0.559}, 3.699^{+0.636}_{-0.762}, 7.714^{+3.316}_{-1.989})$	3.8
Delhaize et al. (2017)	$(0.577^{+0.129}_{-0.115}, 9.287^{+0.188}_{-0.157}, 4.097^{+0.478}_{-0.534}, 3.664^{+0.622}_{-0.734}, 7.74^{+3.32}_{-1.93})$	3.7
Davies et al. (2017)	$(0.300^{+0.132}_{-0.094}, 9.213^{+0.280}_{-0.175}, 3.450^{+0.344}_{-0.466}, 3.007^{+0.585}_{-0.891}, 11.63^{+76.0}_{-3.87})$	5.2
Bell (2003)	$(0.083^{+0.142}_{-0.129}, 9.237^{+0.255}_{-0.200}, 5.166^{+0.486}_{-0.508}, 3.871^{+0.638}_{-0.735}, 10.1^{+43.5}_{-3.04})$	3.9

In Figure 4.11 we also show the CSFD derived using linear SFMS, of Equation 4.10 fitted to our 3 GHz data, as well as the SFMS directly from Pearson et al. (2018). In addition, the results from performing a mean stack (rather than a median; see Appendix B.1.2) are shown. It appears that more careful analysis of the systematic uncertainties is required to obtain a robust census of the dust-unobscured cosmic SFRD at both low and high redshifts.

It is obvious that SFR calibration, and possibly the radio k-corrections play an important role in the variation of SFRD found in Figure 4.11. In section 4.3.1, we chose to adopt the Magnelli et al. (2015) q_{FIR} evolution, a radio power law index of $\alpha = -0.8$, and the Kennicutt & Evans (2012) TIR SFR calibration because they best reproduced the FIR SFRs for our test stacks (the galaxies used in Karim et al. 2011). One particular avenue which we will explore in a follow-up paper is whether the evolving $q_{\rm TIR}$ prescriptions give an accurate conversion from radio luminosity to SFR. Even in the local Universe, there is evidence that the radio luminosity does not scale linearly with SFR (e.g. Bell 2003; Davies et al. 2017). Molnar et al. (in preparation) find that the redshift evolution of $q_{\rm TIR}$ reported by Delhaize et al. (2017) is a result of the increasing radio luminosity probed by the star-forming galaxies in COSMOS with redshift. On the other hand, whether or not the total infrared luminosity of a galaxy gives a reliable SFR, should depend on stellar mass according to studies of the IR/UV ratios in galaxies out to $z < 5$ (e.g., Whitaker et al. 2017; Bouwens et al. 2016; Fudamoto et al. 2017).

4.4.7. Morphology trends

In this Section, we study the SFMS as a function of galaxy morphology out to $z \sim$1.5 using HST morphological measurements in the ZEST catalogue (Scarlata et al., 2007) probing rest-frame optical wavelength (ACS I band).

Taken separately, the SFR – M_* relations for the different morphological classes appear to follow linear relations but have different slopes and normalisation. We find that massive galaxies dominated by a bulge tend to have lower SFRs at fixed mass and redshift (Figure 4.12). The lower panels of Figure 4.12 show that the difference between SFRs of different morphology types becomes prominent at low-z; the sSFR of high-mass bulge-dominated and spheroidal galaxies drops faster than the sSFR of disk-dominated galaxies. Disk-dominated star-forming galaxies follow a steeper SFR – stellar mass relation than other types (with slopes of ~ 0.75 compared to ~ 0.5). When the disk-dominated galaxies are combined with the ET and bulge-dominated galaxies, a flattening in the average SFMS becomes apparent at higher stellar masses where the ET and bulge-dominated galaxies dominate. Irregular galaxies have SFRs above the SFMS at all redshifts, and are more star-forming than pure

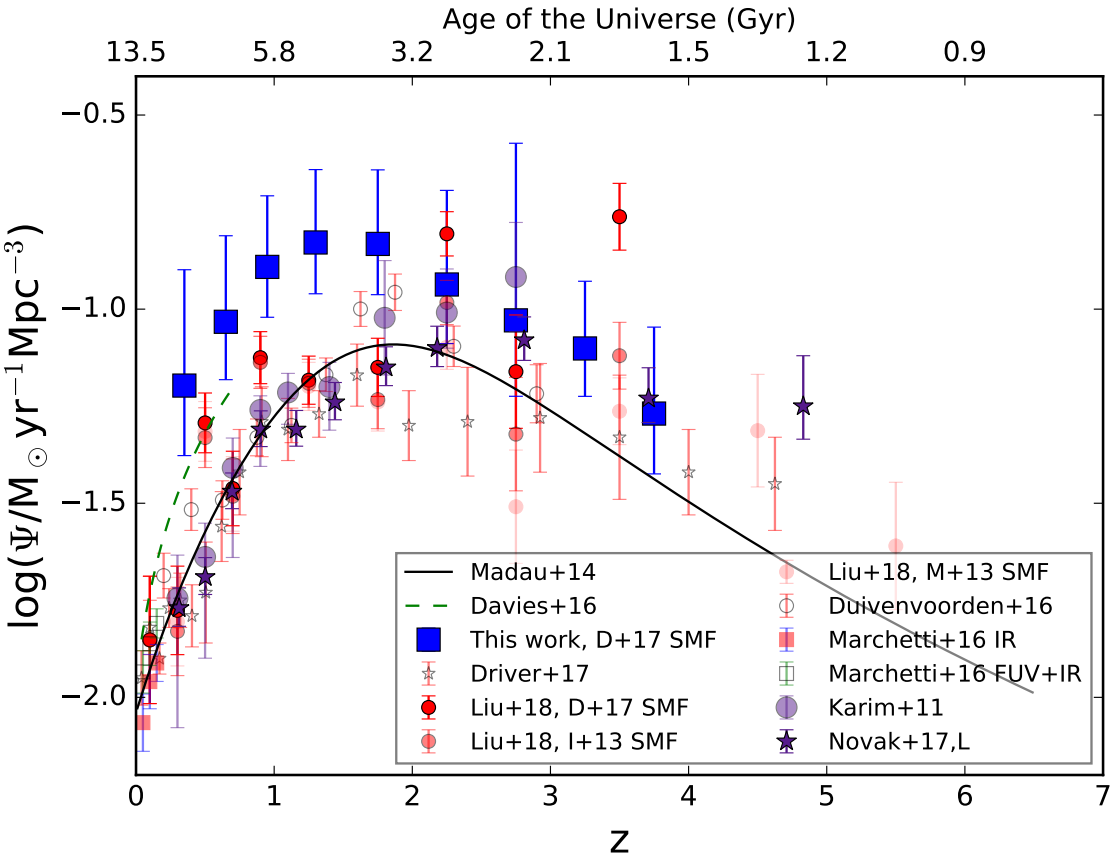

Figure 4.10.: SFR density resulting from integrating the SFR density as a function of stellar mass shown in Figure 4.9 between $M_* = 10^7$ and $10^{12.5}$ $M_\odot$. Results from this work are shown in blue, results from radio-based observations are shown in purple, and results from IR-based observations are indicated in red. See the text for more details.

disks, at least at $z < 1.2$, and $M_* < 10^{11}$ $M_\odot$.

Figure 4.13 shows the fraction of the total SFR occurring in galaxies in each morphological class as a function of stellar mass. The fraction of SFR occurring in disk galaxies decreases with redshift as the number of pure-disk galaxies decreases. By $z < 0.6$ there are no pure disks in the most massive bin of star-forming galaxies. The fraction of star formation in irregular galaxies is roughly constant at around 20% in the four redshift bins shown but is slightly decreased in favour of galaxies classified as spheroidal for masses 10^{11} $M_\odot$.

It is interesting that the SFR contribution from disk-dominated galaxies is peaked around $\log(M/M_\odot) = 10$ at each redshift. This points to no downsizing occurring in disks (unlike the total population) because they have a single power-law SFMS relation and an approximately redshift-independent stellar mass function. Pannella et al. (2009b) also found the stellar mass function of disk-dominated galaxies in the COSMOS field is consistent with being constant with redshift out to $z \approx 1.2$.

In this section, we have used the q_{IR} from Magnelli et al. (2015) to calculate SFR from radio luminosity. More tests (e.g., including UV emission) needs to be done to ensure we can recover the correct SFR in galaxies of different morphological types given that the infrared – radio correlation (Molnár et al., 2018) and perhaps radio spectral index (Gürkan et al.,

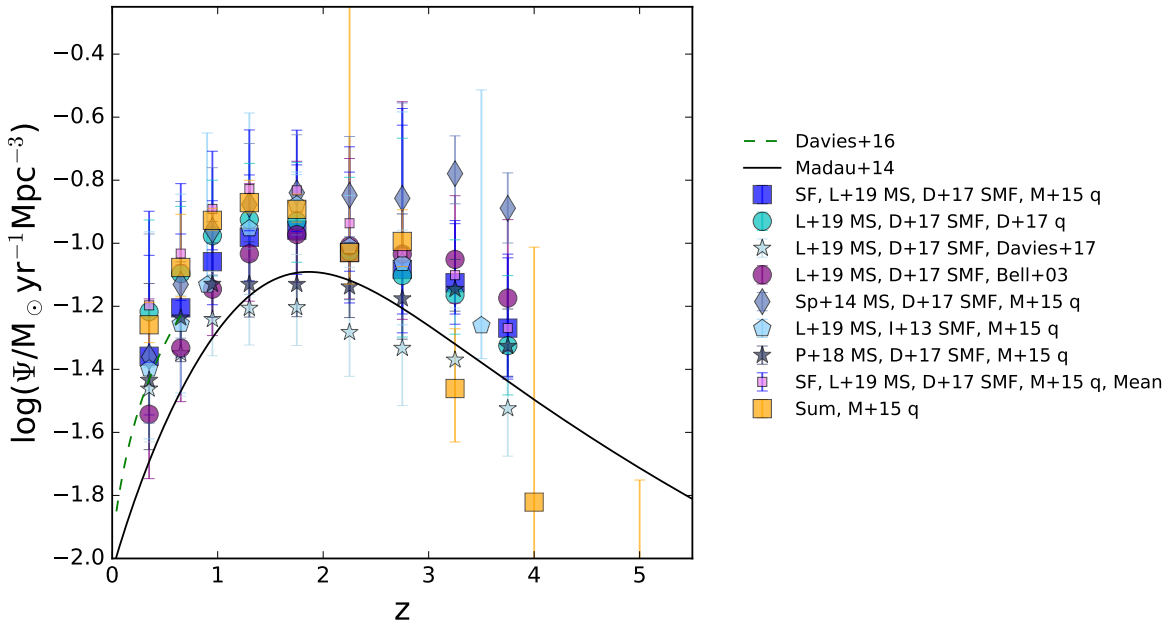

Figure 4.11.: Systematics when calculating the cosmic star-formation rate density for our galaxy sample. Different data points show the different SFR density inferred when different SFR calibrations (M+15 or D+17 q; Magnelli et al. (2015) or Delhaize et al. (2017) evolving q_{TIR}, respectively), stellar mass functions (D+17 or I+13 SMF; Davidzon et al. (2017) or Ilbert et al. (2013) results for active galaxies), and functional forms of the MS (L+19 or Sp+14; Equation 4.13, or the form Equation 4.10 from Speagle et al. (2014)) were used. Gray stars (P+18) represent the SFMS fitted by Pearson et al. (2018) combined with the Davidzon et al. (2017) stellar mass function. Orange squares represent the total SFRD inferred by summing the fluxes measured in the mass-complete stacks directly are are not corrected for incompleteness.

2018) vary between them. We discuss this further in Section 4.5.3 and Appendix B.4.

To summarise, we find the flattening of the high-mass slope can be, in part, explained by the inclusion of bulge-dominated galaxies which follow a shallower SFR – M_* relation than disk-dominated galaxies. As bulges grow more prominent in the low-redshift galaxy population (especially at large stellar masses), the flattening of the main sequence becomes more significant. We discuss these results further in Section 4.5.3 and argue that the star formation activity in the disks of bulge-dominated galaxies is likely suppressed in addition to the bulge having a low SFR[46].

4.4.8. Environment trends

Scoville et al. (2013) found that the contributions to the overall SFRD were uniformly spread across all environments down to $z \sim 0.6$, while at lower redshift the SFR activity shifts to lower density environments. Figures 4.14 and 4.15 show the SFMS for star-forming galaxies in different environments. Using the local density as probed by the normalised number of

[46]However, in our study, bulges are defined from galaxy photometry rather than kinematics, so we cannot rule out significant star formation in the bulge.

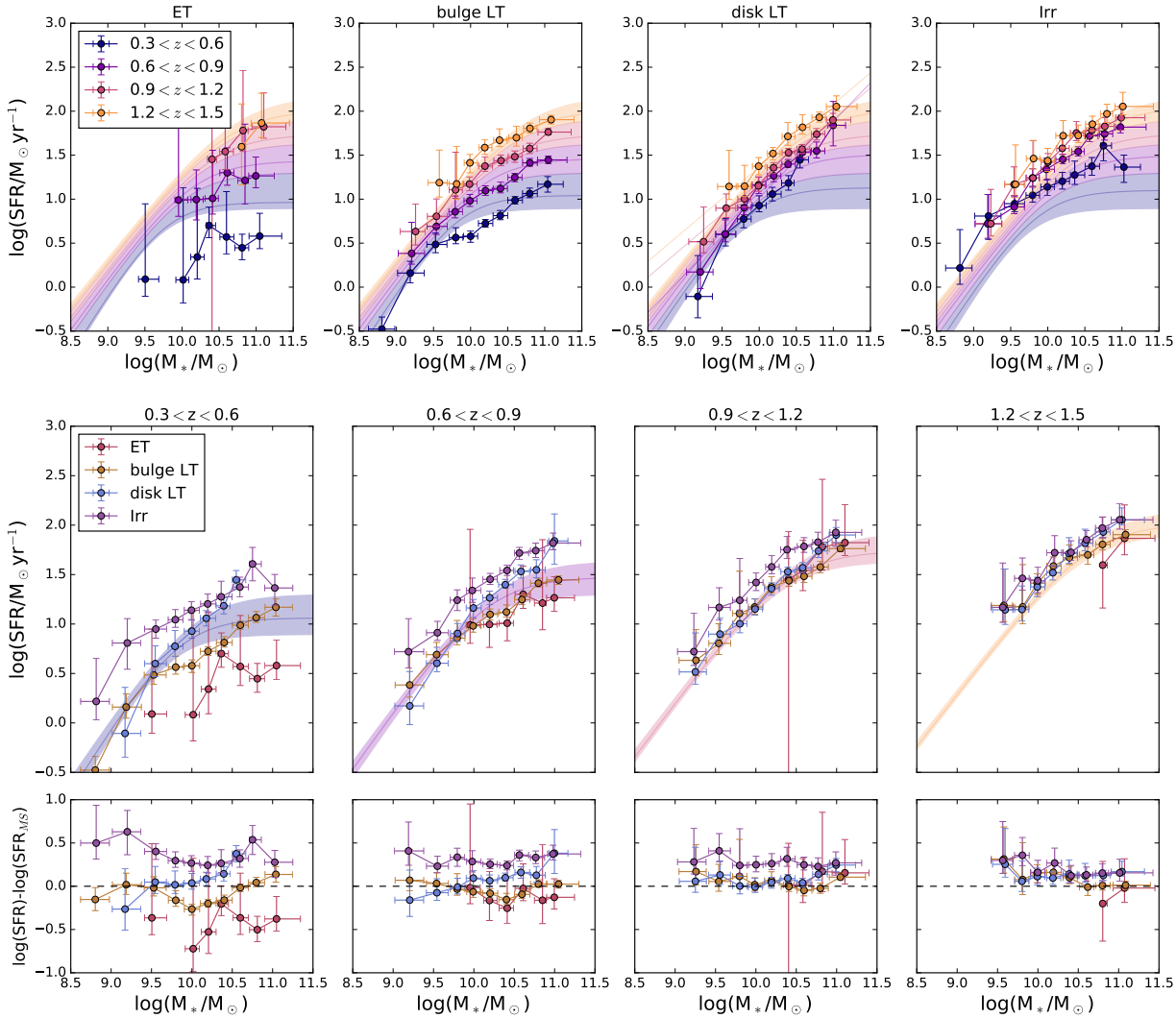

Figure 4.12.: Star-forming galaxy SFMS for different morphological types. The top panels show, from left to right, the SFMS for star-forming galaxies classified as ZEST types 1 (early-type), 2.0-2.1 (late-type with bulges), 2.2-2.3 (disk-dominated late-type), and type 3 (irregular) from a stacking analysis. The SFMS relation determined in Section 4.4.1 for all star-forming galaxies is shown in the background for comparison. The bottom panels show the four redshift bins separately, allowing for an easy comparison of the SFRs at a fixed stellar mass for the different morphological classes (in particular, see the bottom "residuals" panel where the average SFMS from Eq. 4.13 has been subtracted). The difference between the sSFRs of different morphological types becomes very prominent at low-z. Disk galaxies follow a steeper SFR-stellar mass relation than other types, showing no clear evidence for a flattening at high stellar masses.

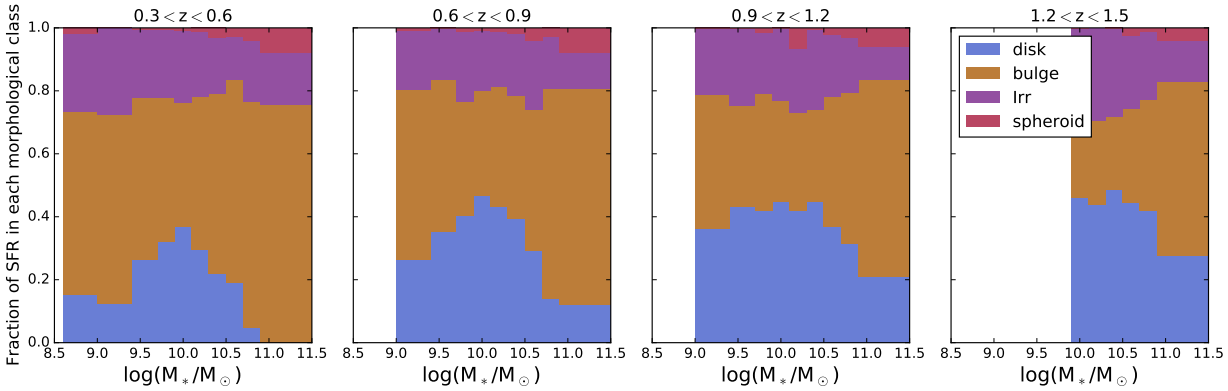

Figure 4.13.: Contributions from different morphological types to the total SFR as a function of mass in three redshift bins. The total SFR is given by multiplying the average from the stack with the number of galaxies in said stack. Only mass complete bins are shown. The fractional contribution from disk-dominated galaxies declines as the contribution from bulge-dominated galaxies increases towards lower redshifts.

galaxies per Mpc^3 (Scoville et al., 2013), we find no statistically significant difference between the SFMS relation for galaxies in different local densities (see Figure 4.14). The same is true when considering "all" galaxies (not shown). In the bottom panel of Fig 4.14, the difference between the SFRs (normalized to the SFMS for all star-forming galaxies) is shown in each redshift bin. Our result is in contrast with Duivenvoorden et al. (2016) who found that the (IR) SFR decreases with local density (at a fixed stellar mass) out to $z < 2$ in the COSMOS field. The completeness corrected total cosmic SFRD from Duivenvoorden et al. (2016) is shown in Figure 4.10, and is consistent with our SFRD at $z \sim 2$.

Figure 4.15 shows the SFMS for galaxies in X-ray groups (solid circles) compared to the SFMS for galaxies in the field (transparent squares) at $0.64 < z < 0.88$ where the statistics are robust. The best fitting SFMS (Eq 4.13) is shaded in the background. As before, we only show SFRs derived when the stacked 3 GHz image has S_p/rms>2 and the stellar mass is complete. We find no significant difference in the SFRs of star-forming galaxies in X-ray groups (halo mass $12.5 < \log(M_{200}/\mathrm{M}_\odot) < 14.5$) compared to star-forming galaxies in the field, consistent with our findings above which used local galaxy number density as a probe for the environment. However, the scatter is very large and larger samples will be required to confirm this result. When we focus on the three most massive X-ray groups (which we refer to as clusters, with halo masses $14 < \log(M_{200}/\mathrm{M}_\odot) < 14.5$), there is an enhancement of the SFR of intermediate mass $10.0 < \log(M/\mathrm{M}_\odot) < 10.5$ members compared to the field. However, there are only 4-7 galaxies per bin when considering only the clusters at $0.64 < z < 0.78$, so this result is not reliable. That being said, at higher redshifts, starburst galaxies could preferentially lie in denser regions, consistent with the observed clustering of bright *Herschel* sources (Cooray et al., 2010; Amblard et al., 2011; Viero et al., 2013). Our median stacking includes starburst galaxies that lie above the SFMS, which could explain why we observe an enhanced SFR in intermediate mass X-ray cluster members at $z \sim 0.76$.

We also show the SFR – M_* relation for all galaxies in the bottom panels of Figure 4.15. In this case, 20-40 galaxies are in X-ray clusters (and more including the groups). There is tentative (not statistically significant) evidence for lower SFR in X-ray group and cluster

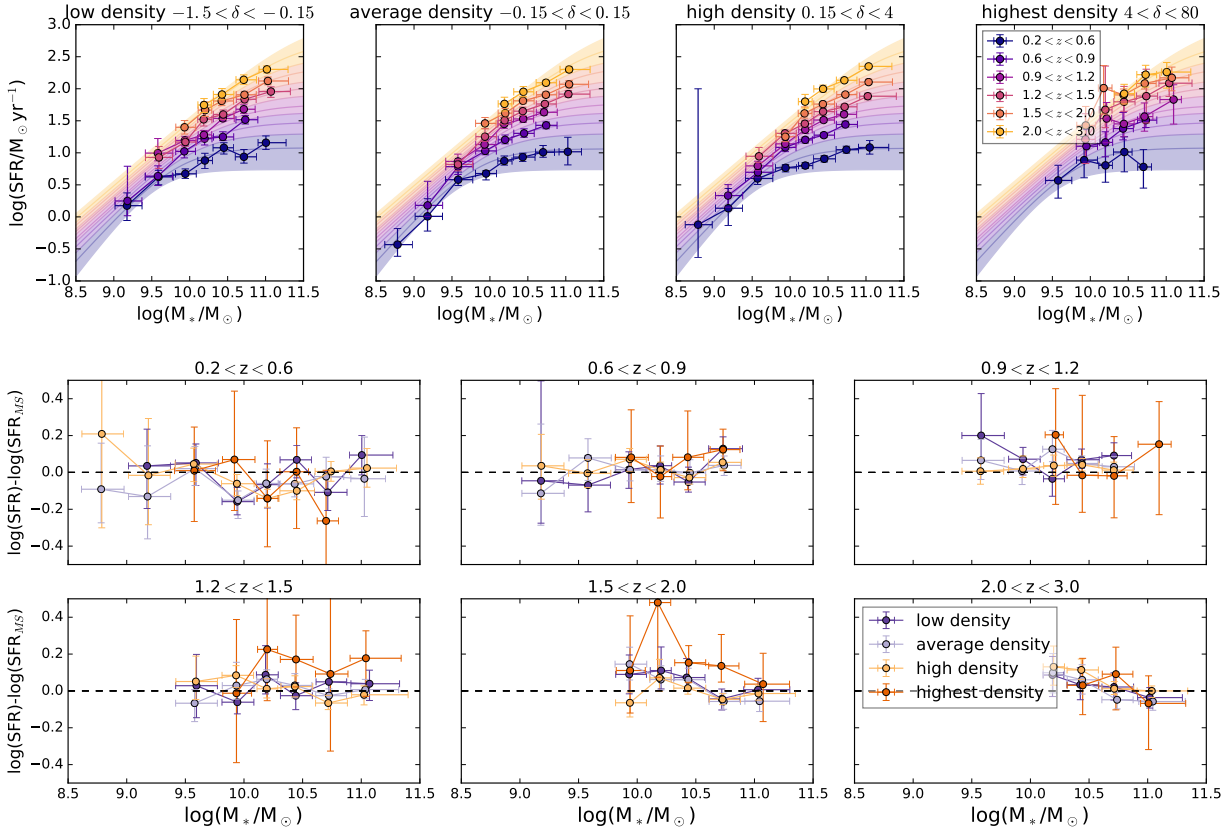

Figure 4.14.: *Top*: SFR as a function of stellar mass for star-forming galaxies in different local densities (as defined by Scoville et al. 2013) out to $z \sim 3$. The relationship between sSFR and M_* remains constant over these different local densities (explained in Section 4.4.8), from galaxies in under-dense regions (left) to galaxies in local over-dense regions (right). Our best fit relation for all SF galaxies is shown in the background, and no panel shows significant deviations from this relation. *Bottom:* Difference between the SFRs of star-forming galaxies compared to the average SFMS in different local environments as a function of redshift.

members with stellar mass $\log(M/\mathrm{M}_\odot) > 10.5$ than in the field.

Using ancillary data from the COSMOS field, we find that galaxy environment probed by X-ray-groups, clusters, and local galaxy number density has little effect on the shape of the main sequence at $z > 0.3$. This could indicate that environmental quenching (e.g., gas strangulation or stripping) is not effective at these redshifts, or that the colours redden before the SFR is suppressed, resulting in the affected galaxy being classified as quiescent and not being included in the SFMS analysis.

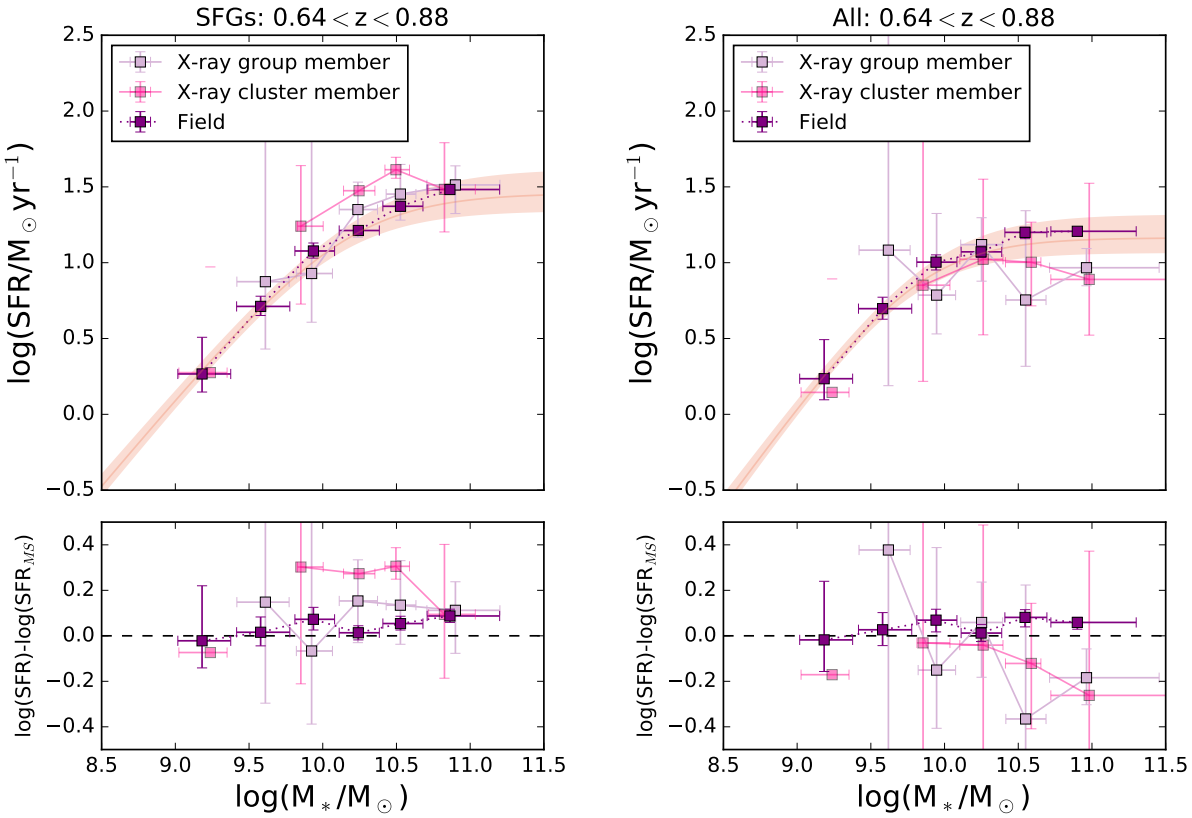

Figure 4.15.: The SFR-stellar mass relation for galaxies residing in X-ray groups and clusters at $z \sim 0.76$. The left panels show SFR vs. mass for SF galaxies and the right ones are for all galaxies. We divide our X-ray group members into two bins based on the halo mass of the X-ray group; here clusters are $M_{200} > 10^{14}\,M_\odot$. The background curve shows the relevant SFR – M_* relation (Eq 4.13). The bottom panels show the difference between the measured SFRs compared to the average SFMS in different X-ray environments.

4.5. Discussion

4.5.1. Comparisons with literature

In Figure 4.16, we show the difference between a selection of literature determinations of the SFMS for star-forming galaxies and the 3 GHz-determined SFMS we found in Sect. 4.4.1. Variations of up to ±0.4 dex occur, and results are particularly divergent at low and high stellar masses, where the effects of completeness and star-forming sample selection become most important, respectively. We include more information about the studies included, and show the differences in literature studies at 6 redshift bins, out to $z = 4.5$, in Appendix B.3. In general, our sSFRs tend to be higher than measured by other studies, but given the large sample-to-sample variation present, and the fact that different SFRs are sensitive to different stellar populations, we do not consider this to be an important shortcoming of our analysis. When compared at $z = 0$, different simulations have a SFMS whose amplitude varies by up to 0.7 dex, and the power-law slopes range from 0.7-1.2 (Hahn et al., 2019). As noted by

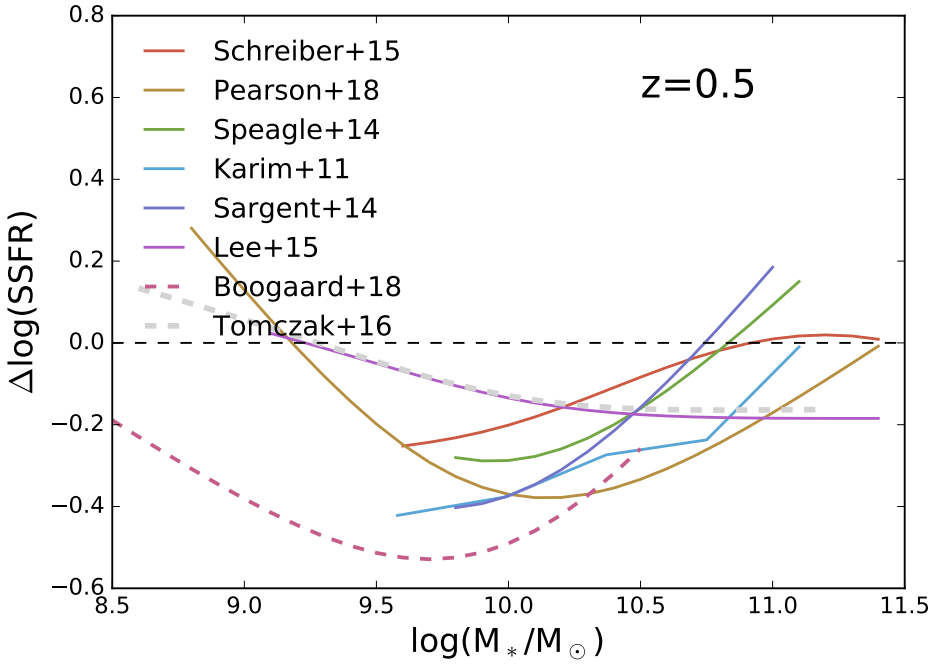

Figure 4.16.: Comparison with literature SFMS relations at $z = 0.5$. Δlog(sSFR) is the ratio of the SFMS sSFR from the literature relative to the SFMS sSFR from this work (Eq 4.13). Dashed line at $\Delta\log(\text{sSFR}) = 0$ indicates where the relations agree. For more redshift bins, see Figure B.6.

Popesso et al. (2019), different indicators used either to define the MS location or to estimate the SFR or galaxy sample selection effects can cause these large variations between studies.

At the high-mass end in the local Universe, $M_* > 10^{11}$ M$_\odot$, there are very few star-forming galaxies and their SFRs are highly uncertain and depend sensitively on the SFR calibration used (Popesso et al., 2019); these galaxies are critical for determining the flattening of the SFMS. As previously mentioned, the SFMS relations reported in different studies vary depending on sample selection, SFR, stellar mass and redshift measurements, and the adopted fitting function. Recently Pearson et al. (2018) use spectral energy distribution (SED) (UV - 160 μm) priors to de-blend the Herschel SPIRE maps and overcome the limitations of confusion in measuring SFRs in the Cosmic Evolution (COSMOS) field. The SED SFRs obtained with CIGALE (Code Investigating GALaxy Emission; Burgarella et al. 2005) are ~ 0.4 dex lower than the SFRs obtained by combining UV and IR SFRs, which has been a standard method since introduced in the SFMS study by Wuyts et al. (2011a). Pearson et al. (2018) report no evidence for a SFMS turn-over which emphasises the sensitivity of the SFMS to the methodology applied in constraining it. Schreiber et al. (2015) used a stacking analysis in the COSMOS and GOODS fields to push to deeper IR luminosities, and reported a high-mass turnover that vanishes by $z \sim 2$. Both Pearson et al. (2018) and Schreiber et al. (2015) (as well as Lee et al. 2015), used the same *Herschel* data in the same fields, and yet these studies resulted in different interpretations. In general, for more robust results, uncertainties specific to each dataset and from the sample selection could be better understood using simulated observations, and systematic uncertainties from stellar mass and SFR derivations should be analysed.

4.5.2. Cosmic SFRD evolution and characteristic stellar mass

The overall normalization of our SFR density lies above that expected from the literature (Madau & Dickinson, 2014). However, it is still likely that the *shape* of our SFMS and thus cosmic SFRD as a function of stellar mass is more-or-less correct because the uncertainty in $q_{\rm TIR}$ mainly acts on the normalization. Our SFR density – stellar mass relationship (Fig 4.9) shows a peak at a characteristic stellar mass of $M_\star \sim 10^{9.9}\,{\rm M}_\odot$ at $z \sim 0.35$ and a characteristic mass that increases with redshift out to $z \sim 1.75$ ($M_\star \sim 10^{10.6}\,{\rm M}_\odot$). This trend was also predicted by Béthermin et al. (2013) who showed that halos with $11.5 < \log(M_h/{\rm M}_\odot) < 13$ contribute 90% of the star formation activity, and that the majority of the star formation activity is hosted in halos that decrease in mass with decreasing redshift, i.e. the bulk of activity comes from cluster progenitors at $z > 3$, groups at $0.5 < z < 3$, then to Milky Way like haloes at $z < 0.5$.

Legrand et al. (2018) studied the stellar-to-halo mass relationship in the COSMOS field using a parametric abundance matching technique and find that the ratio peaks at a characteristic halo mass of $10^{12}\,{\rm M}_\odot$, and that this characteristic mass increases with redshift to $z \sim 2.3$ and then remains flat until $z = 4$. They argue that this is consistent with the picture that star formation is quenched in more massive halos first. Below the characteristic halo mass, the stellar mass build-up (i.e. SFR) "keeps up" with the dark matter accretion rate, whereas above the characteristic mass the galaxy is more likely to be quenched. We interpret the evolution in turn-over mass or characteristic mass towards $z = 0$ to imply that quenching starts in the most massive galaxies at high redshift, and then proceeds to lower-mass galaxies with time.

4.5.3. Morphology trends

We found in Section 4.4.7 that for massive galaxies ($\log(M_* N/{\rm M}_\odot) > 10.0$) galaxy morphology is correlated to the position on the SFMS: at a fixed stellar mass, early-type and bulge-dominated galaxies have lower SFRs than disk-dominated galaxies, which in turn have lower SFRs than irregular galaxies. Galaxy interactions could account for irregular morphologies and also cause a burst of star-formation resulting in irregular type galaxies lying above the SFMS of disk-dominated galaxies. Cibinel et al. (2019) reported that the starburst population across redshifts $0.2 < z < 2$, predominately consists of late-stage mergers. We note that the slope of the SFR-stellar mass relation for these irregular galaxies is *shallower* than for the disks, inconsistent with results from Bisigello et al. (2018) for starburst galaxies.

To further investigate the composition of our ZEST-classified irregular (Type 3) galaxies, we cross-matched our parent sample using the Capak et al. (2007) position coordinates with the 70 μm selected catalogue of 1,503 sources from Kartaltepe et al. (2010a,b), finding 1,142 overlapping sources. Out of the $\sim$2,300 irregular ZEST sources, we found 216 with visual morphological classifications in Kartaltepe et al. (2010b). The authors classified source morphology (e.g. spiral, elliptical) and noted whether each source was clearly undergoing a minor or major merger. We found that for galaxies in both the ZEST and 70μm catalogues, 23.6% are minor mergers and 28.8% are major mergers (total 52.5% mergers). For irregular ZEST galaxies the fraction of mergers is much higher; 80% (30.1% minor mergers and 50% major mergers). This supports the idea that our ZEST Type 3 irregular galaxies have higher star formation rates (and more irregular morphologies) than the disk-dominated sub-sample

because they are undergoing mergers that trigger gas inflows resulting in an enhanced SFR (Barnes & Hernquist, 1996).

One key result from this work is that bulge-dominated galaxies follow a shallower SFMS relation than disk-dominated galaxies. Schreiber et al. (2016) performed bulge-disk decompositions of galaxies with $\log(M_*/\mathrm{M}_\odot) > 10.2$ in CANDELS, and found that the disk component of galaxies at $z = 1$ follows a similar flattening of the SFMS as the total (stacked) population, even for disk-dominated galaxies, in disagreement with our results. They also reported that the lower sSFRs of massive galaxies corresponds to a lower star formation efficiency (not present at $z = 2$) rather than a lower gas fraction. However, the study used *Herschel* data to also infer the gas content which should be confirmed with independent observations. Although Schreiber et al. (2016) found that disk-dominated galaxies exhibit the same flattening as bulge-dominated galaxies, other studies such as Erfanianfar et al. (2016) found that the disk galaxies have a more linear SFMS relation than the bulge-dominated galaxies, consistent with our findings. The number of pure disks at high stellar mass is very low in the low redshift Universe, in fact, our lowest redshift bin $0.3 < z < 0.6$ contains only 4 disk-dominated galaxies above $10^{10.7}\,\mathrm{M}_\odot$. Larger samples at low redshifts, such as those provided by SDSS, have shown that the disk component of galaxies follows a linear SFMS (Abramson et al., 2014).

We explore how the steeper SFMS of disk-dominated galaxies can be related to the shallower SFMS for bulge-dominated galaxies at a fixed redshift. In Figure 4.17, we investigate how much stellar mass (assumed to be in a quiescent bulge) must be added to the disk-dominated galaxies to shift the SFR – M_* relation to be consistent with that of the bulge-dominated late-type galaxies. First, we fit a linear relation to the disk-dominated galaxies (results shown in the third panel of Figure 4.12) and compute the mass of the disk required to provide the SFR observed. We then infer the bulge to disk ratio assuming that the bulge-dominated galaxies consist of a disk (following the disk-SFMS) plus a bulge with zero star-formation activity. This assumption will give a lower-limit to the B/T ratio, as bulges can conceivably contribute a small amount of star formation activity. These resulting B/T ratios are shown in Figure 4.17.

However, there is the possibility that our SFR calibrations based on the infrared-radio correlation could be different for different galaxy types (Molnár et al., 2018). Therefore, we explore two possibilities: 1) we use the same SFR calibration for all stacks (as we have done in Section 4.4.7), and 2) we use the appropriate $q(z)$ relation derived separately for the "disk" and "spheroidal" morphological classes (see Appendix B.4 for more details). As we will find, these two methods produce differences in SFRs of factors of ~ 2, which is similar to the size of the effect that bulges might have on the SFR.

When we use the same q_{TIR} for all galaxies (left-hand panel of figure 4.17), the resulting SFR-derived B/T (bulge mass to total mass) show a clear increase with stellar mass and similar values at all redshifts, consistent with the result from Lang et al. (2014a) for star-forming (sSFR selected) galaxies in the CANDELS/3D-HST fields. We exclude our lowest redshift bin because it is the one most affected by the colour cut used to select star-forming galaxies (Sec 4.4.4) and is not covered by the analysis in Lang et al. (2014a).

On the other hand, when we use different q_{TIR}'s for the disk and bulge-dominated galaxies, the B/T ratios we infer are larger than the measurements from Lang et al. (2014a) (central panel of Figure 4.17). In this case, our assumption that the disks of these galaxies follow the

SFMS measured for pure-disk galaxies is likely not valid; the SFR in the disk component of these bulge-dominated galaxies must also be suppressed compared to the case of a pure disk galaxy with no bulge.

If we adopt the B/T ratios given by the Lang et al. (2014a) measurements, then the amount of SFR that needs to be suppressed in the disk (assuming different $q_{\rm TIR}$ values for different morphological types) is shown in the right-hand panel of Figure 4.17 as a function of total galaxy mass. In other words, we calculate the difference between the expected SFR of the disk components based on the linear fits to the disk-galaxy SFMS and the measured average SFR of the bulge-dominated galaxies. The amount of inferred SFR suppression increases with stellar mass and is slightly higher in the $0.6 < z < 0.9$ bin than required at higher redshift. Under the assumptions that different galaxy types require a different radio – SFR calibration, Figure 4.17 shows that the presence of a bulge with no star-formation is not sufficient to explain the decreased SFR observed in bulge-dominated galaxies; rather the presence of a bulge must also affect the star-formation process of the disk in which it is embedded. Theoretical arguments suggested by Meidt et al. (2018), explain that the gravitational potential of a centrally concentrated bulge can help stabilize the gas against fragmenting (see also simulations from Su et al. 2018). Bulges can also decrease the strength of bars, thereby decreasing the efficiency that gas is funnelled into the galaxy centre (Fragkoudi et al., 2016). We note that if the bulges are also star-forming, then the trend towards disk-suppression would be even stronger and that the $\Delta\log(\mathbf{SFR})$ values in Figure 4.17 are lower limits. The same result was also recovered when we compare stacks of ZEST Type 2.3 (pure-disks) and ZEST Type 2.1 (2.0 is more likely contaminated by early-type galaxies).

Larger sample sizes and a better understanding of SFR calibrations will be required to get the uncertainties on B/T ratios and sSFR suppression to within ~ 0.2 dex, the amount of influence that morphological suppression due to the presence of a bulge is expected to have on the sSFR.

Studies such as Popesso et al. (2019) and Schreiber et al. (2016) have reported that the presence of bulges alone is not sufficient to explain the flattening of the SFMS at very high masses; in addition to the increased mass given by a bulge component, there is also an indication for a decrease of star-formation activity of the disks along the SFMS. Through our comparison with Lang et al. (2014a), we also see evidence that the disks (in bulge-dominated galaxies) have star-formation suppressed at $\log(M)_* > 10.2\,\mathrm{M}_\odot$, by factors of ~ 2 if disk and bulge-dominated galaxies follow different IR-radio correlations. Popesso et al. (2019) speculated that while the quiescence of the bulge component could be explained by super-massive black hole feedback, the lower SFR of the disk at high masses could be due to gas starvation induced by gravitational heating in massive halos.

4.5.4. Environment trends

Results tend to agree that higher density environments increase the fraction of quiescent galaxies and we do see this in the COSMOS field (Peng et al. 2010; McGee et al. 2011; Darvish et al. 2014, 2016). Whether or not the normalization of the SFMS depends on galaxy environment is still under debate, but many studies identify no variations of SFMS with environments such as clusters and voids, e.g., Koyama et al. (2014), Ricciardelli et al. (2014), Tyler et al. (2013), Tyler et al. (2014) (although see Duivenvoorden et al. 2016 who

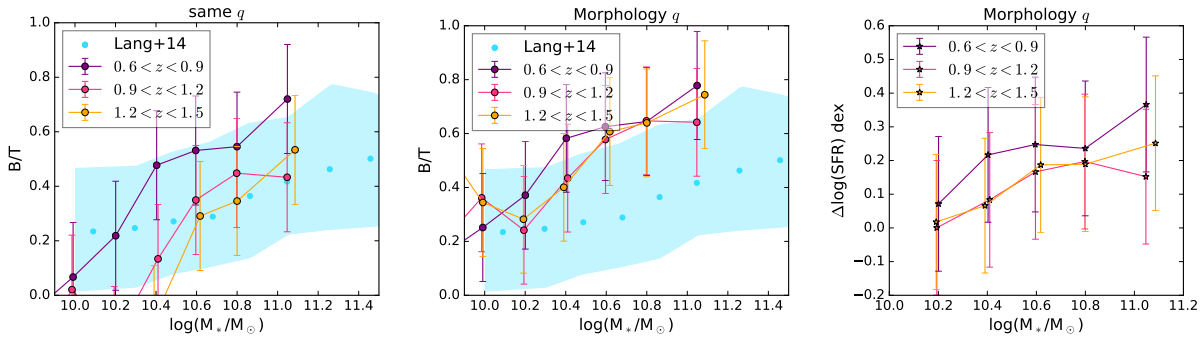

Figure 4.17.: *Left:* Typical bulge-to-total ratio of our bulge-dominated late-type galaxies required to explain their measured sSFR, assuming they consist of a disk component that follows the same SFR – M_* relation as the disk-dominated galaxies, and a bulge that has no star formation (providing a lower limit to the B/T). We fix the error on our B/T ratio to 0.2, which comes from the range of the B/T ratios obtained repeating this method for disk-dominated galaxies (which should have returned zeros). The B/T ratios inferred in this way are consistent with those measured by decompositions of the stellar mass by Lang et al. (2014a) at $0.5 < z < 2.5$ (cyan dots indicate median measured B/T and the shaded region shows the range of values). *Center*: Same as left but assuming different q evolutions for bulge- and disk-dominated galaxies following Molnár et al. (2018). *Right*: Amount of star-formation activity that needs to be suppressed in the disk in order to recover the SFR – M_* relation for the bulge-dominated galaxies if the bulge-dominated galaxies have B/T ratios observed by Lang et al. (2014a) and bulges that have no star formation (assuming different q for disk- and bulge-dominated galaxies).

found a difference at $1.5 < z < 2$ in COSMOS). However, at low redshift ($z < 0.3$) studies have reported a dependence of the SFMS on galaxy environment; von der Linden et al. 2010, Haines et al. 2013, Gu et al. 2018, Paccagnella et al. (2016). Environmental effects appear important at low redshift, where local spatially resolved studies find that environment quenching works on galaxies outside-in (e.g. Schaefer et al. 2019).

It is not surprising that our COSMOS sample does not show clear evidence for an environmental dependence of the sSFR when probing local galaxy number density at $z > 0.3$, or in X-ray groups at $0.64 < z < 0.88$. In simulations, Matthee & Schaye (2019) found that star-forming satellite galaxies only account for ≈ 0.04 dex of the scatter in the SFMS indicating satellites-specific processes are either weak or strong and rapid (such that the satellites quickly drop out of the sample of star-forming galaxies), consistent with our results.

Unlike our results, recent work by Rodríguez-Muñoz et al. (2019) found that not only is the fraction of star-forming galaxies lower in X-ray group environments by a factor of ~ 2, but also the star-forming galaxies in groups have an average sSFR ~ 0.3 dex lower than the field across all redshift ranges probed ($0.1 < z < 0.9$; they have a redshift bin $0.60 < z < 0.89$, similar to ours which consists of 2 clusters). Some differences between their study and ours are the colour-colour selection used to select star-forming galaxies; they use the UVJ diagram, which as we showed in section 4.4.4, can result in different average sSFRs at $z < 0.5$ than the NUVrJ cut used in this work. We also might expect the resolution of the photometry and SFR tracer to have a significant impact on environmental studies because source blending can be an issue if not properly taken into account. Larger cosmological volumes should be probed to understand the importance of environment on the average sSFR of galaxies.

Erfanianfar et al. (2016) separated group and field environments for two redshift bins ($0.15 < z < 0.5, 0.5 < z < 1.1$) and found at $z < 0.5$, that group and cluster galaxies have a reduction of SFR compared to their counterparts in the field (with a larger fraction of disks being redder). They also report that the flattening of the SFMS for field galaxies is due to an increased fraction of bulge-dominated galaxies at high masses and that the associated quenching process must already be in place before $z \sim 1$.

Once a group or cluster is in gravitational equilibrium, the increased local density should decrease the timescales involved in evolution compared to the relevant timescales in the field because of the larger gravitational potential. Indeed Popesso et al. (2015) show that the cosmic SFR activity declines faster (towards $z = 0$) in group size haloes than in the field. This faster evolution increases the scatter around the SFMS and decreases the average SFR when including all galaxies. To summarize, the local density effects the speed of the star-formation evolution more than the mode (SFMS) of evolution (at least from $0.3 < z < 3$).

4.6. Conclusion

Radio continuum emission is a useful dust-unbiased star formation tracer and stacking is an effective way to push current stellar mass limits achievable through direct detections. We have median stacked 3 GHz images for galaxies in the latest COSMOS photometric catalogue (Laigle et al., 2016) to measure the average dust-independent SFR for galaxies as a function of stellar mass, redshift, environment, and morphology. Our findings can be summarized as follows:

- When separating galaxies into star-forming and quiescent based on their rest-frame NUVrJ colours we find that star-forming galaxies follow a SFR – M_* relation that is steeper at low masses than at high-masses (i.e. a turn-over is present). We model the SFMS relation for star-forming galaxies (and all galaxies) with a new function that allows for the turn-over to occur at increasing stellar mass, for the low mass slope to start steeper at $z = 0$ and approach 1 at high redshift, and for the increase in overall normalization with redshift.

- Following the scatter-stacking technique introduced by Schreiber et al. (2015), we estimate the scatter of the SFMS to be $\sigma \sim 0.3$ dex (at $\log(M/\mathrm{M}_\odot) > 10.5$), with an evolution such that the scatter is smaller ($\sigma \sim$0.2 dex) at high redshift ($z \sim 3.5$).

- The cosmic star formation density peaked at $1.5 < z < 2$, but the measurements still contain large systematics such as SFR calibrations and the necessity of assuming a stellar mass function to account for incompleteness.

- We find evidence for downsizing, meaning that massive galaxies are formed and quenched first. This comes from our result that at higher redshift, more massive galaxies contributed more to the SFR density than at lower redshift. This result is driven by the increasing turn-over mass with redshift in our SFMS.

- We find no significant difference in the SFMS for star-forming galaxies located in different environments probed by the local number density, or by X-ray group membership.

However, there is some evidence for SFR elevation in X-ray cluster members of intermediate mass at $z \sim 0.7$.

- Early-type galaxies have the lowest SFRs at a fixed stellar mass, followed by bulge-dominated galaxies, disk-dominated galaxies, and irregulars. We find this to be the case out to $z < 1.5$.

- Bulge-dominated galaxies follow a shallower SFR – M_* relation than disk-dominated galaxies. As the number of bulge-dominated galaxies increases towards low redshift, the contribution of disk-dominated galaxies to the total SFR occurring declines, particularly at high stellar mass. This increase in bulge-dominated galaxies could be related to the mechanisms responsible for downsizing.

- Combining bulge-dominated galaxies and disk-dominated galaxies can explain, in part, the turn-over observed at high stellar masses.

- If we adopt different $q_{\rm TIR}$ values, measured specifically for disk and spheroidal dominated values, our SFR–M_* relations and the bulge-to-disk decomposition done on stellar mass maps by Lang et al. (2014a), can be combined to imply that the bulge-dominated galaxies have a disk component whose star-formation is significantly suppressed.

Future research avenues will be discussed in Chapter 5.

Table 4.5.: 3 GHz stacking results for star-forming mass-selected galaxies

Δz_p	$\langle z_p \rangle$	$\Delta \log(M_*)$	$\langle \log(M_*) \rangle$	$N_{\rm obj}$	S_p	S_t	rms	log(SFR)
		$\log(\mathrm{M}_\odot)$	$\log(\mathrm{M}_\odot)$		μJy/beam	μJy	μJy/beam	$\log(\mathrm{M}_\odot/\mathrm{yr})$
0.2-0.5	0.37	8.6-9.0	8.79	4355	$0.28^{+0.05}_{-0.07}$	$0.84^{+1.41}_{-0.36}$	$0.045^{+0.000}_{-0.000}$	$-0.48^{+0.43}_{-0.24}$
	0.37	9.0-9.4	9.18	3186	$0.57^{+0.07}_{-0.07}$	$3.07^{+0.98}_{-1.14}$	$0.052^{+0.001}_{-0.001}$	$0.08^{+0.12}_{-0.20}$
	0.37	9.4-9.7	9.54	1635	$1.27^{+0.11}_{-0.09}$	$7.94^{+1.48}_{-1.57}$	$0.074^{+0.003}_{-0.002}$	$0.49^{+0.07}_{-0.10}$
	0.36	9.7-9.9	9.80	845	$1.96^{+0.08}_{-0.15}$	$10.87^{+1.72}_{-1.47}$	$0.104^{+0.002}_{-0.002}$	$0.59^{+0.06}_{-0.06}$
	0.36	9.9-10.1	10.00	671	$2.71^{+0.34}_{-0.20}$	$11.86^{+2.40}_{-1.71}$	$0.116^{+0.002}_{-0.001}$	$0.64^{+0.08}_{-0.07}$
	0.37	10.1-10.3	10.20	555	$3.93^{+0.24}_{-0.34}$	$14.70^{+1.59}_{-1.81}$	$0.128^{+0.001}_{-0.001}$	$0.76^{+0.04}_{-0.06}$
	0.36	10.3-10.5	10.40	429	$4.34^{+0.36}_{-0.49}$	$17.77^{+2.01}_{-1.64}$	$0.145^{+0.002}_{-0.004}$	$0.83^{+0.05}_{-0.04}$
	0.37	10.5-10.7	10.60	310	$5.05^{+0.88}_{-0.69}$	$20.87^{+3.14}_{-2.00}$	$0.169^{+0.003}_{-0.002}$	$0.90^{+0.06}_{-0.04}$
	0.35	10.7-10.9	10.80	201	$5.12^{+0.68}_{-0.80}$	$23.78^{+3.60}_{-3.94}$	$0.205^{+0.003}_{-0.003}$	$0.92^{+0.06}_{-0.08}$
	0.35	10.9-11.6	11.05	125	$4.42^{+0.79}_{-1.06}$	$25.25^{+5.89}_{-5.01}$	$0.263^{+0.007}_{-0.006}$	$0.95^{+0.09}_{-0.10}$
0.5-0.8	0.68	9.0-9.4	9.18	6625	$0.46^{+0.04}_{-0.04}$	$1.17^{+0.77}_{-0.30}$	$0.036^{+0.001}_{-0.000}$	$0.22^{+0.22}_{-0.13}$
	0.67	9.4-9.7	9.54	3373	$0.89^{+0.04}_{-0.05}$	$3.18^{+0.69}_{-0.44}$	$0.050^{+0.000}_{-0.000}$	$0.64^{+0.09}_{-0.06}$
	0.67	9.7-9.9	9.80	1637	$1.56^{+0.10}_{-0.13}$	$5.40^{+0.83}_{-0.60}$	$0.073^{+0.002}_{-0.002}$	$0.87^{+0.06}_{-0.05}$
	0.67	9.9-10.1	9.99	1279	$2.26^{+0.13}_{-0.06}$	$7.67^{+0.69}_{-0.78}$	$0.083^{+0.004}_{-0.001}$	$1.02^{+0.04}_{-0.05}$
	0.67	10.1-10.3	10.20	1041	$3.38^{+0.16}_{-0.19}$	$10.17^{+0.88}_{-0.83}$	$0.093^{+0.001}_{-0.004}$	$1.14^{+0.04}_{-0.04}$
	0.67	10.3-10.5	10.40	795	$3.70^{+0.15}_{-0.16}$	$11.75^{+1.03}_{-1.12}$	$0.106^{+0.003}_{-0.002}$	$1.21^{+0.04}_{-0.04}$
	0.67	10.5-10.7	10.59	613	$4.58^{+0.18}_{-0.26}$	$14.92^{+1.21}_{-1.23}$	$0.118^{+0.001}_{-0.000}$	$1.31^{+0.03}_{-0.04}$
	0.67	10.7-10.9	10.80	379	$5.26^{+0.39}_{-0.77}$	$15.72^{+1.31}_{-1.49}$	$0.157^{+0.006}_{-0.004}$	$1.34^{+0.03}_{-0.04}$
	0.67	10.9-11.6	11.03	252	$5.50^{+0.63}_{-0.59}$	$18.32^{+2.44}_{-2.12}$	$0.178^{+0.002}_{-0.001}$	$1.41^{+0.05}_{-0.05}$
0.8-1.1	0.95	9.0-9.4	9.19	8946	$0.38^{+0.05}_{-0.03}$	$0.64^{+0.14}_{-0.13}$	$0.032^{+0.001}_{-0.001}$	$0.26^{+0.08}_{-0.10}$
	0.95	9.4-9.7	9.54	4921	$0.79^{+0.06}_{-0.05}$	$2.15^{+0.50}_{-0.29}$	$0.042^{+0.001}_{-0.001}$	$0.79^{+0.09}_{-0.06}$
	0.94	9.7-9.9	9.80	2499	$1.31^{+0.04}_{-0.05}$	$3.37^{+0.51}_{-0.52}$	$0.060^{+0.001}_{-0.002}$	$0.98^{+0.06}_{-0.07}$
	0.94	9.9-10.1	9.99	1983	$1.97^{+0.06}_{-0.06}$	$4.88^{+0.45}_{-0.45}$	$0.065^{+0.001}_{-0.001}$	$1.14^{+0.04}_{-0.04}$
	0.93	10.1-10.3	10.20	1534	$2.64^{+0.09}_{-0.10}$	$7.43^{+0.67}_{-0.52}$	$0.074^{+0.001}_{-0.003}$	$1.31^{+0.04}_{-0.03}$
	0.93	10.3-10.5	10.40	1185	$3.67^{+0.20}_{-0.14}$	$9.41^{+0.65}_{-0.44}$	$0.086^{+0.001}_{-0.001}$	$1.42^{+0.03}_{-0.02}$
	0.93	10.5-10.7	10.59	892	$4.38^{+0.26}_{-0.19}$	$11.53^{+0.63}_{-0.75}$	$0.099^{+0.001}_{-0.002}$	$1.51^{+0.02}_{-0.03}$
	0.92	10.7-10.9	10.79	522	$5.04^{+0.41}_{-0.27}$	$14.02^{+0.97}_{-1.28}$	$0.130^{+0.001}_{-0.003}$	$1.57^{+0.03}_{-0.04}$
	0.93	10.9-11.6	11.02	353	$6.30^{+0.28}_{-0.39}$	$18.23^{+1.47}_{-1.69}$	$0.156^{+0.003}_{-0.003}$	$1.70^{+0.03}_{-0.04}$
1.1-1.5	1.29	9.4-9.7	9.54	6858	$0.62^{+0.05}_{-0.05}$	$1.30^{+0.18}_{-0.19}$	$0.036^{+0.000}_{-0.000}$	$0.84^{+0.06}_{-0.07}$
	1.29	9.7-9.9	9.79	3487	$1.03^{+0.02}_{-0.04}$	$2.15^{+0.26}_{-0.24}$	$0.050^{+0.000}_{-0.000}$	$1.07^{+0.05}_{-0.05}$
	1.28	9.9-10.1	9.99	2754	$1.57^{+0.05}_{-0.06}$	$3.38^{+0.30}_{-0.32}$	$0.057^{+0.000}_{-0.001}$	$1.26^{+0.04}_{-0.04}$
	1.31	10.1-10.3	10.19	2229	$2.04^{+0.08}_{-0.07}$	$5.28^{+0.40}_{-0.41}$	$0.061^{+0.000}_{-0.000}$	$1.47^{+0.03}_{-0.04}$
	1.32	10.3-10.5	10.39	1660	$2.71^{+0.10}_{-0.06}$	$6.94^{+0.76}_{-0.43}$	$0.074^{+0.001}_{-0.002}$	$1.59^{+0.05}_{-0.03}$
	1.30	10.5-10.7	10.59	1310	$3.44^{+0.10}_{-0.13}$	$8.75^{+0.69}_{-0.67}$	$0.082^{+0.002}_{-0.001}$	$1.68^{+0.03}_{-0.03}$
	1.31	10.7-10.9	10.80	839	$4.74^{+0.28}_{-0.19}$	$10.97^{+0.78}_{-0.58}$	$0.100^{+0.001}_{-0.003}$	$1.78^{+0.03}_{-0.02}$
	1.32	10.9-11.6	11.04	648	$5.46^{+0.35}_{-0.24}$	$13.91^{+1.08}_{-0.87}$	$0.113^{+0.006}_{-0.002}$	$1.90^{+0.03}_{-0.03}$
1.5-2.0	1.75	9.9-10.1	9.99	3062	$1.18^{+0.06}_{-0.06}$	$2.46^{+0.27}_{-0.27}$	$0.053^{+0.000}_{-0.000}$	$1.39^{+0.04}_{-0.05}$
	1.76	10.1-10.3	10.20	2483	$1.68^{+0.06}_{-0.08}$	$4.19^{+0.49}_{-0.42}$	$0.059^{+0.001}_{-0.000}$	$1.62^{+0.05}_{-0.05}$
	1.75	10.3-10.5	10.39	1975	$2.37^{+0.12}_{-0.13}$	$5.87^{+0.38}_{-0.64}$	$0.066^{+0.001}_{-0.000}$	$1.77^{+0.03}_{-0.05}$
	1.76	10.5-10.7	10.59	1446	$3.23^{+0.09}_{-0.08}$	$7.27^{+0.48}_{-0.42}$	$0.078^{+0.002}_{-0.001}$	$1.86^{+0.03}_{-0.03}$

	1.77	10.7-10.9	10.79	954	$3.88^{+0.18}_{-0.15}$	$8.34^{+0.56}_{-0.59}$	$0.095^{+0.001}_{-0.002}$	$1.93^{+0.03}_{-0.03}$
	1.78	10.9-11.6	11.04	739	$5.26^{+0.26}_{-0.41}$	$12.14^{+0.86}_{-0.78}$	$0.107^{+0.002}_{-0.006}$	$2.10^{+0.03}_{-0.03}$
2.0-2.5	2.19	9.9-10.1	9.99	1630	$0.95^{+0.06}_{-0.07}$	$2.37^{+0.50}_{-0.39}$	$0.073^{+0.001}_{-0.000}$	$1.56^{+0.08}_{-0.08}$
	2.19	10.1-10.3	10.19	1321	$1.40^{+0.10}_{-0.09}$	$2.67^{+0.48}_{-0.39}$	$0.080^{+0.001}_{-0.003}$	$1.61^{+0.07}_{-0.07}$
	2.18	10.3-10.5	10.40	986	$2.03^{+0.16}_{-0.11}$	$3.90^{+0.50}_{-0.44}$	$0.094^{+0.003}_{-0.001}$	$1.77^{+0.05}_{-0.05}$
	2.18	10.5-10.7	10.59	855	$3.02^{+0.20}_{-0.24}$	$6.83^{+0.61}_{-0.63}$	$0.103^{+0.003}_{-0.002}$	$2.02^{+0.04}_{-0.04}$
	2.20	10.7-10.9	10.79	616	$3.54^{+0.22}_{-0.15}$	$7.31^{+0.83}_{-0.63}$	$0.120^{+0.002}_{-0.001}$	$2.05^{+0.05}_{-0.04}$
	2.20	10.9-11.6	11.02	512	$6.39^{+0.20}_{-0.26}$	$12.52^{+0.82}_{-0.92}$	$0.131^{+0.003}_{-0.002}$	$2.29^{+0.03}_{-0.03}$
2.5-3.0	2.67	10.1-10.3	10.19	1367	$1.28^{+0.07}_{-0.12}$	$3.96^{+1.28}_{-1.08}$	$0.079^{+0.002}_{-0.001}$	$1.95^{+0.12}_{-0.14}$
	2.66	10.3-10.5	10.40	955	$1.68^{+0.13}_{-0.12}$	$4.92^{+0.76}_{-0.81}$	$0.096^{+0.000}_{-0.000}$	$2.04^{+0.06}_{-0.08}$
	2.67	10.5-10.7	10.60	674	$2.45^{+0.15}_{-0.17}$	$6.88^{+1.03}_{-1.01}$	$0.113^{+0.005}_{-0.004}$	$2.19^{+0.06}_{-0.07}$
	2.68	10.7-10.9	10.80	373	$4.02^{+0.39}_{-0.40}$	$7.79^{+0.97}_{-1.11}$	$0.160^{+0.004}_{-0.003}$	$2.24^{+0.05}_{-0.07}$
	2.67	10.9-11.6	11.05	301	$6.97^{+0.23}_{-0.40}$	$11.72^{+1.05}_{-1.08}$	$0.170^{+0.003}_{-0.002}$	$2.42^{+0.04}_{-0.04}$
3.0-3.5	3.24	10.1-10.3	10.19	731	$1.09^{+0.07}_{-0.07}$	$2.39^{+0.61}_{-0.60}$	$0.108^{+0.003}_{-0.002}$	$1.88^{+0.10}_{-0.13}$
	3.24	10.3-10.5	10.39	468	$1.57^{+0.16}_{-0.11}$	$3.34^{+0.78}_{-0.74}$	$0.134^{+0.002}_{-0.002}$	$2.03^{+0.09}_{-0.11}$
	3.24	10.5-10.7	10.58	278	$2.21^{+0.32}_{-0.19}$	$5.95^{+1.63}_{-1.08}$	$0.176^{+0.003}_{-0.005}$	$2.28^{+0.10}_{-0.09}$
	3.20	10.7-10.9	10.78	123	$3.07^{+0.58}_{-0.88}$	$7.14^{+1.66}_{-1.66}$	$0.266^{+0.003}_{-0.002}$	$2.35^{+0.09}_{-0.12}$
	3.20	10.9-11.6	11.04	95	$4.86^{+0.35}_{-1.08}$	$8.88^{+1.44}_{-1.37}$	$0.299^{+0.005}_{-0.009}$	$2.44^{+0.07}_{-0.07}$
3.5-4.0	3.75	10.3-10.5	10.39	226	$1.47^{+0.29}_{-0.16}$	$3.52^{+2.45}_{-1.13}$	$0.196^{+0.002}_{-0.004}$	$2.17^{+0.23}_{-0.17}$
	3.71	10.5-10.7	10.58	148	$1.25^{+0.34}_{-0.30}$	$2.88^{+9.57}_{-0.87}$	$0.243^{+0.001}_{-0.003}$	$2.07^{+0.64}_{-0.16}$
	3.73	10.7-10.9	10.78	57	$1.71^{+0.44}_{-0.38}$	$6.54^{+5.31}_{-2.86}$	$0.385^{+0.006}_{-0.002}$	$2.43^{+0.26}_{-0.25}$
	3.84	10.9-11.6	11.05	53	$4.51^{+0.41}_{-0.75}$	$7.46^{+2.66}_{-2.12}$	$0.404^{+0.003}_{-0.002}$	$2.51^{+0.13}_{-0.15}$
4.0-6.0	4.63	10.3-10.5	10.39	156	$0.87^{+0.57}_{-0.23}$	$1.38^{+7.50}_{-1.00}$	$0.235^{+0.006}_{-0.003}$	$1.92^{+0.81}_{-0.56}$
	4.65	10.5-10.7	10.57	81	$0.60^{+0.53}_{-0.16}$	$4.25^{+4.05}_{-2.31}$	$0.325^{+0.005}_{-0.006}$	$2.41^{+0.29}_{-0.34}$
	4.62	10.7-10.9	10.80	51	$1.77^{+0.83}_{-0.57}$	$3.03^{+2.52}_{-1.77}$	$0.401^{+0.002}_{-0.006}$	$2.26^{+0.26}_{-0.38}$
	4.71	10.9-11.6	11.24	89	$1.94^{+0.44}_{-0.59}$	$6.93^{+4.62}_{-3.04}$	$0.314^{+0.002}_{-0.005}$	$2.64^{+0.22}_{-0.25}$

Table 4.6.: 3 GHz stacking results for all mass-selected galaxies where our sample is mass-complete.

Δz_p	$\langle z_p \rangle$	$\Delta \log(M_*)$ $\log(M_\odot)$	$\langle \log(M_*) \rangle$ $\log(M_\odot)$	$N_{\rm obj}$	S_p μJy/beam	S_t μJy	rms μJy/beam	log(SFR) $\log(M_\odot/yr)$
0.2-0.5	0.37	8.6-9.0	8.79	4730	$0.26^{+0.05}_{-0.04}$	$0.75^{+0.86}_{-0.23}$	$0.043^{+0.000}_{-0.001}$	$-0.53^{+0.33}_{-0.16}$
	0.37	9.0-9.4	9.18	3454	$0.54^{+0.07}_{-0.06}$	$2.54^{+1.04}_{-0.81}$	$0.050^{+0.000}_{-0.000}$	$-0.01^{+0.15}_{-0.17}$
	0.37	9.4-9.7	9.54	1846	$1.14^{+0.08}_{-0.09}$	$6.32^{+2.01}_{-1.40}$	$0.070^{+0.002}_{-0.002}$	$0.38^{+0.12}_{-0.11}$
	0.36	9.7-9.9	9.80	1016	$1.56^{+0.11}_{-0.17}$	$9.60^{+2.18}_{-1.62}$	$0.095^{+0.002}_{-0.001}$	$0.55^{+0.09}_{-0.08}$
	0.36	9.9-10.1	10.00	847	$2.09^{+0.11}_{-0.17}$	$9.54^{+1.93}_{-1.39}$	$0.102^{+0.001}_{-0.001}$	$0.55^{+0.08}_{-0.07}$
	0.37	10.1-10.3	10.20	752	$2.65^{+0.19}_{-0.27}$	$11.39^{+1.19}_{-1.54}$	$0.109^{+0.000}_{-0.000}$	$0.66^{+0.04}_{-0.06}$
	0.37	10.3-10.5	10.40	641	$2.75^{+0.23}_{-0.17}$	$12.13^{+2.04}_{-1.63}$	$0.122^{+0.002}_{-0.002}$	$0.68^{+0.07}_{-0.06}$
	0.38	10.5-10.7	10.60	537	$2.46^{+0.22}_{-0.19}$	$12.89^{+2.50}_{-1.91}$	$0.129^{+0.002}_{-0.002}$	$0.72^{+0.08}_{-0.07}$
	0.38	10.7-10.9	10.80	392	$3.13^{+0.19}_{-0.27}$	$12.56^{+2.63}_{-1.96}$	$0.148^{+0.001}_{-0.001}$	$0.71^{+0.08}_{-0.07}$
	0.38	10.9-11.6	11.05	396	$3.50^{+0.17}_{-0.23}$	$11.38^{+2.39}_{-1.54}$	$0.151^{+0.002}_{-0.002}$	$0.67^{+0.08}_{-0.06}$
0.5-0.8	0.68	9.0-9.4	9.18	6969	$0.44^{+0.04}_{-0.04}$	$1.19^{+0.65}_{-0.38}$	$0.035^{+0.001}_{-0.000}$	$0.22^{+0.19}_{-0.16}$
	0.67	9.4-9.7	9.54	3614	$0.84^{+0.07}_{-0.05}$	$3.14^{+0.60}_{-0.50}$	$0.049^{+0.001}_{-0.000}$	$0.64^{+0.08}_{-0.08}$
	0.67	9.7-9.9	9.80	1838	$1.32^{+0.08}_{-0.11}$	$4.87^{+0.74}_{-0.62}$	$0.070^{+0.001}_{-0.002}$	$0.83^{+0.06}_{-0.06}$
	0.67	9.9-10.1	10.00	1549	$1.86^{+0.07}_{-0.10}$	$6.71^{+0.64}_{-0.71}$	$0.076^{+0.003}_{-0.001}$	$0.96^{+0.04}_{-0.05}$
	0.67	10.1-10.3	10.20	1383	$2.62^{+0.20}_{-0.14}$	$7.77^{+0.61}_{-0.77}$	$0.081^{+0.001}_{-0.001}$	$1.03^{+0.03}_{-0.05}$
	0.67	10.3-10.5	10.40	1218	$2.19^{+0.18}_{-0.10}$	$7.84^{+1.18}_{-0.83}$	$0.086^{+0.002}_{-0.001}$	$1.04^{+0.06}_{-0.05}$
	0.67	10.5-10.7	10.60	1051	$2.78^{+0.20}_{-0.14}$	$9.72^{+1.32}_{-1.13}$	$0.091^{+0.002}_{-0.002}$	$1.13^{+0.06}_{-0.05}$
	0.68	10.7-10.9	10.80	834	$2.55^{+0.14}_{-0.11}$	$8.55^{+0.71}_{-1.01}$	$0.107^{+0.002}_{-0.002}$	$1.09^{+0.03}_{-0.05}$
	0.68	10.9-11.6	11.06	861	$3.19^{+0.16}_{-0.17}$	$8.94^{+0.93}_{-0.79}$	$0.101^{+0.001}_{-0.002}$	$1.10^{+0.04}_{-0.04}$
0.8-1.1	0.94	9.0-9.4	9.19	9139	$0.38^{+0.03}_{-0.02}$	$0.62^{+0.11}_{-0.10}$	$0.031^{+0.001}_{-0.001}$	$0.25^{+0.07}_{-0.08}$
	0.94	9.4-9.7	9.54	5193	$0.76^{+0.05}_{-0.05}$	$2.04^{+0.43}_{-0.37}$	$0.041^{+0.001}_{-0.001}$	$0.76^{+0.08}_{-0.09}$
	0.94	9.7-9.9	9.80	2755	$1.22^{+0.06}_{-0.07}$	$3.13^{+0.43}_{-0.46}$	$0.056^{+0.001}_{-0.003}$	$0.94^{+0.06}_{-0.07}$
	0.94	9.9-10.1	9.99	2341	$1.65^{+0.04}_{-0.06}$	$4.25^{+0.54}_{-0.34}$	$0.060^{+0.001}_{-0.001}$	$1.08^{+0.05}_{-0.04}$
	0.93	10.1-10.3	10.20	2063	$1.94^{+0.07}_{-0.09}$	$5.83^{+0.67}_{-0.74}$	$0.065^{+0.001}_{-0.001}$	$1.21^{+0.05}_{-0.06}$
	0.93	10.3-10.5	10.40	1869	$2.30^{+0.09}_{-0.13}$	$6.51^{+0.64}_{-0.56}$	$0.069^{+0.001}_{-0.001}$	$1.25^{+0.04}_{-0.04}$
	0.93	10.5-10.7	10.60	1646	$2.25^{+0.09}_{-0.09}$	$6.61^{+0.57}_{-0.60}$	$0.071^{+0.000}_{-0.001}$	$1.26^{+0.04}_{-0.04}$
	0.92	10.7-10.9	10.80	1267	$2.39^{+0.13}_{-0.12}$	$7.21^{+0.89}_{-0.74}$	$0.083^{+0.000}_{-0.000}$	$1.29^{+0.05}_{-0.05}$
	0.92	10.9-11.6	11.05	1354	$3.10^{+0.23}_{-0.20}$	$8.33^{+0.62}_{-0.65}$	$0.081^{+0.003}_{-0.001}$	$1.35^{+0.03}_{-0.04}$
1.1-1.5	1.29	9.4-9.7	9.54	6921	$0.62^{+0.04}_{-0.04}$	$1.29^{+0.28}_{-0.17}$	$0.035^{+0.000}_{-0.000}$	$0.84^{+0.09}_{-0.06}$
	1.29	9.7-9.9	9.80	3574	$1.02^{+0.03}_{-0.04}$	$2.12^{+0.27}_{-0.22}$	$0.050^{+0.000}_{-0.001}$	$1.06^{+0.05}_{-0.05}$
	1.28	9.9-10.1	9.99	2929	$1.47^{+0.10}_{-0.06}$	$3.19^{+0.25}_{-0.37}$	$0.055^{+0.001}_{-0.001}$	$1.23^{+0.03}_{-0.05}$
	1.29	10.1-10.3	10.19	2541	$1.78^{+0.07}_{-0.07}$	$4.51^{+0.43}_{-0.28}$	$0.058^{+0.001}_{-0.000}$	$1.39^{+0.04}_{-0.03}$
	1.30	10.3-10.5	10.40	2056	$2.14^{+0.12}_{-0.19}$	$5.61^{+0.48}_{-0.47}$	$0.066^{+0.001}_{-0.001}$	$1.49^{+0.04}_{-0.04}$
	1.28	10.5-10.7	10.60	1867	$2.17^{+0.09}_{-0.12}$	$6.51^{+0.67}_{-0.69}$	$0.068^{+0.002}_{-0.001}$	$1.54^{+0.04}_{-0.05}$
	1.28	10.7-10.9	10.80	1435	$2.50^{+0.12}_{-0.13}$	$6.69^{+0.54}_{-0.61}$	$0.077^{+0.001}_{-0.001}$	$1.55^{+0.03}_{-0.04}$
	1.27	10.9-11.6	11.05	1341	$3.32^{+0.14}_{-0.13}$	$8.82^{+0.66}_{-0.50}$	$0.081^{+0.002}_{-0.002}$	$1.66^{+0.03}_{-0.03}$
1.5-2.0	1.75	9.9-10.1	9.99	3149	$1.16^{+0.05}_{-0.04}$	$2.39^{+0.27}_{-0.25}$	$0.052^{+0.000}_{-0.000}$	$1.38^{+0.05}_{-0.05}$
	1.75	10.1-10.3	10.20	2656	$1.60^{+0.07}_{-0.08}$	$3.96^{+0.53}_{-0.36}$	$0.057^{+0.000}_{-0.001}$	$1.59^{+0.05}_{-0.04}$
	1.75	10.3-10.5	10.39	2178	$2.20^{+0.09}_{-0.05}$	$5.40^{+0.66}_{-0.44}$	$0.064^{+0.001}_{-0.001}$	$1.73^{+0.05}_{-0.04}$

	1.74	10.5-10.7	10.59	1745	$2.68^{+0.09}_{-0.09}$	$6.33^{+0.39}_{-0.44}$	$0.071^{+0.001}_{-0.000}$	$1.80^{+0.03}_{-0.03}$
	1.73	10.7-10.9	10.79	1338	$2.83^{+0.15}_{-0.17}$	$6.11^{+0.37}_{-0.48}$	$0.081^{+0.000}_{-0.002}$	$1.77^{+0.03}_{-0.04}$
	1.73	10.9-11.6	11.04	1256	$3.23^{+0.16}_{-0.17}$	$8.36^{+0.63}_{-0.64}$	$0.084^{+0.001}_{-0.001}$	$1.91^{+0.03}_{-0.03}$
2.0-2.5	2.19	10.1-10.3	10.19	1364	$1.39^{+0.10}_{-0.07}$	$2.65^{+0.36}_{-0.35}$	$0.080^{+0.002}_{-0.002}$	$1.61^{+0.06}_{-0.06}$
	2.19	10.3-10.5	10.40	1041	$1.88^{+0.15}_{-0.22}$	$3.74^{+0.56}_{-0.47}$	$0.091^{+0.004}_{-0.001}$	$1.76^{+0.06}_{-0.06}$
	2.19	10.5-10.7	10.60	935	$2.77^{+0.12}_{-0.14}$	$6.37^{+0.60}_{-0.60}$	$0.099^{+0.001}_{-0.001}$	$1.99^{+0.04}_{-0.04}$
	2.21	10.7-10.9	10.79	690	$3.08^{+0.15}_{-0.29}$	$6.72^{+0.81}_{-0.70}$	$0.114^{+0.002}_{-0.003}$	$2.02^{+0.05}_{-0.05}$
	2.20	10.9-11.6	11.03	620	$5.31^{+0.53}_{-0.45}$	$10.62^{+0.70}_{-0.84}$	$0.116^{+0.001}_{-0.002}$	$2.22^{+0.03}_{-0.04}$
2.5-3.0	2.67	10.1-10.3	10.19	1382	$1.28^{+0.07}_{-0.09}$	$3.83^{+1.45}_{-0.92}$	$0.079^{+0.002}_{-0.001}$	$1.93^{+0.14}_{-0.12}$
	2.66	10.3-10.5	10.40	987	$1.66^{+0.10}_{-0.10}$	$4.77^{+1.24}_{-0.86}$	$0.094^{+0.001}_{-0.001}$	$2.03^{+0.10}_{-0.09}$
	2.67	10.5-10.7	10.60	729	$2.33^{+0.18}_{-0.22}$	$6.10^{+0.87}_{-1.00}$	$0.109^{+0.002}_{-0.002}$	$2.13^{+0.06}_{-0.08}$
	2.68	10.7-10.9	10.80	431	$3.74^{+0.35}_{-0.40}$	$7.63^{+0.80}_{-0.75}$	$0.145^{+0.002}_{-0.003}$	$2.23^{+0.04}_{-0.04}$
	2.67	10.9-11.6	11.05	354	$6.37^{+0.66}_{-0.60}$	$11.30^{+1.02}_{-0.77}$	$0.158^{+0.003}_{-0.001}$	$2.40^{+0.04}_{-0.03}$
3.0-3.5	3.24	10.3-10.5	10.39	472	$1.56^{+0.11}_{-0.12}$	$3.37^{+0.73}_{-0.65}$	$0.134^{+0.002}_{-0.001}$	$2.03^{+0.08}_{-0.09}$
	3.23	10.5-10.7	10.58	289	$2.10^{+0.22}_{-0.25}$	$5.58^{+1.33}_{-0.94}$	$0.175^{+0.002}_{-0.002}$	$2.25^{+0.09}_{-0.08}$
	3.19	10.7-10.9	10.78	145	$3.05^{+0.27}_{-0.55}$	$7.41^{+1.54}_{-1.37}$	$0.246^{+0.005}_{-0.008}$	$2.36^{+0.08}_{-0.09}$
	3.21	10.9-11.6	11.05	126	$4.72^{+0.62}_{-0.58}$	$8.86^{+1.54}_{-1.62}$	$0.264^{+0.003}_{-0.005}$	$2.44^{+0.07}_{-0.09}$
3.5-4.0	3.71	10.5-10.7	10.58	152	$1.25^{+0.33}_{-0.32}$	$2.78^{+9.02}_{-0.87}$	$0.239^{+0.002}_{-0.004}$	$2.06^{+0.63}_{-0.16}$
	3.74	10.7-10.9	10.78	67	$1.71^{+0.30}_{-0.21}$	$6.08^{+3.01}_{-2.93}$	$0.356^{+0.004}_{-0.002}$	$2.40^{+0.17}_{-0.29}$
	3.81	10.9-11.6	11.09	69	$3.92^{+1.69}_{-0.51}$	$5.87^{+2.52}_{-2.23}$	$0.356^{+0.003}_{-0.002}$	$2.40^{+0.16}_{-0.21}$
4.0-6.0	4.65	10.5-10.7	10.58	91	$0.71^{+0.23}_{-0.39}$	$4.93^{+2.75}_{-2.24}$	$0.309^{+0.003}_{-0.001}$	$2.48^{+0.19}_{-0.26}$
	4.64	10.7-10.9	10.80	54	$1.61^{+0.57}_{-0.43}$	$2.51^{+2.83}_{-1.65}$	$0.384^{+0.008}_{-0.006}$	$2.18^{+0.33}_{-0.46}$
	4.65	10.9-11.6	11.23	106	$1.97^{+0.15}_{-0.44}$	$5.78^{+3.49}_{-2.05}$	$0.282^{+0.001}_{-0.001}$	$2.55^{+0.21}_{-0.19}$

5 Summary and Outlook

5.1. Summary

We started this thesis on a journey through a "cosmic day", following how galaxies form their stars, with the average star formation activity peaking around $z \sim 2$, 10 billion years ago. About 25% of all stellar mass formed before this epoch, and another 25% formed since $z = 0.7$ when the Universe was half its current age (Madau & Dickinson, 2014). What are the important drivers of the cosmic SFRD? What determines the average SFR of galaxies and thereby controls the build-up of stellar mass in the Universe? Astronomers aim to empirically relate galaxy SFR to galaxy properties including stellar mass, morphology, gas mass, environment and black hole activity, with the hope of understanding how the different processes interact. Determining which processes are important in different regimes and different scales is a fundamental aim of galaxy evolution research. This thesis is concerned with the time evolution of galaxy properties and hopes to contribute to our picture of how galaxies develop.

Star formation rates tell us how fast a galaxy is growing, in isolation. Analysing the SFR activity at high redshift ($z > 4$)is currently only possible in rest-frame UV. This presents an obstacle for our understanding of early galaxies. The magnitude of UV light unobserved due to dust-attenuation at $z \gg 2$ is unclear. In this thesis, we have contributed towards answering the following questions:

- How do the amount and spatial distribution of dust affect measurements of SFR?
- How do our high-z measurements of SFR activity change when we use a dust free measurement? What does the SFR distribution of the galaxy population look like as a function of time?
- What role does galaxy morphology and environment play in determining the SFR of galaxies?

We address these questions in a statistical way using large samples of galaxies observed with multiband photometry. These observations allow galaxy properties such as stellar mass and redshift to be modelled.

5.1.1. Clumpier dust and higher FUV attenuation at $z \sim 0.7$

Dust is a small but important component of galaxies, obscuring on average 1/3 of the starlight in local star-forming galaxies. Dust composition and distributions remain poorly constrained. In Chapter 2 we used a novel approach to probe the dust geometry of a statistical sample of disk-dominated galaxies at $z = 0$ (SDSS) and $z = 0.7$ (COSMOS). For edge-on disks, the photons travel through a larger column density than for face-on disks and are therefore more likely to be scattered or absorbed by dust along the line-of-sight. We measured the inclination dependence of galaxy far-ultraviolet (FUV) luminosities to constrain the average optical depth and the clumpiness of the dust by fitting a simple radiative transfer model (Tuffs et al. 2004). We found that UV attenuation has increased between $z \sim 0$ and $z \sim 0.7$ by a factor of ~ 3.5. A higher fraction of clumpy dust around nascent star-forming regions can explain the more substantial UV attenuation at z$\sim$0.7. The fractional increase of clumpy dust matches well the increase in SFR and gas mass with redshift. Our results indicate that the additional dust mass at $z \sim 0.7$ is mostly associated with star forming clumps, rather than a diffuse component.

In Chapter 3, we then evaluated dust-corrected FUV SFRs from different attenuation correction methods based on the hybrid mid-infrared (MIR) plus FUV relation, UV-slope, and radiative transfer. We assessed the performances of the attenuation correction methods by their ability to remove the dependency of the corrected SFR on inclination, as well as returning, on average, the expected population mean SFR. We found that combining MIR (rest-frame $\sim 13\,\mu$m) and FUV luminosities gives the most inclination independent SFRs and reduces the intrinsic SFR scatter most out of the methods tested; this is encouraging because many studies at $z > 1$ rely on such hybrid combinations (e.g.,Whitaker et al. 2014). We also found that more complicated model attenuation curves are required to explain the UV colours of local galaxies – likely because dust is not in a simple distribution, but consists of both clumpy and diffuse components at low redshift.

If our results are confirmed, then using galaxy inclination (from high resolution rest-frame optical/NIR images) and UV observations to probe dust opacity will be a promising technique to learn about the dust distributions for existing samples of galaxies at higher redshift observed with HST/WFC3 and future JWST observations.

5.1.2. Evolution of the main sequence out to $z < 5$ in the COSMOS field

Recently, tension has arisen as to the form of the main sequence, with some studies reporting a flattening at high stellar masses. The form depends on the methods for sample selection as well as on SFR tracers used. In Chapter 4, we measure average SFRs for over 200,000 star-forming galaxies in the 2 square degree COSMOS field using a single uniform SFR tracer – the radio continuum at 3GHz – and find evidence for a flattening of the main sequence at $z < 1.5$. We calculated dust-independent radio-determined SFRs from a stacking analysis out to redshift $z \sim 5$, pushing our analysis out past the peak of cosmic SFR ($1 < z < 3$) to probe the star formation activity in the early Universe. The advantages of our sample in the COSMOS field are (a) the rich ancillary data, providing an excellent input catalog, (b) the deepest ($2.3\,\mu$Jy/beam) and highest resolution ($0.75''$) radio data over such a wide area to date (Smolčić et al., 2017b) and (c) no source confusion that limited previous IR

studies thanks to the radio data's high angular resolution. This work updates that of Karim et al. (2011) who developed a stacking analysis for 1.4 GHz imaging data in COSMOS and analysed a shallower 3.6 μm-selected sample out to $z \sim 3$.

Stacking the observed 3 GHz radio fluxes of all star-forming galaxies in bins of stellar mass and redshift, we found that at low-redshifts, where our input catalogue is complete down to $\log(M_*/\mathrm{M}_\odot) < 9$, that the low mass slope of the SFMS is steeper than one, and that the high-mass slope is shallower than one, with a turn-over mass of $\sim 10^{10}$ $\mathrm{M}_\odot$. We have fit a star-formation main-sequence (SFMS) relationship that describes how the low-mass slope becomes slightly shallower at higher redshift (approaching unity), and we describe the evolution of the turn-over mass, which increases with redshift (consistent with the findings from Tomczak et al. 2016). For galaxies following the functional form proposed in this work, the sSFRs are highly consistent across stellar mass at high redshift (where the slope of the SFMS approaches unity), and become more divergent towards the present time, with massive galaxies evolving faster, decreasing their sSFR. The fact that the turn-over progresses to lower-mass galaxies with redshift is consistent with the hypothesis that quenching starts with the highest mass systems and progresses to lower mass systems over cosmic time.

Morphological transformation: In Chapter 4 we also studied the main sequence as a function of galaxy morphology out to $z \sim 1.5$ using HST morphological measurements (Scarlata et al., 2007) probing rest-frame optical wavelengths. Massive galaxies with a bulge tend to have lower SFRs at fixed mass and redshift. We find the flattening of the high-mass slope can be largely explained by the inclusion of bulge-dominated galaxies which follow a shallower SFR–M_* relation than disk-dominated galaxies. A stellar bulge can provide large-scale shear to inject turbulence thereby stabilizing the gas disk from fragmenting (morphological suppression; Martig et al. 2009). We showed the fraction of SFR activity that is occurring in galaxies of different morphologies and found the fraction contributed by disk-dominated galaxies is highest at stellar masses of $10^{10}\,\mathrm{M}_\odot$. As bulges grow more prominent in the low-redshift galaxy population, particularly at high stellar masses, the flattening of the main sequence becomes more significant.

Environmental effects: Using ancillary data from the COSMOS field, we found that galaxy environment probed by X-ray-groups, clusters, and local galaxy number density has little effect on the shape of the main sequence at $z > 0.3$. Environmental quenching (e.g., gas strangulation or stripping) only becomes important at $z \ll 1$, whereas morphological effects were already in place at $z > 1.5$.

5.1.3. Evolution of star-forming galaxies – from gas to stars

Since cosmic noon, it seems that the accretion of cold gas onto all galaxies has slowed down, which explains the overall decrease in the normalisation of the SFRD at all stellar masses (and the SFMS). But with the latest COSMOS data, we also see a mass-dependent decrease in SFR. At a given redshift, the SFRD is not distributed evenly across all stellar masses, rather there is a characteristic stellar mass that contributes the most to the SFRD out to $z = 2.5$. We found in Chapter 4 that this characteristic stellar mass in which most new stars are formed increases with redshift. The increasing characteristic mass with redshift and the evolving turn-over in the SFMS corresponds to bulge formation and a decline in SFR in massive galaxies. The mechanism that reduces the SFR proceeds to be effective at lower

stellar masses towards the present epoch.

Molecular gas has been observed to be correlated with SFR, both globally and within galaxies from the present epoch to early cosmic times (Carilli & Walter, 2013; Tacconi et al., 2018; Scoville et al., 2017). During this thesis, we have contributed directly to the measurements of galaxy SFR, and indirectly to the measurements of the dust mass for massive star-forming galaxies. Through our group's work on the A^{3}COSMOS project[47], using ALMA observations of cold dust in the COSMOS field, we have also estimated the evolution of gas mass fraction through cosmic time (Liu et al. in prep). The higher molecular gas fraction at intermediate redshifts is likely responsible for both the higher fraction of clumpy dust (Chapter 2) and the higher sSFR (Chapter 4).

5.2. Open issues arising from this thesis

Naturally, this thesis represents a tiny piece in a very large puzzle, and while we have started to answer some questions, more have been identified.

In Chapters 2 and 3 we probed the FUV SFRs and dust properties in massive star-forming disk galaxies at $z \sim 0.7$, and $z \sim 0$. If high redshift galaxies have larger disk scale heights, then we would need to produce a new library of model SEDs to be used because the geometry strongly affects the predictions for the attenuation of stellar light. This would be very interesting to pursue with the Popescu et al. (2011) model and could allow our results from Chapter 2 and 3 to be applied at $z > 0.7$ where scale heights might be expected to be larger due to the larger gas fractions and turbulence (Bournaud et al., 2009). Spatially resolved observations of dust are becoming possible with ALMA, so observations to confirm our interpretation that dust is clumpier at higher redshift are possible[48]. JWST will also be helpful at probing the dust properties of galaxies at intermediate redshifts, and the SFRs of galaxies at high redshift.

We have used the best 3 GHz SFR calibration available for each stack, but more work needs to be done to fully understand the large deviations of the different calibrations. For example, why are the stacking results from Magnelli et al. (2015) different from the survival analysis results of Delhaize et al. (2017) in terms of the infrared radio correlation? And why is the evolution of the infrared-radio correlation different for spheroidal galaxies and disk galaxies? What if we use a direct radio continuum to SFR calibration, rather than relying on the infrared relation? These questions could partly be explained by a non-linear infrared-radio correlation and will be addressed in future work (see Section 5.3).

Our results in Chapter 4 on the SFMS for different morphological types is consistent with the idea that disk galaxies transform into spheroidal galaxies, but they do not suggest how such a transformation could happen. Despite almost 100 years of observing the structures of galaxies, we still do not fully understand how they came about. It is becoming clear

[47] We have downloaded, calibrated, imaged and created source catalogs from all the public data in the ALMA archive in the COSMOS field (first data release will be presented by Liu et al., subm.) https://sites.google.com/view/a3cosmos/home

[48] However, not too easily at sub-kpc resolution (although see Hodge et al. 2018). For example, a high-resolution CO line and dust continuum imaging program of six massive star-forming galaxies at z=0.7 at 0.05" or 300 parsecs resolution with ∼10 min integration per source (PI Freundlich) was not able to detect anything.

that there are many pathways to quiescence. Future observations are required to determine whether the gas in bulge-dominated galaxies is stabilized against fragmentation, or is not present to form stars (either it has been removed by feedback or cold gas is no longer able to be accreted onto the galaxy disk). How do the bulges form? Does the formation mechanism have something to do with quenching? We suggested that mergers can cause elevated SFRs and disturbed morphologies, causing irregular galaxies to have higher SFRs at a fixed stellar mass. What other processes can cause a starburst? How long does a starburst phase last and how important is it for the mass growth of galaxies?

5.3. Outlook

In this section we outline future research directions

5.3.1. Studying star formation at radio wavelengths

We are entering a golden age of radio astronomy with the recent significant instrument advancements (with VLA, LOFAR, MeerKAT, Australian Square Kilometre Array Pathfinder (ASKAP), and with ngVLA and Square Kilometer Array (SKA) being prominent future ones), bringing radio astronomy to the forefront of multiwavelength research (e.g., Padovani 2016). Wider area surveys, such as the upcoming MeerKAT International GHz Tiered Extragalactic Exploration (MIGHTEE) survey, which will cover 20 deg^2 of the most well studied fields (including COSMOS), and should be able to directly detect galaxies with SFR $\sim 15\,\mathrm{M_\odot yr^{-1}}$ to $z = 1$ and SFR $\sim 150\,\mathrm{M_\odot yr^{-1}}$ to $z \sim 3$ (Jarvis et al., 2016), and allow for further minimization of cosmic variance. Next generation radio surveys (e.g. next-generation VLA, Square Kilometer Array, and pre-cursors) will use radio-continuum emission to measure SFRs down to lower masses and out to higher redshifts than currently possible for significant numbers of individual galaxies. For example, the SKA-1 UltraDeep 1 deg^2 survey at ∼1GHz will detect galaxies with SFR $> 50\,\mathrm{M_\odot yr^{-1}}$ out to $z \sim 6$ (Prandoni & Seymour, 2015). However, to fully exploit these new and improved instruments, we need a better quantitative understanding of the radio emission in galaxies.

Common radio–SFR calibrations are bootstrapped from the still poorly understood infrared-radio correlation (IRRC). Recent results in the COSMOS field (Delhaize et al., 2017) show that the average IR-to-radio luminosity ratio, q_{TIR}, decreases with redshift; an evolution in an opposite sense than expected due to the increase by theory (inverse Compton scattering off the cosmic microwave background photons at z>2 is expected to suppress nonthermal radio emission). Tying down the local IRRC is critical for specifying a robust radio–SFR calibration and placing our high redshift results in context. Recently, we have assembled a sample of 90,000 galaxies at $z < 0.2$ from SDSS with publicly available IR (WISE, *Herschel*, or IRAS) or 1.4 GHz (VLA) detections that will be presented in Molnar, Leslie et al. (2019; in prep). Our catalogue contains ∼11,000 sources detected in both IR and radio continuum and is ∼5 times larger and ∼4 times deeper than the previously largest sample in Yun et al. (2001) and with better IR wavelength coverage (see Figure 5.1).

We plan to exploit this new catalogue to investigate what galaxy properties drive the scatter in the IRRC ratio (e.g., stellar mass, metallicity, gas and SFR surface density, and stellar age). If these parameters evolve with redshift, then that would support our understanding

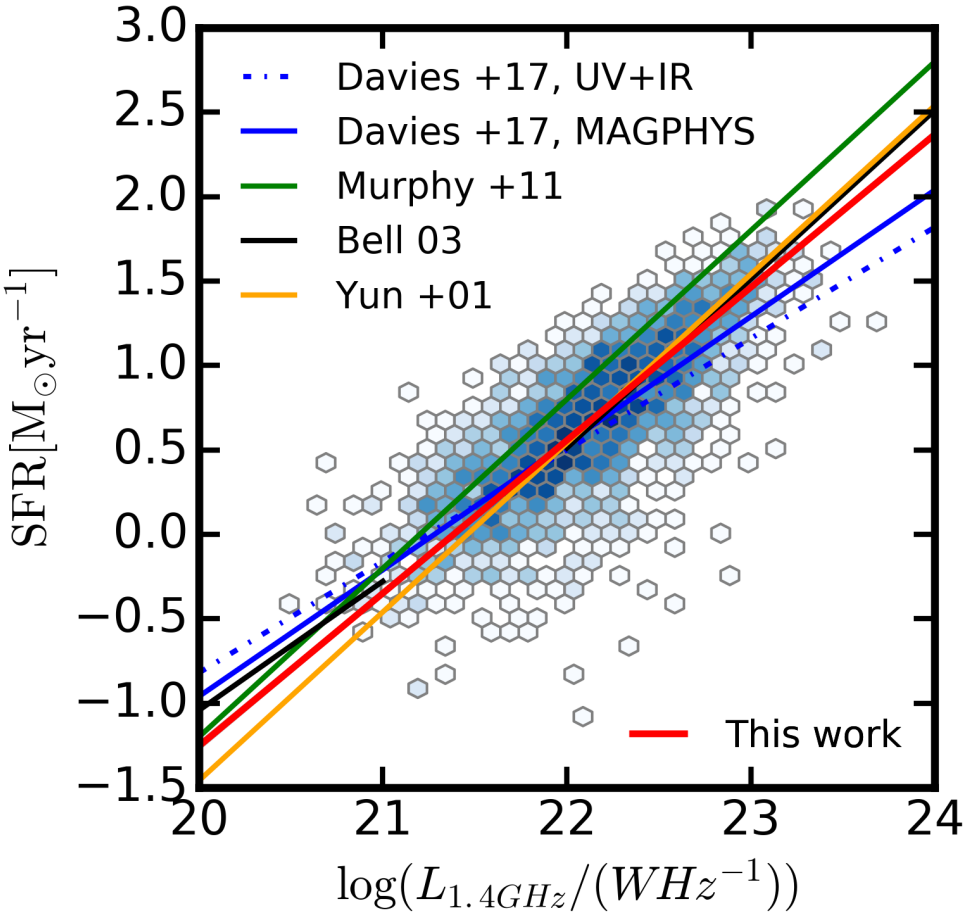

Figure 5.1.: Local radio-SFR calibrations. The star formation rate – $L_{1.4\mathrm{GHz}}$ correlation using a flux-limited sample of star-forming galaxies (Molnar et al. in prep). SED-based SFR values are drawn from the GALEX-SDSS-WISE Legacy Catalog (GSWLC; Salim et al. 2016) for the 2,370 overlapping sources. Other commonly used SFR recipes (Yun et al., 2001; Bell, 2003; Davies et al., 2017), the SFR-conversion inferred using our $L_{1.4\mathrm{GHz}}$-dependent IR-radio ratio, and our best-fit to the data, are shown.

of the IRRC decreasing with redshift. In the COSMOS field, we will use the parent sample described in Delhaize et al. (2017), which contains galaxies out to $z < 5$, to test if high redshift measurements of the IRRC are in agreement with our expectations extrapolated from the local Universe and theoretical predictions from, e.g., Lacki et al. (2010).

Stellar mass and metallicity: Studies have reported that the IRRC breaks down at low luminosities, stellar masses, or metalicities, conditions that were typical in the early Universe (Hunt et al., 2005). We will explore how radio luminosity depends on stellar mass derived from SED fits (Salim et al., 2018) and test the effect of metallicity on the IRRC. In COSMOS, spectra from the zCOSMOS and FMOS-COSMOS surveys can be used to measure metallicity following a stacking approach (Zahid et al., 2014).

Gas mass and surface density: Modern models of the IRRC such as, Lacki et al. (2010), Lacki & Thompson (2010), Schleicher & Beck (2013), expect the SFR surface density ($\Sigma_{\rm SFR}$) and gas density $\rho_{\rm gas}$ to control $q_{\rm TIR}$. Increasing gas and photon energy (SFR) density could complicate radio emission because cooling processes such as inverse Compton, bremsstrahlung, and ionization might become important, as might the ability of the galaxy to retain CR particles (Lacki et al., 2010). With the ALMA sub-mm continuum data provided by the A^{3}COSMOS project, we can investigate the effect of gas mass on the IRRC and test whether the evolution is consistent with the $q_{\rm TIR}$ data.

Star formation history: IR and radio emission can trace SFRs on different timescales. Only when supernovae begin to contribute to the radio emission after ~ 10 Myr will the strong non-thermal component be detected, whereas stars heat dust from their inception. Galaxies with a strong bursty star formation history can be identified using Hδ equivalent width (locally) and SED fits (in COSMOS). We can test the influence of stellar population age, as traced by the D_n4000 spectral indexes, on the radio and IR luminosities of galaxies out to $z \sim 1$. SDSS spectra provide D_n4000 measurements out to $z < 0.2$, and in the COSMOS field, we have D_n4000 measurements for thousands of galaxies from the hCOSMOS ($0.2 < z < 0.5$; Damjanov et al. 2018) and LEGA-C ($0.6 < z < 1$; van der Wel et al. 2016) surveys.

Radio SED: There is mounting evidence that the very well sampled radio SED of the nearby starburst galaxy M82 (e.g., Condon 1992), regularly taken as the typical radio SED for star-forming galaxies, is too simplistic a model to capture the nature of the radio spectrum in local star-forming galaxies (e.g., Leroy et al. 2011a; Tabatabaei et al. 2017). When the application of a k-correction is needed, such as for our study in Chapter 4, the regularly assumed simple, single-power-law shape (with a spectral index of -0.8) of the star-forming galaxy radio SED may easily lead to substantial systematic over- or under-estimation of radio luminosity. Tisanić et al. (2019) constructed the average radio spectral energy distribution for a 1.4 GHz-selected sample of highly star-forming galaxies (SFR $> 100\,{\rm M}_\odot{\rm yr}^{-1}$) in the COSMOS field using 1.4 GHz, 3 GHz, 325 MHz, and 610 MHz observations. Their average SED was found to follow a broken power-law shape, having a steeper spectral index at 10 GHz compared with normal SFGs, which could imply a smaller fraction of thermal emission. Multi-frequency observations for individual galaxies of different types (e.g., on the SFMS, quiescent, disk-dominated, bulge-dominated), across cosmic time, will require hundreds of hours of VLA observations but will be critical for calibrating the radio continuum as a SFR tracer.

5.3.2. Studying dust

The study of dust formation and destruction mechanisms is still in its infancy. Efforts are being made to include dust in semi-analytical models (e.g. Popping et al. 2017) and to include the effect of realistic dust attenuation on mock observations in hydrodynamical simulations (e.g. Camps et al. 2018, Baes et al. 2019). Currently, there are major discrepancies between models and observations, but this will be a promising space to watch in the next few years.

From an observational standpoint, the IR regime is an important diagnostic for understanding dust, but absorption from water vapour in the atmosphere makes observations difficult. Future FIR space observatories are still in the planning stages, but could be launched by the late 2020s/early 2030s eg., the Galaxy Evolution Probe (Glenn et al., 2018), Wide-Field InfraRed Survey Telescope (WFIRST) (Spergel et al., 2015), SPace Infrared telescope for Cosmology and Astrophysics (SPICA) (Spinoglio et al., 2017).

5.3.3. Studying the stellar mass of galaxies

UltraVISTA DR 4, released March 2019, reaches $K_s = 24.9, 24.5$ mag in the Ultra-Deep and Deep field. This will allow a mass-complete sample to be selected down to lower masses by ~ 0.2 dex compared to our study in Chapter 4 (once the multi-band photometric redshifts and stellar masses have been calculated). Many other programs are being carried out in the COSMOS field and other legacy fields. For example, the Hawaii Two-O survey, a companion to a legacy warm Spitzer Program, will cover 20 deg^2 with deep Subaru Hyper Suprime Cam images and should detect $> 500{,}000$ galaxies at $3 < z < 7$. In addition to providing deep, high-resolution NIR/MIR photometry, JWST will take spectroscopic observations facilitating the measurement of exact redshifts, and nebular line emission, quantifying the degree to which some uncertainties have affected the photometric analyses carried out to date.

5.4. Final remarks

The field of galaxy evolution proceeds in a loop: theoretical models and simulations motivate observations, and observations then, in turn, constrain the theoretical models. By analysing the observed properties large numbers of galaxies, we have made statements about the demographics of galaxies. We found that for massive galaxies, the fraction of dust in a clumpy component closely follows the gas fraction evolution resulting in higher FUV attenuation factors at $z \sim 0.7$. SFR calibrations that rely only on UV wavelengths are underestimated for highly inclined galaxies. We showed that galaxy disks are, on average, transparent at radio wavelengths. We then proceeded to use radio continuum to estimate the dust-unbiased SFRs of galaxies out to $z \sim 5$ with a stacking analysis. It became clear in Chapter 4 that radio SFR calibrations still need to be better understood, however, we believe that our important results are qualitatively correct: i.e. there is a bend in the SFR–M_* relation (when it is calculated as the median SFR at a fixed stellar mass), that bulges contribute to this bending, and that galaxies are downsizing (massive galaxies formed at earlier epochs, and their SFR was shut down earlier). Future observations and simulations at smaller physical scales are needed to better understand the detailed physics of galaxy evolution and link with our phenomenological understanding at global scales.

A Appendix to Chapter 2

A.1. Choice of normalisation

Systematic uncertainties in our analysis arise from the normalisation factor adopted to represent the expected 'true' SFR of our galaxies. Here we discuss how our results change as a result of different choices for normalisation; we do not account for all possible differences, but rather focus on a few cases.

A.1.1. Choice of star-forming main sequence

Many different SFMS relations exist in the literature. Different methods for selecting "star-forming" galaxies tend to produce different results (Karim et al., 2011; Speagle et al., 2014). Other differences such as assumed IMF, SFR calibration, and different SED inputs such as star formation histories also make comparisons between studies challenging. Studies such as Schreiber et al. (2015), Lee et al. (2015) and Whitaker et al. (2014), report a turnover or flattening in the galaxy main sequence at high-stellar mass ($\log(M_*/\mathrm{M}_\odot) > 10.3$). The origin of the turnover could be due to samples that include more bulge-dominated galaxies, which lie below the main sequence that is defined for pure disk-dominated galaxies (e.g. Salmi et al. 2012; Lang et al. 2014b; Whitaker et al. 2015). Figure A.1 is a visualisation of different SFMS relations from the literature, including the relations used in this work, at $z \sim 0$ (the relations with lower SFRs) and at $z \sim 0.7$ (higher SFRs). We investigate how our results change when using different main-sequence relations.

Speagle et al. (2014) compiled 25 studies from the literature and found a consensus SFMS relation after converting all observations to a common set of calibrations. We use the best fit

$$\log(\mathrm{SFR}_{\mathrm{SFMS}}) = (0.84 - 0.026t)\log(M_*) - (6.51 - 0.11t), \tag{A.1}$$

where t is the age of the universe in Gyr. Speagle et al. (2014) removed data with $t < 2.5$ Gyr (and $t > 11.5$ Gyr) from their analysis. Their reasons for removing the low-redshift data is because most local studies have been based on the SDSS and most require some aperture corrections. In Figure A.1, we show Equation A.1 extrapolated to the redshift of our local sample, $0.04 < z < 0.1$ is shown in shaded green.

Schreiber et al. (2015) use a method called "scatter stacking" and combine direct UV and FIR light for a mass-complete sample of star-forming galaxies and find a close-to-linear slope of the relation but allow for an observed flattening of the SFMS that takes places at masses $\log(M_*/\mathrm{M}_\odot) > 10.5$ at low redshift. Schreiber et al. (2015) found the following equation to represent the locus of the SFMS:

$$\log(\mathrm{SFR}_{\mathrm{SFMS}}) = m - 0.5 + 1.5\log(1+z) - 0.3\left[\max(0, m - 0.36 - 2.5\log(1+z))\right]^2, \quad \text{(A.2)}$$

where $m = \log(M_*/10^9\mathrm{M}_\odot)$. The error bars on Equations A.1 and A.2 were omitted because we did not incorporate them in our SFR-inclination analysis. Figure A.1 shows the Schreiber et al. (2015) SFMS relation at the redshifts considered for this analysis. The lowest redshift considered in the Schreiber et al. (2015) analysis was $z = 0.3$, therefore the low-redshift relation is also an extrapolation of the data.

For our main analysis, we adopted an updated SFMS relationship based off an inter-sample 'concordance' analysis by Sargent et al. (2014), which unlike the compiled relation by Speagle et al. (2014), includes local studies such as Chang et al. (2015) for constraining the SFMS evolution.

Table A.1 gives the alternative results for our analysis in Section 3 normalising to these alternative SFMS equations. The fitted slope of the $\mathrm{SFR}_{\mathrm{UV}}/\mathrm{SFR}_{\mathrm{SFMS}}$ versus inclination of our local or $z \sim 0.7$ samples relation does depend significantly on the SFMS normalisation selected. On the other hand, the intercept values are different. For the $z \sim 0.7$ sample, the intercepts are lower than our adopted SFMS result for the Speagle and lowest for the Schreiber normalisation. For our $z \sim 0$ sample, the intercept is lowest for the Schreiber SFMS, and highest for the Speagle SFMS. These results are not surprising considering the normalisation differences seen the SFMS relations in Figure A.1.

Using the Speagle et al. (2014) SFMS for normalisation of the $\mathrm{SFR}_{\mathrm{UV}}$ gives best fitting parameters for the Tuffs et al. (2004) models $\tau^f_{B,z=0} = 3.19^{+0.1}_{-0.08}$, $F_{z=0} = 0.02^{+0.01}_{-0.01}$ for the local galaxy sample, and $\tau^f_{B,z=0.7} = 4.6^{+1.3}_{-1.5}$, $\mathrm{F}_{z=0.7} = 0.57^{+0.04}_{-0.03}$ for our COSMOS sample.

On the other hand, using the Schreiber et al. (2015) SFMS results in $\tau^f_{B,z=0} = 2.89^{+0.1}_{-0.1}$, $F_{z=0} = 0.48^{+0.005}_{-0.006}$ and $\tau^f_{B,z=0.7} = 5.4^{+0.8}_{-1.2}$, $\mathrm{F}_{z=0.7} = 0.58^{+0.02}_{-0.03}$.

In these cases, the face-on B-band optical depth increases from $z \sim 0$ to $z \sim 0.7$ as well as the clumpiness factor (which increases by a factor of ~ 28 for the Speagle et al. 2014 SFMS, and by a factor 1.2 for the Schreiber et al. 2015 SFMS).

A.1.2. Attenuation-inclination relations normalised by galaxy $\mathrm{SFR}_{\mathrm{MIR}}$

We investigate the effects that normalising the UV, radio and FIR SFRs by the MIR SFR ($12\,\mu$m at $z \sim 0$ and $24\,\mu$m at $z \sim 0.7$), rather than the SFMS SFR, has on our analysis. By using $\mathrm{SFR}_\lambda/\mathrm{SFR}_{\mathrm{MIR}}$ for our inclination analysis, we remove potential systematic effects related to the M_* dependence of the star-forming SFMS (as discussed above). $\mathrm{SFR}_{\mathrm{MIR}}$ has the practical advantage as the normalising factor (over e.g. $\mathrm{SFR}_{\mathrm{FIR}}$) in that most of our SDSS and COSMOS galaxies are detected in the WISE and MIPS data-sets, respectively.

Attenuation-inclination relations derived using this alternative normalisation are consistent with our results obtained using the SFMS normalisation, with the exception of a few cases which we will now discuss.

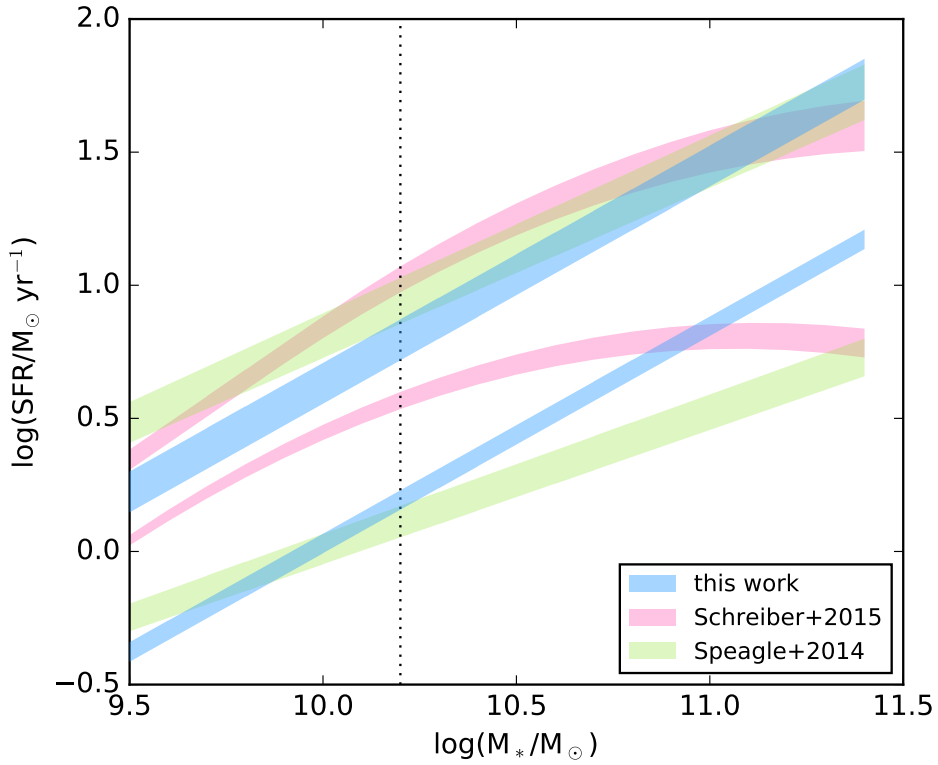

Figure A.1.: Main sequence relations at our two redshift slices. For our analysis we adopt the SFMS given by Equation 9 (blue), but we also compare to SFMS relations with a shallower slope, Speagle et al. (2014) (green) and a SFMS relation with a turn-over at low redshifts and high stellar masses, Schreiber et al. (2015). The vertical dotted line at $\log(M_*/\mathrm{M}_\odot) = 10.2$ shows the mass cut used in this work. We note that the Speagle et al. (2014) and Schreiber et al. (2015) relations shown for comparison were not calibrated at $z = 0$.

The slightly positive slope (0.23 ± 0.21) of the SDSS radio sample is partially due to the fact that the local $\mathrm{SFR}_{12\mu\mathrm{m}}$ has a slight negative trend with inclination (-0.12 ± 0.02), and so normalising by the 12 μm SFR will induce a slight positive slope. The distributions of the FUV slopes now have consistent medians. This could also be in part because the local MIR slope is slightly negative so normalising by the 12 μm SFR will shift the local UV slope. However, this shift of ~ 0.12 would not be enough to fully explain the change in local UV slopes (from -0.78 ± 0.08 to -0.59 ± 0.1) when using a SFMS or $\mathrm{SFR}_{12\mu\mathrm{m}}$ normalisation. Additionally, the COSMOS $\mathrm{SFR}_{\mathrm{UV}}$ slope changes from -0.53 ± 0.17 to -0.6 ± 0.23. The local 60 μm intercept is greater than zero. This corresponds to a difference between the 60 μm and 12 μm SFR calibrations that we discuss in Appendix A.1.2.

$\mathrm{SFR}/\mathrm{SFR}_{\mathrm{SFMS}}$ will vary from galaxy to galaxy as there is an intrinsic scatter to the SFMS (Speagle et al., 2014; Schreiber et al., 2015). We find that the scatter of the $\mathrm{SFR}_{\mathrm{UV}}/\mathrm{SFR}_{\mathrm{SFMS}}$-inclination relation is similar to the scatter of the $\mathrm{SFR}_{\mathrm{UV}}/\mathrm{SFR}_{12\mu\mathrm{m}}$ relation (in fact the $\mathrm{SFR}_{\mathrm{UV}}/\mathrm{SFR}_{12\mu\mathrm{m}}$ ratio shows larger scatter). This is not surprising because the amount of UV emission that escapes will depend, amongst other things, on the star-dust geometry, inclination angle, and the dust mass as well as the SFR. Therefore the $\mathrm{SFR}_{12\mu\mathrm{m}}$

is not readily correlated to the SFR_{UV}, even for our sample that has been selected to have similar M_*, n, and $r_{1/2}$.

A.2. Evolution of UV attenuation with redshift: Studies included in Figure 2.8.

Bouwens et al. (2016) give a "consensus relationship" for IRX – M_* between $2 < z < 3$ by combining the results of Whitaker et al. (2014), Reddy et al. (2010), and Álvarez-Márquez et al. (2016). In Figure 2.8, we show the resulting FUV attenuation obtained by evaluating the "consensus" equation at $\log(M_*/M_\odot) = 10.2 - 10.6$. McLure et al. (2017) fit of the $A_{1600} - M_*$ relation and found the IRX – M_* relation for star-forming galaxies in the Hubble Ultra Deep field is well described by a Calzetti et al. (2000) attenuation law. As done for Bouwens et al. (2016), we show the expected SFR_{UV}/SFR_{tot} for galaxies with M_* ranging from $10^{10.2}$ to $10^{11.4}$ $M_\odot$ according to the IRX – M_* fit of McLure et al. (2017) as a shaded region.

Whitaker et al. (2014) report the average L_{IR}, L_{UV} and SFRs for SF galaxies selected via colour-colour criterea in the CANDELs fields in bins of stellar mass and redshift. From these values we calculate SFR_{UV}/SFR_{tot} and in Figure 2.8 we show the minimum and maximum values found for galaxies with $10.2 < \log(M_*/\mathbf{M}_\odot) < 11.4$ (to match this work). For Wuyts et al. (2011b) we read off the SFR_{UV}/SFR_{IR} fraction at the position of the SFMS at $\log(M_*/M_\odot) = 10.2$, 10.8, and 11.4 from their Figure 6. Their SFMS was approximated with a constant slope of 1. We consider the total SFR to be SFR_{UV} + SFR_{IR} and then solve for SFR_{UV}/SFR_{tot}. The error bars show the range corresponding to the Wuyts et al. (2011b) results at the different stellar masses spanned by this work.

Wang et al. (2016) give the observed uncorrected FUV luminosity and corrected luminosities for galaxies in their Figure 9 for a sample of galaxies in GAMA/H-ATLAS with slightly lower masses than our sample, median $\log(M_*/M_\odot) = 10.13$, and a median redshift $z = 0.077$.

Pannella et al. (2009a) use BzK selection to perform a stacking analysis on 1.4 GHz data to infer the total SFR at $z \sim 2$. Panella report the attenuation at 1500 Å, derived from the stacked $SFR_{FUV}/SFR_{1.4GHz}$, as a function of stellar mass. In Figure 2.8, we include the results from 10.2 to 11.4 as indicated by the error-bars. Pannella et al. (2015) take a mass-complete sample of galaxies in GOODS-N classified as star forming by a UVJ colour-colour selection. We take measurements of A_{FUV} at $10.2 < \log(M_*/M_\odot) < 11.4$ from Figure 7 in Pannella et al. (2015). They find that A_{FUV} increases by 0.3 dex from $z \sim 0.7$ to $z \sim 1$ and then stays constant out to $z \sim 3.3$.

Burgarella et al. (2013) and Cucciati et al. (2012) use a ratio of UV and FIR luminosity functions in the VIMOS-VLT Deep Survey to calculate A_{FUV}. This considers galaxies of all stellar masses. The difference between these studies is that Burgarella et al. (2013) uses a PACS-selected sample and Cucciati et al. (2012) use an I-band selected catalogue.

Reddy et al. (2012) use *Herschel* measurements of UV-selected star-forming $1.6 < z < 2.6$ galaxies in GOODS-North. In Figure 2.8, we show the SFR_{UV}/SFR_{tot} for their samples A (All UV-selected galaxies) and E (Ultra-Luminous Infrared Galaxies; ULIRGs), where the ULIRG sample has SFR_{UV}/SFR_{tot} ratios consistent with massive galaxies. Heinis et al.

(2013) calculated $A_{\rm FUV}$ for a UV-selected sample of galaxies $1.2 < z < 1.7$ from IR and UV data. Dahlen et al. (2007) draw on GOODS-South photometry to measure the rest-frame 1500 and 2800Å luminosity functions. The UV slope is used, assuming the Calzetti attenuation law to calculate the FUV attenuation correction factor required.

Hao et al. (2011) use a number of normal star-forming nearby galaxies from Kennicutt et al. (2003) and Moustakas & Kennicutt (2006). The sample has $\log(\mathrm{SFR}/\mathrm{M}_\odot\mathrm{yr}^{-1})$ values from -3 to 1. Calzetti et al. (2000) combined IR and UV data for a sample of eight nearby galaxies with $\log(\mathrm{SFR}/\mathrm{M}_\odot\mathrm{yr}^{-1})$ ranging from -1 to 1.7.

Buat et al. (2015) calculate the FUV attenuation of IR-selected galaxies from $z \sim 0.2$ to $z \sim 2$ by fitting galaxy SEDs from UV to IR wavelengths. They conclude that galaxies selected in the IR show larger attenuation than galaxies selected in the UV or optical as they are the more massive galaxies (average $\mathrm{M}_* > 10^{10.4}$ $\mathrm{M}_\odot$). In Figure 2.8, we show the average $A_{\rm FUV}$ for each redshift bin quoted in Table 3 of Buat et al. (2015). The error bars show the sample dispersion of 1.3 mags.

Table A.1.: Best fit parameters of the SFR vs. inclination relation under different SFR normalisations. Column 1 is a repeat of Table 3 (to facilitate comparison), Column 2 and 3 show the best fitting parameters obtained when using the Speagle et al. (2014) and Schreiber et al. (2015) SFMS relations to normalise the SFR. Column 4 shows the best-fit parameters when the SFR of each galaxy is normalised by its MIR SFR.

λ	This SFMS		Speagle SFMS		Schreiber SFMS		MIR	
	Slope	Intercept	Slope	Intercept	Slope	Intercept	Slope	Intercept
SFR_{UV} $z \sim 0$	$-0.78^{+0.08}_{-0.09}$	$-0.20^{+0.04}_{-0.03}$	$-0.76^{+0.07}_{-0.08}$	$-0.11^{+0.03}_{-0.03}$	$-0.75^{+0.08}_{-0.08}$	$-0.54^{+0.03}_{-0.03}$	$-0.59^{+0.10}_{-0.09}$	$-0.27^{+0.03}_{-0.03}$
SFR_{MIR} $z \sim 0$	$-0.12^{+0.03}_{-0.02}$	$0.05^{+0.01}_{-0.01}$	$-0.10^{+0.02}_{-0.02}$	$0.14^{+0.01}_{-0.01}$	$-0.08^{+0.02}_{-0.03}$	$-0.29^{+0.01}_{-0.01}$	-	-
SFR_{FIR} $z \sim 0$	$-0.06^{+0.22}_{-0.20}$	$0.68^{+0.09}_{-0.09}$	$-0.02^{+0.19}_{-0.18}$	$0.81^{+0.08}_{-0.08}$	$0.04^{+0.19}_{-0.17}$	$0.40^{+0.08}_{-0.08}$	$0.05^{+0.16}_{-0.16}$	$0.26^{+0.08}_{-0.08}$
SFR_{radio} $z \sim 0$	$-0.10^{+0.20}_{-0.22}$	$0.52^{+0.11}_{-0.09}$	$-0.09^{+0.20}_{-0.17}$	$0.69^{+0.09}_{-0.09}$	$-0.07^{+0.16}_{-0.19}$	$0.31^{+0.10}_{-0.09}$	$0.23^{+0.21}_{-0.21}$	$-0.07^{+0.12}_{-0.24}$
SFR_{UV} $z \sim 0.7$	$-0.54^{+0.18}_{-0.17}$	$-0.74^{+0.08}_{-0.08}$	$-0.59^{+0.17}_{-0.18}$	$-0.85^{+0.09}_{-0.07}$	$-0.59^{+0.17}_{-0.17}$	$-0.94^{+0.08}_{-0.08}$	$-0.60^{+0.23}_{-0.21}$	$-1.00^{+0.09}_{-0.1}$
SFR_{MIR} $z \sim 0.7$	$-0.03^{+0.10}_{-0.09}$	$0.28^{+0.05}_{-0.05}$	$-0.05^{+0.10}_{-0.10}$	$0.16^{+0.06}_{-0.05}$	$-0.04^{+0.09}_{-0.10}$	$0.06^{+0.05}_{-0.05}$	-	-
SFR_{FIR} $z \sim 0.7$	$-0.02^{+0.23}_{-0.25}$	$0.54^{+0.15}_{-0.13}$	$-0.03^{+0.23}_{-0.21}$	$0.43^{+0.12}_{-0.13}$	$-0.03^{+0.22}_{-0.23}$	$0.33^{+0.13}_{-0.12}$	$0.16^{+0.1}_{-0.14}$	$-0.02^{+0.08}_{-0.11}$
SFR_{radio} $z \sim 0.7$	$-0.17^{+0.31}_{-0.33}$	$0.68^{+0.19}_{-0.18}$	$-0.14^{+0.27}_{-0.32}$	$0.55^{+0.18}_{-0.15}$	$-0.13^{+0.30}_{-0.30}$	$0.45^{+0.18}_{-0.15}$	$0.29^{+0.18}_{-0.20}$	$-0.05^{+0.11}_{-0.10}$

B Appendix to Chapter 4

B.1. Stacking analysis: Details and tests

In principle, stacking is a straightforward process, but in practice, there are many subtleties, some of which we discuss here, in particular, the choice of method to measure total flux, and the choice of whether to represent the average as the mean or the median.

Radio images with bright sources must be cleaned to have any hope at detecting sources amongst the side-lobes of the bright source. For this reason, most stacking analysis to date has been performed on cleaned radio images. Sources that lie above the clean threshold will have a point spread function (PSF) corresponding to the Gaussian-shaped clean beam, whereas fainter sources with no cleaned components will have a PSF corresponding to the dirty beam. Stacking a population that includes sources with different PSFs is not an intuitive situation. For the VLA 3 GHz LP, the entire map was cleaned down to 5σ and further down to 1.5σ using tight masks around 5σ sources. The noise level in each individual pointing was around 4-5 μJy beam^{-1}. We have tested further cleaning our stacks (after averaging in the image plane) with the average beam shape, but this removed flux from the already cleaned sources, rather than adding back flux from the side-lobes. One way to address this could be to stack dirty sources below 1.5σ and then clean the resulting stack, but this would have to be done separately for the different VLA pointings, resulting in a loss of signal-to-noise.

Studies such as Mao et al. (2011) with similar numbers of detections and non-detections in each bin, combine detected and non-detected sources separately, weighing the flux from each detected source by 1/N and the stack of undetected sources as n/N, where N is the total number of sources in the bin and n is the number of sources in the stack. There is a significant variation in the fraction of sources detected at $> 5\sigma$ between stellar mass and redshift bins, ranging from 0 to 30% from low to high stellar masses. We decided to treat all sources homogeneously by stacking detected and non-detected sources together, thereby not introducing an arbitrary flux limit above which we consider a source detected. This uniform treatment also has the advantage of allowing errors to be readily calculated by bootstrapping methods.

In the region selected for this analysis, the rms variation is minimal (e.g., rms variations on scales of $\sim 1'$ are less than 2%, Smolčić et al. 2017b) and we found no difference in our mean or median stacked image fluxes by weighting each image by its inverse variance.

B.1.1. Flux Measurement

As mentioned in Section 4.3, astrometric uncertainties and intrinsic source extent require us to measure a total flux rather than the flux contained within one beam around the central object. We consider three primary methods for measuring total fluxes; fitting sources with a 2D Gaussian function, fitting sources with the Blobcat software from Hales et al. (2012), and aperture photometry using a circular aperture. We run the measurement methods on 3 GHz stacks that were created using the input star-forming galaxy sample of Karim et al. (2011), allowing us to compare our results with their published 1.4 GHz fluxes. We have also stacked these sources at infrared wavelengths following Magnelli et al. (2015) and derived a FIR luminosity for the stacks. We chose to focus on $z < 2$ where all samples are reliable and mass $> 10^{10.0}$ $M_\odot$, for completeness. We evaluate the performance of the flux measurements by comparing the resulting 3 GHz SFRs with the infrared SFRs as described in 4.3.1.

Blobcat is a stand-alone Python program that uses the flood fill algorithm to find and catalogue blobs (a group of connected pixels) above a certain signal-to-noise-ratio threshold in images of total intensity. Each detected blob may represent an individual astronomical source or multiple blended sources. Blobcat was run with default parameters and the rms given from the stacking routine. When Blobcat finds more than one blob in the cutout, we only use the central component. The 2D Gaussian fitting is based on code by Adam Ginsberg and allows the sources to be elliptical. We input initial conditions for the fit, using the peak flux from the stacking routine, and the beam size. Our aperture photometry is based on the python function makemask by Ian Crossfield. The 3 GHz PSF has been circularized making the choice for a circular aperture appropriate. We re-ran the flux measurements using apertures with a radius of 0.75, 1.0, 1.5, and 2.0″. If the appropriate aperture size is the angular size of the galaxy convolved with the beam, one might expect the ideal aperture to change with stellar mass and redshift (as there is both a mass-size relation and an evolution of this relation (van der Wel et al., 2014)). However, we found that the peak SNR was obtained at a radius that depended very little on mass and redshift. An aperture of 1.5″ radius best agrees with the Gaussian fluxes, the 1.4 GHz, and IR fluxes, and is therefore adopted for the comparison.

Figure B.1 shows the difference between the 3 GHz and IR SFRs for the three different flux measurement methods considered. For our stacks, we find the Blobcat fluxes are biased towards over-estimating the fluxes because the flood-fill algorithm picks up some of the positive side-lobes but not the negative parts. We note that Blobcat and Gaussian peak fluxes tend to be consistent. Using Gaussian fluxes minimises the scatter between the IR and 3 GHz SFRs, and so we adopt this method for our total flux measurements. The 1.4 GHz and 3 GHz SFRs measured from Gaussian fits to determine the total fluxes agree, as illustrated in Figure 4.3. However, for the low-mass galaxies ($\log(M_*/M_\odot) < 10.0$), the scatter is larger, in part due to the lower SNR in the 1.4 GHz stack.

B.1.2. Mean or median

While the mean of a flux distribution is natural to interpret mathematically, it can be sensitive to outliers. Because the median is robust to the presence of outliers, it has the advantage that all data can be used. However, the median value recovered from a stacked image depends not only on the underlying distribution but also on the noise level. White

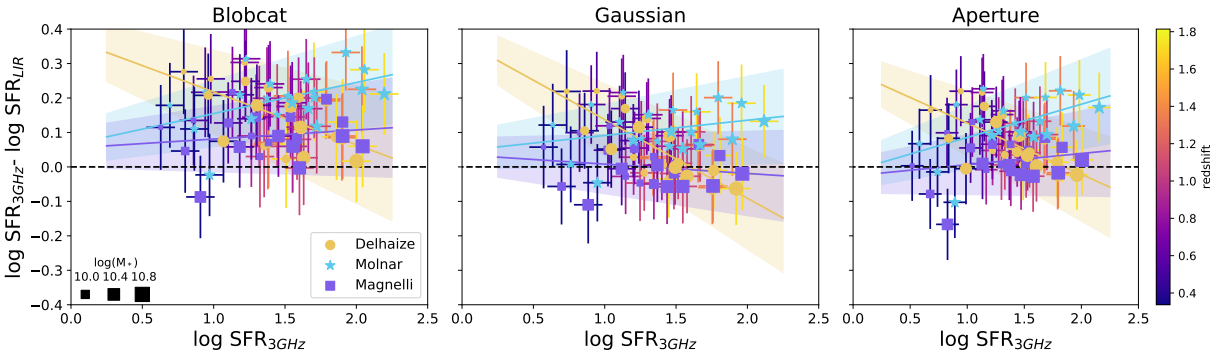

Figure B.1.: Comparison of infrared and 3 GHz SFRs using different source fitting algorithms (described in Section B.1.1) to measure the 3 GHz total flux and for different 3 GHz SFR-calibrations (described in Section 4.3.1). The size of symbols represents the average stellar mass of the stack, the colour of the error bars represents the redshift as indicated in the colour bar on the right-hand side. Purple squares correspond to 3 GHz-SFRs calculated following the q evolution from the stacking analysis of Magnelli et al. (2015) and $\alpha = -0.8$. Amber circles show SFRs calculated assuming the Delhaize et al. (2017) q evolution with $\alpha = -0.7$ and blue stars correspond to the 3 GHz-SFR that relies on the q evolution for pure disk galaxies in Molnár et al. (2018). Solid lines and shaded areas show linear orthogonal distance regression fit and errors, respectively. We find that using the Magnelli et al. (2015) calibration and Gaussian source fluxes gives the lowest scatter between the IR and 3 GHz SFRs.

et al. (2007) showed that in the limit where the individual sources are well below the rms level, the median values trace the population means. These arguments only strictly apply to point sources. The underlying distribution of source fluxes is also not likely a simple Gaussian [49], thus leaving us with a difficult problem that deserves more attention.

First, we investigate whether or not we can recover the mean and median of a list of high-SNR sources. We selected star-forming sources following the selections used for the main stacking analysis (see Sect. 4.4.4) and stack galaxies with $10.4 < \log(M_*) < 10.6$ (mean 10.51, median 10.50) and $0.4 < z < 0.6$ (mean 0.509, median 0.516) detected at $> 5\sigma$ in the 3 GHz catalogue. This gives a sample of 41 galaxies, with a mean and median catalogued total flux of 38.7 μJy and 34.5 μJy, respectively. The standard deviation is 23.4 μJy, and the minimum and maximum fluxes are 12.4 μJy and 133.0 μJy (fluxes ranging over an order of magnitude). The total flux of the median stack $S_t = 34.49 \pm 0.35 \mu$Jy using a 2D Gaussian fit, or $S_t = 36.69 \pm 1.87$ using the Blobcat software. The Gaussian total flux represents the correct median flux (34.46 μJy), while the Blobcat flux over-estimates the median of the catalogue fluxes. For mean stacking, we recover the Gaussian total flux $S_t = 39.6 \pm 0.4\,\mu$Jy and the Blobcat flux is $S_t = 42.8 \pm 0.2\,\mu$Jy. The mean stack Gaussian fit overestimates the mean of the catalogued fluxes (38.7 μJy), again with the Gaussian fit performing better than the Blobcat flux. This points to the median stacking method being more reliable than the mean.

Figure B.2 shows the ratio of total fluxes derived from mean and median stacking bins of star-forming galaxies from our main analysis. In all cases, the mean reported is larger than

[49] The distribution of galaxies in SFR at a fixed M_* and z is thought to consist of two or three components (Bisigello et al., 2018; Hahn et al., 2019), that could be log-normal (or not; Eales et al. 2018b).

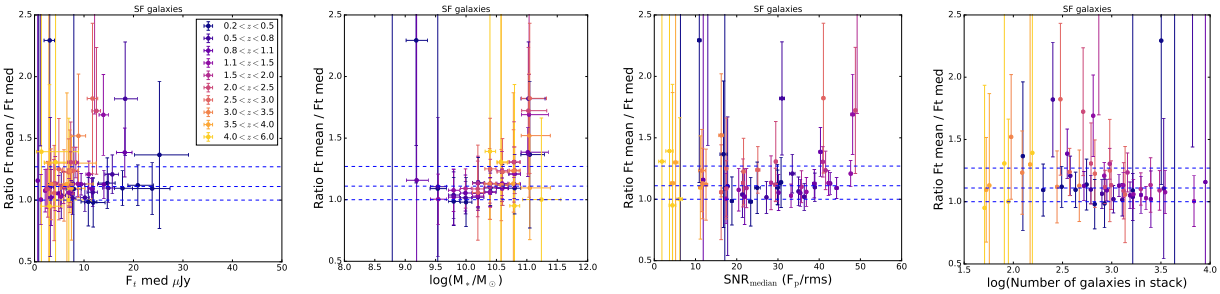

Figure B.2.: Ratio of total fluxes derived from mean and median stacked images as a function of (from left to right) the median total flux, the stellar mass, the median stack signal-to-noise ratio (peak flux/rms), and the number of galaxies in the stack. Error-bars represent the 5-95 % range. Horizontal lines are drawn at $F_{t,mean}/F_{t,median}$=1.0, 1.11, 1.27, which correspond to the values expected if SFR is symmetrically distributed, or if log(SFR) is normally distributed with a $\sigma = 0.2$, $\sigma = 0.3$ dex respectively (and if flux is linearly related to SFR).

the median; which is expected for most SFR distributions. In particular, for a Gaussian distribution in log(SFR) with a given σ, the ratio between the mean SFR and the SFR corresponding to the median log(SFR) (i.e. the peak of the Gaussian) is $e^{2.652\sigma^2}$. We find that the ratio increases with stellar mass. In section 4.4.3, we found that the scatter of the main-sequence decreases with stellar mass, so this trend of increasing ratios is not likely due to increasing scatter. The uncertainty of the median fluxes from our bootstrapping analysis is smaller than the uncertainties on the mean because the median is more robust to the presence of outliers or interloping sources. For these reasons, we have decided to adopt the median stacks for our analysis. The SFRs derived using the mean stacked fluxes are shown in Figure B.3, with the best fit to the median SFRs (Eq 4.13) shown in the background for comparison (and used to calculate residuals). Mean SFRs follow a less-smooth relation than the median SFRs, with higher SFRs at low-masses ($\log(M/\mathrm{M}_\odot) < 9.5$) and high masses ($\log(M/\mathrm{M}_\odot) > 11$).

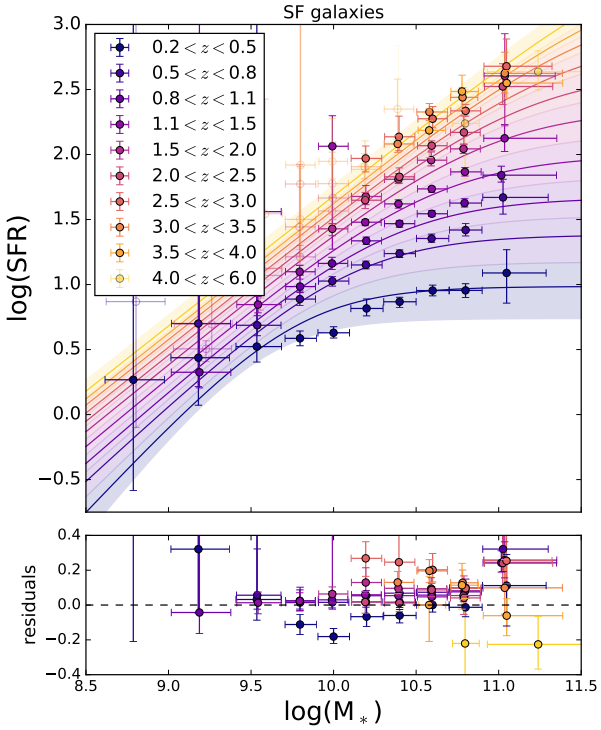

Figure B.3.: The SFRs derived using mean stacks of 3 GHz images in bins of stellar mass and redshift. As a reference to allow comparison with the median stacking results, the best-fit relation from the median SFR – M_* relation (shown in Figure 4.4) is shown here, and the difference between the mean SFR and the median best fit is shown in the bottom panel.

B.2. Selection effects: AGN removal

AGN activity and the SFR activity of their hosts are likely connected, possibly driven by a common fueling mechanism (Vito et al., 2014). The cosmic star formation history and black hole accretion history follow similar volume averaged evolution (Madau & Dickinson, 2014). Identifying AGN is a challenging task because the SED of an AGN and host galaxy can vary widely depending on the geometry and accretion properties in addition to the energy output varying on timescales that are dependent on the wavelength (see e.g, Schawinski et al. 2015; Elitzur et al. 2014; Noda & Done 2018; Buisson et al. 2017) Disentangling the radio emission from the AGN from that related to star-formation is beyond the scope of this paper. However here we investigate the extent to which our SFRs may be biased by AGN contribution to the 3 GHz flux by removing all potential AGN hosts and repeating our stacking analysis. We would like to emphasize that, particularly at high redshifts, AGN hosts can also contain significant amounts of star formation, e.g. Delvecchio et al. (2017).

We combine multiwavelength AGN diagnostics to reach an inclusive AGN sample. For all galaxies in the Laigle et al. (2016) catalog, AGN are identified using Donley et al. (2012) criteria using *Spitzer*-IRAC (3.6, 4.5, 5.8, and 8.0 μm) fluxes. This MIR criterion is only complete for bright AGN $L_X > 10^{44}$. X-ray-AGN were identified using the [0.5-2] keV *Chandra* data, if the luminosity was $L_X > 10^{42}$ erg s^{-1}.For sources in the 3 GHz multiwavelength counterpart catalog of Smolčić et al. (2017a), we have flagged sources iden-

tified there as AGN (X-ray, MIR again) in particular the SED AGN (sources whose SED is best fit with an AGN + galaxy template) and radio excess sources ($\log(L_{1.4}/\mathrm{W\ Hz^{-1}}) > \log(\mathrm{SFR_{IR}}/\mathrm{M_\odot yr^{-1}}) + 21.984 \times (1+z)^{0.013}$) from (Delvecchio et al., 2017). We have also removed sources for which AGN emission contributes $\geq 50\,\%$ to the infrared luminosity (and flag = 1), based on custom MAGPHYS (Multi-wavelength Analysis of Galaxy Physical Properties; da Cunha et al. 2008) plus AGN template fitting to all COSMOS2015 galaxies (Chang et al., 2017) [50]. As before, we also have excluded all multicomponent radio sources (even the three that were classified as star-forming) from Vardoulaki et al. (2019)

We show the results of our stacking analysis after flagging and removing all identified AGN from the parent sample in figure B.4. For galaxies classified as star-forming, the median SFR is not significantly altered from before. This shows that AGN contamination does not have a large effect on our main results. Of course, this does not exclude the possibility that the median SFRs are still biased by low-luminosity AGN that cannot be identified at wavelengths shorter than 10cm. When considering all galaxies, we include galaxies of red colours, which are more likely to host a radio AGN, especially at the massive end (Smolčić, 2009). In the local Universe all galaxies with stellar mass $M_* > 10^{11}$ show radio-AGN activity with $L_{150\mathrm{MHz}} > 10^{21}\,\mathrm{W\ Hz^{-1}}$ (Sabater et al., 2019). The right-hand panel of Figure B.4 shows that when stacking all galaxies, only the most massive bins ($10.9 < \log(M/\mathbf{M}_\odot < 11.6$) are affected by our AGN removal. For these most massive galaxies, the 3 GHz flux over-estimates the SFR when considering galaxies with red NUV-r/r-J colours due to flux contribution from the AGN, and the difference is strongest towards lower redshifts. We also note that this discrepancy at high mass is stronger ($> 4\sigma$) when comparing mean rather than median SFRs for the two different AGN de-selection methods.

[50] http://idv.sinica.edu.tw/yuyenchang/ca.html

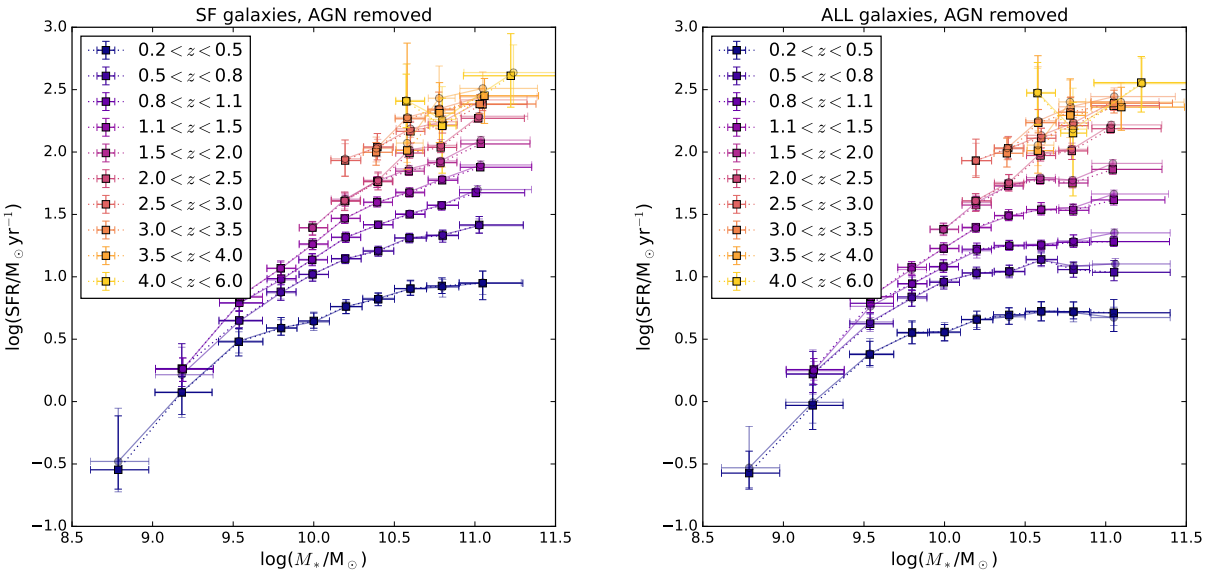

Figure B.4.: The SFMS results when performing a strict AGN de-selection (opaque squares) compared to only excluding multi-component radio AGN (transparent circles). The left panel shows star-forming galaxies and right panel shows all galaxies. AGNs do not affect the overall median SFR (within the errors). There is a slight difference at $M > 10^{10.9}$ $M_\odot$ and $M < 10^9$ $M_\odot$, but these do not affect our results.

B.3. Comparison with Literature

The diversity of sSFRs from different studies as a function of stellar mass and redshift, normalized by the relation given in Equation 4.13 is shown in Figure B.6. All literature relations were converted to the same Chabrier IMF used in this study when necessary (as mentioned below). We do not correct for the small effect that different cosmologies introduce into the relations. The mass range shown in Figure B.6 illustrates where the literature studies are complete. There is a spread of > 0.2 dex between different SFMS relations. Results from the following studies are shown in figure B.6, along with the pertinent details on how they were derived:

- Bisigello et al. (2018) fitted linear SFR – M_* relations for three populations of galaxies in the CANDELS/GOODS-S fields, a starburst, main-sequence, and quiescent population assuming each population follows a log-normal sSFR distribution. They fit galaxies in three bins between $0.5 < z < 3$, and stellar masses down to $\log(M_*/M_\odot) > 7.5$. Bisigello et al. (2018) adopted a $(\Omega_M, \Omega_\Lambda, H_0) = (0.27, 0.73, 70)$ cosmology and Salpeter IMF. In Figure B.6 we include the $1 < z < 2$ relation whose SFRs were calculated from UV plus IR luminosities (where IR luminosity is from Chary & Elbaz (2001) template fitting).

- Boogaard et al. (2018) selected star-forming galaxies at $0.11 < z < 0.91$, with 2 Hydrogen Balmer emission lines detected with SNR > 3 from which they calculated SFR. Star-forming galaxies were further required to have $D_n(4000) < 1.5$, $EW_{H\alpha} > 2$ Å ,

$EW_{H\beta} > 2$ Å. Boogaard et al. (2018) found a linear relation between log(SFR) and $\log(M_*/\mathbf{M}_\odot)$ over the mass range probed ($7 < \log(M_*/\mathbf{M}_\odot) < 10.5$). Their study assumed the same IMF and cosmology as ours.

- Caputi et al. (2017) obtained Hα-derived SFRs from Hα+[NII]+[SII] equivalent width measurements of galaxies in the *Spitzer* Matching Survey of the UltraVISTA Ultra-Deep Stripes over the range $3.9 < z < 4.9$. They report a bi-modal distribution in sSFR interpreted as a main-sequence and starburst population. For the main-sequence population, they report a linear relation, constrained across a mass range $9.2 < \log(M_*/\mathbf{M}_\odot) < 10.8$. Above this stellar mass, they postulate AGN contamination influences the SFR measurements. The same cosmology and IMF as this work was assumed.

- Iyer et al. (2018) used the UVJ colours to select $\sim 18,000$ galaxies in CANDELS GOODS-S field at $0.5 < z < 6$. The galaxy SED-fits provide stellar mass and SFR measurements. In addition, the star formation histories were reconstructed, allowing for more data-points on the SFMS relation at high redshift down to a representative mass of $\log(M_*/\mathbf{M}_\odot) \sim 7$ (90% representative at $z \sim 7.5$).

- Karim et al. (2011) used 1.4 GHz data and the Bell (2003) SFR calibration (assuming $\alpha = -0.8$) to calculate SFRs for COSMOS galaxies across $0.2 < z < 3$. SFGs were selected using NUV-r rest-frame color cuts, and show individual stacked mass complete data points (rather than the fit-function) in Figure B.6.

- Lee et al. (2015) studied star-forming galaxies selected by a NUVrJ colour-colour cut (Ilbert et al., 2013). The SFRs were calculated from IR and UV data assuming Hinshaw et al. (2013) cosmology $(\Omega_M, \Omega_\Lambda, H_0) = (0.28,\ 0.72, 70.4\ \mathrm{km\ s^{-1}\ Mpc^{-2}})$. The mass limit used for fitting was given in their Table 1. Lee et al. (2015) fit the SFMS for galaxies at $0.25 < z < 1.3$ with the functional form 4.7.

- Pearson et al. (2018), fit a linear SFRMS relation over a redshift range $0.2 < z < 6$ in the COSMOS field, calculating SFRs and stellar masses via SED fitting. SFGs were selected using a dependent UVJ color-color cut and a slightly different cosmology was assumed $(\Omega_M, \Omega_\Lambda, H_0) = (0.273, 0.727, 70.4\,\mathrm{km\,s^{-1}\,Mpc^{-2}})$, (Larson et al., 2011). Figure B.6 compares our result to the Pearson et al. (2018) SFMS showing the 90% mass completeness limits calculated for the COSMOS UDeep field K_s band magnitude limit.

- Santini et al. (2017) studied the SFMS in the HST frontier fields at $1.3 < z < 6$. They were able to probe $\log(M_*/\mathbf{M}_\odot) > 7.5$ at $z < 4$ and $\log(M_*/\mathbf{M}_\odot) > 8$ at $z > 4$. They fit the SFMS separately for different redshift bins with a linear relation, selecting main-sequence galaxies by a sigma clipping. Figure B.6 only shows their fits for $3 < z < 4$ and $4 < z < 5$ because these match the z slices at which we are demonstrating. Santini et al. (2017) adopted a Salpeter IMF and calculate SFRs using rest-frame UV data (Castellano et al., 2012).

- Sargent et al. (2014) compiled data from 16 different studies spanning from $0 < z < 7$ and fit a power-law fit to the sSFR-z relation. Two mass scales were considered,

$M_* \sim 5 \times 10^9\,\mathrm{M}_\odot$ and $M_* \sim 5 \times 10^{10}\,\mathrm{M}_\odot$. The samples used by Sargent et al. (2014) include a mix of selection methods and SFR tracers, but all were converted to WMAP-7 cosmology (Larson et al., 2011).

- Schreiber et al. (2015) stacked *Herschel* data in the extragalactic GOODS-North, GOODS-South, UDS, and COSMOS fields to derive SFRs (they also added unobscured UV SFRs). A Salpeter IMF was used. In Figure B.6 we show their function (of form 4.11) only over a mass range where a stacked signal was detected.

- Shivaei et al. (2015) used Hα and Hβ spectroscopy to derive dust-corrected instantaneous SFRs for 261 galaxies spanning $9.5 < \log(M_*/\mathbf{M}_\odot) < 11.5$, $1.37 < z < 2.61$ in the MOSFIRE Deep Evolution Field (MOSDEF) survey.

- Speagle et al. (2014) compiled literature data from 25 studies and we show their best fit for studies that have a"mixed" SFG selection. Speagle et al. (2014) report a 1σ inter-sample scatter of < 0.1 dex. They fit a linear form (of form Eq 4.10) over a stellar mass range $9.7 < \log(M_*/\mathbf{M}_\odot) < 11.1$, and a redshift range of $0.16 < z < 3.15$ (data from the first and last 2 Gyr were removed). They adopted a Kroupa (2001) IMF.

- Tomczak et al. (2016) report a SFMS with a turn-over (of the form 4.12) over a redshift range $0.5 < z < 4$ and mass range $8.5 < \log(M) < 11.0$. SFGs were selected using a UVJ selection. Their SFRs come from UV+IR data from the FourStar Galaxy Evolution Survey (ZFOURGE) in combination with far-IR imaging from the *Spitzer* and *Herschel* observatories.

B.4. Radio – IR correlation as a function of galaxy morphology

Our results in section 4.4.7 were derived using the same radio – SFR conversion for all galaxies (Magnelli et al., 2015). However, Molnár et al. (2018) reported a steeper q evolution for spheroidal galaxies than for disk-dominated galaxies in the COSMOS field using the same parent sample as Delhaize et al. (2017) and the morphological classification of ZEST. Therefore, it could be appropriate to use different SFR calibrations for disk-dominated galaxies and spheroid-dominated galaxies. Disk dominated galaxies in Molnár et al. (2018) were counted as those with ZEST types 2.2, 2.3, and 3 and were found to follow $q_d = 2.67(1+z)^{-0.04}$. Spheroid-dominated galaxies in Molnár et al. (2018) are comprised of ZEST classes 1, 2.0, 2.1 and follow $q_s = 2.81(1+z)^{-0.19}$. In the bottom panels of Figure B.5 we have adopted the infrared-radio correlations found by Molnár et al. (2018)[51], using q_d for our disk-dominated late type (LT) galaxies (ZEST type = 2.2,2.3) and irregular (ZEST type = 3), and q_s for bulge-dominated LT galaxies (ZEST type = 2.0, 2.1) and for elliptical or early type (ET) galaxies (ZEST type = 1).

[51] and a radio spectral index $\alpha = -0.7$

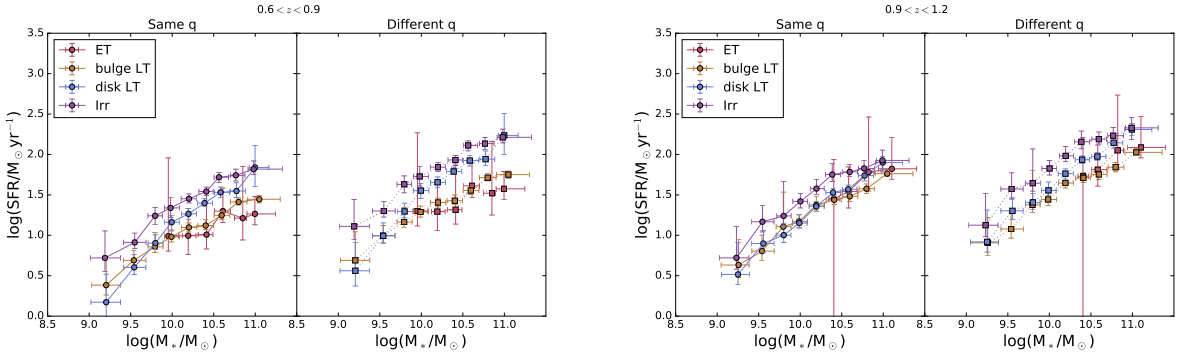

Figure B.5.: Different q evolutions result in stronger SFR differences between the disk and bulge-dominated galaxies at higher redshift. Here we compare the two methods at two redshift bins $0.6 < z < 0.9$ and $0.9 < z < 1.2$. *Left panels:* The same Magnelli et al. (2015) SFR calibration was adopted for all stacks. *Right panels:* q_d was adopted for our "irregular" and "disk-dominated" stacks, whereas q_s was adopted for our "bulge-dominated late-type" and "early-type" galaxies (Molnár et al., 2018). The overall normalization depends on the q relation adopted.

The qualitative trend that, for massive galaxies, the $\mathrm{SFR_{ET}} < \mathrm{SFR_{bulge}} < \mathrm{SFR_{disk}} < \mathrm{SFR_{Irr}}$, still holds at all redshifts, but the difference in SFRs is stronger at $z > 1$ due to the fact that q_s and q_d follow different redshift evolutions.

B.5. Extra Figures

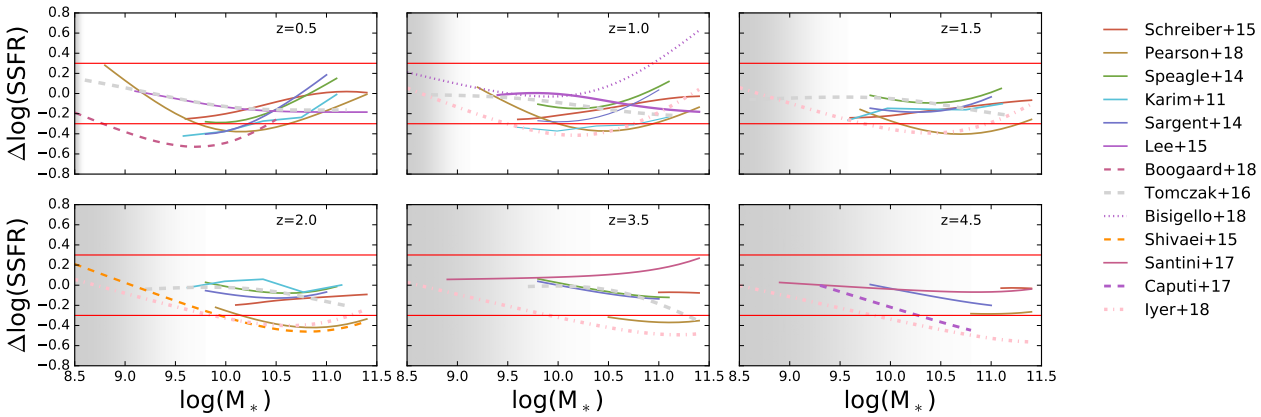

Figure B.6.: Comparison of different SFMS relations measured out to $z \sim 5$. The difference between sSFRs resulting from the literature SFMS relations and the SFMS relation in this work (Equation 4.13). Grey shaded area is to illustrate where this work is complete in stellar mass. Red horizontal lines are drawn at ± 0.3 dex to roughly indicate the intrinsic scatter of the SFMS.

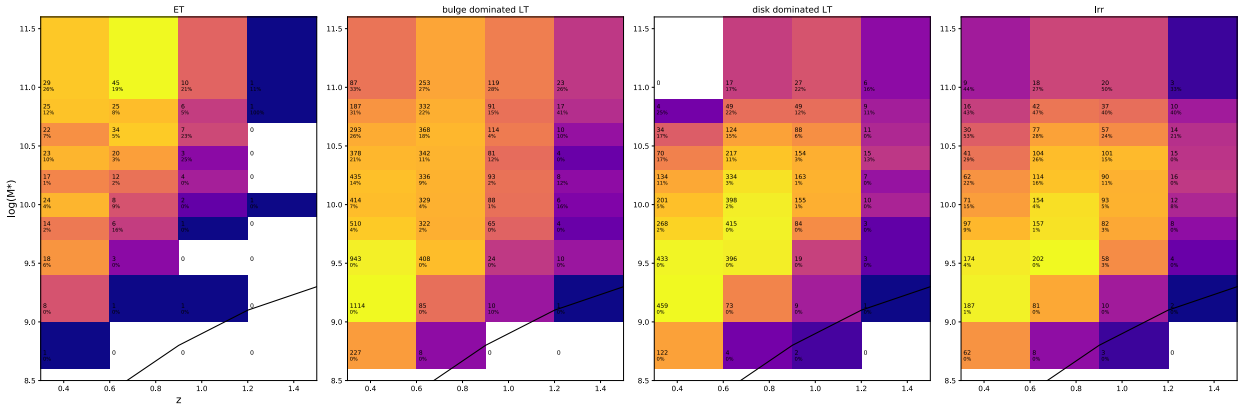

Figure B.7.: Binning scheme for morphology analysis. Star forming galaxies (shown) are selected using NUVrJ color-color cut.

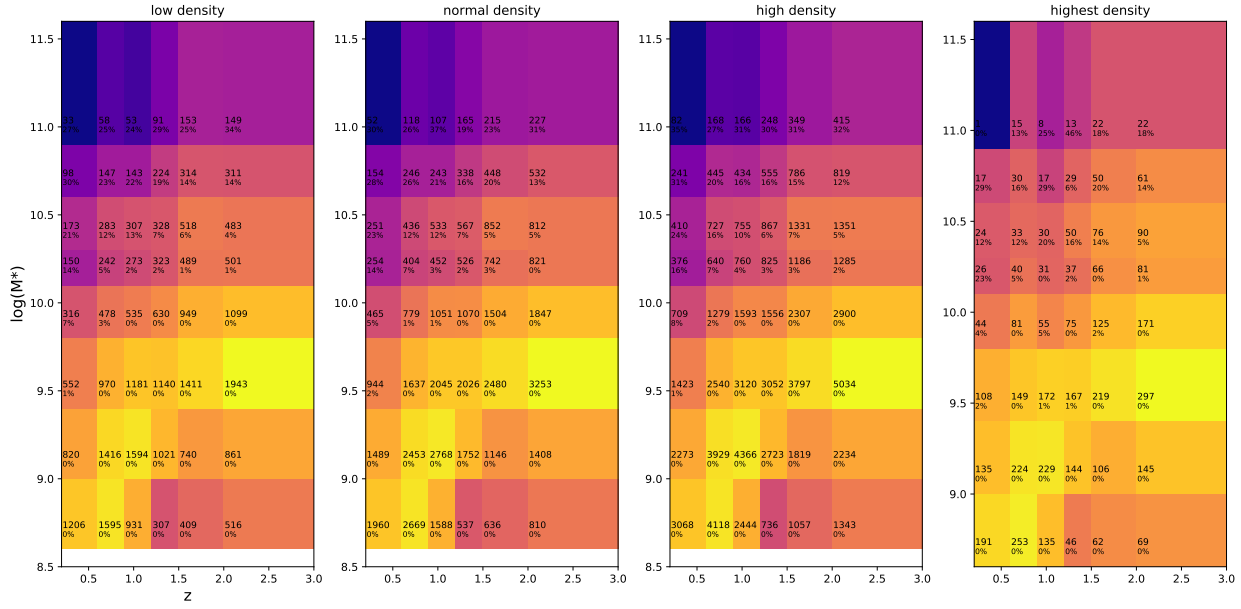

Figure B.8.: Binning scheme for environment analysis using local density estimates from Scoville et al. (2013). Star forming galaxies (shown) are selected using NUVrJ color-color cut.

.

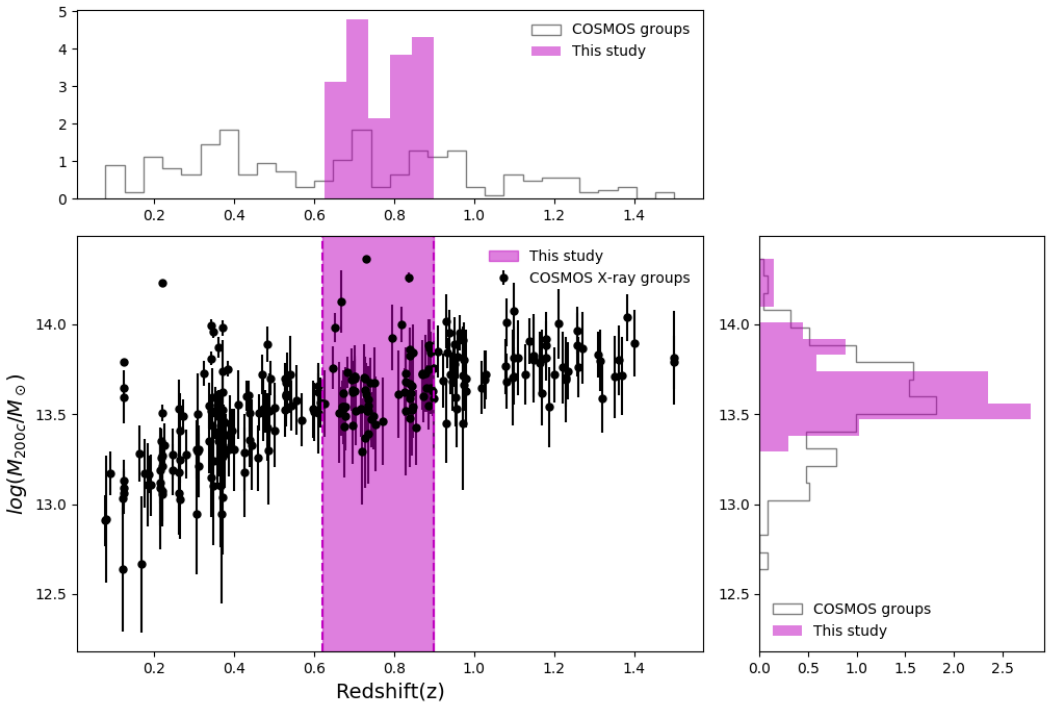

Figure B.9.: The halo mass of X-ray groups (M_{200c}) in the COSMOS field as a function of their redshift (filled black circles). The highlighted magenta region represents 73 groups with a redshift range of $0.62 < z < 0.88$ used in this study. The redshift and halo mass distributions of all X-ray groups and those used in this study are presented in the upper left and lower right panel.

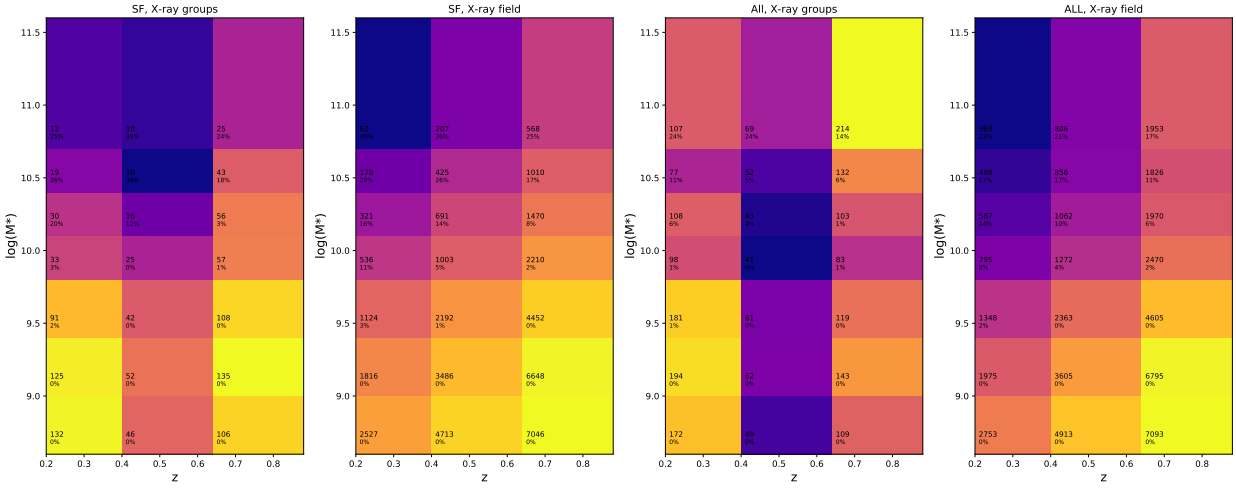

Figure B.10.: Binning scheme for environment analysis using X-ray group member catalog from Gozaliasl et al. (2019) (only highest redshift bin used in our analysis). Star forming galaxies are selected using NUVrJ color-color cut.

C Acronyms

ACS Advanced Camera for Surveys

AEGIS All-Wavelength Extended Growth Strip International Survey

AGB Asymptotic Giant Branch

AGN active galactic nucleus

AIC Akike Information Criterion

AME anomalous microwave emission

ASKAP Australian Square Kilometre Array Pathfinder

AU astronomical unit

BAO baryon acoustic oscillations

CALIFA Calar Alto Legacy Integral Field Area Survey

CANDELS Cosmic Assembly Near-infrared Deep Extragalactic Legacy Survey

CDM cold dark matter

CIGALE Code Investigating GALaxy Emission

COSMOS Cosmic Evolution Survey

CMB cosmic microwave background

DES Dark Energy Survey

DIS Deep Imaging Survey

DM dark matter

DR data release

ECDFS Extended Chandra Deep Field South

EDGES Experiment to Detect the Global Epoch of Reionization Signature

ELT European Extremely Large Telescope

ESA European Space Agency

FIR far-infrared

FIRST Faint Images of the Radio Sky at Twenty Centimeters

FSC Faint Source Catalog

FUV far-ultraviolet

GALEX Galaxy Evolution Explorer

GOODS the Great Observatories Origins Deep Survey

GSWLC GALEX-SDSS-WISE Legacy Catalog

HDF-N Hubble Deep Field North

HIM hot ionized medium

HST *Hubble Space Telescope*

HUDF Hubble Ultra Deep Field

ICL intracluster light

IGL intragroup light

IGM intergalactic medium

IMF initial mass function

IR infrared

IRAS Infrared Astronomical Satellite

IRSA NASA/IPAC infrared science archive

ISM inter-stellar medium

JWST *James Webb Space Telescope*

LOFAR Low Frequency Array

LSST Large Synoptic Survey Telescope

MaNGA Mapping Nearby Galaxies at Apache Point Observatory

MIGHTEE MeerKAT International GHz Tiered Extragalactic Exploration

MIPS Multiband Imaging Photometer

MIR mid-infrared

MOONS Multi Object Optical and Near-infrared Spectrograph

MOSAIC E-ELT Multi-Object Spectrograph

MW Milky Way

NFW Navarro Frenk & White (Navarro et al. 1997)

NIR near-infrared

ngVLA Next Generation Very Large Array

NOAO National Optical Astronomy Observatory

NRAO National Radio Astronomy Observatory

NUV near-ultraviolet

IRAC Infrared Array Camera

NVSS NRAO-VLA Sky Survey

PACS The Photodetector Array Camera and Spectrometer

PAH polycyclic aromatic hydrocarbon

PDF probability distribution function

PSF point spread function

rms root meamilann square

RT radiative transfer

SAM semi-analytic model

SAMI Sydney-Australian-Astronomical-Observatory Multi-object Integral-Field Spectrograph

SDF Subaru Deep Field

SDSS Sloan Digital Sky Survey

SED spectral energy distribution

SFG star-forming galaxy

SFMS star-forming main sequence

SNR signal to noise ratio

SFR star formation rate

SFRD star formation rate density

SKA Square Kilometer Array

SPICA SPace Infrared telescope for Cosmology and Astrophysics

SPIRE Spectral and Photometric Imaging Receiver

SMBH super-massive black hole

sSFR specific star formation rate

SN supernova

TIR total infrared

UKIDSS UK Infrared Deep Sky Survey

UV ultraviolet

VISTA Visible and Infrared Survey Telescope for Astronomy

VLA Very Large Array

WFC3 Wide Field Camera 3

WFIRST Wide-Field InfraRed Survey Telescope

WHIM warm-hot intergalactic medium

WIM warm ionized medium

WISE Wide-field Infrared Survey Explorer

XMM X-ray Multi-Mirror Mission

ZEST Zurich Estimator of Structural Types

ZSMC Zurich Structure and Morphology Catalog

4MOST 4-metre Multi-Object Spectroscopic Telescope

Publications by the author

Publications presented in this thesis

- **S. K. Leslie**, M. T. Sargent, E. Schinnerer, B. Groves, A. van der Wel, G. Zamorani, Y. Fudamoto, P. Lang, and V. Smolcic, "Probing star formation and ISM properties using galaxy disk inclination. I. Evolution in disk opacity since $z \sim 0.7$," *A&A*, vol. 615, p. A7, July 2018 (link, pdf)

- **S. K. Leslie**, E. Schinnerer, B. Groves, M. T. Sargent, G. Zamorani, P. Lang, and E. Vardoulaki, "Probing star formation and ISM properties using galaxy disk inclination. II. Testing typical FUV attenuation corrections out to $z \sim 0.7$," *A&A*, vol. 616, p. A157, Sept. 2018 (link, pdf, data)

Publications that S. K. L. contributed to during PhD.

- D. Liu, P. Lang, B. Magnelli, E. Schinnerer, **S. K. Leslie**, et al. "Automated Mining of the ALMA Archive in the COSMOS Field (A^{3}COSMOS): I. Robust ALMA Continuum Photometry Catalogs and Stellar Mass and Star Formation Properties for ∼700 Galaxies at $z = 0.5$–6", *ApJS*, (submitted)

- P. Lang, E. Schinnerer, I. Smail, U. Dudzeviciute, A. M. Swinbank, D. Liu, **S. K. Leslie**, et al. "Revealing the Stellar Mass and Dust Distributions of Submillimeter Galaxies at Redshift 2" *ApJ*, (in press)

- E. F. Jiménez-Andrade, B. Magnelli, A. Karim, et al. including **S. K. Leslie**, "Radio continuum size evolution of star-forming galaxies over $0.35 < z < 2.25$" *A&A* (in press) arXiv:1903.12217, Mar. 2019

- E. Vardoulaki, E. Jiménez-Andrade, A. Karim, et al. including **S. K. Leslie**, "A closer look at the deep radio sky: Multi-component radio sources at 3-GHz VLA-COSMOS", *A&A* (in press) arXiv:1901.10168 Jan. 2019

- C. McPartland, D. B. Sanders, L. J. Kewley, and **S. K. Leslie**, "Dissecting the main sequence: AGN activity and bulge growth in the local Universe," *MNRAS*, vol. 482, pp. L129-L133, Jan. 2019

- D. C. Molnár, M. T. Sargent, J. Delhaize, et al. including **S. Leslie**, "The infrared-radio correlation of spheroid-and disc-dominated star- forming galaxies to $z \sim 1.5$ in the COSMOS field," *MNRAS*, vol. 475,pp. 827-838, Mar. 2018

- Y. Fudamoto, P. A. Oesch, E. Schinnerer, et al. including. **S. Leslie**, "The dust attenuation of star-forming galaxies at $z \sim 3$ and beyond: New insights from ALMA observations," *MNRAS*, vol. 472, pp. 483-490, Nov. 2017

- N. Lee, K. Sheth, K. S. Scott, et al. including **S. K. Leslie**, "The fine line between normal and starburst galaxies," *MNRAS*, vol. 471, pp. 2124-2142, Oct. 2017

- V. Smolčić, M. Novak, M. Bondi, et al. including **S. Leslie** ,"The VLA-COSMOS 3 GHz Large Project: Continuum data and source catalog release," *A&A*, vol. 602, p. A1, June 2017

Other publications:

First author

- **S. K. Leslie**, J. J. Bryant, I. T. Ho, E. M. Sadler, A. M. Medling, B. Groves, L. J. Kewley, J. Bland-Hawthorn, S. M. Croom, O. I. Wong, S. Brough, E. Tescari, S. M. Sweet, R. Sharp, A. W. Green, et al., "The SAMI Galaxy Survey: disc-halo interactions in radio-selected star-forming galaxies," *MNRAS*, vol. 471, pp. 2438-2452, Oct. 2017 (link, pdf)

- **S. K. Leslie**, L. J. Kewley, D. B. Sanders, and N. Lee, 11Quenching star formation: insights from the local main sequence," *MNRAS*, vol. 455, pp. L82-L86, Jan. 2016 (link, pdf)

- S. K.Leslie, J. A. Rich, L. J. Kewley, and M. A. Dopita, "The energy source and dynamicsof infrared luminous galaxy ESO 148-IG002," *MNRAS*, vol. 444, pp. 1842-1853, Oct. 2014 (link, pdf)

Co-author

- A. M. Medling, L. Cortese, S. M. Croom, et al. including **S. K. Leslie**, "The SAMI Galaxy Survey: spatially resolving the main sequence of star formation," *MNRAS*, vol. 475, pp. 5194-5214, Apr. 2018

- E. Tescari, L. Cortese, C. Power, et al., including **S. K. Leslie** "The SAMI Galaxy Survey: understanding observations of large-scale outflows at low redshift with EAGLE simulations," *MNRAS*, vol. 473, pp. 380-397, Jan. 2018

- E. J. Hampton, A. M. Medling, B. Groves, et al. including **S. Leslie**, "Using an artificial neural network to classify multicomponent emission lines with integral field spectroscopy from SAMI and S7," *MNRAS*, vol. 470,pp. 3395-3416, Sept. 2017

- J. van de Sande, J. Bland-Hawthorn, L. M. R. Fogarty, et al. including **S. K. Leslie**, "The SAMI Galaxy Survey: Revisiting Galaxy Classification through High-order Stellar Kinematics," *ApJ*, vol. 835, p. 104, Jan. 2017

- I. T. Ho, A. M. Medling, J. Bland-Hawthorn, et al. including **S. K. Leslie**, "The SAMI Galaxy Survey: extraplanar gas, galactic winds and their association with star formation history," **MNRAS**, vol. 457, pp. 1257-1278, Apr. 2016

- J. T. Allen, A. L. Schaefer, N. Scott, et al. including **S. K. Leslie**, "The SAMI Galaxy Survey: unveiling the nature of kinematically offset active galactic nuclei," *MNRAS*, vol. 451, pp. 2780-2792, Aug. 2015

- J. J. Bryant, M. S. Owers, A. S. G. Robotham, et al. including **S. K. Leslie**, "The SAMI Galaxy Survey: instrument specification and target selection," *MNRAS*, vol. 447,pp. 2857-2879, Mar. 2015

- R. Sharp, J. T. Allen, L. M. R. Fogarty, et al. including **S. K. Leslie**, "The SAMI Galaxy Survey: cubism and covariance, putting round pegs into square holes," *MNRAS*,vol. 446, pp. 1551-1566, Jan. 2015

Bibliography

Abazajian, K. N., Adelman-McCarthy, J. K., Agüeros, M. A., et al. 2009, ApJS, 182, 543 36, 44

Abraham, R. G., Tanvir, N. R., Santiago, B. X., et al. 1996, MNRAS, 279, L47 25

Abraham, R. G., Valdes, F., Yee, H. K. C., & van den Bergh, S. 1994, ApJ, 432, 75 24

Abramson, L. E., Kelson, D. D., Dressler, A., et al. 2014, ApJL, 785, L36 91, 127

Abuter, R., Amorim, A., Bauboeck, M., et al. 2019, arXiv e-prints, arXiv:1904.05721 10

Accurso, G., Saintonge, A., Catinella, B., et al. 2017, MNRAS, 470, 4750 67

Adams, F., & Laughlin, G. 1999, The Five Ages of the Universe: Inside the Physics of Eternity (Free Press Publishers) 11

Adelman-McCarthy, J. K., & et al. 2008, VizieR Online Data Catalog, 2282, 0 45

Alexander, D. M., & Hickox, R. C. 2012, NewAR, 56, 93 32

Allamandola, L. J., Tielens, A. G. G. M., & Barker, J. R. 1985, ApJL, 290, L25 78

Allen, C. W. 1976, Astrophysical Quantities, ed. 3 (Athlone) 42

Álvarez-Márquez, J., Burgarella, D., Heinis, S., et al. 2016, A&A, 587, A122 148

Amblard, A., Cooray, A., Serra, P., et al. 2011, Nature, 470, 510 122

Anderson, L. D., Bania, T. M., Jackson, J. M., et al. 2009, ApJS, 181, 255 15

Aoyama, S., Hou, K.-C., Shimizu, I., et al. 2017, MNRAS, 466, 105 67

Appleton, P. N., Fadda, D. T., Marleau, F. R., et al. 2004, The Astrophysical Journal Supplement Series, 154, 147 102

Arnouts, S., Cristiani, S., Moscardini, L., et al. 1999, MNRAS, 310, 540 94

Arnouts, S., Moscardini, L., Vanzella, E., et al. 2002, MNRAS, 329, 355 42

Arnouts, S., Walcher, C. J., Le Fevre, O., et al. 2007, A&A, 476, 137 91

Astropy Collaboration, Robitaille, T. P., Tollerud, E. J., et al. 2013, A&A, 558, A33 201

Auer, R. 1999, PhD thesis, Heidelberg Univ. (Germany). Naturwissenschaftlich-Mathematische Gesamtfakultät 22

Bañados, E., Venemans, B. P., Mazzucchelli, C., et al. 2018, Nature, 553, 473 20

Baade, W. 1951, Publications of Michigan Observatory, 10, 7 21

Babcock, H. W. 1939, Lick Observatory Bulletin, 498, 41 12

Baes, M., Trčka, A., Camps, P., et al. 2019, MNRAS, 484, 4069 144

Balcells, M., Graham, A. W., Domínguez-Palmero, L., & Peletier, R. F. 2003, ApJ, 582, L79 24

Baldry, I. K., Balogh, M. L., Bower, R. G., et al. 2006, MNRAS, 373, 469 25

Baldry, I. K., Glazebrook, K., Brinkmann, J., et al. 2004, ApJ, 600, 681 25, 30

Baldry, I. K., Driver, S. P., Loveday, J., et al. 2012, MNRAS, 421, 621 9

Balogh, M. L., Christlein, D., Zabludoff, A. I., & Zaritsky, D. 2001, ApJ, 557, 117 26

Bamford, S. P., Nichol, R. C., Baldry, I. K., et al. 2009, MNRAS, 393, 1324 26

Barnes, J. E., & Hernquist, L. 1996, ApJ, 471, 115 127

Barone, T. M., D'Eugenio, F., Colless, M., et al. 2018, ApJ, 856, 64 28

Basu, A., Wadadekar, Y., Beelen, A., et al. 2015, ApJ, 803, 51 102

Battisti, A. J., Calzetti, D., & Chary, R.-R. 2016, ApJ, 818, 13 72

Battisti, A. J., Calzetti, D., Johnson, B. D., & Elbaz, D. 2015, ApJ, 800, 143 50

Bauermeister, A., Blitz, L., Bolatto, A., et al. 2013, ApJ, 768, 132 67

Becker, R. H., White, R. L., & Helfand, D. J. 1995, ApJ, 450, 559 44, 46

Beckwith, S. V. W., Stiavelli, M., Koekemoer, A. M., et al. 2006, AJ, 132, 1729 36

Beeston, R. A., Wright, A. H., Maddox, S., et al. 2018, MNRAS, 479, 1077 9

Behroozi, P. S., Wechsler, R. H., & Conroy, C. 2013, ApJ, 770, 57 29, 30, 110

Belfiore, F., Maiolino, R., Bundy, K., et al. 2018, MNRAS, 477, 3014 33

Bell, E., Monachesi, A., D'Souza, R., et al. 2017, Galaxies, 5, 95 22

Bell, E. F. 2003, ApJ, 586, 794 26, 102, 103, 117, 118, 142, 158

Bell, E. F., McIntosh, D. H., Katz, N., & Weinberg, M. D. 2003, ApJS, 149, 289 27

Bell, E. F., Wolf, C., Meisenheimer, K., et al. 2004, ApJ, 608, 752 25

Bendo, G. J., Joseph, R. D., Wells, M., et al. 2003, AJ, 125, 2361 18

Bendo, G. J., Wilson, C. D., Pohlen, M., et al. 2010, A&A, 518, L65 40, 72

Bendo, G. J., Boselli, A., Dariush, A., et al. 2012, MNRAS, 419, 1833 40

Benson, A. J. 2010, PhR, 495, 33 33

Bershady, M. A., Jangren, A., & Conselice, C. J. 2000, AJ, 119, 2645 24

Bertone, G., Hooper, D., & Silk, J. 2004, Physics Rports, 405, 279 4

Béthermin, M., Wang, L., Doré, O., et al. 2013, A&A, 557, A66 126

Béthermin, M., Daddi, E., Magdis, G., et al. 2015, A&A, 573, A113 66, 68

Bezanson, R., van der Wel, A., Pacifici, C., et al. 2018, ApJ, 858, 60 27

Bianchi, L., Efremova, B., Herald, J., et al. 2011, MNRAS, 411, 2770 44, 45, 73

Binggeli, B., & Cameron, L. M. 1991, A&A, 252, 27 24

Binggeli, B., Sandage, A., & Tammann, G. A. 1988, ARA&A, 26, 509 29

Birnboim, Y., & Dekel, A. 2003, MNRAS, 345, 349 30

Bisigello, L., Caputi, K. I., Grogin, N., & Koekemoer, A. 2018, A&A, 609, A82 91, 104, 107, 126, 153, 157

Bland-Hawthorn, J., & Gerhard, O. 2016, ARA&A, 54, 529 11

Blandford, R. D. 1990, in Active Galactic Nuclei, ed. R. D. Blandford, H. Netzer, L. Woltjer, T. J. L. Courvoisier, & M. Mayor, 161–275 23

Blanton, M. R., & Moustakas, J. 2009, ARA&A, 47, 159 22

Blanton, M. R., Hogg, D. W., Bahcall, N. A., et al. 2003, ApJ, 592, 819 27

Blanton, M. R., Schlegel, D. J., Strauss, M. A., et al. 2005, AJ, 129, 2562 26, 45

Bloom, J. V., Croom, S. M., Bryant, J. J., et al. 2017, MNRAS, 472, 1809 28

Boissier, S., Boselli, A., Buat, V., Donas, J., & Milliard, B. 2004, A&A, 424, 465 40

Boissier, S., Gil de Paz, A., Boselli, A., et al. 2007, ApJS, 173, 524 40

Bolatto, A. D., Wolfire, M., & Leroy, A. K. 2013, ARA&A, 51, 207 17

Bolzonella, M., Miralles, J.-M., & Pelló, R. 2000, A&A, 363, 476 42

Bondi, M., Zamorani, G., Ciliegi, P., et al. 2018, A&A, 618, L8 101

Boogaard, L. A., Brinchmann, J., Bouché, N., et al. 2018, A&A, 619, A27 157, 158

Boquien, M., Calzetti, D., Combes, F., et al. 2011, AJ, 142, 111 40

Boquien, M., Buat, V., Boselli, A., et al. 2012, A&A, 539, A145 76, 81, 82

Boquien, M., Kennicutt, R., Calzetti, D., et al. 2016, A&A, 591, A6 72, 78, 82

Boulanger, F., Cox, P., & Jones, A. P. 2000, in Infrared Space Astronomy, Today and Tomorrow, ed. F. Casoli, J. Lequeux, & F. David, Vol. 70, 251 18

Bournaud, F., Elmegreen, B. G., & Martig, M. 2009, ApJ, 707, L1 140

Bournaud, F., Chapon, D., Teyssier, R., et al. 2011, ApJ, 730, 4 8

Bouvier, A., & Wadhwa, M. 2010, Nature Geoscience, 3, 637 3

Bouwens, R. J., Illingworth, G. D., Oesch, P. A., et al. 2010, ApJL, 708, L69 90

Bouwens, R. J., Bradley, L., Zitrin, A., et al. 2014, ApJ, 795, 126 90

Bouwens, R. J., Illingworth, G. D., Oesch, P. A., et al. 2015, ApJ, 803, 34 90

Bouwens, R. J., Aravena, M., Decarli, R., et al. 2016, ApJ, 833, 72 65, 118, 148

Bower, R. G., Benson, A. J., Malbon, R., et al. 2006, MNRAS, 370, 645 29

Bowman, J. D., Rogers, A. E. E., Monsalve, R. A., Mozdzen, T. J., & Mahesh, N. 2018a, Nature, 555, 67 7

—. 2018b, Nature, 564, E35 7

Brammer, G. B., Whitaker, K. E., van Dokkum, P. G., et al. 2011, ApJ, 739, 24 30, 91

Bremer, M. N., Phillipps, S., Kelvin, L. S., et al. 2018, MNRAS, 476, 12 91

Brinchmann, J., Charlot, S., White, S. D. M., et al. 2004, MNRAS, 351, 1151 28, 30, 44, 91

Brusa, M., Civano, F., Comastri, A., et al. 2010, ApJ, 716, 348 42

Bruzual, G., & Charlot, S. 2003, MNRAS, 344, 1000 42, 94

Buat, V., Donas, J., Milliard, B., & Xu, C. 1999, A&A, 352, 371 78

Buat, V., & Xu, C. 1996, A&A, 306, 61 39

Buat, V., Oi, N., Heinis, S., et al. 2015, A&A, 577, A141 149

Buisson, D. J. K., Lohfink, A. M., Alston, W. N., & Fabian, A. C. 2017, MNRAS, 464, 3194 155

Bundy, K., Bershady, M. A., Law, D. R., et al. 2015, ApJ, 798, 7 28

Burgarella, D., Buat, V., & Iglesias-Páramo, J. 2005, MNRAS, 360, 1413 125

Burgarella, D., Buat, V., Gruppioni, C., et al. 2013, A&A, 554, A70 148

Byrd, G., & Valtonen, M. 1990, ApJ, 350, 89 32

C., B., & et al. 1988, in Infrared astronomical satellite (IRAS) catalogs and atlases, Vol. 1, Infrared astronomical satellite (IRAS) catalogs and atlases. Volume 1: Explanatory supplement, ed. C. A. Beichman, G. Neugebauer, H. J. Habing, P. E. Clegg, & T. J. Chester 50

Calistro Rivera, G., Williams, W. L., Hardcastle, M. J., et al. 2017, MNRAS, 469, 3468 102

Calura, F., & Matteucci, F. 2004, MNRAS, 350, 351 13

Calzetti, D. 1997, AJ, 113, 162 72, 76

Calzetti, D. 2013, in Secular Evolution of Galaxies, ed. J. Falcón-Barroso & J. H. Knapen (Proceedings of the XXIII Canary Islands Winter School of Astrophysics: 'Secular Evolution of Galaxies'), 419 18, 78

Calzetti, D., Armus, L., Bohlin, R. C., et al. 2000, ApJ, 533, 682 148, 149

Calzetti, D., Kinney, A. L., & Storchi-Bergmann, T. 1994, ApJ, 429, 582 76

Cameron, E., Carollo, C. M., Oesch, P. A., et al. 2011, ApJ, 743, 146 25

Camps, P., Trčka, A., Trayford, J., et al. 2018, ApJS, 234, 20 144

Caon, N., Capaccioli, M., & D'Onofrio, M. 1993, MNRAS, 265, 1013 24

Capak, P. 2016, in The Early Growth of Galaxies: The HST, Spitzer and Herschel Joint Legacy, 6 93

Capak, P., Aussel, H., Ajiki, M., et al. 2007, The Astrophysical Journal Supplement Series, 172, 99 44, 126

Caplar, N., & Tacchella, S. 2019, arXiv e-prints, arXiv:1901.07556 110

Cappelluti, N., Hasinger, G., Brusa, M., et al. 2007, The Astrophysical Journal Supplement Series, 172, 341 42, 94

Caputi, K. I., Deshmukh, S., Ashby, M. L. N., et al. 2017, ApJ, 849, 45 158

Cardelli, J. A., Clayton, G. C., & Mathis, J. S. 1989, ApJ, 345, 245 81

Carilli, C. L., & Walter, F. 2013, ARA&A, 51, 105 140

Carollo, C. M. 1999, ApJ, 523, 566 24

Casey, C. M., Zavala, J. A., Spilker, J., et al. 2018, ApJ, 862, 77 38, 90

Castellano, M., Fontana, A., Grazian, A., et al. 2012, A&A, 540, A39 158

Catalán-Torrecilla, C., Gil de Paz, A., Castillo-Morales, A., et al. 2015, A&A, 584, A87 76, 78, 85, 86

Cavanaugh, J. E., & Shumway, R. H. 1997, Statistica Sinica, 7, 473 105

Chabrier, G. 2003, PASP, 115, 763 53, 74, 92, 94, 111

Chang, Y.-Y., van der Wel, A., da Cunha, E., & Rix, H.-W. 2015, ApJS, 219, 8 44, 45, 52, 53, 146

Chang, Y.-Y., Le Floc'h, E., Juneau, S., et al. 2017, ApJS, 233, 19 156

Charlot, S., & Fall, S. M. 2000, ApJ, 539, 718 40, 87

Charlton, P. J. L., Hudson, M. J., Balogh, M. L., & Khatri, S. 2017, MNRAS, 472, 2367 16

Chary, R., & Elbaz, D. 2001, ApJ, 556, 562 157

Chauke, P., van der Wel, A., Pacifici, C., et al. 2018, ApJ, 861, 13 112

Chevallard, J., Charlot, S., Wandelt, B., & Wild, V. 2013, MNRAS, 432, 2061 40

Chokshi, A., & Turner, E. L. 1992, MNRAS, 259, 421 23

Christlein, D., & Zabludoff, A. I. 2004, The Astrophysical Journal, 616, 192 22

Churazov, E., Sazonov, S., Sunyaev, R., et al. 2005, MNRAS, 363, L91 32

Cibinel, A., Daddi, E., Sargent, M. T., et al. 2019, MNRAS, 485, 5631 126

Ciesla, L., Boselli, A., Smith, M. W. L., et al. 2012, A&A, 543, A161 40

Ciesla, L., Boquien, M., Boselli, A., et al. 2014, A&A, 565, A128 40

Ciotti, L., & Ostriker, J. P. 1997, ApJ, 487, L105 32

Civano, F., Marchesi, S., Comastri, A., et al. 2016, ApJ, 819, 62 94

Clowe, D., Gonzalez, A., & Markevitch, M. 2004, ApJ, 604, 596 12

Cluver, M. E., Jarrett, T. H., Dale, D. A., et al. 2017, ApJ, 850, 68 78, 84, 85, 86

Cluver, M. E., Jarrett, T. H., Hopkins, A. M., et al. 2014, ApJ, 782, 90 52, 78

Cole, S., Aragon-Salamanca, A., Frenk, C. S., Navarro, J. F., & Zepf, S. E. 1994, MNRAS, 271, 781 29

Cole, S., Norberg, P., Baugh, C. M., et al. 2001, MNRAS, 326, 255 26

Condon, J. J. 1992, ARAA, 30, 575 36, 90, 102

Condon, J. J., Cotton, W. D., Greisen, E. W., et al. 1998, AJ, 115, 1693 44, 46

Conroy, C., Schiminovich, D., & Blanton, M. R. 2010, ApJ, 718, 184 47

Conselice, C. J. 2003, ApJS, 147, 1 24, 25

Conselice, C. J., Bershady, M. A., & Gallagher, J. S., I. 2000a, A&A, 354, L21 25

Conselice, C. J., Bershady, M. A., & Jangren, A. 2000b, ApJ, 529, 886 25

Cooray, A., Amblard, A., Wang, L., et al. 2010, A&A, 518, L22 122

Cortese, L., Fogarty, L. M. R., Ho, I. T., et al. 2014, ApJ, 795, L37 28

Cowie, L. L., & McKee, C. F. 1977, ApJ, 211, 135 32

Crocker, A. F., Bureau, M., Young, L. M., & Combes, F. 2011, MNRAS, 410, 1197 23

Croom, S. M., Lawrence, J. S., Bland-Hawthorn, J., et al. 2012, MNRAS, 421, 872 28

Croton, D. J., Springel, V., White, S. D. M., et al. 2006, MNRAS, 365, 11 29, 32

Cucciati, O., Tresse, L., Ilbert, O., et al. 2012, A&A, 539, A31 148

da Cunha, E., Charlot, S., & Elbaz, D. 2008, MNRAS, 388, 1595 40, 50, 87, 156

da Cunha, E., Eminian, C., Charlot, S., & Blaizot, J. 2010, MNRAS, 403, 1894 67

Daddi, E., Dickinson, M., Morrison, G., et al. 2007, ApJ, 670, 156 9

Dahlen, T., Mobasher, B., Dickinson, M., et al. 2007, ApJ, 654, 172 149

Dalal, N., & Griest, K. 2000, Physics Letters B, 490, 1 11

Dalcanton, J. J., Yoachim, P., & Bernstein, R. A. 2004, ApJ, 608, 189 59

Dale, D. A., & Helou, G. 2002, ApJ, 576, 159 50

Dale, D. A., Gil de Paz, A., Gordon, K. D., et al. 2007, ApJ, 655, 863 40

Dale, D. A., Cook, D. O., Roussel, H., et al. 2017, ApJ, 837, 90 84

Damjanov, I., Zahid, H. J., Geller, M. J., Fabricant, D. G., & Hwang, H. S. 2018, ApJS, 234, 21 143

Darvish, B., Mobasher, B., Sobral, D., et al. 2016, ApJ, 825, 113 128

Darvish, B., Sobral, D., Mobasher, B., et al. 2014, ApJ, 796, 51 128

Davé, R., Thompson, R., & Hopkins, P. F. 2016, MNRAS, 462, 3265 115

Davidzon, I., Ilbert, O., Faisst, A. L., Sparre, M., & Capak, P. L. 2018, ApJ, 852, 107 107, 110

Davidzon, I., Ilbert, O., Laigle, C., et al. 2017, A&A, 605, A70 92, 95, 96, 97, 110, 115, 116, 117, 120

Davies, J. I., Phillips, S., Boyce, P. J., & Disney, M. J. 1993, MNRAS, 260, 491 54

Davies, L. J. M., Driver, S. P., Robotham, A. S. G., et al. 2016, MNRAS, 461, 458 79, 80, 110, 117

Davies, L. J. M., Huynh, M. T., Hopkins, A. M., et al. 2017, MNRAS, 466, 2312 52, 63, 117, 118, 142

De Geyter, G., Baes, M., Camps, P., et al. 2014, MNRAS, 441, 869 40

de Jong, R. S. 1996, A&AS, 118, 557 24

de Vaucouleurs, G. 1948, Annales d'Astrophysique, 11, 247 22, 23

—. 1959, Handbuch der Physik, 11, 275 21

De Vis, P., Dunne, L., Maddox, S., et al. 2017, MNRAS, 464, 4680 40, 59

de Zeeuw, T., & Franx, M. 1991, ARA&A, 29, 239 23

Decarli, R., Walter, F., Aravena, M., et al. 2016, ApJ, 833, 69 17, 67

Decarli, R., Walter, F., Gónzalez-López, J., et al. 2019, arXiv e-prints, arXiv:1903.09164 17

Dekel, A., & Mandelker, N. 2014, MNRAS, 444, 2071 33

Dekel, A., Birnboim, Y., Engel, G., et al. 2009, Nature, 457, 451 8

del Peloso, E. F., da Silva, L., de Mello, G. F. P., & Arany-Prado, L. I. 2005, in IAU Symposium, Vol. 228, From Lithium to Uranium: Elemental Tracers of Early Cosmic Evolution, ed. V. Hill, P. Francois, & F. Primas, 485–486 3

Delhaize, J., Meyer, M. J., Staveley-Smith, L., & Boyle, B. J. 2013, MNRAS, 433, 1398 9

Delhaize, J., Smolčić, V., Delvecchio, I., et al. 2017, A&A, 602, A4 90, 102, 103, 117, 118, 120, 140, 141, 143, 153, 159

Delvecchio, I., Smolčić, V., Zamorani, G., et al. 2017, A&A, 602, A3 155, 156

—. 2018, MNRAS, 481, 4971 32

Devour, B. M., & Bell, E. F. 2016, MNRAS, 459, 2054 40, 41, 46

Dickey, J. M. 1991, in Astronomical Society of the Pacific Conference Series, Vol. 18, The Interpretation of Modern Synthesis Observations of Spiral Galaxies, ed. N. Duric & P. C. Crane, 163–173 16

Dieleman, S., Willett, K. W., & Dambre, J. 2015, MNRAS, 450, 1441 24

Diplas, A., & Savage, B. D. 1991, ApJ, 377, 126 16

Disney, M., Davies, J., & Phillipps, S. 1989, MNRAS, 239, 939 40

Djorgovski, S., & Davis, M. 1987, ApJ, 313, 59 27

Dodelson, S. 2003, Modern cosmology (Academic Press) 3

Donley, J. L., Koekemoer, A. M., Brusa, M., et al. 2012, ApJ, 748, 142 42, 155

Donnari, M., Pillepich, A., Nelson, D., et al. 2018, arXiv e-prints, arXiv:1812.07584 29, 112, 113

Dopita, M. A., Groves, B. A., Sutherland, R. S., & Kewley, L. J. 2003, ApJ, 583, 727 78

Draine, B. T. 2003, ApJ, 598, 1017 18

—. 2011, Physics of the Interstellar and Intergalactic Medium, Princeton Series in Astrophysics (Princeton University Press) 18

Draine, B. T., & Li, A. 2007a, ApJ, 657, 810 40

—. 2007b, ApJ, 657, 810 40, 102

Dressler, A. 1980, ApJ, 236, 351 31

Dressler, A. 1987, in Nearly Normal Galaxies. From the Planck Time to the Present, ed. S. M. Faber, 276 27

Driver, S. P., Popescu, C. C., Tuffs, R. J., et al. 2007, MNRAS, 379, 1022 46, 59

Driver, S. P., Hill, D. T., Kelvin, L. S., et al. 2011, MNRAS, 413, 971 52

Driver, S. P., Andrews, S. K., da Cunha, E., et al. 2018, MNRAS, 475, 2891 9, 10, 13, 18

Duivenvoorden, S., Oliver, S., Buat, V., et al. 2016, MNRAS, 462, 277 122, 128

Eales, S., Smith, D., Bourne, N., et al. 2018a, MNRAS, 473, 3507 91, 96

Eales, S. A., Baes, M., Bourne, N., et al. 2018b, MNRAS, 481, 1183 153

Elbaz, D., Daddi, E., Le Borgne, D., et al. 2007, A&A, 468, 33 91

Elbaz, D., Dickinson, M., Hwang, H. S., et al. 2011, A&A, 533, A119 28

Elitzur, M., Ho, L. C., & Trump, J. R. 2014, MNRAS, 438, 3340 155

Ellison, S. L., Patton, D. R., Mendel, J. T., & Scudder, J. M. 2011, MNRAS, 418, 2043 16

Emsellem, E., Cappellari, M., Krajnović, D., et al. 2007, MNRAS, 379, 401 23

—. 2011, MNRAS, 414, 888 23

Erfanianfar, G., Popesso, P., Finoguenov, A., et al. 2016, MNRAS, 455, 2839 112, 127, 129

Erwin, D. H., Laflamme, M., Tweedt, S. M., et al. 2011, Science, 334, 1091 3

Erwin, P., Beckman, J. E., & Pohlen, M. 2005, ApJ, 626, L81 22

Eskridge, P. B., & Frogel, J. A. 1999, Ap&SS, 269, 427 22

Event Horizon Telescope Collaboration, Akiyama, K., Alberdi, A., et al. 2019, ApJ, 875, L1 33

Ewen, H. I., & Purcell, E. M. 1951, Nature, 168, 356 16

Faber, S. M., & Jackson, R. E. 1976, ApJ, 204, 668 27

Faber, S. M., Willmer, C. N. A., Wolf, C., et al. 2007, ApJ, 665, 265 91

Fabian, A. C. 2012, ARA&A, 50, 455 32

Fall, S. M., & Efstathiou, G. 1980, MNRAS, 193, 189 8, 15

Fan, X. 2006, NewAR, 50, 665 7, 8

Feldmann, R. 2017, MNRAS, 470, L59 91

Fernández, X., Gim, H. B., van Gorkom, J. H., et al. 2016, ApJ, 824, L1 17

Ferrarese, L., & Ford, H. 2005, SSRv, 116, 523 7

Ferrarese, L., & Merritt, D. 2000, ApJ, 539, L9 19

Ferrière, K. M. 2001, Reviews of Modern Physics, 73, 1031 17

Finoguenov, A., Guzzo, L., Hasinger, G., et al. 2007, The Astrophysical Journal Supplement Series, 172, 182 98

Foreman-Mackey, D. 2016, The Journal of Open Source Software, 24, doi:10.21105/joss.00024 200

—. 2017, Fitting a plane to data, http://dfm.io/posts/fitting-a-plane/ 74, 81

Foreman-Mackey, D., Hogg, D. W., Lang, D., & Goodman, J. 2013, PASP, 125, 306 58, 74

Förster Schreiber, N. M., Genzel, R., Lehnert, M. D., et al. 2006, ApJ, 645, 1062 8

Förster Schreiber, N. M., Genzel, R., Bouché, N., et al. 2009, ApJ, 706, 1364 66, 88

Fox, A. J., Wakker, B. P., Barger, K. A., et al. 2014, ApJ, 787, 147 11

Fragkoudi, F., Athanassoula, E., & Bosma, A. 2016, MNRAS, 462, L41 128

Fraknoi, A. 2017, The Physics Teacher, 55, 502 23

Franx, M., Illingworth, G., & Heckman, T. 1989, ApJ, 344, 613 23

Freeman, K. C. 1970, ApJ, 160, 811 12, 24

Friedmann, A. 1922, Zeitschrift fur Physik, 10, 377 6

Fudamoto, Y., Oesch, P. A., Schinnerer, E., et al. 2017, MNRAS, 472, 483 118

Fukugita, M., Hogan, C. J., & Peebles, P. J. E. 1998, ApJ, 503, 518 9

Gabor, J. M., Davé, R., Finlator, K., & Oppenheimer, B. D. 2010, MNRAS, 407, 749 31

Galliano, F., Galametz, M., & Jones, A. P. 2018, ARA&A, 56, 673 14

Galliano, F., Hony, S., Bernard, J.-P., et al. 2011, A&A, 536, A88 40

Garrett, M. A. 2002, A&A, 384, L19 102

Gavazzi, G., Consolandi, G., Dotti, M., et al. 2015, A&A, 580, A116 115

Gebhardt, K., Bender, R., Bower, G., et al. 2000, ApJ, 539, L13 19

Genzel, R., Newman, S., Jones, T., et al. 2011, ApJ, 733, 101 8, 9

Genzel, R., Tacconi, L. J., Lutz, D., et al. 2015, ApJ, 800, 20 67

George, M. R., Leauthaud, A., Bundy, K., et al. 2011, ApJ, 742, 125 98

Gerola, H., & Seiden, P. E. 1978, ApJ, 223, 129 22

Giavalisco, M., Steidel, C. C., & Macchetto, F. D. 1996, ApJ, 470, 189 25

Gini, C. 1912, Variabilità e mutabilità 25

Giovanelli, R., Haynes, M. P., Salzer, J. J., et al. 1994, AJ, 107, 2036 40

—. 1995, AJ, 110, 1059 40

Gladders, M. D., Oemler, A., Dressler, A., et al. 2013, ApJ, 770, 64 112

Glenn, J., Bradford, C. M., Amini, R., et al. 2018, in Society of Photo-Optical Instrumentation Engineers (SPIE) Conference Series, Vol. 10698, 106980L 144

Gloeckler, G., & Fisk, L. A. 2016, in Journal of Physics Conference Series, Vol. 767, 012011 10

González, R. A., Allen, R. J., Dirsch, B., et al. 1998, ApJ, 506, 152 40

Gott, J. R., I. 1977, ARA&A, 15, 235 23

Gozaliasl, G., Finoguenov, A., Tanaka, M., et al. 2019, MNRAS, 483, 3545 98, 99, 162

Graham, A. W. 2001, AJ, 121, 820 24

—. 2013, Planets, Stars and Stellar Systems, 6, 91 22

Graham, A. W., Driver, S. P., Petrosian, V., et al. 2005, AJ, 130, 1535 24

Graham, J. R., & Dey, A. 1996, ApJ, 471, 720 24

Grasha, K., Calzetti, D., Adamo, A., et al. 2019, MNRAS, 483, 4707 15

Grazian, A., Fontana, A., Santini, P., et al. 2015, A&A, 575, A96 110

Griffith, R. L., Cooper, M. C., Newman, J. A., et al. 2012, ApJS, 200, 9 24

Grootes, M. W., Tuffs, R. J., Popescu, C. C., et al. 2013, ApJ, 766, 59 59, 61, 62, 79, 80

—. 2017, AJ, 153, 111 79, 80

Groves, B., Krause, O., Sandstrom, K., et al. 2012, MNRAS, 426, 892 72

Gu, Y., Fang, G., Yuan, Q., Cai, Z., & Wang, T. 2018, ApJ, 855, 10 129

Guillet, V., Fanciullo, L., Verstraete, L., et al. 2018, A&A, 610, A16 14

Gunn, J. E., & Gott, J. Richard, I. 1972, ApJ, 176, 1 32

Gunn, J. E., & Peterson, B. A. 1965, ApJ, 142, 1633 7

Guo, K., Zheng, X. Z., & Fu, H. 2013, ApJ, 778, 23 112

Guo, Q., White, S., Li, C., & Boylan-Kolchin, M. 2010, MNRAS, 404, 1111 29

Gürkan, G., Hardcastle, M. J., Smith, D. J. B., et al. 2018, MNRAS, 475, 3010 119

Guth, A. H. 1981, PhRvD, 23, 347 3

Guthrie, B. N. G. 1992, Astronomy and Astrophysics Supplement, 93, 255 46

Hahn, C., Starkenburg, T. K., Choi, E., et al. 2019, ApJ, 872, 160 104, 124, 153

Haines, C. P., Pereira, M. J., Smith, G. P., et al. 2013, ApJ, 775, 126 129

Hales, C. A., Murphy, T., Curran, J. R., et al. 2012, MNRAS, 425, 979 92, 152

Han, J. L. 2017, ARA&A, 55, 111 19

Han, J. L., & Qiao, G. J. 1994, A&A, 288, 759 19

Hansen, C., Steven, D., & Trimble, V. 2004, Stellar interiors: physical principles, structure, and evolution (Springer-Verlag) 15

Hao, C.-N., Kennicutt, R. C., Johnson, B. D., et al. 2011, ApJ, 741, 124 71, 78, 149

Harrison, C. M., Alexander, D. M., Swinbank, A. M., et al. 2012, MNRAS, 426, 1073 32

Hart, R., & Berendzen, R. 1971, Journal for the History of Astronomy, 2, 109 21

Hasinger, G., Cappelluti, N., Brunner, H., et al. 2007, ApJS, 172, 29 42

Heinis, S., Buat, V., Béthermin, M., et al. 2013, MNRAS, 429, 1113 148

Helou, G., Soifer, B. T., & Rowan-Robinson, M. 1985, ApJL, 298, L7 102

Henriques, B. M. B., White, S. D. M., Lilly, S. J., et al. 2019, MNRAS, 485, 3446 30

Henriques, B. M. B., White, S. D. M., Thomas, P. A., et al. 2015, MNRAS, 451, 2663 29, 30

Hernández-Monteagudo, C., Ma, Y.-Z., Kitaura, F. S., et al. 2015, PhRvL, 115, 191301 9

Herpich, J., Stinson, G. S., Rix, H. W., Martig, M., & Dutton, A. A. 2017, MNRAS, 470, 4941 22

Herpich, J., Stinson, G. S., Dutton, A. A., et al. 2015, MNRAS, 448, L99 22

Herrera Ruiz, N., Middelberg, E., Deller, A., et al. 2018, A&A, 616, A128 92

Hill, A., Reynolds, R., Haffner, L., Wood, K., & Madsen, G. 2015, Highlights of Astronomy, 16, 574 18

Hills, R., Kulkarni, G., Meerburg, P. D., & Puchwein, E. 2018, Nature, 564, E32 7

Hinshaw, G., Larson, D., Komatsu, E., et al. 2013, The Astrophysical Journal Supplement Series, 208, 19 158

Hockney, R. W., & Eastwood, J. W. 1981, Computer Simulation Using Particles (McGraw-Hill) 33

Hodge, J. A., Smail, I., Walter, F., et al. 2018, arXiv e-prints, arXiv:1810.12307 140

Holmberg, E. 1958, Meddelanden fran Lunds Astronomiska Observatorium Serie II, 136, 1 40

—. 1975, Magnitudes, Colors, Surface Brightness, Intensity Distributions Absolute Luminosities, and Diameters of Galaxies, ed. A. Sandage, M. Sandage, & J. Kristian (the University of Chicago Press), 123 40

Holwerda, B. W., Gonzalez, R. A., Allen, R. J., & van der Kruit, P. C. 2005, AJ, 129, 1396 40

Hopkins, A. M., & Beacom, J. F. 2006, ApJ, 651, 142 117

Hopkins, J. 2011, in American Astronomical Society Meeting Abstracts, Vol. 217, American Astronomical Society Meeting Abstracts #217, 224.02 8

Hopkins, P. F., Quataert, E., & Murray, N. 2012, MNRAS, 421, 3522 32

Hsieh, B.-C., Wang, W.-H., Hsieh, C.-C., et al. 2012, The Astrophysical Journal Supplement Series, 203, 23 94

Hubble, E. P. 1926, ApJ, 64, 321 20, 46

—. 1936, Realm of the Nebulae (Yale University Press) 20

Huber, P. J. 1981, Robust statistics (Wiley) 53

Huertas-Company, M., Tasca, L., Rouan, D., Kneib, J. P., & Le Fèvre, O. 2008, in American Institute of Physics Conference Series, ed. C. A. L. Bailer-Jones, Vol. 1082, 144–150 25

Huertas-Company, M., Kaviraj, S., Mei, S., et al. 2014, arXiv e-prints, arXiv:1406.1175 25

Huertas-Company, M., Gravet, R., Cabrera-Vives, G., et al. 2015, ApJS, 221, 8 24

Huizinga, J. E., & van Albada, T. S. 1992, MNRAS, 254, 677 40, 47

Hunt, L., Bianchi, S., & Maiolino, R. 2005, A&A, 434, 849 143

Hunt, L. K., Draine, B. T., Bianchi, S., et al. 2015, A&A, 576, A33 40

Hunter, C. 1977, AJ, 82, 271 23

Hurvich, C., & Tsai, C.-L. 1989, Biometrika, 76, 297 105

Ilbert, O., Arnouts, S., McCracken, H. J., et al. 2006, A&A, 457, 841 42

Ilbert, O., Capak, P., Salvato, M., et al. 2009, ApJ, 690, 1236 94

Ilbert, O., Salvato, M., Le Floc'h, E., et al. 2010, ApJ, 709, 644 91

Ilbert, O., McCracken, H. J., Le Fèvre, O., et al. 2013, A&A, 556, A55 30, 42, 43, 92, 94, 96, 98, 117, 120, 158

Ilbert, O., Arnouts, S., Le Floc'h, E., et al. 2015, A&A, 579, A2 42, 94, 112

Ilbert, O., Capak, P., Salvato, M., et al. 2017, VizieR Online Data Catalog, J/ApJ/690/1236 97

Illingworth, G. 1977, ApJ, 218, L43 23

Ivezić, Ž., Menou, K., Knapp, G. R., et al. 2002, AJ, 124, 2364 46

Ivison, R. J., Alexander, D. M., Biggs, A. D., et al. 2010a, MNRAS, 402, 245 102

Ivison, R. J., Magnelli, B., Ibar, E., et al. 2010b, A&A, 518, L31 102

Iyer, K., Gawiser, E., Davé, R., et al. 2018, ApJ, 866, 120 107, 158

Iyer, K. G., Gawiser, E., Faber, S. M., et al. 2019, arXiv e-prints, arXiv:1901.02877 112

Izotova, I. Y., & Izotov, Y. I. 2018, Ap&SS, 363, 47 79

Jarrett, T. H., Cohen, M., Masci, F., et al. 2011, ApJ, 735, 112 78

Jarvis, M., Taylor, R., Agudo, I., et al. 2016, in Proceedings of MeerKAT Science: On the Pathway to the SKA. 25-27 May, 6 141

Jeans, J. H. 1919, JRASC, 13, 215 21

Jedrzejewski, R., & Schechter, P. L. 1989, AJ, 98, 147 23

Jenkins, E. B. 2013, ApJ, 764, 25 17

Jerjen, H. 2000, Luminosity Function of Galaxies, ed. P. Murdin (Encyclopedia of Astronomy and Astrophysics), 2604 26

Jiménez-Andrade, E. F., Magnelli, B., Karim, A., et al. 2019, arXiv e-prints, arXiv:1903.12217 101

Johnston, R., Vaccari, M., Jarvis, M., et al. 2015, MNRAS, 453, 2540 91, 113

Jones, A. P., Fanciullo, L., Köhler, M., et al. 2013, A&A, 558, A62 40

Jones, A. P., Tielens, A. G. G. M., & Hollenbach, D. J. 1996, ApJ, 469, 740 40

Jonsson, P., Groves, B. A., & Cox, T. J. 2010, MNRAS, 403, 17 66

Kampczyk, P., Lilly, S. J., Carollo, C. M., et al. 2007, ApJS, 172, 329 41

Karim, A., Schinnerer, E., Martínez-Sansigre, A., et al. 2011, ApJ, 730, 61 53, 90, 91, 92, 96, 100, 102, 103, 113, 115, 117, 118, 139, 145, 152, 158

Kartaltepe, J. S., Sanders, D. B., Le Floc'h, E., et al. 2010a, ApJ, 709, 572 126

—. 2010b, ApJ, 721, 98 126

Kassin, S. A., Weiner, B. J., Faber, S. M., et al. 2012, ApJ, 758, 106 9, 66, 88

Katsianis, A., Zheng, X., Gonzalez, V., et al. 2019, arXiv e-prints, arXiv:1905.02023 112, 113

Kauffmann, G., White, S. D. M., & Guiderdoni, B. 1993, MNRAS, 264, 201 29

Kauffmann, G., Heckman, T. M., Tremonti, C., et al. 2003, MNRAS, 346, 1055 24, 30, 44

Kautsch, S. J. 2009, PASP, 121, 1297 21

Kay, S. T., Pearce, F. R., Frenk, C. S., & Jenkins, A. 2002, MNRAS, 330, 113 29

Keel, W. C., & White, III, R. E. 2001, AJ, 121, 1442 40

Kelvin, L. S., Driver, S. P., Robotham, A. S. G., et al. 2014, MNRAS, 444, 1647 27

Kennicutt, R. C., & Evans, N. J. 2012, ARA&A, 50, 531 50, 52, 62, 78, 90, 102, 118

Kennicutt, Jr., R. C., Armus, L., Bendo, G., et al. 2003, PASP, 115, 928 149

Kennicutt, Jr., R. C., Hao, C.-N., Calzetti, D., et al. 2009, ApJ, 703, 1672 78

Keres, D., Yun, M. S., & Young, J. S. 2003, ApJ, 582, 659 9

Kewley, L. J., Groves, B., Kauffmann, G., & Heckman, T. 2006, MNRAS, 372, 961 44

Kewley, L. J., Jansen, R. A., & Geller, M. J. 2005, PASP, 117, 227 44

Kimball, A. E., & Ivezić, Ž. 2008, AJ, 136, 684 46

—. 2014, ArXiv e-prints, arXiv:1401.1535 44, 46

Klessen, R. S. 2018, arXiv e-prints, arXiv:1807.06248 6

Knapen, J. H., Pérez-Ramírez, D., & Laine, S. 2002, MNRAS, 337, 808 22

Koekemoer, A. M., Aussel, H., Calzetti, D., et al. 2007, ApJS, 172, 196 43, 98

Kormendy, J. 1977, ApJ, 218, 333 27

Kormendy, J., & Djorgovski, S. 1989, ARA&A, 27, 235 22

Kormendy, J., & Kennicutt, Robert C., J. 2004, ARA&A, 42, 603 22

Kormendy, J., & Richstone, D. 1995, ARA&A, 33, 581 7, 19, 23

Koyama, Y., Kodama, T., Tadaki, K.-i., et al. 2014, ApJ, 789, 18 128

Krajnović, D., Emsellem, E., den Brok, M., et al. 2018, MNRAS, 477, 5327 9

Krauss, L. M., & Chaboyer, B. 2003, Science, 299, 65 3

Kroupa, P. 2001, MNRAS, 322, 231 41, 73, 159

Lacey, C., & Silk, J. 1991, ApJ, 381, 14 29

Lacki, B. C., & Thompson, T. A. 2010, ApJ, 717, 196 143

Lacki, B. C., Thompson, T. A., & Quataert, E. 2010, ApJ, 717, 1 102, 143

Lackner, C. N., & Gunn, J. E. 2012, MNRAS, 421, 2277 24

Laigle, C., McCracken, H. J., Ilbert, O., et al. 2016, ApJS, 224, 24 42, 77, 92, 93, 94, 95, 96, 97, 98, 99, 114, 130, 155

Lamers, H. J., & M. Levesque, E. 2017, Understanding Stellar Evolution, 2514-3433 (IOP Publishing), doi:10.1088/978-0-7503-1278-3 15

Lang, P., Wuyts, S., Somerville, R. S., et al. 2014a, ApJ, 788, 11 127, 128, 129, 131

—. 2014b, ApJ, 788, 11 145

Larson, D., Dunkley, J., Hinshaw, G., et al. 2011, The Astrophysical Journal Supplement Series, 192, 16 53, 74, 158, 159

Larson, R. B., Tinsley, B. M., & Caldwell, C. N. 1980, ApJ, 237, 692 32

Lauer, T. R., Gebhardt, K., Faber, S. M., et al. 2007, ApJ, 664, 226 23

Laughlin, G., Bodenheimer, P., & Adams, F. C. 1997, ApJ, 482, 420 11

Law, D. R., Steidel, C. C., Erb, D. K., et al. 2007, ApJ, 656, 1 25

Le Floc'h, E., Aussel, H., Ilbert, O., et al. 2009, ApJ, 703, 222 44, 94

Leauthaud, A., Finoguenov, A., Kneib, J.-P., et al. 2010, ApJ, 709, 97 99

Lee, B., Giavalisco, M., Whitaker, K., et al. 2018, ApJ, 853, 131 106, 107, 115

Lee, J. C., Hwang, H. S., & Ko, J. 2013, ApJ, 774, 62 25, 52

Lee, N., Sanders, D. B., Casey, C. M., et al. 2015, ApJ, 801, 80 91, 104, 105, 106, 107, 108, 116, 125, 145, 158

Leger, A., & Puget, J. L. 1984, A&A, 137, L5 78

Legrand, L., McCracken, H. J., Davidzon, I., et al. 2018, arXiv e-prints, arXiv:1810.10557 126

Leitherer, C., Tremonti, C. A., Heckman, T. M., & Calzetti, D. 2011, AJ, 141, 37 76

Leitherer, C., Schaerer, D., Goldader, J. D., et al. 1999, ApJS, 123, 3 71

Leitner, S. N. 2012, ApJ, 745, 149 110

Lemaître, G. 1927, Annales de la Société Scientifique de Bruxelles, 47, 49 6

Leroy, A. K., Evans, A. S., Momjian, E., et al. 2011a, ApJ, 739, L25 143

Leroy, A. K., Bolatto, A., Gordon, K., et al. 2011b, ApJ, 737, 12 67

Leslie, S. K., Kewley, L. J., Sanders, D. B., & Lee, N. 2016, MNRAS, 455, L82 32

Leslie, S. K., Schinnerer, E., Groves, B., et al. 2018a, A&A, 616, A157 71

Leslie, S. K., Sargent, M. T., Schinnerer, E., et al. 2018b, A&A, 615, A7 39, 72

Lian, J., Yan, R., Zhang, K., & Kong, X. 2016, ApJ, 832, 29 31

Licquia, T. C., & Newman, J. A. 2015, ApJ, 806, 96 11

Lilly, S. J., & Carollo, C. M. 2016, ApJ, 833, 1 28

Lin, C. C., & Shu, F. H. 1964, ApJ, 140, 646 21

Liu, D., Daddi, E., Dickinson, M., et al. 2018, ApJ, 853, 172 117

Lotz, J. M., Primack, J., & Madau, P. 2004, AJ, 128, 163 24, 25

Loveday, J., Peterson, B. A., Efstathiou, G., & Maddox, S. J. 1992, ApJ, 390, 338 29

Lutz, D., Mainieri, V., Rafferty, D., et al. 2010, ApJ, 712, 1287 32

Lutz, D., Poglitsch, A., Altieri, B., et al. 2011, A&A, 532, A90 43, 44, 94

Lynden-Bell, D. 1969, Nature, 223, 690 19

MacArthur, L. A., Courteau, S., & Holtzman, J. A. 2003, ApJ, 582, 689 24

Madau, P., & Dickinson, M. 2014, ARA&A, 52, 415 4, 35, 42, 53, 71, 90, 117, 126, 137, 155

Magdis, G. E., Rigopoulou, D., Huang, J.-S., & Fazio, G. G. 2010, MNRAS, 401, 1521 91

Magdis, G. E., Daddi, E., Béthermin, M., et al. 2012, ApJ, 760, 6 50

Magnelli, B., Lutz, D., Saintonge, A., et al. 2014, A&A, 561, A86 66, 72, 104

Magnelli, B., Ivison, R. J., Lutz, D., et al. 2015, A&A, 573, A45 90, 101, 102, 103, 117, 118, 119, 120, 140, 152, 153, 159, 160

Magorrian, J., Tremaine, S., Richstone, D., et al. 1998, AJ, 115, 2285 28

Maller, A. H., Berlind, A. A., Blanton, M. R., & Hogg, D. W. 2009, ApJ, 691, 394 40, 47

Man, A., & Belli, S. 2018, Nature Astronomy, 2, 695 31

Mandelker, N., Nagai, D., Aung, H., et al. 2019, MNRAS, 484, 1100 8, 15

Mao, M. Y., Huynh, M. T., Norris, R. P., et al. 2011, ApJ, 731, 79 151

Marchesi, S., Civano, F., Elvis, M., et al. 2016, ApJ, 817, 34 94

Marín, F. A., Gnedin, N. Y., Seo, H.-J., & Vallinotto, A. 2010, ApJ, 718, 972 9

Markevitch, M., Gonzalez, A., Clowe, D., & Vikhlinin, A. 2004, in Astrophysics and Space Science Library, ed. M. Plionis, Vol. 301, 263 12

Martig, M., Bournaud, F., Teyssier, R., & Dekel, A. 2009, ApJ, 707, 250 139

Martin, D. C., Fanson, J., Schiminovich, D., et al. 2005, ApJL, 619, L1 71

Masters, K. L., Nichol, R., Bamford, S., et al. 2010a, MNRAS, 404, 792 40, 47

Masters, K. L., Mosleh, M., Romer, A. K., et al. 2010b, MNRAS, 405, 783 26

Mateos, S., Alonso-Herrero, A., Carrera, F. J., et al. 2012, MNRAS, 426, 3271 45

Mathis, J. S. 1990, ARA&A, 28, 37 40

Matthee, J., & Schaye, J. 2019, MNRAS, 484, 915 107, 113, 129

Mayer, L., Kazantzidis, S., & Escala, A. 2008, MmSAI, 79, 1284 16

Mazzucchelli, C., Bañados, E., Venemans, B. P., et al. 2017, ApJ, 849, 91 20

McConnell, N. J., & Ma, C.-P. 2013, ApJ, 764, 184 19

McCracken, H. J., Capak, P., Salvato, M., et al. 2010, ApJ, 708, 202 94

McCracken, H. J., Milvang-Jensen, B., Dunlop, J., et al. 2012, A&A, 544, A156 93, 94

McGee, S. L., Balogh, M. L., Wilman, D. J., et al. 2011, MNRAS, 413, 996 128

McLure, R. J., Dunlop, J. S., Cullen, F., et al. 2017, ArXiv e-prints, arXiv:1709.06102 65, 66, 148

McNamara, B. R., & Nulsen, P. E. J. 2012, New Journal of Physics, 14, 055023 32

McPartland, C., Sanders, D. B., Kewley, L. J., & Leslie, S. K. 2019, MNRAS, 482, L129 91

Mebold, U., Winnberg, A., Kalberla, P. M. W., & Goss, W. M. 1982, A&A, 115, 223 17

Medling, A. M., Cortese, L., Croom, S. M., et al. 2018, MNRAS, 475, 5194 28

Meert, A., Vikram, V., & Bernardi, M. 2016, MNRAS, 455, 2440 24

Meidt, S. E., Leroy, A. K., Rosolowsky, E., et al. 2018, ApJ, 854, 100 128

Merloni, A., & Heinz, S. 2007, MNRAS, 381, 589 19

Merritt, A., van Dokkum, P., Abraham, R., & Zhang, J. 2016, ApJ, 830, 62 16

Merritt, D. 1983, ApJ, 264, 24 32

Meurer, G. R., Heckman, T. M., & Calzetti, D. 1999, ApJ, 521, 64 76, 78

Mihos, J. C. 2004, in Clusters of Galaxies: Probes of Cosmological Structure and Galaxy Evolution, ed. J. S. Mulchaey, A. Dressler, & A. Oemler, 277 32

Misiriotis, A., Popescu, C. C., Tuffs, R., & Kylafis, N. D. 2001, A&A, 372, 775 59

Mitra, S., Davé, R., Simha, V., & Finlator, K. 2017, MNRAS, 464, 2766 110

Mo, H., van den Bosch, F. C., & White, S. 2010, Galaxy Formation and Evolution (Cambridge University Press) 21, 24, 29

Mo, H. J., Mao, S., & White, S. D. M. 1998, MNRAS, 295, 319 8

Moffett, A. J., Lange, R., Driver, S. P., et al. 2016, MNRAS, 462, 4336 9

Möllenhoff, C., Popescu, C. C., & Tuffs, R. J. 2006, A&A, 456, 941 47

Molnar, D. C., Sargent, M. T., Delhaize, J., et al. 2017, ArXiv e-prints, arXiv:1710.07655 52

Molnár, D. C., Sargent, M. T., Delhaize, J., et al. 2018, MNRAS, 475, 827 102, 103, 119, 127, 129, 153, 159, 160

Moore, B., Katz, N., Lake, G., Dressler, A., & Oemler, A. 1996, Nature, 379, 613 32

Morganti, R. 2017, Nature Astronomy, 1, 39 32

Morić, I., Smolčić, V., Kimball, A., et al. 2010, ApJ, 724, 779 97

Moriondo, G., Giovanelli, R., & Haynes, M. P. 1998, A&A, 338, 795 40

Morselli, L., Renzini, A., Popesso, P., & Erfanianfar, G. 2016, MNRAS, 462, 2355 50

Moshir, M., & et al. 1990, in IRAS Faint Source Catalogue, version 2.0 (1990), 0 44, 46

Mosleh, M., Tacchella, S., Renzini, A., et al. 2017, ApJ, 837, 2 28

Moster, B. P., Macciò, A. V., Somerville, R. S., Naab, T., & Cox, T. J. 2012, MNRAS, 423, 2045 30

Moustakas, J., & Kennicutt, Jr., R. C. 2006, ApJS, 164, 81 149

Muñoz-Mateos, J. C., Gil de Paz, A., Boissier, S., et al. 2009, ApJ, 701, 1965 40

Mueller, M. W., & Arnett, W. D. 1976, ApJ, 210, 670 22

Mullaney, J. R., Pannella, M., Daddi, E., et al. 2012, MNRAS, 419, 95 32

Murdin, P., ed. 2000, Kant, Immanuel (1724-1804) (Encyclopedia of Astronomy and Astrophysics), 3759 11

Murphy, E. J., Condon, J. J., Schinnerer, E., et al. 2011, ApJ, 737, 67 50, 71, 90

Murray, N. 2011, ApJ, 729, 133 17

Mutlu-Pakdil, B., Seigar, M. S., & Davis, B. L. 2016, ApJ, 830, 117 9

Muzzin, A., Marchesini, D., Stefanon, M., et al. 2013, ApJ, 777, 18 30, 117

Natta, A., & Panagia, N. 1984, ApJ, 287, 228 72

Navarro, J. F., Frenk, C. S., & White, S. D. M. 1997, ApJ, 490, 493 12, 14, 165

Nelson, D., Pillepich, A., Springel, V., et al. 2018, MNRAS, 475, 624 33, 34, 66

Nelson, E. J., van Dokkum, P. G., Förster Schreiber, N. M., et al. 2016, ApJ, 828, 27 33

Nipoti, C., Giocoli, C., & Despali, G. 2018, MNRAS, 476, 705 9

Noda, H., & Done, C. 2018, MNRAS, 480, 3898 155

Noeske, K. G., Weiner, B. J., Faber, S. M., et al. 2007, ApJL, 660, L43 28, 52, 91

Novak, M., Smolčić, V., Schinnerer, E., et al. 2018, A&A, 614, A47 90

Novak, M., Smolčić, V., Delhaize, J., et al. 2017, A&A, 602, A5 90, 102, 117

Nulsen, P. E. J., Stewart, G. C., Fabian, A. C., et al. 1982, MNRAS, 199, 1089 32

Odewahn, S. C., Cohen, S. H., Windhorst, R. A., & Philip, N. S. 2002, ApJ, 568, 539 24

Oesch, P. A., Bouwens, R. J., Illingworth, G. D., et al. 2013, ApJ, 773, 75 90

Oesch, P. A., Brammer, G., van Dokkum, P. G., et al. 2016, ApJ, 819, 129 7

Ohno, H., & Shibata, S. 1993, MNRAS, 262, 953 19

Oliver, S. J., Bock, J., Altieri, B., et al. 2012, MNRAS, 424, 1614 94

Overzier, R. A., Heckman, T. M., Wang, J., et al. 2011, ApJL, 726, L7 76

Paccagnella, A., Vulcani, B., Poggianti, B. M., et al. 2016, ApJ, 816, L25 129

Padilla, N. D., & Strauss, M. A. 2008, MNRAS, 388, 1321 21

Padmanabhan, N., Schlegel, D. J., Finkbeiner, D. P., et al. 2008, ApJ, 674, 1217 45

Padovani, P. 2016, A&A Rv, 24, 13 141

Pannella, M., Carilli, C. L., Daddi, E., et al. 2009a, ApJL, 698, L116 65, 90, 148

Pannella, M., Gabasch, A., Goranova, Y., et al. 2009b, ApJ, 701, 787 119

Pannella, M., Elbaz, D., Daddi, E., et al. 2015, ApJ, 807, 141 65, 66, 90, 148

Papovich, C., Dickinson, M., Giavalisco, M., Conselice, C. J., & Ferguson, H. C. 2005, ApJ, 631, 101 25

Papovich, C., Labbé, I., Quadri, R., et al. 2015, ApJ, 803, 26 8

Patel, S. G., Holden, B. P., Kelson, D. D., et al. 2012, ApJL, 748, L27 47

Patel, S. G., van Dokkum, P. G., Franx, M., et al. 2013, ApJ, 766, 15 8

Pavesi, R., Sharon, C. E., Riechers, D. A., et al. 2018, ApJ, 864, 49 17

Pearson, W. J., Wang, L., Hurley, P. D., et al. 2018, A&A, 615, A146 91, 112, 113, 118, 120, 125, 158

Peebles, P. J. E. 1980, The large-scale structure of the universe (Princeton University Press) 6

Peebles, P. J. E., & Ratra, B. 2003, Rev. Mod. Phys., 75, 559 9

Peek, J. E. G., & Schiminovich, D. 2013, ApJ, 771, 68 45

Peletier, R. F., & Willner, S. P. 1992, AJ, 103, 1761 40

Peng, Y.-j., Lilly, S. J., Kovač, K., et al. 2010, ApJ, 721, 193 31, 91, 128

Pérez-González, P. G., Kennicutt, Jr., R. C., Gordon, K. D., et al. 2006, ApJ, 648, 987 40

Pillepich, A., Springel, V., Nelson, D., et al. 2018, MNRAS, 473, 4077 33

Planck Collaboration, Ade, P. A. R., Aghanim, N., et al. 2014, A&A, 571, A16 5

—. 2016, A&A, 594, A13 13

Poglitsch, A., Waelkens, C., Geis, N., et al. 2010, A&A, 518, L2 43, 44

Polletta, M., Tajer, M., Maraschi, L., et al. 2007, ApJ, 663, 81 94

Popescu, C. C., Misiriotis, A., Kylafis, N. D., Tuffs, R. J., & Fischera, J. 2000, A&A, 362, 138 56

Popescu, C. C., & Tuffs, R. J. 2008, in American Institute of Physics Conference Series, Vol. 1043, American Institute of Physics Conference Series, ed. V. Mioc, C. Dumitrche, & N. A. Popescu, 380–386 40

Popescu, C. C., Tuffs, R. J., Dopita, M. A., et al. 2011, A&A, 527, A109 40, 58, 59, 73, 79, 80, 140

Popescu, C. C., Tuffs, R. J., Madore, B. F., et al. 2005, ApJL, 619, L75 40

Popesso, P., Biviano, A., Finoguenov, A., et al. 2015, A&A, 579, A132 130

Popesso, P., Concas, A., Morselli, L., et al. 2019, MNRAS, 483, 3213 104, 112, 125, 128

Popping, G., Somerville, R. S., & Galametz, M. 2017, MNRAS, 471, 3152 67, 144

Prandoni, I., & Seymour, N. 2015, in Advancing Astrophysics with the Square Kilometre Array (AASKA14), 67 141

Pritchard, J. R., & Loeb, A. 2012, Reports on Progress in Physics, 75, 086901 7

Putman, M. E., Gibson, B. K., Staveley-Smith, L., et al. 1998, Nature, 394, 752 11

Ramasawmy, J., Stevens, J., Martin, G., & Geach, J. E. 2019, MNRAS, 1037 32

Reddy, N., Dickinson, M., Elbaz, D., et al. 2012, ApJ, 744, 154 112, 148

Reddy, N. A., Erb, D. K., Pettini, M., Steidel, C. C., & Shapley, A. E. 2010, ApJ, 712, 1070 148

Rees, M. J., & Ostriker, J. P. 1977, MNRAS, 179, 541 8, 15

Rémy-Ruyer, A., Madden, S. C., Galliano, F., et al. 2014, A&A, 563, A31 68

Renne, P. R., Deino, A. L., Hilgen, F. J., et al. 2013, Science, 339, 684 3

Renzini, A., & Peng, Y.-j. 2015, ApJ, 801, L29 104

Reynolds, R. J. 1984, ApJ, 282, 191 18

—. 1989, ApJ, 339, L29 18

Rhee, J., Lah, P., Briggs, F. H., et al. 2018, MNRAS, 473, 1879 13, 17

Ricciardelli, E., Cava, A., Varela, J., & Quilis, V. 2014, MNRAS, 445, 4045 128

Riess, A. G., Filippenko, A. V., Challis, P., et al. 1998, The Astronomical Journal, 116, 1009 9

Roberts, M. S., & Rots, A. H. 1973, A&A, 26, 483 12

Rodighiero, G., Cimatti, A., Gruppioni, C., et al. 2010, A&A, 518, L25 115

Rodighiero, G., Daddi, E., Baronchelli, I., et al. 2011, ApJ, 739, L40 112

Rodriguez-Gomez, V., Snyder, G. F., Lotz, J. M., et al. 2019, MNRAS, 483, 4140 16

Rodríguez-Muñoz, L., Rodighiero, G., Mancini, C., et al. 2019, MNRAS, 485, 586 129

Rodríguez-Puebla, A., Primack, J. R., Behroozi, P., & Faber, S. M. 2016, MNRAS, 455, 2592 28

Rosario, D. J., Santini, P., Lutz, D., et al. 2012, A&A, 545, A45 32

Rowlands, K., Dunne, L., Dye, S., et al. 2014, MNRAS, 441, 1017 67

Rubin, V. C., Ford, W. K., J., & Thonnard, N. 1978, ApJ, 225, L107 12

—. 1980, ApJ, 238, 471 12

Ryden, B., & Pogge, R. 2016, Interstellar and Intergalactic Medium (The Ohio State University) 16

Sabater, J., Best, P. N., Hardcastle, M. J., et al. 2019, A&A, 622, A17 156

Sackmann, I. J., Boothroyd, A. I., & Kraemer, K. E. 1993, ApJ, 418, 457 10

Salim, S., Boquien, M., & Lee, J. C. 2018, ApJ, 859, 11 143

Salim, S., Lee, J. C., Janowiecki, S., et al. 2016, ApJS, 227, 2 45, 142

Salmi, F., Daddi, E., Elbaz, D., et al. 2012, ApJL, 754, L14 145

Salmon, B., Papovich, C., Long, J., et al. 2016, ApJ, 827, 20 72

Sánchez, S. F., Kennicutt, R. C., Gil de Paz, A., et al. 2012, A&A, 538, A8 28

Sánchez, S. F., Barrera-Ballesteros, J. K., Sánchez-Menguiano, L., et al. 2017, MNRAS, 469, 2121 28

Sandage, A. 1961, The Hubble Atlas of Galaxies (Carnegie Institution) 21, 25

—. 1975, Classification and Stellar Content of Galaxies Obtained from Direct Photography, ed. A. Sandage, M. Sandage, & J. Kristian (Chicago Press), 1 20

Sanders, D. B., Salvato, M., Aussel, H., et al. 2007, ApJS, 172, 86 44

Sandstrom, K. M., Leroy, A. K., Walter, F., et al. 2013, ApJ, 777, 5 67

Santini, P., Maiolino, R., Magnelli, B., et al. 2014, A&A, 562, A30 68, 72

Santini, P., Fontana, A., Castellano, M., et al. 2017, ApJ, 847, 76 158

Sargent, M. T., Béthermin, M., Daddi, E., & Elbaz, D. 2012, ApJ, 747, L31 67, 107, 112

Sargent, M. T., Carollo, C. M., Lilly, S. J., et al. 2007, ApJS, 172, 434 24, 43, 45, 73, 98

Sargent, M. T., Schinnerer, E., Murphy, E., et al. 2010, ApJ, 714, L190 41, 42, 46, 59, 102

Sargent, M. T., Daddi, E., Béthermin, M., et al. 2014, ApJ, 793, 19 53, 67, 68, 74, 146, 158, 159

Scarlata, C., Carollo, C. M., Lilly, S., et al. 2007, ApJS, 172, 406 24, 43, 98, 118, 139

Schaefer, A. L., Croom, S. M., Scott, N., et al. 2019, MNRAS, 483, 2851 129

Schawinski, K., Koss, M., Berney, S., & Sartori, L. F. 2015, MNRAS, 451, 2517 32, 155

Schawinski, K., Lintott, C., Thomas, D., et al. 2009, MNRAS, 396, 818 26

Schawinski, K., Urry, C. M., Simmons, B. D., et al. 2014, MNRAS, 440, 889 25

Schechter, P. 1976, ApJ, 203, 297 115

Schinnerer, E., Carilli, C. L., Scoville, N. Z., et al. 2004, AJ, 128, 1974 91

Schinnerer, E., Smolčić, V., Carilli, C. L., et al. 2007, The Astrophysical Journal Supplement Series, 172, 46 91

Schinnerer, E., Sargent, M. T., Bondi, M., et al. 2010, The Astrophysical Journal Supplement Series, 188, 384 91, 92

Schinnerer, E., Groves, B., Sargent, M. T., et al. 2016, ApJ, 833, 112 17

Schlegel, D. J., Finkbeiner, D. P., & Davis, M. 1998, ApJ, 500, 525 42

Schleicher, D. R. G., & Beck, R. 2013, A&A, 556, A142 143

Schreiber, C., Elbaz, D., Pannella, M., et al. 2016, A&A, 589, A35 127, 128

Schreiber, C., Pannella, M., Elbaz, D., et al. 2015, A&A, 575, A74 55, 67, 91, 101, 106, 107, 109, 110, 112, 125, 130, 145, 146, 147, 150, 159

Scoville, N., Abraham, R. G., Aussel, H., et al. 2007, ApJS, 172, 38 36, 92

Scoville, N., Arnouts, S., Aussel, H., et al. 2013, The Astrophysical Journal Supplement Series, 206, 3 49, 98, 120, 122, 123, 161

Scoville, N., Aussel, H., Sheth, K., et al. 2014, ApJ, 783, 84 17

Scoville, N., Lee, N., Vanden Bout, P., et al. 2017, ApJ, 837, 150 13, 140

Sersic, J. L. 1968, Atlas de Galaxias Australes (Cordoba, Argentina: Observatorio Astronomico) 24

Seymour, N., Huynh, M., Dwelly, T., et al. 2009, MNRAS, 398, 1573 102

Shankar, F., Salucci, P., Granato, G. L., De Zotti, G., & Danese, L. 2004, MNRAS, 354, 1020 9

Shao, Z., Xiao, Q., Shen, S., et al. 2007, ApJ, 659, 1159 46

Shen, S., Mo, H. J., White, S. D. M., et al. 2003, MNRAS, 343, 978 28

Shivaei, I., Reddy, N. A., Shapley, A. E., et al. 2015, ApJ, 815, 98 159

Shlosman, I. 2013, in Secular Evolution of Galaxies, by Jesús Falcón-Barroso, and Johan H. Knapen, Cambridge, UK: Cambridge University Press, 2013, p.555, ed. J. Falcón-Barroso & J. H. Knapen, 555 15

Shull, J. M., Smith, B. D., & Danforth, C. W. 2012, ApJ, 759, 23 9, 13

Silk, J. 1977, ApJ, 211, 638 8

—. 2013, ApJ, 772, 112 32

Simard, L., Mendel, J. T., Patton, D. R., Ellison, S. L., & McConnachie, A. W. 2011, ApJS, 196, 11 24, 45, 48, 49, 73

Simard, L., Willmer, C. N. A., Vogt, N. P., et al. 2002, ApJS, 142, 1 43

Simon, L. E., & Hamann, F. 2010, MNRAS, 407, 1826 20

Siudek, M., Małek, K., Scodeggio, M., et al. 2017, A&A, 597, A107 115

Smith, D. J. B., Dunne, L., da Cunha, E., et al. 2012, MNRAS, 427, 703 67

Smith, J. D. T., Draine, B. T., Dale, D. A., et al. 2007, ApJ, 656, 770 78

Smith, M. W. L., Eales, S. A., De Looze, I., et al. 2016, MNRAS, 462, 331 40

Smolčić, V. 2009, ApJ, 699, L43 97, 156

Smolčić, V., Novak, M., Bondi, M., et al. 2017a, A&A, 602, A1 37, 42, 43, 44, 94, 101, 102, 155

Smolčić, V., Delvecchio, I., Zamorani, G., et al. 2017b, A&A, 602, A2 37, 43, 44, 90, 92, 102, 138, 151

Sobral, D., Best, P. N., Smail, I., et al. 2014, MNRAS, 437, 3516 113

Somerville, R. S., & Davé, R. 2015, Annual Review of Astronomy and Astrophysics, 53, 51 29, 33

Sparke, L. S., & Gallagher, John S., I. 2000, Galaxies in the universe : an introduction (Cambridge University Press) 22

Speagle, J. S., Steinhardt, C. L., Capak, P. L., & Silverman, J. D. 2014, ApJS, 214, 15 53, 91, 96, 106, 107, 109, 111, 112, 120, 145, 146, 147, 150, 159

Spergel, D., Gehrels, N., Baltay, C., et al. 2015, arXiv e-prints, arXiv:1503.03757 144

Spinoglio, L., Alonso-Herrero, A., Armus, L., et al. 2017, PASA, 34, e057 144

Springel, V. 2005, MNRAS, 364, 1105 29

—. 2010, ARA&A, 48, 391 33

Stanley, F., Harrison, C. M., Alexander, D. M., et al. 2015, MNRAS, 453, 591 32

Starkenburg, T. K., Tonnesen, S., & Kopenhafer, C. 2019, ApJ, 874, L17 33

Steidel, C. C., Giavalisco, M., Pettini, M., Dickinson, M., & Adelberger, K. L. 1996, ApJ, 462, L17 25

Stiavelli, M. 2009, From First Light to Reionization: The End of the Dark Ages (Wiley) 8

Stocke, J. T., Keeney, B. A., Danforth, C. W., et al. 2013, ApJ, 763, 148 9

Stott, J. P., Swinbank, A. M., Johnson, H. L., et al. 2016, MNRAS, 457, 1888 88

Strateva, I., Ivezić, Ž., Knapp, G. R., et al. 2001, AJ, 122, 1861 25

Su, K.-Y., Hopkins, P. F., Hayward, C. C., et al. 2018, arXiv e-prints, arXiv:1809.09120 128

Szomoru, D., Franx, M., Bouwens, R. J., et al. 2011, ApJ, 735, L22 25

Tabatabaei, F. S., Schinnerer, E., Krause, M., et al. 2017, ApJ, 836, 185 90, 143

Tacchella, S., Dekel, A., Carollo, C. M., et al. 2016, MNRAS, 457, 2790 11, 110

Tacchella, S., Trenti, M., & Carollo, C. M. 2013, ApJ, 768, L37 8

Tacchella, S., Lang, P., Carollo, C. M., et al. 2015, ApJ, 802, 101 29

Tacchella, S., Carollo, C. M., Forster Schreiber, N. M., et al. 2017, ArXiv e-prints, arXiv:1704.00733 68

Tacconi, L. J., Neri, R., Genzel, R., et al. 2013, ApJ, 768, 74 52

Tacconi, L. J., Genzel, R., Saintonge, A., et al. 2017, ArXiv e-prints, arXiv:1702.01140 67, 68

—. 2018, ApJ, 853, 179 140

Takamiya, M. 1999, ApJS, 122, 109 25

Tasca, L. A. M., Le Fèvre, O., Hathi, N. P., et al. 2015, A&A, 581, A54 67, 110

Taylor, E. N., Hopkins, A. M., Baldry, I. K., et al. 2011, MNRAS, 418, 1587 44

Taylor, M. B. 2005, in Astronomical Society of the Pacific Conference Series, Vol. 347, Astronomical Data Analysis Software and Systems XIV, ed. P. Shopbell, M. Britton, & R. Ebert, 29 201

Thomas, D., Maraston, C., Schawinski, K., Sarzi, M., & Silk, J. 2010, MNRAS, 404, 1775 115

Tielens, A. G. G. M. 2005, The Physics and Chemistry of the Interstellar Medium (Cambridge University Press) 18

Tinsley, B. M. 1980, FCPh, 5, 287 16

Tisanić, K., Smolčić, V., Delhaize, J., et al. 2019, A&A, 621, A139 143

Tojeiro, R., Masters, K. L., Richards, J., et al. 2013, MNRAS, 432, 359 25

Tomczak, A. R., Quadri, R. F., Tran, K.-V. H., et al. 2014, ApJ, 783, 85 30

—. 2016, ApJ, 817, 118 91, 106, 107, 109, 112, 115, 139, 159

Torrey, P., Vogelsberger, M., Hernquist, L., et al. 2018, MNRAS, 477, L16 107

Trayford, J. W., Camps, P., Theuns, T., et al. 2017, MNRAS, 470, 771 66

Tremonti, C. A., Heckman, T. M., Kauffmann, G., et al. 2004, ApJ, 613, 898 28

Treyer, M., Schiminovich, D., Johnson, B. D., et al. 2010, ApJ, 719, 1191 78

Trinkaus, E. 2005, Annual Review of Anthropology, 34, 207 3

Tuffs, R. J., Popescu, C. C., Völk, H. J., Kylafis, N. D., & Dopita, M. A. 2004, A&A, 419, 821 41, 43, 55, 56, 58, 59, 65, 66, 73, 75, 79, 80, 87, 146

Tully, R. B., & Fisher, J. R. 1977, A&A, 500, 105 27

Tully, R. B., Pierce, M. J., Huang, J.-S., et al. 1998, AJ, 115, 2264 40

Turner, O. J., Cirasuolo, M., Harrison, C. M., et al. 2017, MNRAS, 471, 1280 88

Tyler, K. D., Bai, L., & Rieke, G. H. 2014, ApJ, 794, 31 128

Tyler, K. D., Rieke, G. H., & Bai, L. 2013, ApJ, 773, 86 128

Valentijn, E. A. 1990, Nature, 346, 153 40

van de Sande, J., Scott, N., Bland-Hawthorn, J., et al. 2018, Nature Astronomy, 2, 483 28

van der Kruit, P. C., & Freeman, K. C. 2011, ARA&A, 49, 301 22

van der Marel, R. P., Besla, G., Cox, T. J., Sohn, S. T., & Anderson, J. 2012, ApJ, 753, 9 10

van der Wel, A., Franx, M., van Dokkum, P. G., et al. 2014, ApJ, 788, 28 8, 28, 152

van der Wel, A., Noeske, K., Bezanson, R., et al. 2016, ApJS, 223, 29 143

van Dokkum, P. G. 2001, arXiv e-prints, astro 34

van Dokkum, P. G., Whitaker, K. E., Brammer, G., et al. 2010, ApJ, 709, 1018 8

Vardoulaki, E., Jiménez Andrade, E. F., Karim, A., et al. 2019, arXiv e-prints, arXiv:1901.10168 92, 97, 156

Veilleux, S., Cecil, G., & Bland-Hawthorn, J. 2005, ARA&A, 43, 769 32

Venemans, B. P., Walter, F., Decarli, R., et al. 2017, ApJ, 851, L8 20

Viero, M. P., Wang, L., Zemcov, M., et al. 2013, ApJ, 772, 77 122

Villaver, E., & Livio, M. 2007, ApJ, 661, 1192 11

Vito, F., Gilli, R., Vignali, C., et al. 2014, MNRAS, 445, 3557 155

Vlahakis, C., Dunne, L., & Eales, S. 2005, MNRAS, 364, 1253 9

Volonteri, M. 2012, Science, 337, 544 19

von der Linden, A., Wild, V., Kauffmann, G., White, S. D. M., & Weinmann, S. 2010, MNRAS, 404, 1231 129

Walcher, J., Groves, B., Budavári, T., & Dale, D. 2011, Ap&SS, 331, 1 12

Walter, F., Brinks, E., de Blok, W. J. G., et al. 2008, AJ, 136, 2563 16

Walter, F., Decarli, R., Sargent, M., et al. 2014, ApJ, 782, 79 9

Wang, L., Norberg, P., Gunawardhana, M. L. P., et al. 2016, MNRAS, 461, 1898 77, 78, 81, 82, 148

Wang, W., Faber, S. M., Liu, F. S., et al. 2017, MNRAS, 469, 4063 68

Weinberger, R., Springel, V., Hernquist, L., et al. 2017, MNRAS, 465, 3291 33

Whitaker, K. E., Pope, A., Cybulski, R., et al. 2017, ApJ, 850, 208 67, 118

Whitaker, K. E., van Dokkum, P. G., Brammer, G., & Franx, M. 2012, ApJ, 754, L29 28, 112

Whitaker, K. E., Labbé, I., van Dokkum, P. G., et al. 2011, ApJ, 735, 86 114

Whitaker, K. E., Franx, M., Leja, J., et al. 2014, ApJ, 795, 104 28, 65, 91, 104, 138, 145, 148

Whitaker, K. E., Franx, M., Bezanson, R., et al. 2015, ApJL, 811, L12 28, 145

White, III, R. E., Keel, W. C., & Conselice, C. J. 2000, ApJ, 542, 761 40

White, R. L., Helfand, D. J., Becker, R. H., Glikman, E., & de Vries, W. 2007, ApJ, 654, 99 115, 152

White, S. D. M., & Frenk, C. S. 1991, ApJ, 379, 52 29

White, S. D. M., & Rees, M. J. 1978, MNRAS, 183, 341 15, 29

Wild, V., Charlot, S., Brinchmann, J., et al. 2011, MNRAS, 417, 1760 87

Wilde, S. A., Valley, J. W., .H., P. W., & C.M., G. 2001, Nature, 409, 175 3

Williams, R. J., Quadri, R. F., Franx, M., van Dokkum, P., & Labbé, I. 2009, ApJ, 691, 1879 43

Williams, R. J., Quadri, R. F., Franx, M., et al. 2010, ApJ, 713, 738 59

Wisnioski, E., Förster Schreiber, N. M., Wuyts, S., et al. 2015, ApJ, 799, 209 9, 66

Wolf, M. 1909, Publikationen des Astrophysikalischen Instituts Koenigstuhl-Heidelberg, 3, 149 20

Wolfire, M. G., & Konigl, A. 1991, ApJ, 383, 205 17

Wong, O. I., Koss, M. J., Schawinski, K., et al. 2016, MNRAS, 460, 1588 90

Wright, A. H., Robotham, A. S. G., Driver, S. P., et al. 2017, MNRAS, 470, 283 9

Wright, E. L., Eisenhardt, P. R. M., Mainzer, A. K., et al. 2010, AJ, 140, 1868 44, 45

Wright, T. 1750, An original theory or new hypothesis of the universe : founded upon general phaenomena of the visible creation; and particularly the Via the laws of nature, and solving by mathematical principles : the Lactea ...compris'd in nine familiar letters from the author to his friendand : illustrated with upward of thirty graven and mezzotinto plates ..., doi:10.3931/e-rara-28672 11

Wuyts, S., Labbé, I., Förster Schreiber, N. M., et al. 2008, ApJ, 682, 985 50, 78, 79, 85, 86

Wuyts, S., Förster Schreiber, N. M., van der Wel, A., et al. 2011a, ApJ, 742, 96 25, 28, 29, 91, 106, 125

—. 2011b, ApJ, 742, 96 50, 65, 66, 68, 148

Wuyts, S., Förster Schreiber, N. M., Lutz, D., et al. 2011c, ApJ, 738, 106 50, 72

Wuyts, S., Förster Schreiber, N. M., Genzel, R., et al. 2012, ApJ, 753, 114 8

Xilouris, E. M., Byun, Y. I., Kylafis, N. D., Paleologou, E. V., & Papamastorakis, J. 1999, A&A, 344, 868 40

Yang, X., Mo, H. J., & van den Bosch, F. C. 2009, ApJ, 695, 900 27

Yip, C.-W., Szalay, A. S., Wyse, R. F. G., et al. 2010, ApJ, 709, 780 47

York, D. G., Adelman, J., Anderson, Jr., J. E., et al. 2000, AJ, 120, 1579 36

Young, J. S., & Scoville, N. Z. 1991, ARA&A, 29, 581 17

Yuan, Q.-r., & Zhu, C.-x. 2004, Chinese Astronomy and Astrophysics, 28, 127 46

Yun, M. S., Reddy, N. A., & Condon, J. J. 2001, ApJ, 554, 803 102, 141, 142

Zahid, H. J., Dima, G. I., Kewley, L. J., Erb, D. K., & Davé, R. 2012, ApJ, 757, 54 52

Zahid, H. J., Dima, G. I., Kudritzki, R.-P., et al. 2014, ApJ, 791, 130 67, 143

Zamojski, M. A., Schiminovich, D., Rich, R. M., et al. 2007, ApJS, 172, 468 50, 94

Zaritsky, D., Zabludoff, A. I., & Gonzalez, A. H. 2008, ApJ, 682, 68 28

Zwaan, M. A., Meyer, M. J., Staveley-Smith, L., & Webster, R. L. 2005, MNRAS, 359, L30 9

Zwart, J. T. L., Jarvis, M. J., Deane, R. P., et al. 2014, MNRAS, 439, 1459 90

Zwicky, F. 1933, Helvetica Physica Acta, 6, 110 12

Acknowledgements

Thesis Comitee

First and foremost, I would like to thank my supervisor Eva Schinnerer. Thank you for selecting me to undertake my PhD studies with you. I am excited by the science being done by our group and look forward to continued collaboration. Thank you for being understanding and encouraging. Thank you for letting me choose my own path. Thank you for always providing feedback and for supporting my attendance at many conferences. I would like to acknowledge financial support from Deutsche Forschungsgemeinschaft (DFG) Grant BE 1837 / 13-1 r.

I would like to thank my thesis committee members Prof. Ralf Klessen and Prof. Hans-Walter Rix for your scientific advice and for kindly agreeing to referee this work.

Scientific collaborators

Thanks to Daizhong Liu and Philipp Lang, the COSMOS post-docs in our group for our weekly meetings. Thanks to Mark Sargent and Brent Groves for being essential collaborators on the papers presented in this thesis.

Thanks to our collaborators in Bonn and the A^{3}COSMOS team: Alex Karim, Benjamin Magnelli, Eric Jimenez-Andrade, Eleni Vardoulaki, Frank Bertoldi, Kevin Harrington, Toma Badescu.

Thanks to the VLA-COSMOS team and others in the RMS-COSMOS: Vernesa Smolčić, Jacinta Delhaize, Mladen Novak, Daniel Molnar, Ivan Delvecchio, Marco Bondi, Lana Ceraj, Paolo Ciliegi, Yoshinobu Fudamoto, Oskari Miettinen, Giovanni Zamorani, Krešimir Tisanić.

Thanks to the extended COSMOS family: particularly, Jeyhan Kartaltepe, Caitlin Casey, Iary Davidzon, Andreas Faisst, Ivana Barišić, Conor McPartland, Ghassem Gozaliasl, and for the leadership of Peter Capak and Nic Scoville. Thank you Iary for sharing your photo-z catalogue, and to Ghassem for sharing your X-ray group member catalogues for chapter 3.

Thanks to people who helped me propose for and reduce ALMA data that did not make it into this thesis: Miguel Querejeta Daizhong Liu, Toshiki Saito, Nick Lee, Kartik Seth. Thanks to Dániel Molnár for all your hard work on the local IRRC correlation.

Life and Science at MPIA

It has been a pleasure to be a part of the Galaxy and Cosmology department at MPIA; so thank you to our director Hans-Walter Rix for cultivating an excellent scientific work environment. Thanks to my office mates Christina Eilers, Felix Bosco, Nico Krieger, Jakob Herpich, and Simon Bihr for your company and support. Thank you, Felix, for your careful translating of the abstract. I would like to acknowledge the IMPRS-HD program run by Christian Fendt. I was very happy to be a member of the 12th generation. Thank you also to the 11th generation for adopting

me when I joined in January 2016. Thanks to the Schinnerer group members for making me feel welcome and for our discussions. Current members: I-Ting Ho, Kathryn Kreckel, Rebecca McElroy, Neven Tomčić, Toshiki Saito, Francesco Santoro, Ismael Pessa, Daizhong Liu, Philipp Lang. Past members: Miguel Querejeta, Paolo Bianchini, Emer Brady (my predecessor), Sharon Meidt. Thanks to all the students and postdocs at MPIA for friendship and for coffee. Thank you to my thesis writing peers, Alex Hygate, Marcelo Tala Pinto, Hans Baehr, Matthias Samland for joining me in the library, and to Andreas Schreiber for sharing his Latex template. Thanks, Neven for letting me sit in your defence. I appreciate the support received from MPIA staff members, particularly Uli Hiller from IT, and Ingrid Apfel, Ina Beckmann and Heide Seifert from the administration.

Career development

Thanks to Lisa Kewley, my undergraduate and masters advisor for writing me reference letters and taking the time to mentor me. I always appreciate your advice. Thank you also to Dave Sanders and Mark Sargent for writing me letters of reference for. Thanks to Jacqueline Hodge for supporting my application for the Oort Fellowship in Leiden. Other people not previously mentioned who gave me mentoring and career advice that I valued include Ashley Ruiter, Anne Medling, Jabran Zahid, Katherine Alatalo, Elizabete Da Cunha, Annalisa Pillepich, Ilse Cleeves, and Rosalie McGurk.

Personal

Thanks to James Leslie my husband for your love and support every day. Thanks to my friends Melanie K and Melanie H for looking out for me during stressful times. Thank you to everyone in my family for supporting my decisions, such as studying astrophysics in Germany. Thank you, Russell Leslie, for proofreading my job applications and this thesis. I'm very grateful for the time you spent reading and understanding my work.

Facilities and software acknowledgements:

Based on data products from observations made with ESO Telescopes at the La Silla Paranal Observatory under ESO programme ID 179.A-2005 and on data products produced by TERAPIX and the Cambridge Astronomy Survey Unit on behalf of the UltraVISTA consortium. Based on observations obtained with XMM-Newton, an ESA science mission with instruments and contributions directly funded by ESA Member States and NASA. The National Radio Astronomy Observatory is a facility of the National Science Foundation operated under cooperative agreement by Associated Universities, Inc. AllWISE makes use of data from WISE, which is a joint project of the University of California, Los Angeles, and the Jet Propulsion Laboratory/California Institute of Technology, and NEOWISE, which is a project of the Jet Propulsion Laboratory/California Institute of Technology. WISE and NEOWISE are funded by the National Aeronautics and Space Administration.

This research has made use of Astropy13, a community-developed core Python package for Astronomy (Astropy Collaboration et al., 2013) and the CORNER python package (Foreman-Mackey, 2016). This research has made use of NumPy(Walt et al., 2011), SciPy, and MatPlotLib (Hunter, 2007).

This research has made use of NASA's Astrophysics Data System. This research has made use of the NASA/IPAC Infrared Science Archive, which is operated by the Jet Propulsion Laboratory, California Institute of Technology, under contract with the National Aeronautics and Space

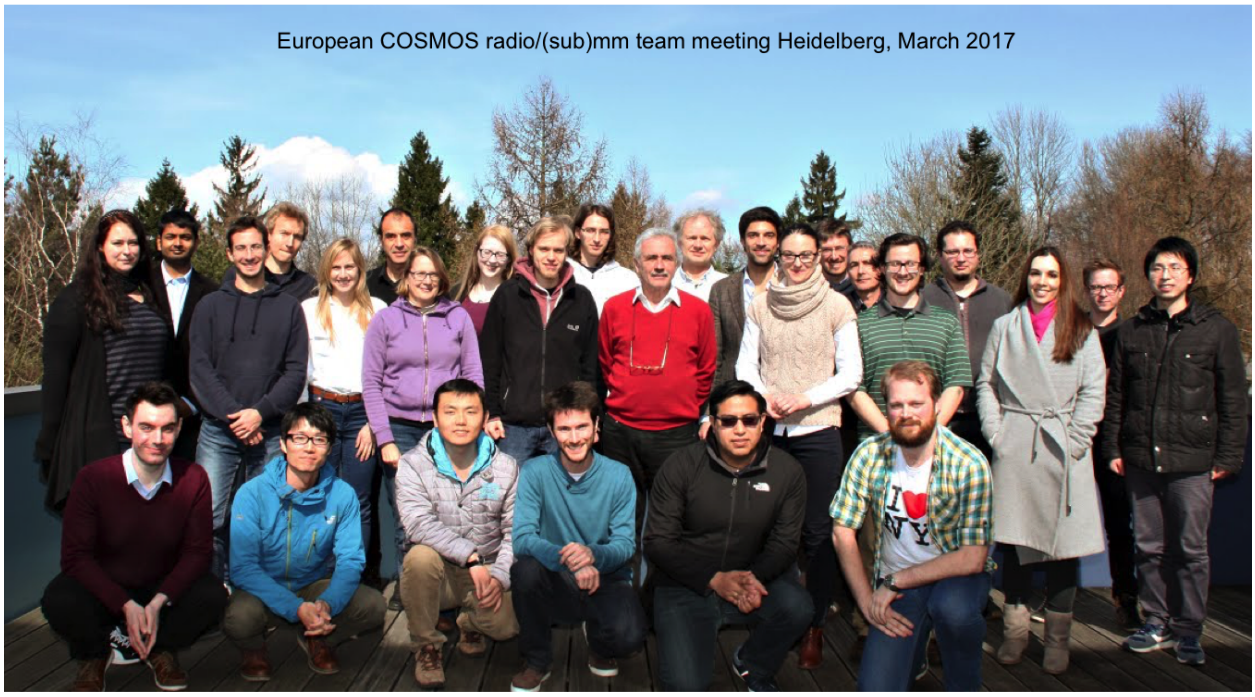

Administration. This research made use of ds9, a tool for data visualization supported by the Chandra X-ray Science Center (CXC) and the High Energy Astrophysics Science Archive Center (HEASARC) with support from the JWST Mission office at the Space Telescope Science Institute for 3D visualization. This research made use of Astropy, a community-developed core Python package for Astronomy (Astropy Collaboration et al., 2013) This research made use of TOPCAT, an interactive graphical viewer and editor for tabular data (Taylor, 2005). This research has made use of the SVO Filter Profile Service (http://svo2.cab.inta-csic.es/theory/fps/) supported by the Spanish MINECO through grant AyA2014-55216.